Light-matter interactions: Artificial and solid-state crystals embedded in an optical cavity

Dissertation

zur Erlangung des Grades

der Doktorin der Naturwissenschaften

der Naturwissenschaftlich-Technischen Fakultät

der Universität des Saarlandes

und

der Université Grenoble Alpes

von

Katharina Rojan

Saarbrücken / Grenoble

2017

Tag des Kolloquiums: 14.06.2017

Dekan: Univ.-Prof. Dr. Guido Kickelbick

Mitglieder des
Prüfungsausschusses: Prof. Dr. Rolf Pelster
Prof. Dr. Giovanna Morigi
Prof. Dr. Dario Gerace
Dr. Jonathan Keeling
Dr. Adam Wysocki
Dr. Anna Minguzzi
Dr. Maxime Richard

Für meine deutsch-französische Familie.

Das Bekannte ist endlich, das Unbekannte unendlich. Geistig stehen wir auf einer kleinen Insel inmitten eines Ozeans von Unerklärlichkeiten. Unsere Aufgabe ist es, in jeder Generation ein bisschen mehr Land trocken zu legen.
Thomas Henry Huxley

Eidesstattliche Versicherung

Hiermit versichere ich an Eides statt, dass ich die vorliegende Arbeit selbstständig und ohne Benutzung anderer als der angegebenen Hilfsmittel angefertigt habe. Die aus anderen Quellen oder indirekt übernommenen Daten und Konzepte sind unter Angabe der Quelle gekennzeichnet. Die Arbeit wurde bisher weder im In- noch im Ausland in gleicher oder ähnlicher Form in einem Verfahren zur Erlangung eines akademischen Grades vorgelegt.

Ort, Datum

Grenoble, 12.7.2017

_____

Unterschrift

_____

Abstract

This thesis is devoted to the characterization of crystalline structures for quantum technological applications. It is composed of two parts.

In a first project we study the localization transition of one particle in an one-dimensional artificial quasiperiodic crystal, whose potential depends on the particle position. We consider an ultracold atom in an optical lattice, embedded in an optical cavity. The atom strongly couples to the cavity, leading to a second optical potential. The position of the atom within the cavity affects the cavity field, thus the atomic motion backacts on the potential it is subjected to. For incommensurate wavelengths, we show that the competition between the two potentials yields a quasiperiodic potential. We determine the parameters for which we reproduce the Aubry-André model and discuss the effects of the backaction on the localization transition.

In the second project we propose a frequency down-conversion scheme to generate THz radiation using the exciton-phonon coupling in a semiconductor crystal. Our idea is based on a chain of interactions that are naturally present in a pumped semiconductor microcavity. We derive the crucial exciton-phonon coupling, starting from the electron-phonon interaction via the deformation potential and taking into account the crystal symmetry properties. We identify conditions necessary for THz emission, estimate the emission power and show that the exciton-phonon interaction provides a second-order susceptibility.

Zusammenfassung

Diese Arbeit befasst sich mit der Charakterisierung kristalliner Strukturen für quantentechnologische Anwendungen. Sie besteht aus zwei Teilen.

Im ersten Teil untersuchen wir den Lokalisierungsübergang eines Teilchens in einem künstlichen quasiperiodischen Kristall, dessen Potential von der Teilchenposition abhängt. Wir betrachten ein ultrakaltes Atom, in einem optischen Gitter, innerhalb eines optischen Resonators. Die Atom-Resonator-Kopplung führt zu einem zweiten optischen Potential. Die Atomposition beeinflusst das Resonatorfeld. Somit entsteht eine Rückkopplung der Atombewegung auf das Potential. Für inkommensurable Wellenlängen zeigen wir, dass die Überlagerung der beiden Potentiale ein quasiperiodisches Potential zur Folge hat. Wir bestimmen den Parameterbereich, in dem wir das Aubry-André Modell reproduzieren und diskutieren Effekte der Resonatorrückkopplung auf den Lokalisierungsübergang.

Beim zweiten Projekt handelt es sich um ein Frequenzkonversionsschema zur Erzeugung von THz-Strahlung. Unsere Idee beruht auf einer Reihe von Wechselwirkungen in einem gepumpten Halbleiterresonator. Wir leiten die entscheidende Exziton-Phonon-Wechselwirkung, ausgehend von der Elektron-Phonon-Wechselwirkung über das Deformationspotential her, unter Berücksichtigung der Symmetrie des Halbleiters. Wir identifizieren die Bedingungen für THz-Emission, berechnen die Emissionsleistung und zeigen, dass die Exziton-Phonon-Wechselwirkung eine nichtlineare Suszeptibilität zweiter Ordnung liefert.

Résumé

Ce manuscrit est consacré à la caractérisation de structures cristallines pour des applications de technologie quantique. Il est composé de deux parties.

Dans un premier projet, nous étudions la transition d'une particule d'un état étendu à un état localisé dans un cristal artificiel quasipériodique, dont le potentiel dépend de la position de la particule. Nous considérons un atome ultrafroid, confiné par un réseau optique et incorporé dans une cavité optique. Le dipôle atomique est en interaction forte avec le champ électrique dans la cavité, ce qui mène à un deuxième potentiel optique pour l'atome. La position de l'atome dans la cavité influence notamment le champ intracavité : le mouvement de l'atome a donc un effet rétroactif sur le potentiel dans lequel il est confiné. Pour des longueurs d'onde incommensurables, nous montrons que la compétition entre les deux réseaux optiques donne lieu à un potentiel quasipériodique pour l'atome. Nous déterminons les paramètres pour lesquels nous reproduisons le modèle Aubry-André et nous discutons les effets de la rétroaction de la cavité sur la transition de localisation.

Le deuxième projet est une proposition pour générer une radiation THz, en utilisant le couplage entre excitons et phonons dans un cristal semi-conducteur. Nous proposons un schéma de conversion de fréquence, basé sur une chaîne d'interactions naturellement présentes dans une cavité semi-conductrice pompée. La partie cruciale du schéma de conversion de fréquence est l'interaction faible entre des excitons et des phonons transverses optiques. Nous la dérivons en commençant avec l'interaction électron-phonon via le potentiel de déformation et en prenant en compte les propriétés de symétrie du cristal. Nous identifions les conditions nécessaires pour générer une radiation THz, nous estimons la puissance de l'émission et nous montrons que l'interaction entre excitons et phonons transverses optiques fournit une susceptibilité non linéaire d'ordre deux.

Contents

Introduction

Crystals are solids whose building blocks are atoms or groups of atoms that are periodically arranged [1]. As macroscopic objects, crystals seem to be static but many of their properties, such as thermal or electric conductivity, originate from the dynamics of elementary crystal excitations like electrons or vibrations. In this thesis we present two projects that deal with light-matter interaction in different kind of crystals. The projects are based on two distinct platforms that both involve the strong coupling with the electromagnetic field of an optical cavity. On the one hand, we consider a single ultracold atom in an artificial quasiperiodic crystal inside a resonator, in the prospect of quantum simulation of disordered systems. On the other hand, we employ phonons and their coupling with excitons in a semiconductor crystal, embedded in a semiconductor microcavity, to generate THz radiation via a frequency conversion scheme. The two experimental platforms we are dealing with are different and studied in our work for distinct purposes. However they share some common features, such as their driven-dissipative character or the strong coupling with the electromagnetic field of an optical cavity. In both cases we use the same formalism for open quantum systems, i.e. the Heisenberg-Langevin approach. We systematically compare the two platforms, once they both have been introduced, at the end of Chapter 4.

A quantum simulator is a well-known and highly controlled quantum system that mimics the evolution of another complex system that can not easily be studied itself [2]. The idea of simulating nature using quantum mechanical devices comes from Richard F. Feynman [3]. A quantum simulator represents a particularly valuable tool for condensed matter physics, since solid crystals typically consist of many atoms ($\sim 10^{23}/\,\mathrm{cm}^3$) and there are many corresponding degrees of freedom, thus it is impossible to deal with all of them on a classical computer. Neutral ultracold atoms on optical lattices are a well-suited platform for quantum simulation. They can be considered as artificial crystals of light [4], in which the atoms, mimicking the electrons, move in a potential landscape, called optical lattice, that is formed by interfering laser beams. Ultracold atoms in optical lattices

provide desirable features of a quantum simulator as they are clean (defect free), the lattice geometries and dimensions are flexible and the interactions between the atoms can be tuned [2, 4].

A key feature of solid state systems is their electrical conductivity. Thus it is particularly interesting to study metal-insulator transitions and understand what affects electrical conductivity in a solid [5]. The workhorse in this field is the Anderson model [6]. It explains the insulating character of a crystal in spite of the presence of free electrons: As Anderson pointed out, random disorder leads to the metal-insulator transition due to the exponential localization of the wave function of the free carrier. The Anderson model has been realized experimentally using ultracold atoms [7]. One drawback of the Anderson model is that dimensions larger than two are required to observe a transition between an Anderson-localized phase (insulator) and an extended phase (metal), while all the states are localized in one dimension [8]. Furthermore, in condensed matter the random disorder is difficult to control. In contrast, the Aubry-André model [9] or Harper model [10] describes the motion of a single particle in an one-dimensional quasiperiodic lattice and gives rise to a transition from extended to localized already in one dimension. In the quasiperiodic lattice the minima are not randomly distributed as it is the case for the Anderson model: the translation invariance is still broken, but the distribution of the minima follows a rule. The Aubry-André model has been studied experimentally, for example using ultracold atoms and two superimposed optical lattices with incommensurate wavelength [11].

In the first project of this work, we investigate the localization transition of a single particle in a quasiperiodic potential, which dynamically depends on the particle position within the potential landscape. This configuration is realized by a single ultracold atom, confined in an optical lattice within a high-finesse optical cavity. The atom strongly couples to one cavity mode, whose wavelength is incommensurate with the wavelength of the optical lattice. The quasiperiodic potential arises from the superposition of the optical lattice and the effective potential originating from the strong atom-cavity coupling. The cavity field depends on the position of the atom within the resonator [12], thus the atom backacts on the cavity field and correspondingly influences the potential landscape in which it is moving. As an effect of the backaction, the resulting quasiperiodic potential contains higher harmonics than in the usual Aubry-André potential, as we will show in detail in Part I.

In the second project of this thesis, we consider a semiconductor crystal lattice vibration and its coupling to excitons as a resource for THz radiation generation via a frequency

conversion scheme. It is challenging but very desirable to create THz radiation, because THz sources are needed for many applications, e.g. they could complement scientific and medical imaging techniques, increase data transfer rates or improve non-destructive detection [13]. In particular there is a quest for a compact, solid-state based THz source operating at room temperature. Among several existing THz emitting devices, the Quantum Cascade Laser [14, 15] is especially promising since it provides frequency tunability and improving maximum operating temperatures; however room temperature operation still remains a challenge [16].

Alternative strategies for THz radiation emission based on semiconductor microcavities with an embedded semiconductor slab have been put forward. The cavity is externally pumped by a laser. In these systems, the intracavity photons strongly interact with excitons in the semiconductor and form light states dressed with matter [17], the so called exciton-polaritons. Exciton-polaritons are well known in the context of quantum fluids of light [17] and allow e.g. to study out-off equilibrium quantum phase transitions [18, 19]. In this work, we are interested in the fact that the typical splitting between upper and lower exciton-polariton branch amounts to several THz, which makes them natural candidates for THz generation. However there is no direct dipole transition between upper and lower exciton-polariton branch. Several strategies have been proposed to bypass this problem, as e.g. the two-photon excitation of a p exciton state [20] or the use of a noncentrosymmetric semiconductor with intrinsic second-order susceptibility $\chi^{(2)}$ [21], to name a few. In this work, we suggest a frequency conversion scheme which is based on the interaction between transverse optical phonons (TO) and excitons. We show in Part II that this interaction, which is naturally present in the semiconductor, provides an effective second-order susceptibility $\chi^{(2)}$ able to drive visible to THz light conversion.

The thesis is organized as follows: Part I is dedicated to the study of the localization transition of a single ultracold atom in presence of cavity backaction. For this purpose, in Chapter 1, we first introduce ultracold atoms in general and then specify their use in two different environments, namely in an optical lattice or in a high-finesse optical cavity, which we combine in our work. We then present our modified Aubry-André model in Chapter 2, starting with the corresponding Bose-Hubbard Hamiltonian. We show that we reproduce the Aubry-André model in a certain parameter regime. Furthermore we derive the Bose-Hubbard Hamiltonian from a microscopic model of a single ultracold atom in an optical lattice that is dispersively coupled to a single mode of a high-finesse optical cavity. The phase diagrams characterizing the localization transition in presence of cavity backaction are discussed in Chapter 3, as well as possible realizations using existing

experimental setups.

In Part II we discuss the THz radiation emission by phonon-coupled Rabi oscillations of exciton-polaritons. Our proposal is a frequency conversion scheme, relying on a chain of interactions that are naturally present in a semiconductor microcavity. In Chapter 4 we introduce the basics on excitons in semiconductor microcavities and the strong coupling between excitons and photons in microcavities, which leads to the formation of polaritons. For our frequency conversion scheme the interaction between transverse optical phonons and bright excitons is of particular importance. This interaction is derived in Chapter 5, starting from the microscopic structure of the semiconductor of our choice, CdTe. In Chapter 6 we present our frequency conversion scheme which is based on the previously derived exciton-phonon interaction.

Part I.

Localization transition in presence of cavity backaction

Cavity quantum electrodynamics (CQED) with cold atoms provides a rich framework to study the wave-particle duality of light and matter [12, 22, 23]. In this environment, the interaction of a single photon with a single atom has been brought to a level of control that is sensitive to the finite spatial localization of the atom within the cavity mode [24–29]. This property is at the basis of several protocols, which exploit the optomechanical coupling between atoms and photons in CQED in order to cool the atomic motion [12, 30–32], to perform high precision measurements [33], and to create novel sources of quantum light [34–37], to provide some examples.

Cavity backaction, moreover, modifies the dynamics to the extent that photons and atoms become strongly correlated: Since the photon field depends on the atomic position within the resonator, the mechanical forces that the atom experiences depend on the center-of-mass wave function within the cavity mode [38, 39]. This nonlinearity is at the basis of several collective phenomena, such as the formation of spatial patterns [40–42] and exotic phases of ultracold matter [43–47]. Even at the level of a single particle it can give rise to peculiar behaviors as we will see in the following.

In this part, we theoretically investigate the regime in which cavity backaction can induce the transition to localization of the atomic center-of-mass wave function. The system we consider is illustrated in Fig.2.1 (a): a single atom is tightly confined by an external optical lattice within a high-finesse cavity, its dipole strongly couples with one standing-wave mode of the resonator. In the regime in which this coupling is dispersive, the mechanical effects of the cavity field are described by a second periodic potential, that we will derive in Section 1.9. We choose the two lattice wavelengths with periods which are incommensurate with each other. The combination of these two characteristic lengths gives rise to a quasiperiodic potential.

In the limit where the cavity backaction can be neglected, the system is described by the Aubry-André model [9] or the Harper model [10] that we will introduce in details in Section 1.6. It predicts a transition from an extended to a localized phase when the ratio between the depths of the two potentials exceeds a critical value. This localization transition has been observed experimentally, as described in Section 1.7, with ultracold atoms confined by bichromatic optical lattices [11, 48, 49]. The effect of interactions on the Aubry-André model has been investigated theoretically both in the mean-field weakly interacting regime [50] as well as for arbitrary interactions at low lattice filling [51, 52]. Quasiperiodic potentials have also been realized with exciton-polaritons in semiconductor microcavities [53]. The Aubry-André quasiperiodic potential has also been implemented in photonic crystals, where it provides a confinement mechanism for light resulting in a

photonic crystal cavity [54].

Differing from these realizations, the strong coupling with the cavity introduces a novel feature: The depth of the cavity potential is proportional to the number of intracavity photons, as we will show in Section 1.9, which is a dynamical variable coupling optomechanically with the atomic motion. In this setting we will analyze the effect of the cavity backaction on the localization transition and discuss possible experimental regimes where it could be observed.

This part of the thesis is organized as follows. In Chapter 1 we present the basics on ultracold atoms and then specify their use in two different environments, namely in an optical lattice or in a high-finesse optical cavity, which we combine in our work. We briefly discuss relevant experiments and relate them with the theory which will be used in this part. In Chapter 2 we introduce our theoretical model, which encompasses the effect of the cavity nonlinearity, and show that we can recover the Aubry-André model in the limit where the cavity effect is negligible. We then demonstrate how our modified Aubry-André model results from the optomechanical coupling of a single atom with the single mode of a lossy cavity. In Chapter 3 we analyze the phase diagram for the ground state as a function of the cavity parameters, discuss experimental realizations in cavity QED setups, and draw the conclusions to this part.

This part of the thesis is based on the article:

- Katharina Rojan, Rebecca Kraus, Thomás Fogarty, Hessam Habibian, Anna Minguzzi, and Giovanna Morigi, *Localization transition in presence of cavity backaction*, Physical Review A **94**, 013839 (2016).

Chapter 1

Basics on ultracold atoms

In this part of the thesis we study the localization transition of a single ultracold atom confined by an one-dimensional optical lattice, within a high-finesse cavity. The atom-cavity coupling yields an effective secondary lattice potential, whose wavelength is incommensurate with the periodicity of the optical lattice. This configuration has not yet been realized experimentally. In this chapter we discuss experiments that motivated our model and we introduce the necessary theoretical concepts one by one.

We start from ultracold atoms, confined in optical lattices. We review the dynamics of a single particle in an one-dimensional optical lattice. This leads us to the description of N interacting atoms in an optical lattice, in presence of an external potential, via the Bose-Hubbard Hamiltonian in Section 1.5. We then specialize the general Bose-Hubbard Hamiltonian to the case of a single particle subjected to a quasiperiodic lattice. This leads us to introduce the Aubry-André model. We briefly present the experimental realization of this model using noninteracting ultracold atoms in a bichromatic lattice in Section 1.7.

Besides the optical lattice, the second important ingredient for our model is the optical cavity. Ultracold atoms have also been studied in presence of a cavity [12]. The atom-photon system is then driven dissipative as it is externally pumped by a laser and couples to the electromagnetic environment yielding dissipation and noise. In order to describe these open quantum systems, we choose the Heisenberg-Langevin formalism that we introduce in Section 1.8. We directly use this formalism in the following section to derive the Hamiltonian describing the optomechanical coupling between a single cavity mode and the motion of an ultracold atom. In Section 1.10 we exemplarily sketch an experiment on ultracold atoms that optomechanically couple to a high-finesse cavity mode.

1.1. What are ultracold atoms?

In order to create a gas of ultracold atoms, in a first step an atomic vapor is precooled using laser cooling to temperatures in the mK regime. It can then be confined in a trap that can be either magnetic or optical and further cooling techniques, typically evaporative cooling, can be applied to reach temperatures of several hundreds of nK [55, 56]. For bosonic atoms of mass m the regime of quantum degeneracy (Bose-Einstein condensation) is reached when the thermal de-Broglie wavelength

$$\lambda_{dB} = (2\pi\hbar^2/mk_BT)^{1/2} \tag{1.1}$$

is comparable to the interparticle distance $n^{-1/3}$. Ultracold gases are very clean and versatile systems: the two-body interaction can be tuned via Feshbach resonances, thereby allowing to study many body physics [57]. Various experimental observables are accessible as the momentum distribution of the atomic cloud after expansion from the trap (time of flight image) or the atomic density distribution in situ. Fig.1.1 shows the time of flight image of the first BEC [55]. Furthermore, ultracold gases can be confined in various
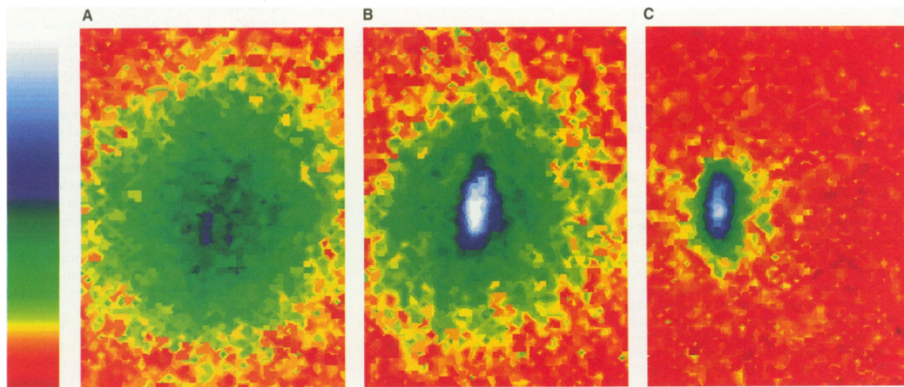
Figure 1.1.: Momentum distribution of the atomic cloud. Condensate fraction (in blue and white) (a) just before the appearance of the condensate, (b) just after the appearance of the condensate and (c) nearly pure condensate. The image is taken from Ref. [55].

geometries like pancake or cigar shape using magnetic traps. They can also be confined in more complex geometries as rings [58] and lattices [4] using optical dipole traps. In this thesis we focus in particular on an one-dimensional optical lattice.

1.2. Ultracold atoms in optical lattices

Let us consider an atom as a two-level system with transition frequency ω_0 that interacts with a laser of frequency ω. If the laser is far detuned from the atomic transition, the interaction, characterized by the Rabi frequency ϑ, can be treated as a perturbation and leads to an effective level shift, also known as Stark Shift or Light Shift [59]. The energy shift experienced by the ground state is given by

$$\delta\mathcal{E} = \frac{\hbar\vartheta^2}{\Delta},$$

(1.2)

with $\Delta = \omega - \omega_0$. The derivation of the Light Shift is shown in more details in Appendix A. The shift experienced by the excited state has an opposite sign. The shift of the ground state corresponds to the dipole potential for the two-level atom. If one can assume that the atom is mainly in the ground state, one can interpret the light shifted ground state as the potential that determines the motion of the atom [59], as depicted in Fig.1.2.
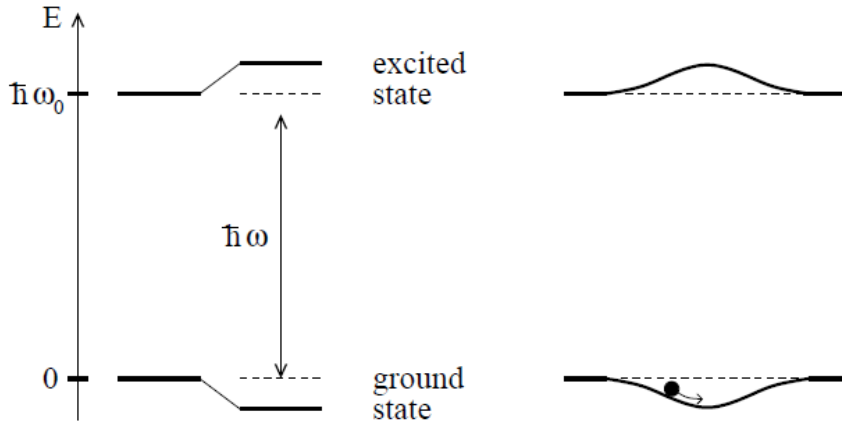
Figure 1.2.: Left: A two level atom with transition frequency ω_0 is driven by a laser with frequency ω. The laser is red detuned $\Delta = \omega - \omega_0 < 0$ and shifts the ground state down and the excited state up. Right: If the light field is spatially varying it results in a ground-state potential well that traps the atom. This is the basic idea of an optical lattice. The figure is adapted from Ref. [59].

Now, how can the potential landscape be tailored in a periodical way? For simplicity we assume that we are in one dimension, along the x axis. Along the y and z axis there exists a tight harmonic confinement which confines the particles in the transverse ground state. We neglect the additional harmonic confinement along x due to the Gaussian laser beam

profile. The Rabi frequency ϑ is proportional to the amplitude of the electric field $E(x)$

$$\vartheta(x) = \frac{-\mu E(x)}{\hbar}, \tag{1.3}$$

with μ the dipole moment of the considered atomic transition [60]. For a standing wave, formed by two counterpropagating laser beams of the same polarization, the electric field amplitude is periodically modulated in space according to

$$E(x) = E_0 \cos(k_0 x), \tag{1.4}$$

with $\lambda_0 = 2\pi/k_0$ the wavelength of the electric field. Thus the atom experiences a periodic potential[1]

$$W_{\text{ext}}(x) = W_0 \cos^2(k_0 x), \tag{1.5}$$

with the potential depth $W_0 = \frac{\mu^2 E_0^2}{\hbar \Delta}$ and periodicity $d_0 = \lambda_0/2 = \pi/k_0$. The sign of the potential is determined by the sign of the detuning Δ: For a blue detuned laser, $\Delta > 0$, the sign of the potential depth is positive, thus the minima of the potential are at the nodes and so the atoms are confined where the intensity is zero. In contrast, for a red detuned laser, $\Delta < 0$, the sign of the potential depth is negative, the minima of the potential are at the antinodes and the atoms are confined where the intensity is maximal. The situation is depicted in Fig.1.3. We will call the possible positions of the atoms, the local minima of
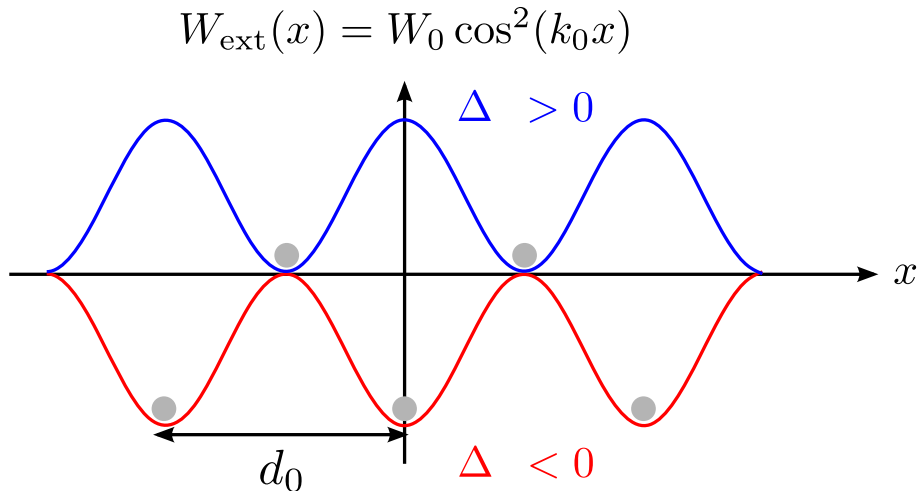
Figure 1.3.: Sketch of the periodic potential $W_{\text{ext}}(x)$ for a blue ($\Delta > 0$) and a red ($\Delta < 0$) detuned laser.

---

[1]The actual the potential in three dimensions reads $W_{\text{ext}}(x, y, z) = W_0 \cos^2(k_0 x) + \frac{1}{2} m \omega_\perp^2 (y^2 + z^2)$.

the potential, lattice sites. They are situated at

$$x_j = \frac{j\pi}{k_0} = jd_0, \quad \text{with} \quad j \in [-(L-1)/2; (L-1)/2]. \tag{1.6}$$

where L is the total number of lattice sites of the optical lattice that we choose odd. The length of the lattice is $L_0 = Ld_0$. In the following we will consider $W_0 < 0$. Notice that in the forthcoming Chapter 2 we will consider an atom confined in an optical lattice within a cavity, where either the atom or the cavity is pumped by an external laser. In this context, the atomic transition used to create the optical lattice, is not the same as the transition that is coupled to the cavity mode and pumped by the external laser.

The potential landscapes for ultracold atoms, tailored on the basis of the spatially inhomogeneous Light shift, can have different forms and dimensionalities. Fig.1.4 shows different possible lattice geometries: Superimposing one, two or three orthogonal standing waves as depicted on the left side, leads to an optical lattice consisting of (a) pancakes, (b) cigars or (c) spheres. A detailed discussion of optical lattices can be found in Ref. [4, 59, 60].

1.3. Dynamics of a single particle in an one-dimensional periodic lattice

We consider a single particle of mass m, that is moving in an one-dimensional periodic lattice with L lattice sites. Its dynamics is governed by the Hamiltonian

$$\hat{H} = \frac{\hat{p}^2}{2m} + \hat{W}_{\text{ext}}(\hat{x}), \tag{1.7}$$

where $\hat{W}_{\text{ext}}(\hat{x} + d_0) = W_{\text{ext}}(\hat{x})$ isgiven by Eq.(1.5) and $d_0 = \lambda_0/2$ denotes the periodicity of the lattice. The eigenfunctions are the Bloch functions, which, assuming periodic boundary conditions [1, 60], read

$$\psi_{\mathsf{m},k}(x) = \frac{e^{ikx}}{\sqrt{L_0}} u_{\mathsf{m},k}(x), \tag{1.8}$$

where k corresponds to the quasi-momentum and m denotes the energy band ($\mathsf{m} = 1$ means eigenfunction with lowest eigenenergy). They build an orthonormal basis, with the
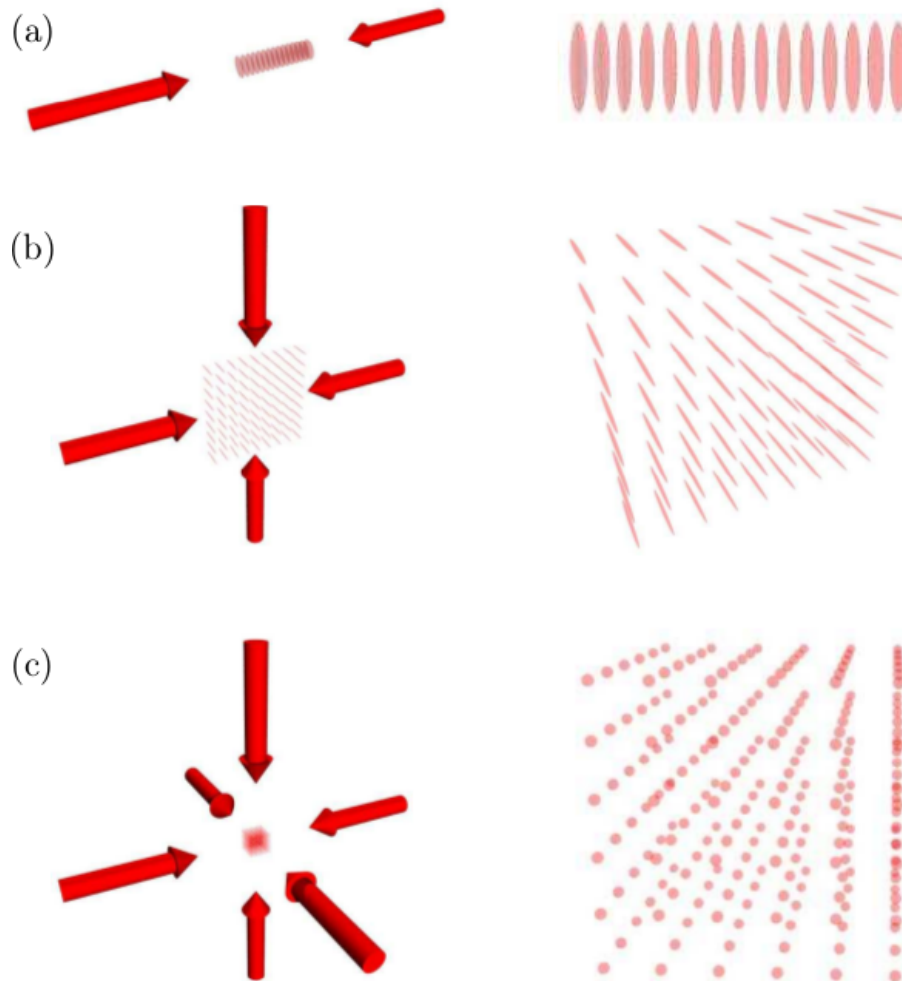
Figure 1.4.: Superimposing (a) one, (b) two or (c) three orthogonal standing waves yields optical lattices of different geometries: (a) pancake, (b) cigar shape or (c) spherical. The figures on the right hand side show the light intensity for the corresponding lattice geometry. The figure is taken from Ref. [61].

orthogonality relation

$$\int_{-L_0/2}^{L_0/2} \psi_{\mathsf{m},k}^*(x)\psi_{\mathsf{m}',k'}(x)dx = \delta_{\mathsf{m},\mathsf{m}'}\delta_{k,k'}, \tag{1.9}$$

with $L_0 = Ld_0$. The functions $u_{\mathsf{m},k}(x)$ are also periodic, with period d_0 and normalized according to

$$\int_{-d_0/2}^{d_0/2} u_{\mathsf{m}}^*(x)u_{\mathsf{m}'}(x)dx = d_0\delta_{\mathsf{m},\mathsf{m}'}. \tag{1.10}$$

They can be expanded in a Fourier series

$$u_{\mathsf{m},k}(x) = \sum_{l\in[-L/2;L/2]} c_l^{(\mathsf{m})}(k)e^{2ilk_0x}. \tag{1.11}$$

Inserting Eq.(1.8) in the stationary Schrödinger equation

$$\hat{H}\psi_{\mathsf{m},k}(x) = E^{(\mathsf{m})}(k)\psi_{\mathsf{m},k}(x),$$

with $\hat{H}$ given by Eq.(1.7) leads to the so called central equation [1, 60]

$$\sum_l e^{i(2lk_0-k)x}\left[\left(\left(2l-\frac{k}{k_0}\right)^2 + \frac{W_0}{2E_R} - \frac{E^{(\mathsf{m})}(k)}{E_R}\right)c_l^{(\mathsf{m})}(k) + \frac{W_0}{4E_R}\left(c_{l+1}^{(\mathsf{m})}(k) + c_{l-1}^{(\mathsf{m})}(k)\right)\right]$$
$$= 0, \tag{1.12}$$

that we expressed in units of the recoil energy $E_R = \frac{\hbar^2 k_0^2}{2m}$. By numerical diagonalization, one finds the energy bands $E^{(\mathsf{m})}(k)/E_R$ as a function of k/k_0 within the first Brillouin zone, as depicted in Fig.1.5 for different lattice depths. For a very small potential strength of $W_0 = -1E_R$ the dispersion relation is nearly quadratic and can be obtained from the one of a free particle after folding the curves within the Brillouin zone (Fig.1.5 (a)). For increasing potential strengths gaps of increasing width open at the center and the edge of the first Brillouin zone (Fig.1.5 (b) and (c)).

1.4. Wannier functions

The Bloch functions are delocalized over the whole space. It is sometimes more convenient and intuitive to use the Fourier transformed basis, called the Wannier basis, which is

(a)

(b)

(c)
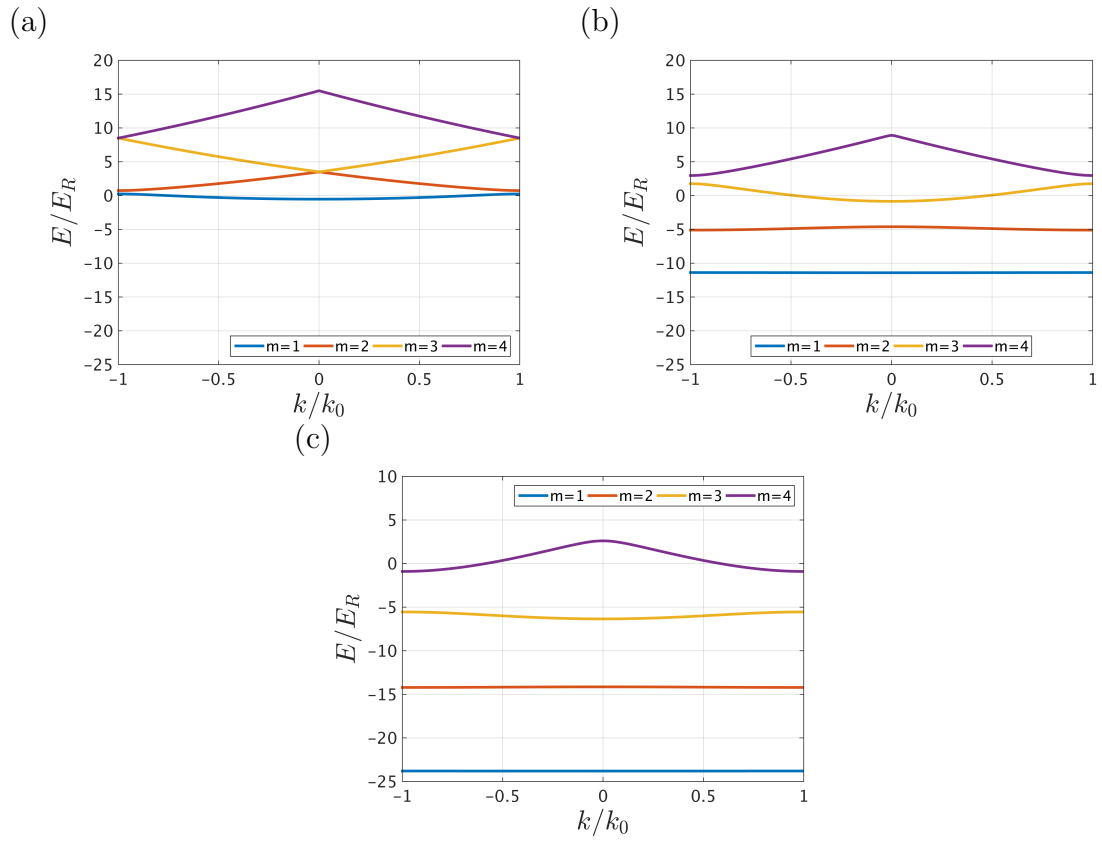
Figure 1.5.: Energy bands in units of the recoil energy $E^{(\mathsf{m})}(k)/E_R$ as a function of $\frac{k}{k_0}$, for bands $\mathsf{m} = 1, 2, 3, 4$ and potential strengths (a) $W_0 = -1 E_R$, (b) $W_0 = -15 E_R$ and (c) $W_0 = -29 E_R$.

composed of functions that are localized at the lattice sites. In the case of a finite lattice with L sites, the Wannier function of band m, centered at lattice site x_j, is defined as [62]

$$w_{\mathsf{m},j}(x) = w_{\mathsf{m}}(x - x_j) = \frac{1}{\sqrt{L}} \sum_{k=-k_0}^{k_0} e^{-ikx_j} \psi_{\mathsf{m},k}(x). \qquad (1.13)$$

Notice that the Wannier function, centered at lattice site $x_j = jd_0$, can be obtained by translating the Wannier function, centered at lattice site $j = 0$

$$w_{\mathsf{m},0}(x - jd_0) = w_{\mathsf{m},j}(x). \qquad (1.14)$$

The Wannier functions form a basis, with orthogonality relation

$$\int_{-L_0/2}^{L_0/2} dx \; w_{\mathsf{m}}^*(x - x_j) w_{\mathsf{m}'}(x - x_{j'}) = \delta_{\mathsf{m},\mathsf{m}'} \delta_{j,j'}, \qquad (1.15)$$

where m, m' are the energy band indices and j, j' denote the lattice site. Fig.1.6 displays the Wannier functions $w_{\pm 1}(x)$ and $w_0(x)$ for three different values of the potential depth $W_0 = -1E_R, -5E_R, -15E_R$. Notice that for a deep optical lattice the Wannier functions are well localized onto a single lattice site.

(a) (b)

(c)
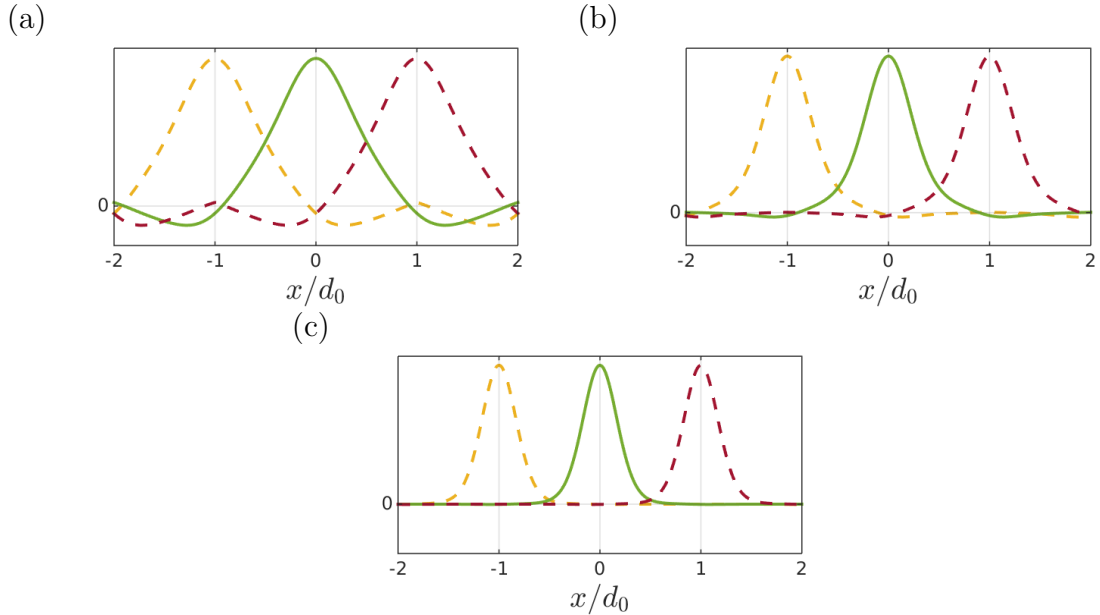
Figure 1.6.: Wannier functions $w_{\pm 1}(x)$ and $w_0(x)$ for (a) $W_0 = -1E_R$, (b) $W_0 = -5E_R$ and (c) $W_0 = -15E_R$.

1.5. Bose-Hubbard Hamiltonian for ultracold atoms

Ultracold atoms in optical lattices can be used to simulate lattice models as e.g. the Bose-Hubbard model that we introduce in this section, following the lines of Ref. [63]. In Chapter 2 we will use a Bose-Hubbard type of Hamiltonian, specialized to the case of a single particle, to describe the localization transition in presence of cavity backaction. Here we first introduce the most general case of N interacting, ultracold bosons of mass m in an one-dimensional optical lattice with L sites along x. The Hamiltonian reads

$$\hat{H} = \sum_{n=1}^{N} \frac{\hat{p}_n^2}{2m} + \hat{W}_{\text{ext}}(\hat{x}_n) + \hat{V}_{\text{pert}}(\hat{x}_n) + \frac{1}{2} \sum_{n \neq n'} \hat{v}(\hat{x}_n - \hat{x}_{n'}), \tag{1.16}$$

with $\hat{W}_{\text{ext}}(x_n)$ the external optical lattice potential that atom n is feeling, given by Eq.(1.5). $\hat{V}_{\text{pert}}(x_n)$ corresponds to an additional spatially varying external potential (e.g. additional harmonic trapping potential in the case of Ref. [63]). We assume that the only interactions between particles are two-body interactions, described by the contact potential

$$\hat{v}(x_n - x_{n'}) = \frac{4\pi\hbar^2 a_s}{m} \delta(x_n - x_{n'}), \tag{1.17}$$

where a_s denotes the s-wave scattering length. In second quantization the Hamiltonian has the form [63]

$$\hat{H} = \int_{-L_0/2}^{L_0/2} dx \ \hat{\Psi}^\dagger(x) \left(-\frac{\hbar^2}{2m} \frac{\partial^2}{\partial x^2} + \hat{W}_{\text{ext}}(x) + \hat{V}_{\text{pert}}(x) \right) \hat{\Psi}(x)$$
$$+ \frac{2\pi\hbar^2 a_s}{m} \int_{-L_0/2}^{L_0/2} dx \ \hat{\Psi}^\dagger(x)\hat{\Psi}^\dagger(x)\hat{\Psi}(x)\hat{\Psi}(x), \tag{1.18}$$

where $L_0 = Ld_0$. We assume that we are in the tight-binding regime, corresponding to a deep lattice regime. Furthermore we use the single-band approximation: we assume that the confining potential $\hat{W}_{\text{ext}}(x)$ is sufficiently deep that only the lowest Bloch band is occupied. In this limit, the bosonic field operator $\hat{\Psi}(x)$ can be expanded in Wannier functions [63] according to

$$\hat{\Psi}(x) = \sum_{n=1}^{L} \langle x|n\rangle \hat{b}_n = \sum_{n=1}^{L} w(x - x_n)\hat{b}_n, \tag{1.19}$$

where $|n\rangle$ denotes the Wannier state, centered at lattice site n, and $\hat{b}_n^\dagger$ and $\hat{b}_n$ are the creation and annihilation operators of a bosonic atom at the site n. They fulfill the commutation relation

$$[\hat{b}_n, \hat{b}_l^\dagger] = \delta_{nl}$$
$$[\hat{b}_n^\dagger, \hat{b}_l^\dagger] = [\hat{b}_n, \hat{b}_l] = 0. \tag{1.20}$$

If we insert the Wannier decomposition in Eq. (1.18), we obtain the Bose-Hubbard Hamiltonian [63]

$$\hat{H} = -t \sum_{\langle n,l \rangle} \hat{b}_n^\dagger \hat{b}_l + \hat{b}_l^\dagger \hat{b}_n + \sum_{n=1}^{L} \delta\epsilon_n \hat{N}_n + \frac{1}{2} U \sum_{n=1}^{L} \hat{N}_n (\hat{N}_n - 1), \tag{1.21}$$

where $\langle n,l \rangle$ sums over neighboring sites and $\hat{N}_n = \hat{b}_n^\dagger \hat{b}_n$ counts the number of bosonic atoms at lattice site n. The parameter t is defined as

$$t = \langle n| \frac{\hat{p}^2}{2m} + \hat{W}_{\text{ext}}(\hat{x}) |l\rangle = \int_{-L_0/2}^{L_0/2} dx \ w^*(x - x_n) \left(-\frac{\hbar^2}{2m} \frac{\partial^2}{\partial x^2} + \hat{W}_{\text{ext}}(x) \right) w(x - x_l) \tag{1.22}$$

and denotes the tunneling matrix element between neighboring sites n, l. In the tight-binding regime tunneling between more distant lattice sites is completely suppressed [64], due to the localization of the Wannier functions. Similarly we have defined

$$U = \frac{4\pi \hbar^2 a_s}{m} \int_{-L_0/2}^{L_0/2} dx \ |w(x)|^4 \tag{1.23}$$

corresponding to the strength of the onsite interaction. The energy offset of each lattice site is given by

$$\delta\epsilon_n = \langle n| \hat{V}_{\text{pert}}(\hat{x}) |n\rangle = \int_{-L_0/2}^{L_0/2} dx \ w^*(x - x_n) \hat{V}_{\text{pert}}(x) w(x - x_n). \tag{1.24}$$

The competition between the tunneling strength t and the onsite repulsive interaction U gives rise to a quantum phase transition from superfluid ($t \gg U$) to Mott insulator ($t \ll U$), predicted in Ref. [65] and observed with ultracold atoms [66], as sketched in Fig.1.7. The phase transition can be monitored by the time-of-flight images: in the Mott insulator state the number of atoms per site is fixed but there is no phase coherence, thus the momentum distribution shows no interference. In the superfluid state the number

of atoms per site fluctuates but as it is a giant matter wave, it displays an interference pattern in the momentum distribution due to phase coherence [4].
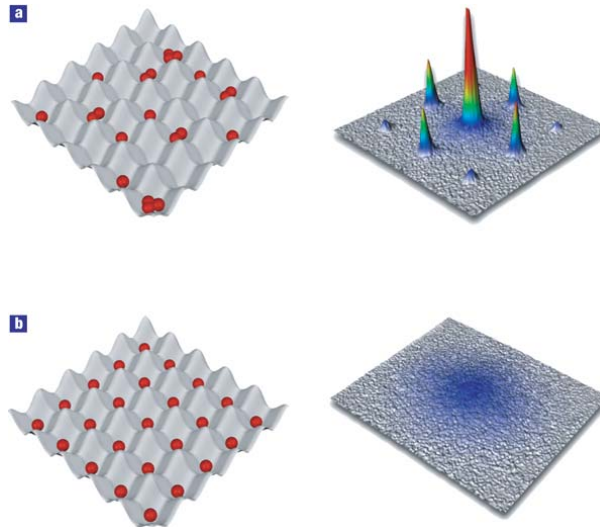
Figure 1.7.: Sketch of the transition from a (a) superfluid ($t \gg U$) to a (b) Mott insulator ($t \ll U$) state with corresponding time-of flight image. The figure is taken from Ref. [4].

1.6. The Aubry-André model

Ultracold atoms in optical lattices are very convenient quantum simulators for condensed matter systems, since the atoms play the role of the electrons that move in a periodic potential. One important feature of solid state systems is their electrical conductivity. Thus it is particularly interesting to study metal-insulator transitions and understand what affects electrical conductivity in a solid [5]. As Anderson pointed out, random disorder leads to a metal-insulator transition due to exponential localization of the wave function of the electron [6]. A famous model to study the extended to localized transition of a single particle in an one-dimensional quasidisordered crystal is the Aubry-André model [9] or Harper model [10] that we present in the following.

The Hamiltonian of the André-Aubry model [9] corresponds to a special case of the Bose-Hubbard Hamiltonian given in Eq.(1.21). It describes the motion of a single particle

in an one-dimensional lattice of L sites [8]

$$\hat{H}_{\mathrm{AA}[n]} = -t \sum_{n=1}^{L-1} (|n\rangle \langle n+1| + |n+1\rangle \langle n|) + \sum_{n=1}^{L} \delta\epsilon_n |n\rangle \langle n|, \qquad (1.25)$$

with site dependent onsite energy

$$\delta\epsilon_n = v_0 \cos(2\pi\beta n), \qquad (1.26)$$

where β is the period of the potential and $|n\rangle$ denotes the Wannier state, centered at site n. If β is an irrational number, the site-dependent onsite potential is quasiperiodic [9] and the model shows a phase transition at the critical disorder strength $v_c^{AA} = 2t$: If $v_0 < v_c^{AA}$ the particle's wavefunction is spatially extended, while for $v_0 > v_c^{AA}$ the wavefunction decays exponentially indicating Anderson-like localization [6, 8, 9]. In experiments and in numerical calculations all numbers are in practice rational and system sizes are finite. Despite these limitations, it is possible to create an effective quasiperiodic lattice and to observe the transition from extended to localized: one needs a potential period which is at least as large as the system size to avoid periodic repetitions [67]. In order to get a good numerical approximation of a quasiperiodic potential for finite lattice sizes, it is convenient to choose the golden mean for the period $\beta = (\sqrt{5} - 1)/2$ and the system size L as a Fibonacci number F_i, because the period β can be approximated by the rational series $\beta_i = F_{i-1}/F_i$, which tends asymptotically to β for large F_i [5, 8].

There are several ways to identify the critical point v_c^{AA}. One way is to numerically study the inverse participation ratio (IPR) [68]

$$P_x = \sum_{n=1}^{L} |\langle n|\Phi\rangle|^4, \qquad (1.27)$$

where $|\Phi\rangle$ denotes the state of the particle. The IPR is of the order $1/L$ if the particle's spatial wavefunction is uniform over the lattice, whereas it approaches unity when the particle is localized on one single lattice site.

Fig.1.8 (a) from Ref. [8] shows the inverse participation ratio P_x as a function of the disorder strength λ which corresponds in our notation to v_0/t for different system sizes. For the potential strength $\lambda < 2$ the system is in the extended phase, for $\lambda > 2$ it is in the localized phase. Depending on the sign of the amplitude of the potential, there is either one global minimum at the center of the lattice or there are two minima symmetric to the
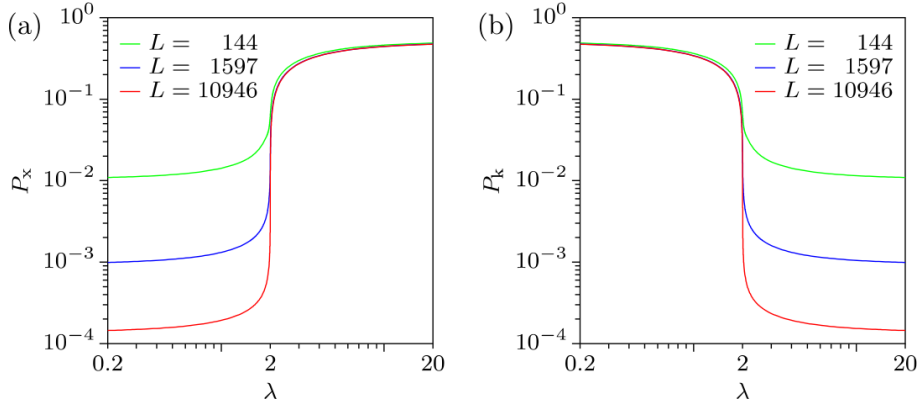
Figure 1.8.: Inverse participation ratio in real (a) and momentum space (b) as a function of the potential strength λ for system sizes $L = 144, 1597, 10946$. Note that in our notation λ corresponds to v_0/t. The two plots are mirror images of each other. This shows the duality of the Aubry-André model. The image is taken from Ref. [8].

lattice center. In the case where there are two minima, the ground state is degenerated and so one needs to average over the two possible configurations so the maximum value of P_x is 0.5. The curves for the different system sizes all change from $P_x = 1/L$ to $P_x = 0.5$ at $\lambda = 2$. This indicates that the André-Aubry model shows a sharp transition from an extended to a localized phase in one dimension [8].

Another, very elegant, way to find the critical point makes use of the duality of the André-Aubry model. This duality can be seen by transforming $\hat{H}_{\mathrm{AA}[n]}$ in momentum space with the help of new basis states [8]

$$\left|\bar{k}\right\rangle = \frac{1}{\sqrt{L}} \sum_{n=1}^{L} \exp\left(i2\pi\bar{k}\beta n\right) \left|n\right\rangle . \tag{1.28}$$

The Hamilton in the new basis states reads

$$\hat{H}_{\mathrm{AA}[\bar{k}]} = \frac{v_0}{2} \sum_{\bar{k}=1}^{L} \left|\bar{k}\right\rangle \left\langle\bar{k}+1\right| + \left|\bar{k}+1\right\rangle \left\langle\bar{k}\right| - 2t \sum_{\bar{k}=1}^{L} \cos(2\pi\beta\bar{k}) \left|\bar{k}\right\rangle \left\langle\bar{k}\right| . \tag{1.29}$$

The self-dual point (the point where both Hamiltonians $\hat{H}_{\mathrm{AA}[n]}$ and $\hat{H}_{\mathrm{AA}[\bar{k}]}$ are the same) is $v_0 = 2t^2$ and corresponds to the critical point v_c^{AA}. For values of $v_0 < 2t$ the state is extended in real space and localized in the momentum space. The opposite situation

---

[2]The sign of t is not relevant. It can be absorbed using a gauge transformation.

occurs for $v_0 > 2t$, where the state is localized in real space and extended in the momentum space. This duality is shown in Fig.1.8 (a) and (b), displaying the inverse participation ratio in real space P_x and its analog in momentum space P_k, as defined in Ref. [8]. The two plots are mirror images of each other.

Another quantity that can be studied to characterize the localization behavior of a state $|\Phi\rangle$, is the characteristic exponent γ, also called Lyapunov exponent [9]

$$\gamma = -\lim_{n \to \infty} \frac{\log(|\langle n|\Phi\rangle|^2)}{2n} \, . \tag{1.30}$$

It measures the exponential decay of the wavefunction in the localized phase and thus vanishes for an extended state. According to Thouless' formula [69], in the spatially localized regime of the Aubry-André model it reads

$$\gamma = \log\left(\frac{v_0}{v_c^{\mathrm{AA}}}\right) . \tag{1.31}$$

1.7. Experiment on ultracold atoms in a quasiperiodic optical lattice

In this section we describe the experimental realization of the Aubry-André model in the group of Florence [11,67]. They use a BEC of ^{39}K atoms where interactions can be switched off using a Feshbach resonance. The localization is studied in a one-dimensional bichromatic potential arising due to the superposition of an optical lattice, as defined in Eq.(1.5), where the wavevector is here denoted k_1. The main optical lattice is perturbed by a second, weak lattice with a different wavevector k_2, playing the role of $V_{\mathrm{pert}}(x)$ in Eq.(1.16). If the two wavevectors are incommensurate, i.e. $k_2/k_1 \neq i/j$, with $i, j \in \mathbb{N}$, the superposition of these two optical lattices constitutes an experimental realization of a quasiperiodic lattice as we show in Section 2.2. The extended to localized transition is monitored by studying both spatial and momentum distribution as a function of the disorder strength in units of the tunneling, here denoted as Δ/J. Changing the heights of primary and secondary optical lattice allows to control the relevant energies J and Δ independently in the experiment. The panels **a** and **b** in Fig.1.9 show the spatial distribution of the atomic wave packets in the extended phase for $\Delta/J = 1$ and in the localized phase for $\Delta/J = 15$. Since the atoms are further confined by a harmonic trap, the tails of the spatial distribution are fitted with a function of the form $f_\alpha(x) \sim \exp(-|(x - x_0)/l|^\alpha)$. The fitting parameter α

is displayed in Fig.1.9 **c** as a function of the disorder strength. For small values of the disorder the density distribution is well described by a Gaussian, i.e. $\alpha = 2$, corresponding to the ground state of a single particle in a harmonic trap in absence of disorder. As the disorder increases the value of α changes smoothly to one, indicating exponential localization in space to a size smaller than the typical harmonic oscillator length. The
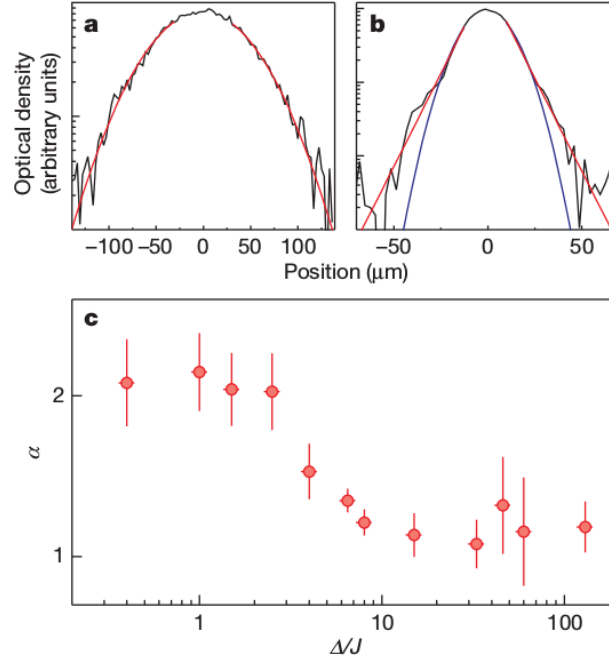
Figure 1.9.: Experimental profiles of the spatial distribution and the fitting function $f_\alpha(x)$ (red) for $\Delta/J = 1$ (**a**) and $\Delta/J = 15$ (**b**). (**c**) Dependence of the fitting parameter α on Δ/J: transition from a Gaussian to an exponential distribution. The image is taken from Ref. [11]. Note that in our notation Δ/J corresponds to v_0/t.

momentum distribution, depicted in Fig.1.10 shows the inverse behavior (from top to bottom): without disorder, the wave packet is localized in momentum space, with peaks at $k = 0, \pm 2k_1$, where k_1 is the wavevector of the main optical lattice. For small disorder ($\Delta/J = 1.1$) additional momentum peaks, indicating the beating of the two competing lattices, are visible at $\pm 2(k_1 - k_2)$. Increasing the disorder further yields a broadening of the momentum distribution. Note that the critical disorder strength differs from the value of $v_c^{\text{AA}} = \Delta/J = 2$, theoretically predicted by the Aubry-André model. One possible reason is the additional harmonic confinement. Furthermore the actual incommensurability in the experiment is not the maximally irrational value of $\beta = k_2/k_1 = (\sqrt{5} - 1)/2$ but rather $\beta = 1032/862$, which leads to a smoothening of the transition [67, 70].
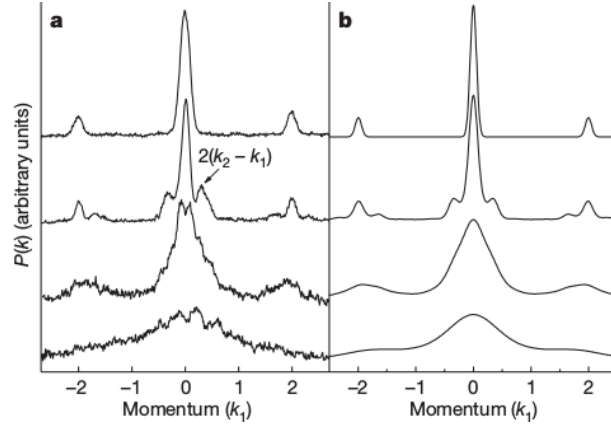
Figure 1.10.: Experimental and theoretical momentum distributions for $\Delta/J = 0, 1.1, 7.2, 25$ from top to bottom. k_1 and k_2 are the wavevectors of the main and the perturbing lattice respectively. The image is taken from Ref. [11]

1.8. The Heisenberg-Langevin equation

In the following we are going to consider driven dissipative systems, namely in Section 1.9 and Chapter 2 an ultracold atom in a high-finesse optical cavity and later in the thesis exciton polaritons in a semiconductor microcavity (introduced in Chapter 4). Both systems exchange energy with their environment in two ways: There is an external pump which is coherently driving the system[3]. Furthermore they are subjected to dissipation and noise. In this work we have described these open systems using the Heisenberg-Langevin equation. This is a quantum stochastic differential equation which successfully describes many driven-dissipative systems. Noise and dissipation are modelled by a coupling to a bath of harmonic oscillators[4]. It is an alternative approach to the description via the Master equation, as it is based on the use of time dependent operators instead of density matrices. In this section, which is based on [72, 73], we will derive a general form of the Heisenberg-Langevin equation. We start with the Hamiltonian

$$\hat{H} = \hat{H}_{\mathrm{sys}} + \hat{H}_{\mathrm{bath}} + \hat{H}_{\mathrm{int}}, \tag{1.32}$$

---

[3]We neglect noise arising from fluctuations in the pump laser light.
[4]In condensed matter physics a similar treatment has been suggested by Caldeira and Legget [71].

where $\hat{H}_{\text{sys}}$ is the Hamiltonian of a generic system. We assume that the bath Hamiltonian is a set of harmonic oscillators

$$\hat{H}_{\text{bath}} = \int_{-\infty}^{\infty} \hbar\omega \hat{b}^{\dagger}(\omega)\hat{b}(\omega) \, d\omega \tag{1.33}$$

with bosonic annihilation and creation operators $\hat{b}(\omega)$ and $\hat{b}^{\dagger}(\omega)$ that obey the commutation relation

$$\left[\hat{b}(\omega), \hat{b}^{\dagger}(\omega')\right] = \delta(\omega - \omega'). \tag{1.34}$$

We further assume that the system-bath interaction is linear in the bath harmonic oscillator operators and can be written as

$$\hat{H}_{\text{int}} = \int_{-\infty}^{\infty} i\hbar\kappa(\omega) \left[\hat{b}^{\dagger}(\omega)\hat{c} - \hat{c}^{\dagger}\hat{b}(\omega)\right] \, d\omega, \tag{1.35}$$

where the $\kappa(\omega)$ is the bath-system coupling and $\hat{c}$ denotes exemplarily one of the system's operator. The form of the interaction Hamiltonian is based on the rotating wave approximation which can be justified in the following way: Assume that the interaction between bath and system $\kappa(\omega)$ is small and the time dependence of the operator $\hat{c}$ is essentially determined by the system Hamiltonian and given by $e^{i\chi t}$, thus the counterrotating terms $\hat{b}^{\dagger}\hat{c}^{\dagger}$ and $\hat{b}\hat{c}$ evolve according to $e^{i(\chi+\omega)t}$ and $e^{-i(\chi+\omega)t}$. These terms are rapidly varying in comparison to the time dependence of $\hat{c}^{\dagger}\hat{b}$ and $\hat{b}^{\dagger}\hat{c}$ which is $e^{-i(\omega-\chi)t}$ and $e^{i(\omega-\chi)t}$, especially for $\chi \approx \omega$. So the counterrotating terms can be neglected[5]. Note that the lower limit of the ω integration in Eq.(1.33) and (1.35) is extended from the physically meaningful limit 0 to $-\infty$. This extension is required for the definition of a delta correlated quantum white noise. It is justified if one assumes that only interaction terms close to resonance ($\omega \approx \chi$) contribute significantly.

The Heisenberg equation of motion for the bath operator is given by

$$\dot{\hat{b}}(\omega) = -\frac{i}{\hbar}\left[\hat{b}(\omega), \hat{H}\right] = -i\omega\hat{b}(\omega) + \kappa(\omega)\hat{c}. \tag{1.36}$$

---

[5]For a more detailed description of the rotating wave approximation see [74].

The Heisenberg equation of motion for an arbitrary system operator $\hat{a}$ reads

$$\dot{\hat{a}} = -\frac{i}{\hbar} \left[\hat{a}, \hat{H} \right]$$
$$= -\frac{i}{\hbar} \left[\hat{a}, \hat{H}_{\text{sys}} \right] + \int_{-\infty}^{\infty} \kappa(\omega) \left(\hat{b}^{\dagger}(\omega) [\hat{a}, \hat{c}] - [\hat{a}, \hat{c}^{\dagger}] \hat{b}(\omega) \right) \, d\omega. \tag{1.37}$$

Eq.(1.36) can be solved in terms of initial conditions at a time $t_0 < t$, corresponding to the input, or in terms of final conditions at a time $t_1 > t$, corresponding to the output [75]. For $t_0 < t$ the solution has the form

$$\hat{b}(\omega) = e^{-i\omega(t-t_0)} \hat{b}_0(\omega) + \kappa(\omega) \int_{t_0}^{t} e^{-i\omega(t-t')} \hat{c}(t') \, dt', \tag{1.38}$$

where $\hat{b}_0(\omega)$ is the initial, input condition for $\hat{b}(\omega)$ at the time $t = t_0$. For $t_1 > t$ the solution of Eq.(1.36) is

$$\hat{b}(\omega) = e^{-i\omega(t-t_1)} \hat{b}_1(\omega) - \kappa(\omega) \int_{t}^{t_1} e^{-i\omega(t-t')} \hat{c}(t') \, dt', \tag{1.39}$$

where $\hat{b}_1(\omega)$ is the final, output condition for $\hat{b}(\omega)$ at the time $t = t_0$. In both cases the first term on the right-hand side corresponds to the free evolution of the bath operator and the second term arises from the interaction between bath and system. The substitution of Eq.(1.38) into Eq.(1.37) leads to

$$\dot{\hat{a}} = -\frac{i}{\hbar} \left[\hat{a}, \hat{H}_{\text{sys}} \right] + \int_{-\infty}^{\infty} \kappa(\omega) \left(e^{i\omega(t-t_0)} \hat{b}_0^{\dagger}(\omega) [\hat{a}, \hat{c}] - [\hat{a}, \hat{c}^{\dagger}] e^{-i\omega(t-t_0)} \hat{b}_0(\omega) \right) \, d\omega$$
$$+ \int_{-\infty}^{\infty} \kappa(\omega)^2 \int_{t_0}^{t} \left(e^{i\omega(t-t')} \hat{c}^{\dagger}(t') [\hat{a}, \hat{c}] - [\hat{a}, \hat{c}^{\dagger}] e^{-i\omega(t-t')} \hat{c}(t') \right) \, dt' \, d\omega. \tag{1.40}$$

Now we assume that the bath-system coupling constant is independent of the frequency and can be written as

$$\kappa(\omega) = \sqrt{\frac{\Gamma}{2\pi}}, \tag{1.41}$$

where Γ will be referred to as decay rate. This approximation is known as the Markov approximation. It allows us to perform the integration over ω in the second integral in Eq.(1.40), where thanks to the extension of the lower limit to $-\infty$ we are able to use $\int_{-\infty}^{\infty} e^{-i\omega(t-t')} = 2\pi\delta(t-t')$. Note that the operators $\hat{a}$ and $\hat{c}$ in the commutator in

Eq.(1.40) depend on t but not on t' so the time integration can be performed, leading to the general Heisenberg-Langevin equation for an arbitrary system operator $\hat{a}$

$$\dot{\hat{a}} = -\frac{i}{\hbar}\left[\hat{a}, \hat{H}_{\text{sys}}\right] + \left(\sqrt{\Gamma}\hat{a}_{\text{in}}^{\dagger}(t) + \frac{\Gamma}{2}\hat{c}^{\dagger}\right)[\hat{a}, \hat{c}] - [\hat{a}, \hat{c}^{\dagger}]\left(\frac{\Gamma}{2}\hat{c} + \sqrt{\Gamma}\hat{a}_{\text{in}}(t)\right), \qquad (1.42)$$

where we defined the input field operator [75]

$$\hat{a}_{\text{in}}(t) = -\frac{1}{\sqrt{2\pi}}\int_{-\infty}^{\infty} e^{-i\omega(t-t_0)}\hat{b}_0(\omega), \qquad (1.43)$$

satisfying the commutation relation

$$[\hat{a}_{\text{in}}(t), \hat{a}_{\text{in}}^{\dagger}(t')] = \delta(t-t'). \qquad (1.44)$$

As a result of the Markov approximation the Heisenberg-Langevin equation is a first order differential equation: the future time evolution of an operator now only depends on the knowledge of all operators in the present. But the definition of the input field operator $\hat{a}_{\text{in}}(t)$ depends on the initial state of the bath. It can be interpreted as noise if system and bath are initially independent and noninteracting, hence the density operator of the system and bath factorizes at $t = t_0$. Furthermore, for a meaningful noise definition, the initial state of the bath needs to be incoherent. We assume that the bath is in a thermal state, which leads to [72]

$$\langle \hat{a}_{\text{in}}(t) \rangle = \langle \hat{a}_{\text{in}}^{\dagger}(t) \rangle = 0 \qquad (1.45)$$

$$\langle \hat{a}_{\text{in}}^{\dagger}(t)\hat{a}_{\text{in}}(t') \rangle = \bar{n}(\omega)\delta(t-t') \qquad (1.46)$$

$$\langle \hat{a}_{\text{in}}(t)\hat{a}_{\text{in}}^{\dagger}(t') \rangle = (\bar{n}(\omega)+1)\delta(t-t'), \qquad (1.47)$$

with the frequency dependent occupation of the thermal bath at temperature T

$$\bar{n}(\omega) = \frac{1}{e^{\hbar\omega/k_B T} - 1}. \qquad (1.48)$$

Note that the expectation value of an operator $\hat{o}(t)$ is defined as $\langle \hat{o}(t) \rangle = \text{Tr}\{\hat{\rho}\hat{o}(t)\}$, where $\hat{\rho} = \hat{\rho}_{\text{sys}} \otimes \hat{\rho}_{\text{bath}}$ denotes the total density operator, which can be written as direct product of the density operator of the system and the one of the bath at time $t = t_0$.

Analogously to the definition of the input field operator one defines the output field [75]

$$\hat{a}_{\text{out}}(t) = \frac{1}{\sqrt{2\pi}} \int_{-\infty}^{\infty} e^{-i\omega(t-t_1)} \hat{b}_1(\omega). \tag{1.49}$$

Input and output fields are related by [75]

$$\hat{a}_{\text{out}}(t) + \hat{a}_{\text{in}}(t) = \sqrt{\Gamma} \hat{c}(t). \tag{1.50}$$

In the following section we will use the Heisenberg-Langevin equation to derive the optomechanical coupling between cavity photons and a single atom.

1.9. A single atom in an optical cavity

In this section we introduce the mechanical effect of light on an atom in a cavity. For this purpose we first consider a single two-level atom of mass m and transition frequency ω_a, coupled to a single mode[6] of a high-finesse optical cavity with frequency ω_c and wavevector k as depicted in Fig.1.11. We assume that the atom moves only in one dimension along the x direction due to a tight confinement in y and z. We neglect the additional harmonic confinement along x due to the Gaussian laser beam profile. The annihilation and creation operators of a cavity photon are $\hat{a}$ and $\hat{a}^{\dagger}$ with $[\hat{a}, \hat{a}^{\dagger}] = 1$. The atomic ground state and excited states are denoted by $|g\rangle$ and $|e\rangle$ respectively and we introduce the lowering and raising operators $\hat{\sigma} = |g\rangle \langle e|$ and $\hat{\sigma}^{\dagger} = |e\rangle \langle g|$. We consider an external coherent driving laser of frequency ω_p that either pumps the cavity mode at normal incidence with real coupling strength η or the internal degree of freedom of the atom with Rabi frequency ξ.[7] With the rotating wave and dipole approximation [74] the Hamiltonian of the system in the frame rotating at the frequency of the driving laser ω_p reads [12]

$$\hat{H}_{\text{initial}} = \frac{\hat{p}^2}{2m} + \hat{H}_{\text{JC}} + \hat{H}_{\text{pump}}, \tag{1.51}$$

where the detunings between atom and pump and between cavity and pump are denoted as $\Delta_a = \omega_p - \omega_a$ and $\delta_c = \omega_p - \omega_c$ and with the Jaynes-Cummings Hamiltonian [76] in the

---

[6]The single mode approximation is valid for a cavity with large spectral range $\Delta\omega = c/2l$, where c is the speed of light and l the distance between the cavity mirrors.

[7]In principle it is also possible to pump both atom and cavity at the same time. But in that case we can not derive an effective potential V_{eff} as desired for our study of localization, see Section 2.3.1.
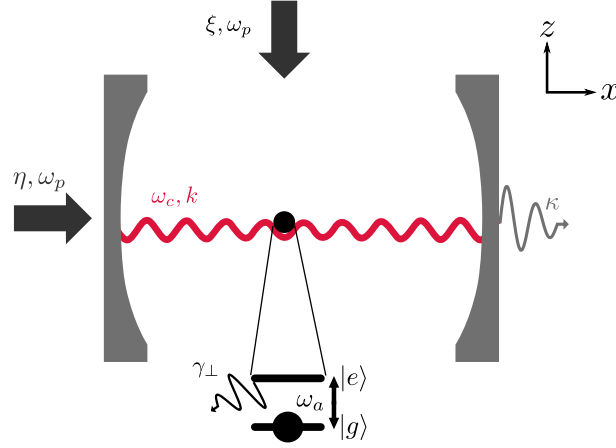
Figure 1.11.: A single two level atom with transition frequency ω_a is coupled to a single mode of a high-finesse cavity with frequency ω_c and wavevector k. The motion of the atom is only along the x axis. We consider two different pump scenarios: either the cavity mode is pumped at normal incidence with frequency ω_p and pump strength η or the atom is transversally pumped with frequency ω_p and pump strength ξ. The atom decays into the electromagnetic field outside the cavity with a decay rate $\gamma_\perp$ and the cavity mode loses photons via the partially transmitting mirrors with a loss rate κ.

frame rotating at the frequency of the driving laser ω_p

$$\hat{H}_{\mathrm{JC}} = -\hbar\Delta_a\hat{\sigma}^\dagger\hat{\sigma} - \hbar\delta_c\hat{a}^\dagger\hat{a} + \hbar g(\hat{x})(\hat{a}^\dagger\hat{\sigma} + \hat{\sigma}^\dagger\hat{a}). \tag{1.52}$$

The position-dependent atom-cavity coupling strength is $g(\hat{x}) = g_0\cos(k\hat{x})$, with $g_0 = \sqrt{\frac{\omega_c}{2\epsilon_0 V\hbar}}\mu$ the vacuum Rabi frequency, where V is the effective cavity mode volume and μ the atomic dipole moment along the cavity mode polarization that we choose along z [12, 74]. In the case of the pumped cavity mode, the pump Hamiltonian is given by

$$\hat{H}_{\mathrm{pump}} = \hbar\eta(\hat{a}^\dagger + \hat{a}). \tag{1.53}$$

The Hamiltonian $\hat{H}_{\mathrm{initial}}$, with $\hat{H}_{\mathrm{pump}}$ given by Eq. (1.53), corresponds to the one particle scenario of the Hamiltonian discussed in Ref. [44]. In the case of the pumped atom, the pump Hamiltonian reads

$$\hat{H}_{\mathrm{pump}} = \hbar\xi(\hat{\sigma}^\dagger + \hat{\sigma}), \tag{1.54}$$

corresponding to the one particle scenario of Ref. [39, 77].

The excited state of the atom and the cavity mode both radiatively couple to the external electromagnetic field. The atom decays spontaneously with a rate $\gamma_\perp$[8] and the cavity loses photons due to the finite transmittivity of the mirrors at a rate κ. We use the Heisenberg-Langevin formalism, introduced in Section 1.8, to describe the driven-dissipative dynamics: we obtain the Heisenberg-Langevin equation for the cavity field operator $\hat{a}$ if we identify $\hat{a}$ with the operator $\hat{c}$ in Eq.(1.37) and use the Hamiltonian $\hat{H}_{\text{initial}}$, given by Eq.(1.51) for the system Hamiltonian $\hat{H}_{\text{sys}}$. In this case, the Heisenberg-Langevin equation for the cavity field operator $\hat{a}$ is given by [44]

$$
\begin{aligned}
\dot{\hat{a}}(t) &= \frac{i}{\hbar}[\hat{H}_{\text{initial}}, \hat{a}] - \kappa\hat{a} + \sqrt{2\kappa}\hat{a}_{\text{in}}, \\
&= \begin{cases} (i\delta_c - \kappa)\,\hat{a} - i\eta - ig(\hat{x})\hat{\sigma} + \sqrt{2\kappa}\hat{a}_{\text{in}}, \text{for the pumped cavity.} \\ (i\delta_c - \kappa)\,\hat{a} - ig(\hat{x})\hat{\sigma} + \sqrt{2\kappa}\hat{a}_{\text{in}}, \text{for the pumped atom.} \end{cases}
\end{aligned}
\tag{1.55}
$$

For the Heisenberg-Langevin equation of the atomic lowering operator $\hat{\sigma}$ we identify $\hat{\sigma}$ with the operator $\hat{c}$ in Eq.(1.37), use the Hamiltonian $\hat{H}_{\text{initial}}$, given by Eq.(1.51) for the system Hamiltonian $\hat{H}_{\text{sys}}$ and use $\gamma_\perp$ instead of Γ. The Heisenberg-Langevin equation for the atomic lowering operator $\hat{\sigma}$ reads [44]

$$
\begin{aligned}
\dot{\hat{\sigma}}(t) &= \frac{i}{\hbar}[\hat{H}_{\text{initial}}, \hat{\sigma}] - \frac{\gamma_\perp}{2}\hat{\sigma} + \sqrt{\gamma_\perp}\hat{\sigma}_z f_{\text{in}}(t), \\
&= \begin{cases} i\Delta_a\hat{\sigma} + ig(\hat{x})\hat{a}\hat{\sigma}_z - \frac{\gamma_\perp}{2}\hat{\sigma} + \sqrt{\gamma_\perp}\hat{\sigma}_z\hat{f}_{\text{in}}(t), \text{for the pumped cavity,} \\ i\Delta_a\hat{\sigma} + ig(\hat{x})\hat{a}\hat{\sigma}_z + i\xi\hat{\sigma}_z - \frac{\gamma_\perp}{2}\hat{\sigma} + \sqrt{\gamma_\perp}\hat{\sigma}_z\hat{f}_{\text{in}}(t), \text{for the pumped atom,} \end{cases}
\end{aligned}
\tag{1.56}
$$

where the input noise operators $\hat{a}_{\text{in}}$ and $\hat{f}_{\text{in}}$ obey the relations defined in equations (1.45)-(1.47). The occupation of the thermal bath $\bar{n}(\omega)$ for the cavity or the atomic frequency (both are typically in the optical range [78]) is negligible at room temperature, hence the two time correlation functions are only given by $\langle\hat{a}_{\text{in}}(t)\hat{a}_{\text{in}}^\dagger(t')\rangle = \delta(t - t')$ and $\langle\hat{f}_{\text{in}}(t)\hat{f}_{\text{in}}^\dagger(t')\rangle = \delta(t - t')$.

---

[8]The spontaneous emission of the atom with rate $\gamma_\perp$ is directed in the plane transverse to the cavity axis.

The dynamics of the external degree of freedom of the atom is governed by

$$\dot{\hat{p}}(t) = \frac{i}{\hbar}[\hat{H}_{\text{initial}}, \hat{p}]$$
$$= \hbar g_0 k \sin(k\hat{x})(\hat{a}^\dagger \hat{\sigma} + \hat{\sigma}^\dagger \hat{a}) \tag{1.57}$$

$$\dot{\hat{x}}(t) = \frac{i}{\hbar}[\hat{H}_{\text{initial}}, \hat{x}] = \frac{\hat{p}}{m}. \tag{1.58}$$

We assume that the time scale on which the atom reaches its internal state is much smaller than the time scale of its center of mass motion[9], namely $|\Delta_a| \gg \frac{k\Delta p}{m}$ and much smaller than the dynamics of the cavity mode $|\Delta_a| \gg |\delta_c|, \kappa$ [39]. So the changes of the atomic position or the cavity field are negligible on the time scale of the internal atomic degree of freedom and we can solve the Heisenberg-Langevin equation for $\hat{\sigma}$, Eq.(1.56), at a fixed value of the atomic position x and of the annihilation operator $\hat{a}$ [43]. For $|\Delta_a| \gg g_0\sqrt{\langle \hat{a}^\dagger \hat{a} \rangle}, \xi \gg \gamma_\perp/2$ the internal structure of the atom is not resolved and dissipation due to spontaneous decay can be discarded [80]. The atom is always in its ground state and we can neglect the population of the excited state, hence we can use $\langle \hat{\sigma}_z(t) \rangle \approx 1$ and $\dot{\hat{\sigma}} = 0$ to obtain the solutions of Eq.(1.56) [12, 44]

$$\hat{\sigma} = \begin{cases} \frac{g(\hat{x})\hat{a}}{\Delta_a}, \text{for the pumped cavity.} \\ \frac{g(\hat{x})\hat{a}+\xi}{\Delta_a}, \text{for the pumped atom.} \end{cases} \tag{1.59}$$

A detailed derivation of these equations for general mode functions in three dimensions can be found in Ref. [81]. The regime in which the detuning $|\Delta_a|$ is the largest frequency characterizing the dynamics, is referred to as dispersive limit. The effective Hamiltonian $\hat{H}_{\text{elim.at}}$ for the cavity field and the external degree of freedom of the atom can be determined by inserting the expression for $\hat{\sigma}$, given in Eq.(1.59), in the Heisenberg-Langevin equation for the cavity annihilation operator Eq.(1.55) and in the Heisenberg equation for the momentum operator Eq.(1.57). The effective Hamiltonian can be identified as

$$\hat{H}_{\text{elim.at}} = \frac{\hat{p}^2}{2m} + \hat{H}_{\text{opto}}, \tag{1.60}$$

where the optomechanical coupling between the cavity mode and the atomic motion is

---

[9]Or in other words during the atomic relaxation time the atom travels over a small distance compared to the cavity wave length [79].

described by [38, 39]

$$\hat{H}_{\text{opto}} = -\hbar\delta_c\hat{a}^\dagger\hat{a} + \hbar U_0\cos^2(\beta k_0\hat{x})\hat{a}^\dagger\hat{a} + \hbar\zeta(\hat{x})(\hat{a}^\dagger + \hat{a}),\tag{1.61}$$

with the Stark shift due to the atom-cavity mode coupling

$$U_0 = \frac{g_0^2}{\Delta_a}.\tag{1.62}$$

The function $\zeta(\hat{x})$ is given by the constant

$$\zeta(\hat{x}) = \eta,\tag{1.63}$$

when the pump is set directly on the cavity mirror and by

$$\zeta(\hat{x}) = \cos(\beta k_0\hat{x})\xi g_0/\Delta_a,\tag{1.64}$$

when instead the atom is transversally driven by the laser. The Hamiltonian $\hat{H}_{\text{opto}}$ as defined in Eq.(1.61) shows that the presence of the atom shifts the cavity resonance frequency in a position dependent, nonlinear way. The strength of this nonlinearity is controlled by U_0. Furthermore the cavity field gives rise to an optical potential

$$V_{\text{eff.pot}}(\hat{x}) = \hbar U_0\cos^2(\beta k_0\hat{x})\hat{a}^\dagger\hat{a}\tag{1.65}$$

for the atom [12]. The depth of the potential depends on the photon number and on U_0. If the atom is transversally driven by the laser the coherent photon scattering yields an effective cavity pump term that depends on the atomic position. It is proportional to the scattering amplitude $\xi g_0/\Delta_a$ with which a photon is scattered by the atom between the laser mode and the cavity mode [77].

1.10. Experiment on ultracold atoms in an optical cavity

It is possible experimentally to combine cavity QED with the physics of ultracold atoms in optical lattices. Groups that are doing this are for example the one of Tilmann Esslinger in Zürich [41, 47] and the one of Andreas Hemmerich in Hamburg [46]. In Chapter 2, when discussing the localization transition of a single ultracold atom in the presence of cavity

backaction, we will refer respectively to the experiments of both groups.

In this section we present exemplarily one experiment of the group of Tilman Esslinger in Zürich on ultracold atoms, that optomechanically couple to a mode of an optical cavity, in order to introduce the context and the setup. In Ref. [41] they discuss the experimental realization of the Dicke model [82] describing an ensemble of two-level atoms coupled to a single electromagnetic field mode. The model predicts a superradiant phase with macroscopic occupation of the field mode. The experimental setup is sketched in Fig.1.12 (a): they use a BEC of ^{87}Rb atoms that is confined within a high-finesse optical cavity of length of $h = 178\,\mu$m. The cavity consists of two mirrors with a radius of curvature of $75\,$mm [83]. The BEC is transversally driven by a far-detuned pump laser. The pump laser frequency is close to the frequency of one cavity mode. They are in the dispersive limit we described in the previous section: the cavity frequency depends on the position of the atoms and the atoms scatter light into the cavity in a position dependent way. If the atoms are homogeneously distributed the scattered light destructively interferes and no cavity field builds up. Above a critical external pump strength the atoms self-organize in a checkerboard pattern and start to constructively scatter into the cavity mode. This transition can be observed by monitoring the intracavity photon number as a function of the external pump strength, as depicted in Fig.1.12 (b). The self-organized (superradiant) phase can also be monitored by the appearance of additional momentum peaks at $(p_x, p_z) = (\pm\hbar k, \pm\hbar k)$ in the time-of-flight images.
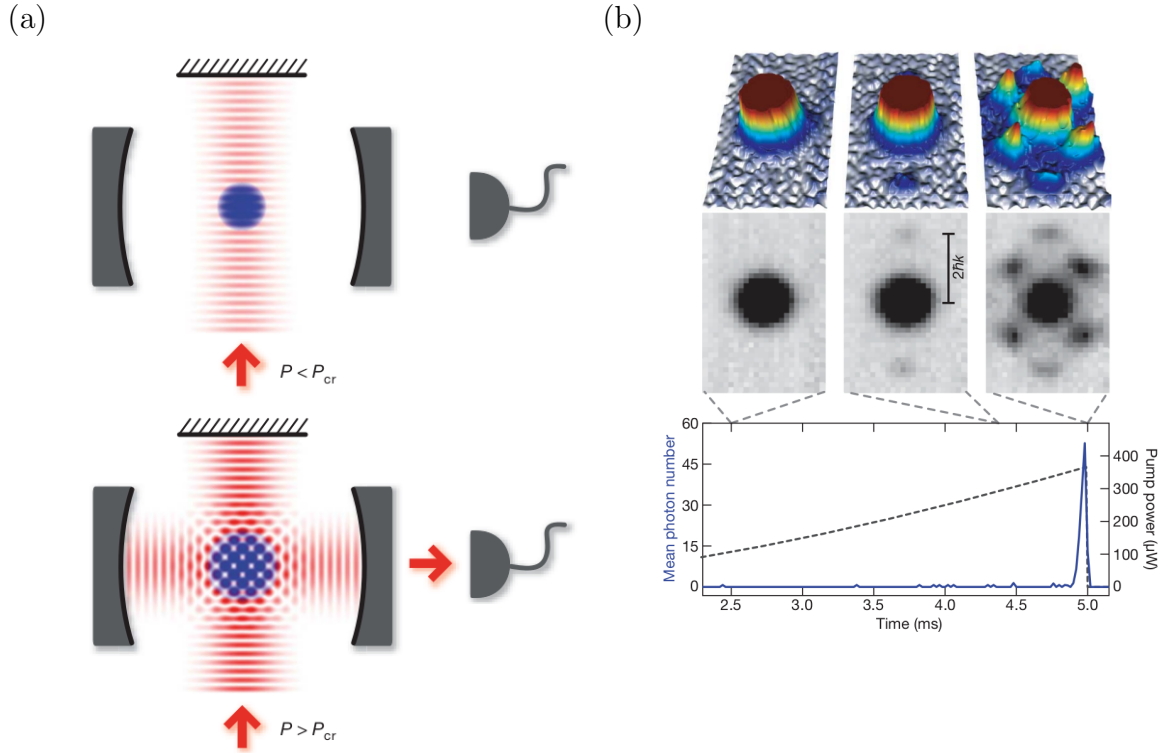
Figure 1.12.: (a) Experimental setup. A BEC is confined within a high-finesse optical cavity and transversally driven by a far-detuned pump laser. The pump laser frequency is close to the frequency of one cavity mode, thus the atoms scatter light into the cavity in a position dependent way. If the atoms are homogeneously distributed (top picture) the scattered light destructively interferes and no cavity field builds up. In the self-organized phase, for a pump strength above the critical pump power (bottom picture) the atoms scatter light constructively into the cavity mode. (b) Experimental observables. Bottom picture: The mean intra cavity photon number is shown for an increasing pump strength. Top picture: The momentum distribution after ballistic expansion (time-of-flight) is shown for three different pump strengths. The superradiant (self-organized) phase can be identified by the sudden build-up of the cavity field. Furthermore the time-of-flight images shows additional momentum peaks at $(p_x, p_z) = (\pm\hbar k, \pm\hbar k)$, with k the wavevector of the pump. The image is taken from Ref. [41].

Chapter 2

The Aubry-André model in presence of cavity backaction

This chapter is devoted to the study of the Aubry-André model in presence of cavity backaction. We first introduce the general theoretical model at the basis of our analysis, which is a Bose-Hubbard model for one particle with a site-dependent onsite energy resulting from a second, incommensurate potential. We then identify the parameters for which one recovers the Aubry-André [9] or Harper model [10]. We further discuss the conditions under which the Bose-Hubbard model describes a cold atom which optomechanically interacts with the mode of a high-finesse optical cavity.

2.1. Bose-Hubbard model for cavity QED with one cold atom

The model at the basis of our analysis results from the one-dimensional dynamics of a particle of mass m in two periodic potentials, of which one, denoted by $\hat{W}_{\text{ext}}(\hat{x})$ and defined in Eq.(1.5), tightly traps the particle at its minima while the second, $\hat{V}_{\text{eff}}(\hat{x})$, is a perturbation to the first potential, in the spirit of $\hat{V}_{\text{pert}}$ that we introduced in Section 1.5. The Hamiltonian reads

$$\hat{H}_{\text{eff}} = \frac{\hat{p}^2}{2m} + \hat{W}_{\text{ext}}(\hat{x}) + \hat{V}_{\text{eff}}(\hat{x}), \tag{2.1}$$

with $\hat{p}$ and $\hat{x}$ the canonically-conjugate momentum and position. The cavity and external potentials are periodic with wavenumbers k and k_0, respectively, where $k = \beta k_0$ and β is an irrational number. Therefore, the Hamiltonian is quasiperiodic. Specifically $\hat{W}_{\text{ext}}(\hat{x}) = \hat{W}_{\text{ext}}(\hat{x} + \pi/k_0)$, while $\hat{V}_{\text{eff}}(\hat{x}) = \hat{V}_{\text{eff}}(\hat{x} + \pi/k)$. For later convenience we write

$\hat{V}_{\text{eff}}(\hat{x}) = v_0 f(\hat{x})$, where v_0 has the dimensions of an energy, and $f(\hat{x}) = f(\hat{x} + \pi/k)$ is a dimensionless function. In the limit in which the dynamics can be restricted to the lowest band of the deep lattice $\hat{W}_{\text{ext}}(\hat{x})$ [84], we can describe it by means of the Bose-Hubbard Hamiltonian

$$\hat{H}_{BH} = -t \sum_{n=1}^{L-1} (|n\rangle \langle n+1| + |n+1\rangle \langle n|) + \sum_{n=1}^{L} \delta\epsilon_n |n\rangle \langle n| , \qquad (2.2)$$

where $|n\rangle$ denotes the state of the particle at site n of the external lattice potential $\hat{W}_{\text{ext}}$, with $n = 1, \ldots, L$ and L the total number of sites. We recall that (see again Section 1.5) the Bose-Hubbard Hamiltonian is composed of the hopping term, scaled by the tunneling coefficient $t = \langle n| \hat{p}^2/(2m) + \hat{W}_{\text{ext}}(\hat{x}) |n+1\rangle$, and by the diagonal term in the basis $\{|n\rangle\}$, whose coefficients are given by the onsite energy $\delta\epsilon_n = \langle n| \hat{H}_{\text{eff}} |n\rangle$. The onsite enery is site dependent since the Hamiltonian is quasiperiodic. After subtracting an arbitrary energy constant, we can rewrite these coefficients as

$$\delta\epsilon_n = \langle n| \hat{V}_{\text{eff}}(\hat{x}) |n\rangle = v_0 \int_{-L_0/2}^{L_0/2} dx \ w_n(x) f(x) w_n(x) , \qquad (2.3)$$

where $w_n(x) = \langle x |n\rangle = w(x - x_n)$ are the real valued Wannier functions [85], as defined in Eq.(1.13) which are centered at lattice site n for a given Wannier state $|n\rangle$ and $L_0 = L\pi/k_0$.

We analyze the localization transition when the incommensurate potential is given by the function

$$f(x) = \arctan\left(-\delta'_c + C \cos^2(\beta k_0 x)\right) . \qquad (2.4)$$

The functional form $f(x)$ as given in Eq.(2.4) is reminiscent of the one considered in Ref. [86] and is typically encountered in optomechanical problems in CQED [43, 87–89]. The parameters δ'_c and C are real valued and can take both positive and negative values. The parameter δ'_c is responsible for the appearance of nontrivial poles. The parameter C controls the functional form of the second potential $f(x)$, as illustrated in Fig.2.1 (b) for $\delta'_c = 0$.

We show in Section 2.2, that for $|C| \ll 1$ the onsite energy essentially reduces to Eq.(1.26), with a new amplitude $v'_0 = |C| v_0/[2(\delta'^2_c + 1)]$, yielding a critical point v_c^{cav} that is different from the Aubry-André critical point v_c^{AA}.

For $|C| \simeq 1$, higher harmonics $\cos^{2n} kx$ of the Taylor expansion in C of Eq.(2.4) become relevant and change the functional form of $f(x)$, as illustrated in Fig.2.1 (b). Differing from the Aubry-André model, this is the regime where the model is not self-dual. In
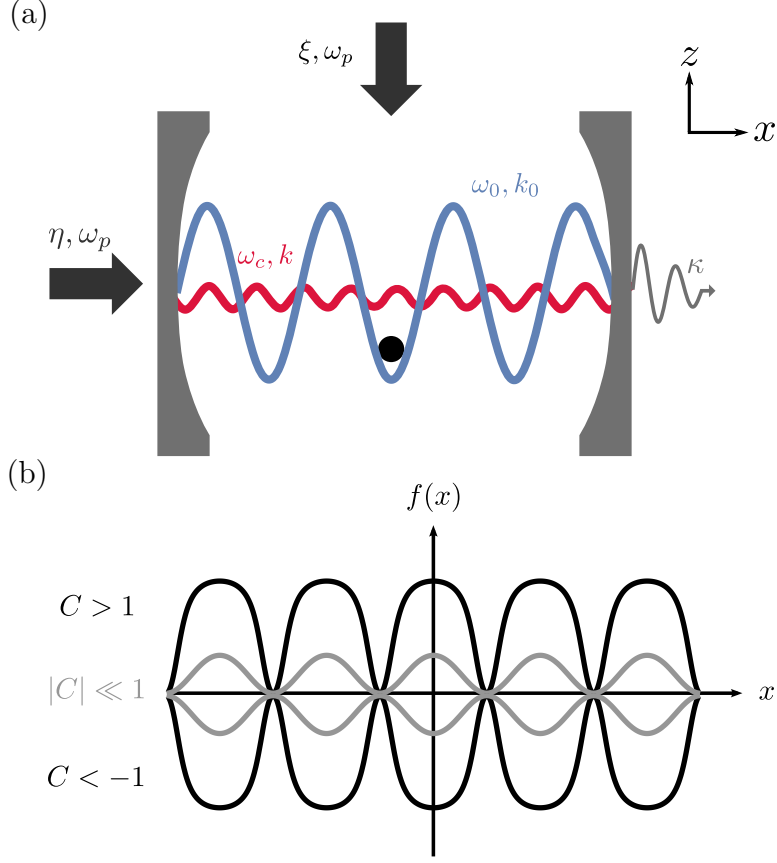
Figure 2.1.: (a) A single atom is confined by an optical lattice, sketched as blue line, with wavenumber $k_0 = 2\pi/\lambda_0$ and frequency ω_0 within a standing-wave resonator. Its motion optomechanically interacts with a high-finesse mode, shown in red, at frequency ω_c and wavenumber $k = 2\pi/\lambda$, whose wavelength λ is incommensurate with the optical lattice periodicity $\lambda_0/2$. The depth of the cavity lattice is determined by the balance between a pump with frequency ω_p, and the losses at rate κ. We consider two different pump schemes: either the cavity mode is pumped with a pump strength η or the atom is transversally driven with a pump strength ξ. We study the localization transition in this setup, where the nonlinearity due to strong coupling with the cavity (given by the cooperativity C) modifies the effective incommensurate potential. The optomechanical potential $f(x)$ as defined in Eq.(2.4) is illustrated in (b) as a function of x for four different values of the cooperativity C and when the laser is resonant with the cavity ($\delta_c' = 0$). The limit $|C| \ll 1$ corresponds to the Aubry-André model.

Section 2.3 we will derive the potential Eq.(2.4) from a microscopic model describing an atom in a high-finesse cavity, subjected to an optical lattice, as illustrated in Fig.2.1 (a). By means of this model one can identify C with the cooperativity of CQED, which measures the strength of cavity backaction on the atom's scattering properties [90].

We study the transition to spatial localization. We determine numerically the ground state $|\Psi_0\rangle$ of Hamiltonian (2.2) with potential (2.4) as a function of C, δ'_c, and the ratio v_0/t. We characterize the transition by means of the inverse participation ratio (IPR) P_x [68], as defined in Eq.(1.27) where the state $|\Phi\rangle$ is given by the ground state $|\Psi_0\rangle$.

We also monitor the degree of localization by the Lyapunov exponent [9], as defined in Eq.(1.30). According to Thouless' formula [69], in the localized regime of the Aubry-André model it is given by Eq.(1.31), whereas for $\delta\epsilon_n$ given by Eq.(2.3) the critical point in the Thouless formula corresponds to v_c^{cav} from Eq.(2.9). In our calculation we obtain the Lyapunov exponent γ by fitting the spatial decay of the wavefunction by means of an exponential function.

2.2. Reproducing the Aubry-André model

In this section we want to identify the regime in which we can reproduce the Aubry-André model.

For small cooperativities $|C| \ll 1$ we can linearize the site-dependent onsite potential $\delta\epsilon_n$, given by Eq. (2.3), to

$$\delta\epsilon_n = v_0 \int_{-L_0/2}^{L_0/2} dx \; w_n(x) \left(\arctan(-\delta'_c) + \frac{\cos^2(\beta k_0 x)}{1 + \delta'^2_c} |C| \right) w_n(x). \tag{2.5}$$

Neglecting the constant energy offset $v_0 \arctan(-\delta'_c)$ and with the help of trigonometry identities we have

$$\delta\epsilon_n = \frac{v_0|C|}{2(1 + \delta'^2_c)} \int_{-L_0/2}^{L_0/2} dx \; w_n(x) \left[1 + \cos(2\beta k_0 x) \right] w_n(x).$$

Now we shift x to $x + x_n$, recalling that $w_n(x) = w(x - x_n)$, which leads to

$$\delta\epsilon_n = \frac{v_0|C|}{2(1 + \delta'^2_c)} \int_{-L_0/2-x_n}^{L_0/2-x_n} dx \; w_0(x) \left[1 + \cos(2\beta k_0(x + x_n)) \right] w_0(x).$$

We use again trigonometry and neglect the constant energy offset to cast the site-dependent

onsite potential in the form

$$\delta\epsilon_n = \frac{v_0|C|}{2(1 + \delta_c'^2)}\alpha\cos(2\beta k_0 x_n), \tag{2.6}$$

with $\alpha(\beta) = \int_{-L_0/2-x_n}^{L_0/2-x_n} dx \, w_0(x)\cos(2\beta k_0 x)w_0(x)$. Using $k = \beta k_0$ and $x_n = -\frac{(L-1)}{2}\pi/k_0 + (n-1)\pi/k_0$, the Hamiltonian reduces to the final form of the Aubry-André Hamiltonian as defined in Eq.(1.25)

$$\hat{H}_{\text{cav,[n]}} = -t\sum_{n=1}^{L-1}|n\rangle\langle n+1| + |n+1\rangle\langle n|$$

$$- v_0'\sum_{n=1}^{L}\alpha\cos(2\beta\pi n + \phi')|n\rangle\langle n|, \tag{2.7}$$

with a new amplitude $v_0' = |C|v_0/[2(\delta_c'^2 + 1)]$ and $\phi' = -\beta\pi(L+1) + \pi$.

We determine the critical potential strength for the modified Aubry-André model, following the method used in the original Aubry-André derivation (see Section 1.6 and Ref. [9]). For this purpose, it is useful to perform the basis transformation, defined in Eq.(1.28), which leads to the Hamiltonian in the momentum space

$$\hat{H}_{\text{cav,[}\bar{k}]} = -\frac{v_0'}{2}\alpha\sum_{\bar{k}=1}^{L}e^{-i\phi'}|\bar{k}\rangle\langle\bar{k}+1| + e^{i\phi'}|\bar{k}+1\rangle\langle\bar{k}|$$

$$- v_0'\sum_{\bar{k}=1}^{L}\frac{2t}{v_0'}\cos(2\pi\beta\bar{k})|\bar{k}\rangle\langle\bar{k}|. \tag{2.8}$$

The constant phase ϕ' can be eliminated by a gauge transformation[1]. For $v_0' = 2t/\alpha$ the Hamiltonians (2.7) and (2.8) are identical, thereby identifying the self-dual point, which is the critical point for the transition from the extended to the localized phase

$$v_c^{\text{cav}} = \frac{4t}{\alpha(\beta)}\frac{\delta_c'^2 + 1}{|C|}. \tag{2.9}$$

We find that, at difference from the original Aubry-André model, in the cavity case the critical point depends on the incommensurability parameter β, through the parameter $\alpha(\beta)$. For $\delta_c' = 0$ and $|C| = 1$ this corresponds to the result found in Ref. [67], where the

---

[1]We can define $|\tilde{k}\rangle\langle\tilde{k}+1| = e^{-i\phi'}|\bar{k}\rangle\langle\bar{k}+1|$, which leaves the onsite energy part unchanged $|\tilde{k}\rangle\langle\tilde{k}| = |\bar{k}\rangle\langle\bar{k}|$.

quasiperiodic lattice is created by superimposing two incommensurate optical lattices.

Fig.2.2 shows the inverse participation ratio P_x for the original Aubry-André model, Eq.(2.2), with $\delta\epsilon_n$ as in Eq.(1.26), and for the modified Aubry-André model, as given in Eq.(2.2), with $\delta\epsilon_n$ as in Eq.(2.3), for $\beta = (\sqrt{5}-1)/2$ and $\beta = (\sqrt{5}+1)/2$ respectively, for $\delta'_c = 0$ and $C = -0.5$ (subplot (a)) and for $\delta'_c = 1$ and $C = -0.1$ (subplot (b)). The system size is $L = 233$. The Aubry-Andé transition takes place at $v_0/t = v_c^{\mathrm{AA}}/t = 2$ and is independent of the value of the incommensurability β. The transition of the modified Auby-André model occurs at $v_c^{\mathrm{cav}}/t = 9$ and $v_c^{\mathrm{cav}}/t = 14$ for $\delta'_c = 0$ and $C = -0.5$ and $\beta = (\sqrt{5}-1)/2$ and $\beta = (\sqrt{5}+1)/2$ respectively (Fig.2.2 (a)), and at $v_c^{\mathrm{cav}}/t = 87$ and $v_c^{\mathrm{cav}}/t = 137$ for $\delta'_c = 1$ and $C = -0.1$ and $\beta = (\sqrt{5}-1)/2$ and $\beta = (\sqrt{5}+1)/2$ respectively (Fig.2.2 (b)), thus confirming the prediction of Eq.(2.9). Note that for the parameter choice of these simulations, we were guided by the values of Ref. [41]. In particular we consider a ^{87}Rb atom and the cooperativity $C = U_0/\kappa$, with the cavity damping rate $\kappa = 2\pi \times 1.3\,\mathrm{MHz}$ and $U_0 = g_0^2/\Delta_a$, where $g_0 = 2\pi \times 14.1\,\mathrm{MHz}$ is the coupling strength between atomic dipole and cavity mode. $\Delta_a = \omega_p - \omega_0$ denotes the tunable detuning between external pump frequency ω_p and atomic transition frequency ω_0. The detuning corresponds to $\delta'_c = \delta_c/\kappa$, where $\delta_c = \omega_p - \omega_c$ is the detuning between external pump frequency and cavity mode frequency ω_c. The wavevector of the optical lattice is $k_0 = 2\pi/830\,\mathrm{nm}$ and the optical lattice depth is taken $W_0 = -29E_r$, where $E_r = \hbar^2 k_0^2/2m$ denotes the recoil energy.

2.3. Self-induced localization in cavity QED

In this section we derive the Bose-Hubbard Hamiltonian of Eq.(2.2) starting from the optomechanical coupling of a lossy cavity field and a single atom, confined by an optical lattice, as depicted in Fig.2.1 (a).

The relevant degrees of freedom for the atom are the momentum $\hat{p}$ along x and the canonically-conjugated position $\hat{x}$. The cavity mode degrees of freedom are the photon annihilation and creation operators $\hat{a}$ and $\hat{a}^\dagger$, respectively, with the commutation relation $[\hat{a}, \hat{a}^\dagger] = 1$. We denote by m the atomic mass and by ω_c the cavity mode frequency, with wavelength $\lambda = 2\pi c/\omega_c$, wavenumber $k = \beta k_0$ and spatial mode function $\cos(\beta k_0 x)$.

The system is driven by a laser, which is described by a classical field. The laser frequency ω_p is the reference frequency: the atom transition frequency ω_a is given by the detuning $\Delta_a = \omega_p - \omega_a$ and the cavity mode frequency by the detuning $\delta_c = \omega_p - \omega_c$. In the dispersive limit, in which $|\Delta_a|$ is the largest frequency characterizing the dynamics, the atom's internal degrees of freedom are eliminated as discussed in Section 1.9: In this regime

(a)

(b)
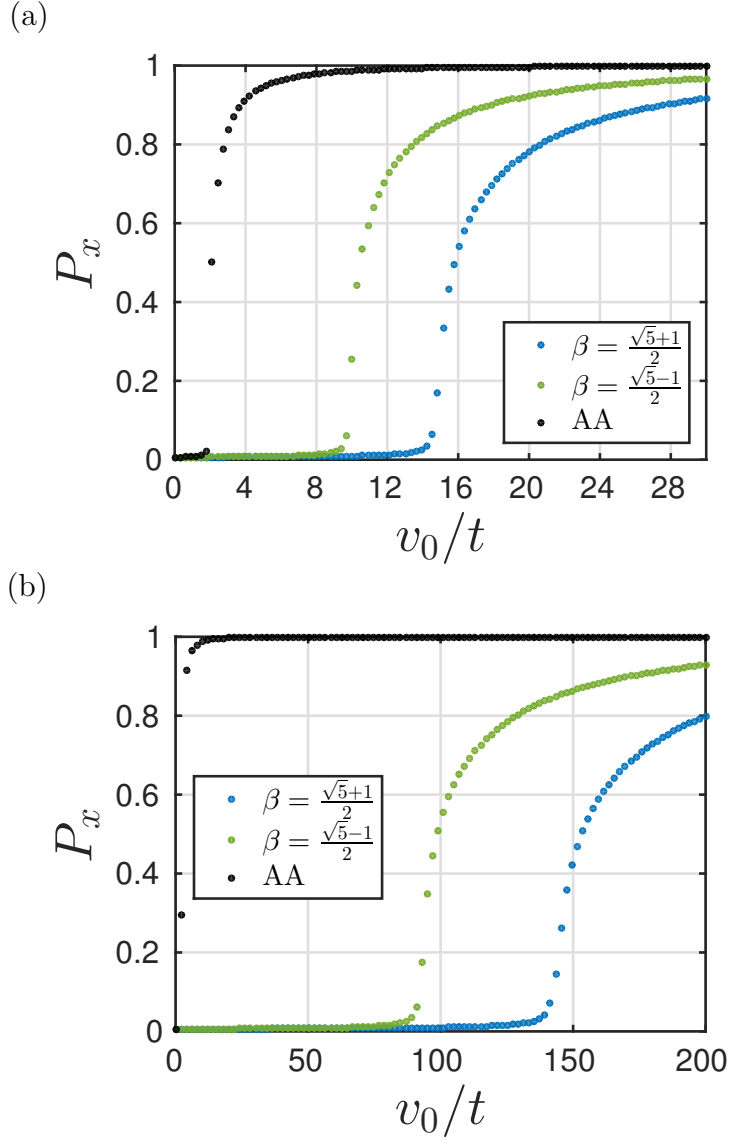
Figure 2.2.: Inverse participation ratio P_x as a function of the strength of the quasiperiodic potential v_0 in units of the tunneling t for the original Aubry-André model, Eq.(2.2), with $\delta\epsilon_n$ as in Eq.(1.26), and for the modified Aubry-André model, as given in Eq.(2.2), with $\delta\epsilon_n$ as in Eq.(2.3), for $\beta = (\sqrt{5}-1)/2$ and $\beta = (\sqrt{5}+1)/2$ respectively. In subplot (a) the detuning is $\delta_c' = 0$ and $C = -0.5$, leading to shifted critical point $v_c^{cav}/t = 9$ and $v_c^{cav}/t = 14$. In subplot (b) the detuning corresponds to $\delta_c' = 1$ and $C = -0.1$ and shifted critical points $v_c^{cav}/t = 87$ and $v_c^{cav}/t = 137$ as obtained from Eq.(2.9). The system size is $L = 233$.

the atomic dipole behaves as a classical dipole and spontaneous decay is neglected. The cavity loses photons at a rate κ due to the mirror finite transmittivity. The Hamiltonian $\hat{H}$ is given by

$$\hat{H} = \frac{\hat{p}^2}{2m} + \hat{W}_{\text{ext}}(\hat{x}) + \hat{H}_{\text{opto}}, \qquad (2.10)$$

where the first term on right-hand side (RHS) is the kinetic energy and the potential $\hat{W}_{\text{ext}}(\hat{x})$, defined in Eq.(1.5), is periodic with period π/k_0 and tightly binds the atom at its minima. The Hamiltonian $\hat{H}_{\text{opto}}$ is derived in Section 1.9 and given in Eq.(1.61). It includes the cavity degrees of freedom and their optomechanical coupling with the atomic motion. We recall that it reads [38, 39]

$$\hat{H}_{\text{opto}} = -\hbar\delta_c\hat{a}^\dagger\hat{a} + \hbar U_0\cos^2(\beta k_0\hat{x})\hat{a}^\dagger\hat{a} + \hbar\zeta(\hat{x})(\hat{a}^\dagger + \hat{a}), \qquad (2.11)$$

where frequency U_0 scales the dynamical Stark shift due to the coupling between atom and cavity mode, $U_0 = g_0^2/\Delta_a$, with the vacuum Rabi frequency g_0, which determines the strength of the coupling between the dipole and one cavity photon. The frequency U_0 can be either positive or negative depending on the sign of Δ_a. The last term on the RHS in Eq.(2.11) corresponds to the effect induced by an external pump on the cavity mode. The pump, in particular, can couple either directly to the cavity, by impinging on a mirror, or via the atom, which coherently scatters photons into the cavity mode, as illustrated in Fig. 2.1 (a). When the pump is set directly on the cavity mirror, the strength of this coupling is given by a constant value

$$\zeta(\hat{x}) = \eta. \qquad (2.12)$$

When instead the atom is transversally driven by the laser, then $\zeta(\hat{x})$ takes the form

$$\zeta(\hat{x}) = \cos(\beta k_0\hat{x})\xi g_0/\Delta_a \qquad (2.13)$$

and is thus weighted by the cavity spatial mode function at the atomic position. Moreover, it is proportional to the laser Rabi frequency ξ, which determines the strength of the coupling between the dipole and the laser.

2.3.1. Time-scale separation and effective dynamics

We consider the limit in which there is a time-scale separation between cavity and atomic motion dynamics and assume that the cavity field follows adiabatically the atomic motion.

This assumption requires that the cavity relaxes much faster to its steady state than the density distribution of the atom varies[2], which is the case if the cavity linewidth is much larger than the atom Doppler broadening [39]

$$|\kappa + i\delta_c| \gg \frac{k\Delta p}{m}, \tag{2.14}$$

where $\Delta p = \sqrt{\langle \hat{p}^2 \rangle}$ is the variance of the atomic momentum. The kinetic energy of the atom can be linked to an effective temperature via $k_B T = \Delta p^2/(2m)$, leading to an alternative condition for the time-scale separation $|\kappa + i\delta_c| \gg \sqrt{\frac{4\omega_r k_B T}{\hbar}}$, with $\omega_r = \frac{\hbar k^2}{2m}$.

We then identify the coarse-grained time scale δt, which is sufficiently short with respect to the time scale of the atomic external degrees of freedom and yet sufficiently long that during δt the cavity field reaches a local steady state

$$\frac{1}{|\kappa + i\delta_c|} \ll \delta t \ll \sqrt{\frac{\hbar}{4\omega_r k_B T}}. \tag{2.15}$$

The treatment is best illustrated in the Heisenberg picture and is detailed in Ref. [43, 91]. We report here some relevant steps. The equations of motion of the atom and of the cavity field operator read

$$\dot{\hat{p}} = 2\hbar k U_0 \cos(k\hat{x}) \sin(k\hat{x})\hat{a}^\dagger \hat{a} + 2k_0 W_0 \cos(k_0 \hat{x}) \sin(k_0 \hat{x}), \tag{2.16}$$

$$\dot{\hat{a}} = -\kappa \hat{a} + i(\delta_c - U_0 \cos^2(k\hat{x}))\hat{a} - i\eta + \sqrt{2\kappa}\hat{a}_{\text{in}}, \tag{2.17}$$

if the cavity is pumped by the laser. When the atom is pumped instead, they read

$$\dot{\hat{p}} = 2\hbar k U_0 \cos(k\hat{x}) \sin(k\hat{x})\hat{a}^\dagger \hat{a} + 2k_0 W_0 \cos(k_0 \hat{x}) \sin(k_0 \hat{x})$$

$$+ \hbar k \frac{\xi g_0}{\Delta_a} \sin(k\hat{x})(\hat{a}^\dagger + \hat{a}), \tag{2.18}$$

$$\dot{\hat{a}} = -\kappa \hat{a} + i(\delta_c - U_0 \cos^2(k\hat{x}))\hat{a} - i\frac{\xi g_0}{\Delta_a} \cos(k\hat{x}) + \sqrt{2\kappa}\hat{a}_{\text{in}}, \tag{2.19}$$

where $\hat{a}_{\text{in}}(t)$ is the input noise operator, with $\langle \hat{a}_{\text{in}}(t) \rangle = 0$ and $\langle \hat{a}_{\text{in}}(t)\hat{a}_{\text{in}}^\dagger(t') \rangle = \delta(t - t')$ [75]. Within the time step δt, defined by Eq.(2.15), we identify the coarse-grained field operator

---

[2]Or in other words during the relaxation time of the cavity the atom travels over a small distance compared to the cavity wave length [79].

$\hat{a}_{\text{st}}$, which is defined by the equation

$$\int_{t}^{t+\delta t} \hat{a}(\tau)d\tau/\delta t \approx \hat{a}_{\text{st}}, \tag{2.20}$$

such that $\int_{t}^{t+\delta t} \dot{\hat{a}}_{\text{st}}(\tau)d\tau = 0$, with $\dot{\hat{a}}$ given in Eq.(2.17) and in Eq.(2.19) respectively. Furthermore we can assume that the atomic position doesn't change on the time scale δt, hence $\hat{x}(t + \delta t) \approx \hat{x}(t)$. With this we can solve the Heisenberg-Langevin equation for the cavity field, Eq.(2.17) and (2.19) respectively, on the timescale δt and identify the "stationary" cavity field as shown in more details in Appendix B: it is a function of the atomic operators at the same (coarse-grained) time, and in the limit where the time averaged quantum noise $\bar{\hat{a}}_{\text{in}} = \int_{t}^{t+\delta t} \hat{a}_{\text{in}}(\tau)d\tau/\delta t$ can be neglected, it takes the form

$$\hat{a}_{\text{st}} \approx \frac{\zeta(\hat{x})}{(\delta_c - U_0 \cos^2(k\hat{x})) + i\kappa}. \tag{2.21}$$

Notice that this expression corresponds both to the case where the cavity is pumped or the atom is pumped, by using respectively Eq.(2.12) or Eq.(2.13) for $\zeta(x)$. A condition for which this expression is correct, is that $2\kappa/\delta t \ll \zeta^2$ as shown in Appendix B. In this limit, according to Eq.(1.50), the field at the cavity output reads

$$\langle \hat{a}^{\dagger}_{\text{out}} \hat{a}_{\text{out}} \rangle = 2\kappa \langle \hat{a}^{\dagger}_{\text{st}} \hat{a}_{\text{st}} \rangle, \tag{2.22}$$

and allows one to monitor the state of the atoms [75, 91, 92]. Using Eq. (2.21) for the field $\hat{a}$ in Eq. (2.16) and in Eq.(2.18), leads to an equation of motion for the atomic variables which depends solely on the atomic variables [43]. Claiming

$$\dot{\hat{p}} = -\frac{dW_{\text{ext}}(x)}{dx}\bigg|_{x=\hat{x}} - \frac{dV_{\text{eff}}(x)}{dx}\bigg|_{x=\hat{x}}, \tag{2.23}$$

then allows to identify the conservative effective potential $\hat{V}_{\text{eff}}(\hat{x})$ resulting from the optomechanical coupling between atom and cavity mode. The corresponding effective Hamiltonian reads

$$\hat{H}_{\text{eff}} = \frac{\hat{p}^2}{2m} + W_0 \cos^2(k_0\hat{x}) + \hat{V}_{\text{eff}}(\hat{x}), \tag{2.24}$$

where

$$\hat{V}_{\text{eff}}(\hat{x}) = v_0 f(\hat{x}). \tag{2.25}$$

The function $f(x)$ is given in Eq.(2.4), with now $\delta_c' = \delta_c/\kappa$ and $C = U_0/\kappa$, thereby linking the parameters of our model to the microscopic theory. The energy v_0 takes a different form depending on whether the atom or the cavity is driven. When the cavity is pumped, then

$$v_0 = \frac{\hbar}{\kappa}\eta^2\,,\tag{2.26}$$

while when the atom is transversally pumped it takes the form

$$v_0 = \hbar\frac{\xi^2}{\Delta_a}\delta_c'\,.\tag{2.27}$$

Varying the value of v_0 changes the importance of the perturbing lattice and thus corresponds to a change of the quasidisorder strength. Pumping both cavity and atom simultaneously doesn't allow to identify a conservative effective potential $\hat{V}_{\text{eff}}(\hat{x})$ due to additional interference terms.

The Hamiltonian (2.24) is quasiperiodic and contains the nonlinear coupling due to the cavity field in the functional form $f(x)$. It can be cast in a Bose-Hubbard form using the single particle Wannier basis $\{w_n\}$ of the optical lattice $\hat{W}_{\text{ext}}(\hat{x})$. Using this change of basis, in the tight-binding and single-band approximation, one obtains Eq.(2.2) from Eq.(2.24), where the onsite energy $\delta\epsilon_n$ is given by Eq.(2.3), with $f(x)$ as defined in Eq.(2.4). The tunneling t has the same form as Eq.(1.22), i.e.

$$t = -\int_{-L_0/2}^{L_0/2} dx \ w_n(x)\left(\frac{-\hbar^2}{2m}\frac{d^2}{dx^2} + W_0\cos^2(k_0 x)\right)w_{n+1}(x)\,.\tag{2.28}$$

We have verified that the site-dependent tunneling terms due to the cavity potential,

$$t_n = -\int_{-L_0/2}^{L_0/2} dx \ w_n(x)V_{\text{eff}}(x)w_{n+1}(x)\,,\tag{2.29}$$

are negligible for the parameters we choose and that we will specify in the next chapter. We remark that, while the resulting dynamics is coherent, its validity relies on a separation between the typical time scale of the cavity, which is intrinsically lossy, and the one of the atomic motion.

Chapter 3

Results

In this chapter we determine the phase diagram for the ground state $|\Psi_0\rangle$ of Hamiltonian (2.2), analyze in detail the properties of the localization transition in the framework of CQED, and then discuss possible realizations with existing experimental setups of CQED with cold atoms. Finally we draw a conclusion.

3.1. Phase diagrams

We determine the inverse participation ratio (IPR), given in Eq.(1.27), as function of the strength of the perturbing potential v_0 and as a function of the parameter C which controls the form of the perturbing potential (see Fig.2.1 (b)). We take a lattice with open boundaries (hard walls) and choose $\beta = \frac{\sqrt{5}-1}{2}$. The plots we show are evaluated for $L = 233$. We checked that the IPR and the phase diagrams remain substantially unvaried when scaling up the lattice size L [81]. Furthermore we verify numerically that the effective potential $\hat{V}_{\mathrm{eff}}(\hat{x})$ is only a perturbation for the main lattice $\hat{W}_{\mathrm{ext}}(\hat{x})$. We also checked that the single-band approximation is valid[1]. We further note that, since the confining lattice has a minimum at $x = 0$, after adding the perturbing potential of Eq.(2.4) for $C < 0$ the total potential exhibits a minimum at the center (see Fig.3.1 (a)). For $C > 0$ the center is a local maximum of the perturbing potential (see Fig.3.1(b)). The symmetry by mirror reflection about the center, thus, gives that for $C < 0$ the localized state is in the center, while for $C > 0$ it is a coherent superposition of two sites equally distant from $x = 0$, as illustrated in Fig. 3.1. In order to get an unique localized state for all values of C, for $C > 0$ we take

$$f(x) = \arctan\left(-\delta'_c + C\sin^2(\beta k_0 x)\right). \tag{3.1}$$

---

[1]Therefor we require $\Delta E = \sqrt{4E_R|W_0|} \gg |\max|\delta\epsilon_j| + v_0\arctan(\delta_c/\kappa)|$, where ΔE is the energy difference between first and second band [77].

This choice allows us to directly compare the localization transition for positive and negative values of C, thus to analyze the sole effect of the potential minimum, which for $C > 1$ is a narrow well while for $C < -1$ is shallow about $x = 0$ (see Fig. 2.1(b)).

(a)

(b)
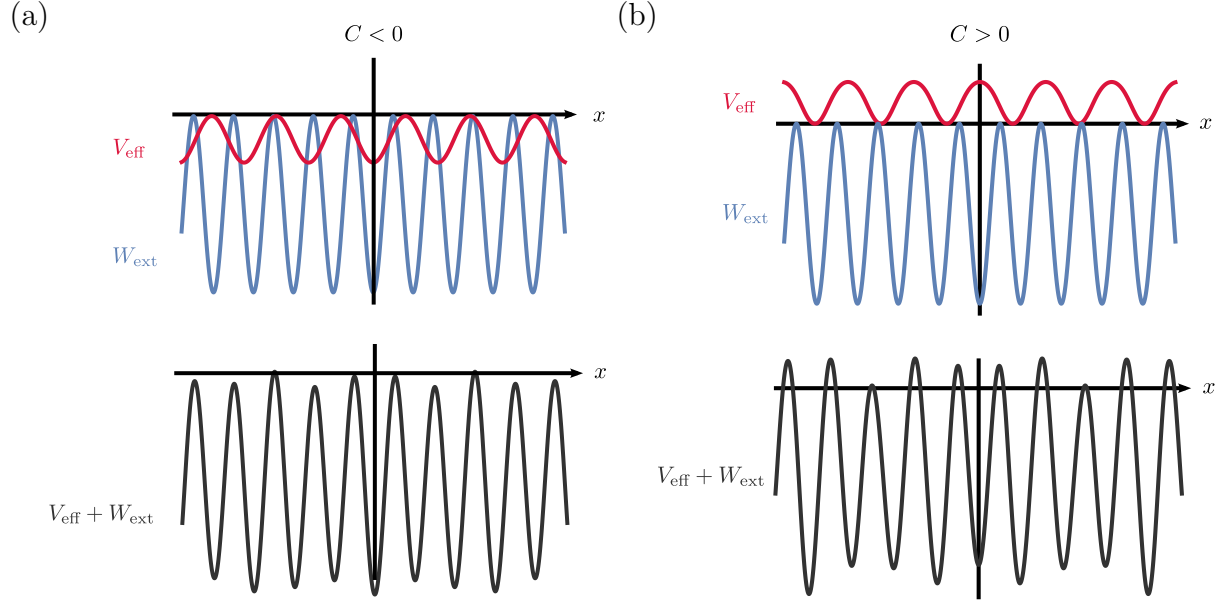
Figure 3.1.: Sketch of the effective potential $\hat{V}_{\text{eff}}$, as defined in Eq.(2.25), the main optical lattice $\hat{W}_{\text{ext}}$ and the sum of the two potentials, as a function of x for $C < 0$ (subplot (a)) and for $C > 0$ (subplot (b)). For $C < 0$ the global minimum of the resulting quasiperiodic lattice is at $x = 0$, whereas in the case of $C > 0$ there are two minima at equal distance from $x = 0$. Note that for both subplots $|C| \ll 1$.

For all considered values of C and δ'_c the IPR as a function of v_0, the strength of the perturbing second lattice, exhibits a sharp transition, as visible in Fig.3.2 (a) for various values of C. The critical value at which the transition occurs is given in good approximation by the one in Eq.(2.9) for $|C| \ll 1$, while it differs from this value the larger $|C|$ becomes. This is clearly visible in Fig.3.2 (b), which displays the contour plot of the IPR as a function of v_0/t and C for $\delta'_c = 0$. Here, the solid lines correspond to Eq.(2.9), which predicts the transition value for the corresponding dual model. They are visibly shifted with respect to the transition we identify between extended (dark region) and localized state (light region). This is a fingerprint of the backaction which becomes more and more important for increasing C. It implies that higher harmonics of the Aubry-André potential become relevant. Furthermore we observe an asymmetry of the transition between positive and negative values of C. Intuitively it can be explained by the different form of the potential minima given in Eq.(2.4) and depicted in Fig.2.1: for $C < -1$ the minima of the

perturbing lattice are broader than for $C > 1$ and thus the onset of localization requires a higher potential strength.

We also analyze the properties at the transition by plotting the probability density distribution $|\langle j|\Psi_0\rangle|^2$ as a function of the lattice site $j = \frac{xk_0}{\pi}$, as defined in Eq.(1.6). Here $|j\rangle$ denotes the Wannier state centered at lattice site j and $|\Psi_0\rangle$ the ground state of the Hamiltonian (2.2). Typical probability densities are shown in the insets of Fig.3.3 (a) and (b). We observe that in the localized phase the probability density always exhibits an exponential decay, although for $|C| > 1$ we also find that for same parameter regimes at large distances from the lattice center the density profile shows an extended component (see inset of Fig.3.3 (b)). We have checked that this uniform background is not a numerical artifact. It also appears for $|C| > 1$ as well as for $|C| < -1$ in the case of nonzero detuning, as depicted in Fig.3.5. We remark that deviations from a purely exponential profile have been observed in the localized phase of a Bose-Einstein condensate of weakly interacting atoms, where the ground state was the superposition of several localized states [93] due to the effect of interactions. In our case, the observed density profile can be viewed as the overlap between a localized and an extended state. This behavior is due to the higher harmonics of the cavity potential, Eq.(2.4): Indeed, we checked that the background appears already by truncating the Taylor expansion of Eq.(2.4) in $|C|$ to second order (to third order if $\delta'_c = 0$) [81].

Fig.3.3 (a) and (b) display the Lyapunov exponent γ, as defined in Eq.(1.30), as a function of v_0 for $C < 0$ and $C > 0$, respectively. The values are extracted by performing a fit of the central localized region of the density profiles (see insets). This procedure introduces an uncertainty in the determination of the Lyapunov exponent, which is not shown here since it is comparable with the size of the markers. The dependence of γ on C for fixed v_0/v_c is shown in subplots (c) and (d), where now the error bars give the uncertainty in the value we fitted. For $C < 0$ the Lyapunov exponent (and thus localization) increases with $|C|$ and is larger than the value of Eq.(1.31), to which it tends for $C \to 0^-$. The behavior is qualitatively different for $C > 0$, as visible in subplot (d): As C is increased from 0, the Lyapunov exponent decreases monotonically from the value of Aubry's model. The curve seems to tend to a nonvanishing asymptotic constant value for $C \to \infty$, which is the limit of a sequence of infinitely narrow wells as shown in Fig.2.1 (b).

We now explore the dependence of γ and of the IPR on the detuning δ'_c. We have checked several values and take $\delta'_c = -2$ in order to provide a representative example. For this value we analyze the IPR (Fig.3.4) and the corresponding dependence of the

(a)

(b)
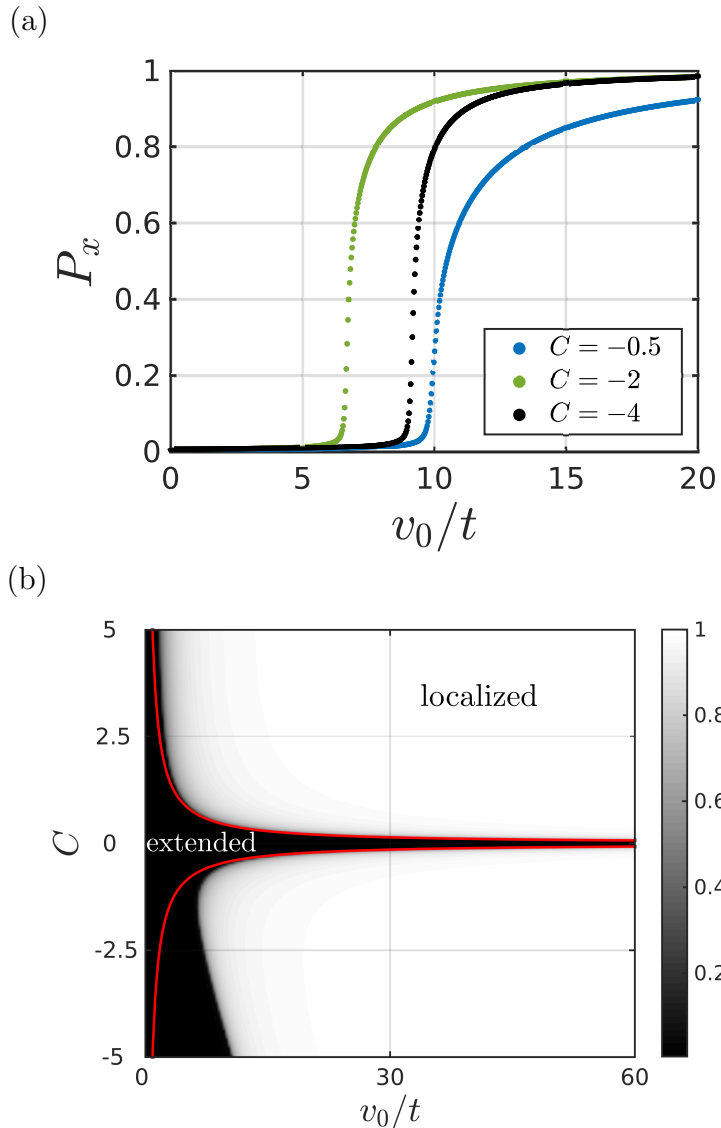
Figure 3.2.: (a) Inverse participation ratio (IPR), Eq.(1.27), as a function of v_0 (in units of t) for $\delta'_c = 0$ and $C = -0.5, -2, -4$ (see legend). (b) Contour plot of the IPR as a function of v_0 (in units of t) and of C, for $\delta'_c = 0$. The red solid lines correspond to Eq.(2.9). For calculating $\delta\epsilon_n$ in Eq.(2.4) we used the Wannier function for a confining potential of depth $W_0 = -29E_r$, with $E_r = \hbar^2 k_0^2/(2m)$ the recoil energy.
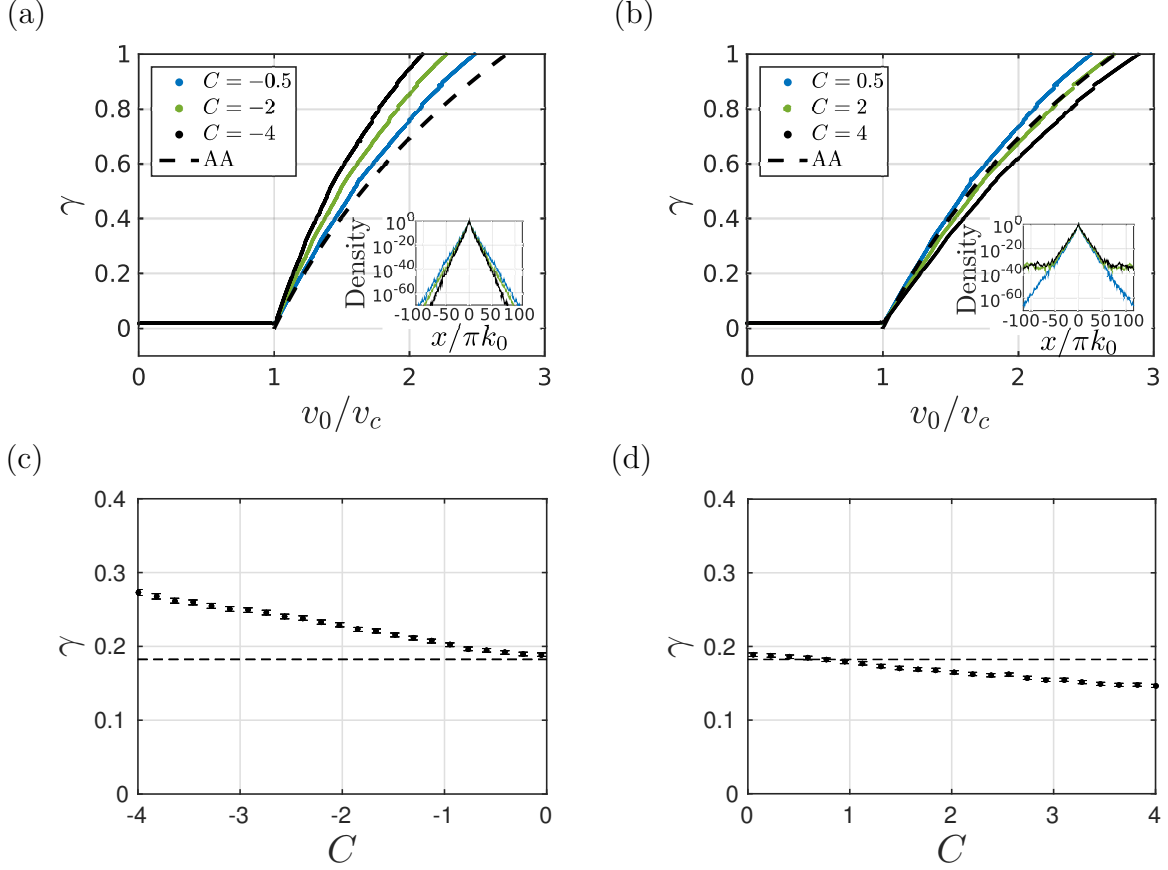
Figure 3.3.: Lyapunov exponent as a function of v_0, in units of the critical depth v_c, which we extract from the numerical behavior of the IPR in Fig.3.2, for $\delta'_c = 0$ and for (a) $C = -0.5, -2, -4$ (b) $C = 0.5, 2, 4$. The black dashed line corresponds to the functional behavior of the Lyapunov exponent in Aubry-André's model, Eq.(1.31). The insets display the probability densities as a function of x for the corresponding values of C of the curves in the onset and for $v_0/v_c = 2$. Subplots (c) and (d) displays the Lyapunov exponent as a function of C for the fixed ratio $v_0/v_c = 1.2$, the horizontal line indicates the value predicted by Eq.(1.31) (v_c depends on C, for each value of C it is extracted from the curves of the IPR as in Fig.3.2 (a)). For calculating $\delta\epsilon_n$ in Eq.(2.4) we used the Wannier function for a confining potential of depth $W_0 = -29E_r$, with $E_r = \hbar^2 k_0^2/(2m)$ the recoil energy.

Lyapunov exponents on C (Fig.3.5). The contour plot shows that for $C < 0$ the extended phase shrinks with respect to the case $\delta'_c = 0$ (Fig.3.2 (b)) and we observe an enhanced asymmetry with respect to the horizontal at $C = 0$. The smaller critical value v_c is found at about $C \sim -2$. Correspondingly, the Lyapunov exponent as a function of C possesses a minimum at the same value of the cooperativity. This value corresponds to the root of the function $f(x)$, Eq.(2.4), for $\cos^2(kx) \approx 1$, which is fulfilled when the atom is localized at the minimum of the total potential. This root is an optomechanical resonance which maximizes the intracavity photon number when the atom is in a localized state, as we will show below.
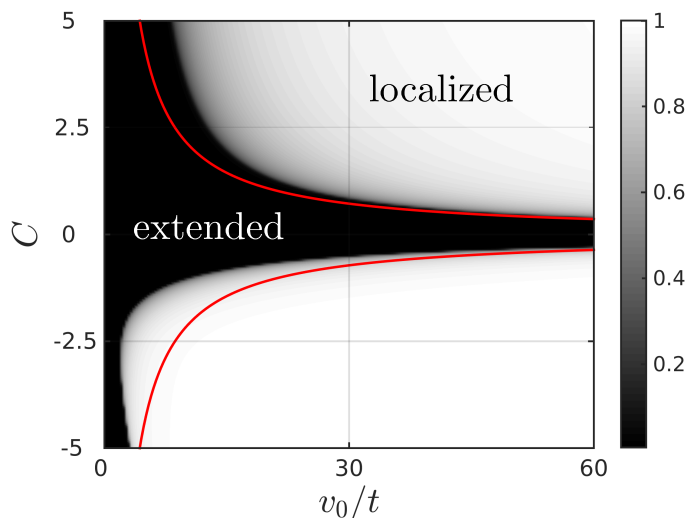
Figure 3.4.: Contour plot of the IPR as a function of v_0 (in units of t) and of C, for $\delta'_c = -2$. The red solid lines correspond to Eq.(2.9). The other parameters are the same as in Fig.3.3.

3.2. Experimental realization

Single atoms and ions have been trapped inside cavities and cooled to very low temperatures [22, 23], the dispersive coupling with the cavity field as in Eq.(2.24) has been realized [12]. These implementations rely on the existence of an external trapping potential, that is typically harmonic. This breaks the discrete translational invariance along the direction of motion and thus drastically changes the properties of the extended state. However, a sufficiently shallow trap does not affect the transition to localization as long as the size of the localized state is much smaller than the harmonic oscillator length [11]. Inclusion of

(a)

(b)
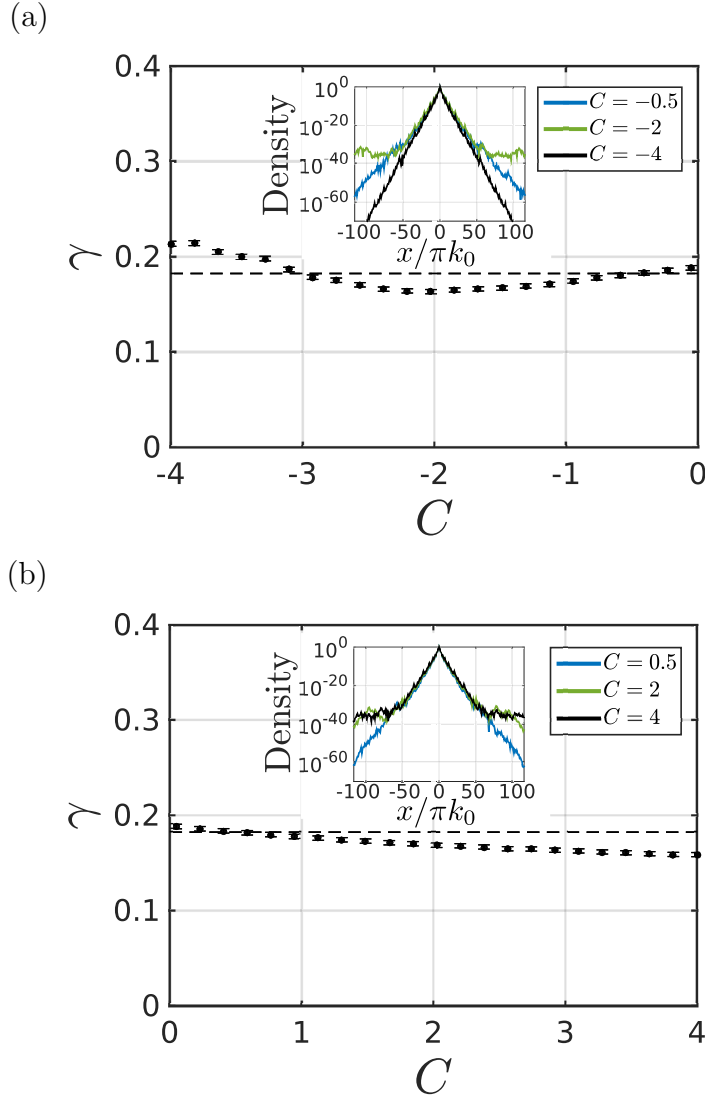
Figure 3.5.: Lyapunov exponents as a function of C for $v_0/v_c = 1.2$ and $\delta'_c = -2$, the black horizontal dashed line indicates the value predicted by Eq.(1.31). The insets display probability densities as a function of x for different values of C and for the fixed ratio $v_0/v_c = 2$. The other parameters are the same as in Fig.3.3.

the harmonic confinement would be a straightforward extension of the present model. We do not include the harmonic trapping in the present work since under typical experimental conditions (see eg Ref. [78]) the harmonic oscillator length ($a_{\mathrm{ho}} = \sqrt{\hbar/(m\omega_{\mathrm{ho}})} \sim 5\mu$m for a trapping frequency of $\omega_{\mathrm{ho}} = 25$Hz of ^{87}Rb atoms) is larger than the size of the localized wavefunction. Here we assumed that in the localized state, the density distribution is given by $|\langle j|\Psi_0\rangle|^2 = e^{-\frac{|jd_0|}{l}}$, with l the localization length and $d_0 = \pi/k_0$. Thus the Lyapunov exponent can be approximated by $\gamma \approx \frac{d_0}{2l}$, which leads to $l \sim 1\mu$m for $\gamma = 0.2$ and $k_0 = 2\pi/830$nm.

Note that in an experiment the optical lattice within the cavity would also be realized by a cavity mode. In order to get an effective quasiperiodic lattice, one requires the cavity mode that constitutes the optical lattice and the one that strongly couples to the atom, to have wavenumbers whose quotient is not an integer (e.g. $\beta = k/k_0 = 830/1361 = 0.61$). Furthermore the lattice size needs to be chosen carefully to avoid periodic replicas [67].

The transition to localization with cold atoms can be revealed by means of time-of-flight measurement, as realized in Ref. [11], or in-situ imaging [94, 95]. Another possibility is to analyze the spectrum of light emitted by the resonator, since this contains the information about the system excitations and allows one to monitor the dynamics [88, 92].

Figures 3.6 (a) and (c) display the phase diagram obtained from the IPR in the case where the cavity is pumped, here reported as a function of the pump strength η, of the cooperativity C and of the detuning δ_c, for the parameters of the setup of Ref. [46, 78]. In particular we consider the cooperativity $C = U_0/\kappa$, with the cavity damping rate $\kappa = 2\pi \times 4.45\,\mathrm{kHz} \approx E_R/\hbar$ and $U_0 = g_0^2/\Delta_a$, where $g_0 = 2\pi \times 44.5\,\mathrm{kHz}$ is the coupling strength between atomic dipole and cavity mode. The optical lattice depth is taken $W_0 = -15E_r$, where $E_r = \hbar^2 k_0^2/2m$ denotes the recoil energy. Note that for these parameters the elimination of the excited state of the atom, we discussed in Section 1.9 is justified. The conditions for the time scale separation we performed in Section 2.3 and for the neglect of the noise are fulfilled for a temperature of the atom of $T < 1n\,$K and $|\delta_c| > E_r/\hbar$.

We determine the mean intracavity photon number $\bar{n}$, according to the equation

$$\bar{n} = \langle\Psi_0|\hat{a}_{\mathrm{st}}^\dagger\hat{a}_{\mathrm{st}}|\Psi_0\rangle$$

$$\simeq \sum_{m=1}^{L} |\langle m|\Psi_0\rangle|^2 \int dx\, w_m^2(x)\frac{\zeta^2}{\left(\delta_c - U_0 h(x)\right)^2 + \kappa^2} \,. \tag{3.2}$$

where $h(x) = \cos^2(kx)$ for $C < 0$ and $h(x) = \sin^2(kx)$ for $C > 0$. Its form shows that

for $C < 0$ the root of Eq.(2.4) and for $C > 0$ the root of Eq.(3.1) is an optomechanical resonance in the cavity field [96]. This means that the cavity mode, whose frequency depends nonlinearly on the atomic position, is pumped resonantly and thus the intracavity photon number is maximized.

Figures 3.6 (b) and (d) show the intracavity photon number for the parameters of the phase diagrams in subplots (a) and (c), respectively. In Fig.3.6 (b) we observe that for $C < 0$ the intracavity photon number is maximized whereas for $C > 0$ it is suppressed. Experimentally tuning the detuning δ_c is easier than tuning the cooperativity C. Fig.3.6(c) and (d) show the phase diagram of the IPR and the mean intracavity photon number as a function of the detuning δ_c. We see that in principle the photon number can reflect the onset of localization but the signal is very weak. We conjecture that this problem could be overcome by increasing the photon number necessary for the localization by using N atoms. Than the role of interactions, both short and cavity mediated infinite range, needs to be taken into account.

3.3. Conclusion

In this part of the thesis we have analyzed the localization transition in a modified Aubry-André model, where the quasiperiodic potential a single ultracold atom is subjected to, is created by the combination of an external optical lattice and a mode of a high-finesse cavity with incommensurate wavelengths. Its effective optomechanical potential results from the sum of all the harmonics of the Aubry-André potential and arises from the light scattered by the atom which backacts on the atomic position. We have identified two different regimes: the limit of small cooperativity $C \ll 1$, reproduces the Aubry-André model with a modified critical point v_c^{cav}; for large cooperativities $|C| > 1$ higher harmonics of the Aubry-André potential are relevant. We find that several features of the Aubry-André model are preserved. Novel features are the shift of the localization in the phase diagram and the behavior of the Lyapunov exponent, which is a function of the cooperativity and shows peculiar features close to the parameters where the system exhibits an optomechanical resonance.

The localization-delocalization transition we predict could be measured with bosonic gases confined in state of the art setups [41, 46, 78]. Our study sheds light into the effect of nonlinearities in the quantum regime and complements the studies on glassiness of bosons [91], and on static friction [89] in interacting gases induced by cavity backaction in frustrated geometries.
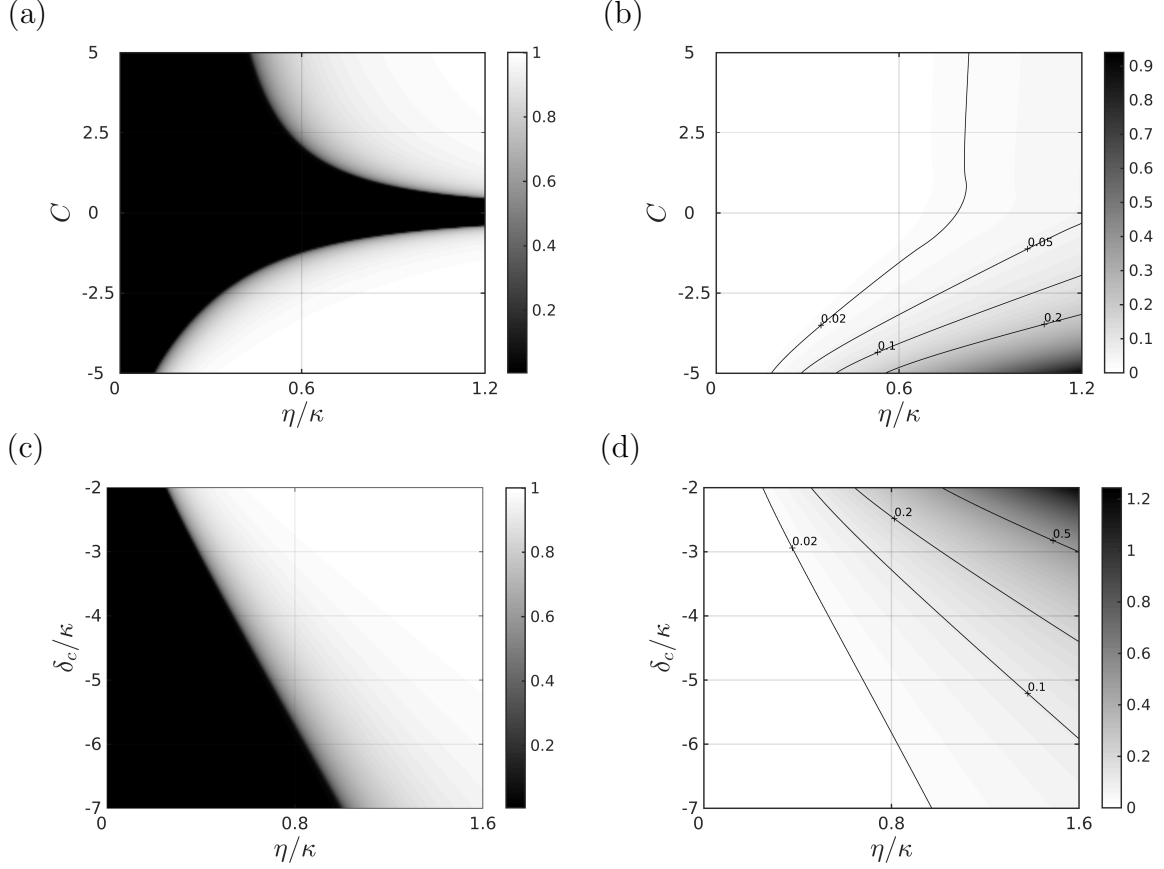
Figure 3.6.: (a) Inverse participation ratio, Eq.(1.27), and (b) mean intra cavity photon number $\bar{n}$, Eq.(3.2), as a function of the parameters η and $C = U_0/\kappa$ in the setup where the resonator is driven and for detuning $\delta_c = -5.5\kappa$. Here, η is the strength of the laser and U_0 is the strength of the optomechanical coupling. In (a) and (b) the potential depth is fixed to $W_0 = -15E_r$, where E_r is the recoil energy associated with the D line of ^{87}Rb atoms. Subplots (c) and (d) show the IPR and $\bar{n}$ as a function of η and δ_c (in units of κ) for $C = -1$ and $W_0 = -14E_r$. The other parameters are the number of sites $L = 233$ and $\beta = \frac{\sqrt{5}-1}{2}$. For the parameters of Ref. [46,78], where $\kappa \approx E_r/\hbar = 2\pi \times 4.45\,\text{kHz}$, the time-scale separation at the basis of our model and the neglect of the noise is warranted when the detuning, $|\delta_c| > E_r/\hbar$ and the atoms' temperature, $T < 1n\text{K}$.

Part II.

Phonon mediated conversion of exciton-polaritons Rabi oscillations into THz radiation

A room temperature compact solid-state THz source is a highly desirable piece of equipment, needed in many domains like communication, health or security [13]. Different semiconductor based techniques already exist, for example based on cascade laser structures [13, 16], but they require rather deep cooling so far.

It turns out that semiconductor microcavities in the strong coupling regime [97] exhibit the right energy scale for THz electromagnetic radiation. Indeed the normal mode - (Rabi) splitting, i.e. the energy splitting between the upper and lower exciton-polariton states, typically ranges from $h\nu = 3.5\,\mathrm{meV}$ (i.e. $\nu = 0.85\,\mathrm{THz}$) in Gallium Arsenide (GaAs) microcavities, to hundreds of meV (i.e. tens of THz) in large band gap semiconductors systems. Such a transition cannot be used directly to generate or absorb THz photons as it is dipole forbidden. Indeed, the exciton that takes part in the upper and lower polariton states is in both cases a $1s$ exciton and thus the symmetry is the same.

To circumvent this problem, several strategies have been proposed. In a pioneering experiment, an in-plane static electric field was used to hybridize excitonic states with different parities (i.e. s-like and p-like), resulting in a nonzero dipole moment between the upper and lower polariton branches [98]. More recently, taking advantage of the bosonic nature of polaritons, it has been proposed to optically excite p-like excitons by two-photons absorption, and to achieve bright THz emission by stimulated relaxation toward the lower polariton branch [20, 99]. However, due to ultrafast relaxation of the p-excitons, this mechanisms has remained elusive so far [100]. Other promising idea have been put forward like e.g. intersubband polaritons microcavities involving doped asymmetrical quantum wells [101], or microcavities embedding a $\chi^{(2)}$ active material like [111]-oriented GaAs [21].

The common point in these proposals is to modify the microcavity structure, either by applying an external field, or by engineering the material, in order to build up a $\chi^{(2)}$ optical nonlinearity resonant with the polariton states. In our work, we show that the transverse optical (TO) phonons, the mechanical vibration mode related to a deformation of the lattice unit cell, can play exactly this role when the Rabi splitting is brought in resonance with its frequency. With this mechanism, THz emission should be achievable without resorting to externally applied field, or new materials.

The most extensively used material to fabricate microcavities in the strong coupling regime is Gallium Arsenide [17]. In this material, this resonance condition is hard to meet as the typical achievable Rabi splitting is in general significantly smaller than the TO phonon energy ($\hbar\omega_{TO} = 33.3\,\mathrm{meV}$). A CdTe-based microcavity will be considered in this work, as such microcavities exhibit excellent optical properties and a near perfect match between the typical microcavity Rabi splitting [102] and the TO phonon energy

$\hbar\omega_{TO} = 18\,\text{meV}$, at the expense of a weaker stability at room temperature.

Our proposal relies entirely on a combination of three different mechanisms already present in current state-of-the art microcavities, namely : (i) the strong coupling regime between optical cavity photons and excitons yielding exciton-polaritons, (ii) the strong coupling regime between THz photons and TO phonons yielding phonon-polaritons, and (iii) the interaction between the excitonic hole states and the TO phonons mediated by the deformation potential. The latter mechanism can be described by an optomechanical-like coupling Hamiltonian. It provides the effective $\chi^{(2)}$ nonlinearity enabling the conversion of laser-pumped upper and lower exciton-polariton field into THz photons. A similar frequency conversion scheme based on an optomechanical coupling is reported in Ref. [103].

This part of the thesis is organized as follows: Chapter 4 is devoted to the basics on excitons in semiconductor microcavities and the strong coupling between excitons and photons in microcavities which leads to the formation of polaritons. We briefly discuss a seminal experiment on exciton-polaritons to introduce the typical setup. Besides we compare the two experimental platforms we deal with in this thesis, namely exciton-polaritons in semiconductor microcavities and ultracold atoms in an high-finesse optical cavity. In Chapter 5 we introduce the key constituent of our frequency conversion scheme, which is the TO phonon-exciton interaction. For this purpose we first present some microscopic details of CdTe, which will then enable us to derive the exciton-TO phonon interaction, starting from the general electron-phonon interaction. Thereby we take into account that the excitons are also strongly coupled to cavity photons. In Chapter 6 we discuss the frequency conversion scheme starting from a microscopic model. We calculate the emission power of THz photons and relate our results to an effective $\chi^{(2)}$ description.

This part of the thesis is based on the article:

- Katharina Rojan, Yoan Léger, Giovanna Morigi, Maxime Richard, and Anna Minguzzi, *Phonon mediated conversion of exciton-polaritons Rabi oscillations into THz radiation*, in preparation.

62

Chapter 4

Basics on exciton-polaritons in semiconductor microcavities

In this chapter we enter the world of condensed matter physics. First we introduce excitons, elementary excitations of a semiconductor, that will be the object of our analysis. In the second section we describe a solid-state based cavity made out of semiconductor materials. The two concepts of excitons and semiconductor cavity are combined in Section 4.3, where we present the quasiparticles that arise from the strong coupling between excitons and photons in a semiconductor cavity, the exciton-polaritons. Exciton-polaritons provide a platform to investigate many-body quantum effects in solid-state systems. In Section 4.4 we discuss one seminal experiment showing the Bose-Einstein condensation of exciton-polaritons, in order to introduce the experimental setup. Note that in the following we are going to exploit the physics of exciton-polaritons to derive a frequency conversion scheme, that we present in Chapter 6. Finally, we compare the two experimental platforms we use in this thesis, ultracold atoms in an optical cavity and exciton-polaritons in a semiconductor microcavity, in Section 4.5.

4.1. What are excitons?

A semiconductor is a solid where in the ground state, at $T = 0\,\mathrm{K}$, there is an energy gap E_G between the highest state of the filled valence band and the lowest state of the conduction band [104, 105]. Typical values of energy gaps are of the order of few eV. There are direct band gap semiconductors where the top of the valence band is at the same position k in the Brillouin zone as the bottom of the conduction band, and indirect band gap semiconductors, where the top of the valence band and the bottom of the conduction band

are separated in k space. We restrict our considerations to direct band gap semiconductors. In particular we will consider CdTe, where the band gap is $E_G = 1.607\,\text{eV}$ at $T = 0\,\text{K}$ [1]. If one valence electron absorbs a photon with energy $\hbar\omega$ larger than the band gap E_G, it results in a free electron in the conduction band and a free hole in the valence band [1]. Note that a filled band has total wavevector zero [1] and due to the translation invariance of the crystal, the total momentum (wavevector) is conserved. This imposes selection rules for absorption and emission processes. Assume one electron at wavevector $\boldsymbol{k}_h$ is missing in the valence band, hence the wavevector of the valence band electrons is $-\boldsymbol{k}_h$. The missing of an electron is called a hole and it is depicted at $\boldsymbol{k}_h$, see Fig.4.1, but it is associated with a wavevector $-\boldsymbol{k}_h$. If there is an electron in the conduction band at $\boldsymbol{k}_e$, the wavevector of the total system is $\boldsymbol{K} = \boldsymbol{k}_e - \boldsymbol{k}_h$. Momentum is conserved in the creation of an electron-hole pair by photon absorption, and the final momentum $\hbar\boldsymbol{K}$ of the pair coincides with the photon momentum. Due to the large value of speed of light, the photon momentum $\hbar|\boldsymbol{k}_p| = \hbar\omega/c$ is negligible and one typically assumes $\boldsymbol{K} \approx 0$.

If one valence electron absorbs a photon with a certain energy $\hbar\omega$ smaller than the band gap E_G, an exciton can be created if the photon energy matches the exciton's energy, that we will derive below. An exciton is an electron-hole bound state [105] reminiscent of a hydrogen atom. One distinguishes two different classes of excitons the so-called Frenkel and Wannier excitons. The Frenkel exciton describes an electron and a hole which are tightly bound and localized at the same lattice position, i.e. at the same atom or molecule [105,106]. Frenkel excitons are typically encountered in crystals of weakly interacting atoms (large lattice constants) for example in molecular crystals [105,106]. In the opposite case of weak electron-hole interaction, the electron is delocalized over the whole crystal and electron and hole are separated by several lattice constants [105,106]. In this limit one can assume that electron and hole only interact via the direct, screened Coulomb interaction, neglecting exchange effects [105]. The corresponding exciton is referred to as Wannier exciton, that we are going to consider in the following. For simplicity we consider a two-band model with one valence band and one conduction band and a direct band gap at the center of the Brillouin zone $\Gamma \equiv k = 0$ and follow Ref. [104]. In the effective-mass approximation the energies of conduction and valence band can be written as

$$E_c(k) = E_G + \frac{\hbar^2 k^2}{2m_e}$$
$$E_v(k) = -\frac{\hbar^2 k^2}{2m_h}, \tag{4.1}$$

where m_e and m_h are the effective masses of the electron and the hole[1] as depicted in Fig.4.1.
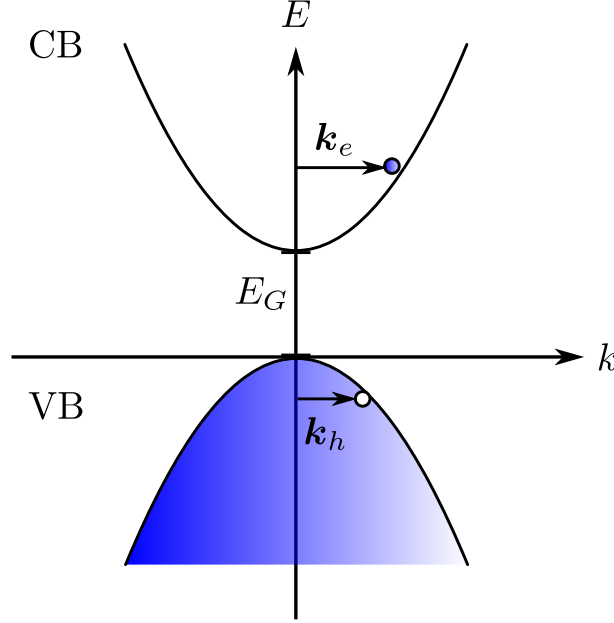
Figure 4.1.: Sketch of the simplified band structure of a direct band gap semiconductor in an excited state, where one electron is in the conduction band. Note that in this simplified picture it is not possible to sketch a correlation between electron and hole and thus an exciton [104]. The top of the valence band (VB) and and the bottom of the conduction band (CB) lie at $k = 0$ in the first Brillouin zone and are separated by the band gap of energy E_G. The electron in the conduction band moves with a wavevector $\boldsymbol{k}_e$. The hole in the valence band is depicted at $\boldsymbol{k}_h$ but it moves with a wavevector $-\boldsymbol{k}_h$.

The motion of the electron-hole pair can be divided in the center of mass motion and in the relative motion [104]

$$\boldsymbol{R}_{\mathrm{com}} = \frac{1}{m_{\mathrm{e}} + m_{\mathrm{h}}} \left(m_h \boldsymbol{R}_h + m_e \boldsymbol{R}_e \right), \tag{4.2}$$

$$\boldsymbol{r} = \boldsymbol{R}_e - \boldsymbol{R}_h, \tag{4.3}$$

where $\boldsymbol{R}_h$ and $\boldsymbol{R}_e$ are the coordinates of hole and electron respectively. The center of mass motion is the one of a free particle with mass $M = m_e + m_h$, so the wavefunction is given by a plane wave. The relative motion is hydrogen like, with quantized bound states and continuum states, where the exciton is ionized into a free electron and a free hole. The

---

[1]The effective mass of the hole is assumed to be positive, that's why there is the negative sign [1].

stationary Schrödinger equation, governing the relative motion, is given by

$$\left(-\frac{\hbar^2}{2\mu}\nabla_{\boldsymbol{r}}^2 - \frac{e^2}{\epsilon|\boldsymbol{r}|} \right) \phi_{nlm}(\boldsymbol{r}) = E_n \phi_{nlm}(\boldsymbol{r}), \tag{4.4}$$

with eigenvalues

$$E_n = E_G - \frac{R^*}{n^2}.$$

In analogy to the hydrogen atom, the Rydberg constant of the exciton[2] is defined as

$$R^* = \frac{\mu e^4}{2\hbar^2\epsilon^2} = \frac{\hbar^2}{2\mu(a_B^*)^2}, \tag{4.5}$$

with e the electron's charge, ϵ the dielectric constant of the semiconductor and the reduced mass of the exciton $\mu = \frac{m_h m_e}{m_e + m_h}$. The Rydberg constant of the exciton corresponds to its binding energy for $n = 1$. Furthermore we introduced the Bohr radius of the exciton

$$a_B^* = \frac{\hbar^2\epsilon}{\mu e^2}. \tag{4.6}$$

In the case of the semiconductor CdTe we are going to consider, the Bohr radius of the excitons is in the order of 70Å and thus almost two orders of magnitude larger than the Bohr radius of the hydrogen atom. The exciton's binding energy R^* is of the order of $11\,\text{meV}$ [104], which is very weak in comparison to the binding energy of the hydrogen $R = 13.6\,\text{eV}$. The wavefunction ϕ_{nlm}, describing the relative motion of electron and hole, is characterized by the principal quantum number n, the angular momentum quantum number l, and the magnetic quantum number m. The total energy of the exciton is given by

$$\hbar\omega_x(\boldsymbol{K}) = \frac{\hbar^2\boldsymbol{K}^2}{2M} + E_n, \tag{4.7}$$

where $\boldsymbol{K} = \boldsymbol{k}_e - \boldsymbol{k}_h$ denotes the wavevector of the center of mass motion of the exciton [105]. The energy dispersion of an exciton is sketched in Fig.4.2 for different values of n. Notice that the analogy to the hydrogen atom has its limits: in the case of an exciton, the ground state corresponds to the recombination of electron and hole [107].

We introduce the creation and annihilation operators $\hat{c}^\dagger_{\alpha,\boldsymbol{K}}$ and $\hat{c}_{\alpha,\boldsymbol{K}}$ for an exciton with

---

[2]In Gaussian/cgs units.
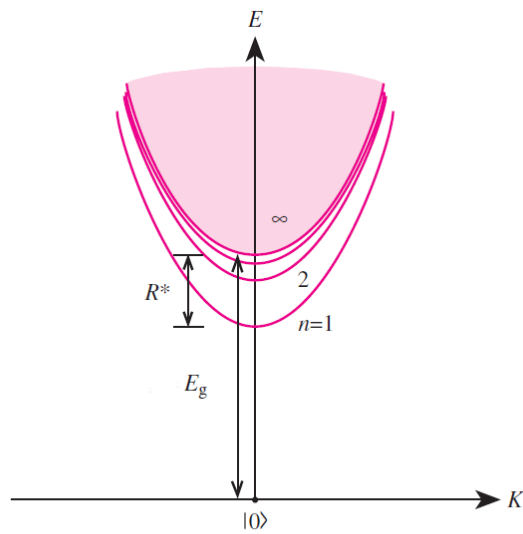
Figure 4.2.: Sketch of the energy states of the Wannier exciton, as given by Eq.(4.7) for the hydrogenic states with principal quantum numbers $n = 1, 2, 3$ and the continuum states. The band gap is here denoted with E_g and the exciton Rydberg constant R^* denotes the exciton binding energy for $n = 1$. The ground state, in which electron and hole recombine in the valence band, is denoted by $|0\rangle$. The image is taken from Ref. [104].

wavevector $\boldsymbol{K}$ and polarization α. The Hamiltonian of the exciton reads [17]

$$\hat{H}_{\text{exc}}(\boldsymbol{K}) = \sum_{\alpha,\boldsymbol{K}} \hbar\omega_x(\boldsymbol{K})\hat{c}^\dagger_{\alpha,\boldsymbol{K}}\hat{c}_{\alpha,\boldsymbol{K}}, \tag{4.8}$$

where the exciton's energy is given by Eq.(4.7). If the mean distance between two excitons is much larger than the exciton's Bohr radius, it can be shown that excitons can be described as bosons [17, 108], with $[\hat{c}_{\alpha',\boldsymbol{K}'}, \hat{c}^\dagger_{\alpha,\boldsymbol{K}}] = \delta_{\alpha',\alpha}\delta_{\boldsymbol{K}',\boldsymbol{K}}$. This is the situation we are going to consider in the following. In order to go beyond the bosonic approximation, for high excitonic densities, the internal structure of the exciton needs to be taken into account [109].

We want to construct an exciton in the most general way. For this purpose we will use the representation of the many body wavefunction of the exciton as suggested in Ref. [110]: We consider a crystal consisting of N Wigner-Seitz cells and N valence electrons at positions $\boldsymbol{x}_1, ...\boldsymbol{x}_N$. The positions of the Wigner-Seitz cells determine the sites of the crystal lattice and are denoted with $\boldsymbol{R}_j$, with $j = 1, ...N$. We note that the electron and the hole, that together constitute the exciton, can both be at every lattice site, so the general wavefunction for an exciton in the hydrogenic state λ with wavevector $\boldsymbol{K}$ reads

$$\Psi_{\lambda,\boldsymbol{K}}(\boldsymbol{x}_1, \boldsymbol{x}_2, ...\boldsymbol{x}_N) = \frac{1}{\sqrt{N}} \sum_{m,l=1}^{N} e^{i\boldsymbol{K}\cdot\boldsymbol{R}^{m,l}_{\text{com}}}\phi_\lambda(\boldsymbol{R}_l)A_{v,c}(m, m+l). \tag{4.9}$$

We identify its components: the center of mass motion is described by a plane wave with wavevector $\boldsymbol{K}$ and $\boldsymbol{R}^{m,l}_{\text{com}}$ the generalized center of mass coordinate, which is given by the generalized version of Eq.(4.2)

$$\boldsymbol{R}^{m,l}_{\text{com}} = \frac{1}{m_{\text{e}} + m_{\text{h}}}(m_h\boldsymbol{R}_m + m_e\boldsymbol{R}_{m+l}) = \boldsymbol{R}_m + \frac{m_{\text{e}}}{m_{\text{e}} + m_{\text{h}}}\boldsymbol{R}_l. \tag{4.10}$$

$\boldsymbol{R}_m$ is the position of the hole. The position of the electron that constitutes the exciton, is defined as function of the hole's position according to $\boldsymbol{R}_{m+l} = \boldsymbol{R}_m + \boldsymbol{R}_l$, where $\boldsymbol{R}_l$ is the distance between electron and hole. It corresponds to the generalized version of the relative coordinate as defined in Eq.(4.3). The indices m and l go over the hole crystal lattice. Fig.4.3 sketches the positions of electron and hole in the lattice in valence band v and conduction band c. The function $\phi_\lambda(\boldsymbol{R}_l)$ denotes the relative motion and is a solution of Eq.(4.4). λ is an index that unifies the hydrogen-like quantum numbers $\{n, l, m\}$. $A_{v,c}(m, m+l)$ is the Slater determinant describing the configuration in which a
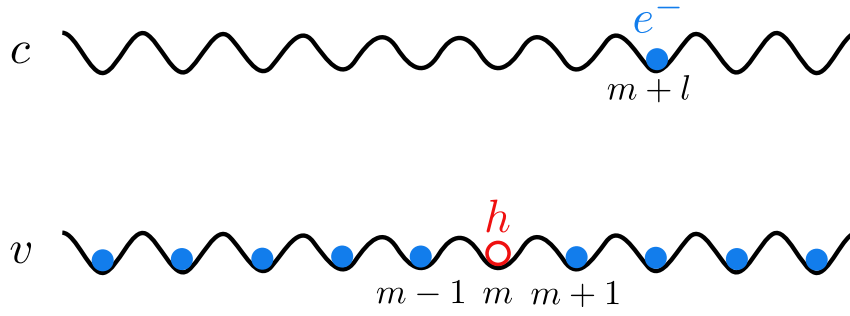
Figure 4.3.: Sketch of the positions of electron and hole that we use in the Slater determinant in Eq.(4.9). For simplicity we depict the crystal lattice, that consists of N sites, given by the N Wigner-Seitz cells, in one dimension. In the conduction band c and in the valence band v are thus N sites available. The hole position is denoted by the lattice site index m while the electron position in the conduction band is denoted by the lattice site index $m + l$.

valence electron at site m is excited from valence band v into the conduction band c at the $m + l$th site. The single-particle wavefunctions in the Slater determinant are given by Wannier functions [62], that we defined in one dimension in Eq.(1.13). More precisely, the Slater determinant consists of N single-electron Wannier functions, out of which $N - 1$ electrons occupy the valence band v and one electron occupies the conduction band c. The Wannier function for an electron at $\boldsymbol{x}_1$ in the valence band v, centered at lattice site m is denoted as $w_{v,\boldsymbol{R}_m}(\boldsymbol{x}_1) = w_v(\boldsymbol{x}_1 - \boldsymbol{R}_m)$. The Slater determinant can be also written in terms of the antisymmetrizing operator $\hat{\mathcal{A}}$

$$A_{v,c}(m, m + l) = \sqrt{N!}\hat{\mathcal{A}}\left(w_{v,\boldsymbol{R}_1}(\boldsymbol{x}_1)w_{v,\boldsymbol{R}_2}(\boldsymbol{x}_2)...w_{v,\boldsymbol{R}_{m-1}}(\boldsymbol{x}_{m-1})w_{c,\boldsymbol{R}_{m+l}}(\boldsymbol{x}_m)...w_{v,\boldsymbol{R}_N}(\boldsymbol{x}_N)\right),$$

where

$$\hat{\mathcal{A}} = \frac{1}{(N)!} \sum_{\sigma \in S_N} (-1)^\sigma \hat{\sigma}, \tag{4.11}$$

with $\hat{\sigma}$ the permutation operator and the sum going over all possible permutations. We note that $\hat{\mathcal{A}}$ is Hermitian and $\hat{\mathcal{A}}^2 = \hat{\mathcal{A}}$.

For convenience we will define [110]

$$U_{\lambda,\boldsymbol{K}}(\boldsymbol{R}_l) \equiv e^{i\boldsymbol{K}\cdot\frac{m_e}{m_e+m_h}\boldsymbol{R}_l}\phi_\lambda(\boldsymbol{R}_l), \tag{4.12}$$

leading to an alternative form of the wavefunction, where the terms depending on the

relative coordinate $\boldsymbol{R}_l$ are grouped together

$$\Psi_{\lambda,\boldsymbol{K}}(\boldsymbol{x}_1, \boldsymbol{x}_2, ...\boldsymbol{x}_N) = \frac{1}{\sqrt{N}} \sum_{m,l=1}^{N} e^{i\boldsymbol{K}\cdot\boldsymbol{R}_m} U_{\lambda,\boldsymbol{K}}(\boldsymbol{R}_l) A_{v,c}(m, m+l). \qquad (4.13)$$

4.2. The semiconductor microcavity

We consider a semiconductor microcavity of Fabry-Pérot type, with the cavity axis along z as sketched in Fig.4.4. It consists of two planar dielectric mirrors (also called distributed Bragg reflectors (DBR) or Bragg mirrors), separated by a distance h which is typically in the order of several μm, therefore the name microcavity. The cavity only accepts modes with a certain wavelength λ_c, which is determined by $h = j\frac{\lambda_c}{2}$, with j a positive integer that indicates the jth eigenmode. We assume that inside the cavity there is a dielectric medium with refractive index n_c. In many experiments, quantum wells are embedded in the cavity, but in this thesis we are going to consider a bulk semiconductor slab inside the cavity.

The Bragg mirrors are made of alternating layers of two materials with different refractive index n_1 and n_2. Their advantages, with respect to metallic mirrors, are little losses and the fact that the reflectivity can be tuned by varying the number of layers or the refractive index of the layers [108]. The reflectivity of a Bragg mirror depends on the wavelength. In order to build mirrors for a cavity mode wavelength of λ_c, the best reflectivity is achieved for a layer thickness of $\lambda_c/4$ [108]. The dispersions relation of an intracavity photon of wavevector $\boldsymbol{k}$ is given by

$$\hbar\omega_c(\boldsymbol{k}) = \hbar\frac{c}{n_c}|\boldsymbol{k}| = \hbar\frac{c}{n_c}\sqrt{k_z^2 + |\boldsymbol{k}_\parallel|^2}, \qquad (4.14)$$

with c the speed of light and $|\boldsymbol{k}_\parallel|$ the absolute value of the in-plane cavity vector $\boldsymbol{k}_\parallel = (k_x, k_y)^T$. Note that we assume here that the frequency of the cavity photon does not depend on its polarization. The wavevector along z is quantized according to

$$k_z = j\frac{\pi}{h}, \qquad (4.15)$$

with j a positive integer. The in-plane motion is not confined. Due to the planar mirrors the microcavity is translational invariant in the cavity plane (x, y) and the corresponding
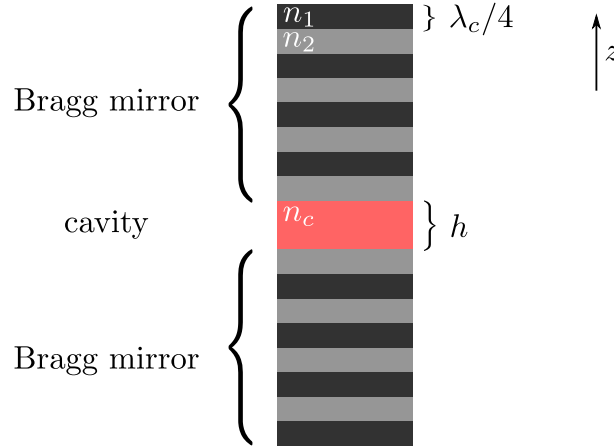
Figure 4.4.: Sketch of a semiconductor microcavity: it consists of two planar Bragg mirrors which are build up by alternating layers of two material with different refractive indices n_1 and n_2. The layer thickness is $\lambda_c/4$ in order to get the best reflectivity for the cavity mode with λ_c. The cavity has a length of h and is filled with a dielectric of refractive index n_c.

in-plane wavevector $\boldsymbol{k}_\parallel$ is conserved [17][3]. This allows to monitor the in-plane dispersion as we will see now: assume the cavity is pumped by an external laser with wavevector $\boldsymbol{k}_p$, where the wavevector encloses an angle θ_{in} with the cavity axis z. Its frequency is $\omega_p = c|\boldsymbol{k}_p|$. The in-plane component of the wavevector of the pump is given by $|\boldsymbol{k}_{p,\parallel}| = \sin\theta_{\text{in}}\omega_p/c$. It matches the in-plane wavevector inside the cavity, due to the translational symmetry $|\boldsymbol{k}_{p,\parallel}| = |\boldsymbol{k}_\parallel|$. Thus, there is a direct link between the incident angle of the pump and the motion in the cavity plane. Analogously, the external emission at an angle θ_{out} can be connected to the in-plane wavevector of the cavity field according to $|\boldsymbol{k}_\parallel| = \sin\theta_{\text{out}}\omega_p/c$ [17]. This relation between the motion in the cavity plane and the emission angle allows to experimentally measure the in-plane dispersion in situ. It is an observable which is not accessible in cavity QED experiments with ultracold atoms as the one presented in Section 1.10, because in the case of curved mirrors there is no translation invariance in the cavity plane and thus no conservation of the in-plane wavevector.

We consider a bulk semiconductor material with refractive index n_c inside the cavity and $|\boldsymbol{k}_\parallel| \ll k_z$, which allows to expand the dispersion relation given in Eq.(4.14)

$$\hbar\omega_c(\boldsymbol{k}_\parallel) \simeq \hbar\omega_c^0 + \frac{\hbar^2|\boldsymbol{k}_\parallel|^2}{2m_c},\tag{4.16}$$

---

[3]This can also be shown by Snell's law.

where $\hbar\omega_c^0 = \hbar c k_z / n_c$ and k_z fixed by Eq.(4.15). Furthermore we introduced the effective mass of the cavity photon [17]

$$m_c = \frac{\hbar n_c k_z}{c}, \tag{4.17}$$

which in our case will be in the order of $10^{-5} m_{e,0}$, with $m_{e,0}$ the electron mass.

The Hamiltonian of the electromagnetic field inside the cavity reads in second quantization

$$\hat{H}_{\mathrm{cav}}(\boldsymbol{k}_\parallel) = \sum_{\boldsymbol{k}_\parallel, \alpha} \hbar\omega_c(\boldsymbol{k}_\parallel) \hat{a}_{\alpha\boldsymbol{k}_\parallel}^\dagger \hat{a}_{\alpha,\boldsymbol{k}_\parallel}, \tag{4.18}$$

with $\hbar\omega_c(\mathbf{k}_\parallel)$ given by Eq.(4.16). The operators $\hat{a}_{\alpha,\boldsymbol{k}_\parallel}$ and $\hat{a}_{\alpha,\boldsymbol{k}_\parallel}^\dagger$ denote the bosonic annihilation and creation operator of a photon with in-plane wavevector $\boldsymbol{k}_\parallel$ and polarization α. Their commutator is given by $[\hat{a}_{\alpha,\boldsymbol{k}_\parallel}, \hat{a}_{\alpha',\boldsymbol{k}'_\parallel}^\dagger] = \delta_{\alpha',\alpha}\delta_{\boldsymbol{k}'_\parallel,\boldsymbol{k}_\parallel}$. Note that we neglected the vacuum energy contribution.

4.3. Exciton-polaritons in semiconductor microcavities

A semiconductor microcavity represents a platform to study light-matter interaction. For $\omega_c \approx \omega_x$ the system can be in the strong light-matter coupling regime, i.e. the light-matter coupling is larger than the decay rates of exciton and cavity photon.[4] In this regime, the photon and the matter excitation hybridize and form a new mixed quasiparticle which is called polariton [17]. In this section we will focus on polaritons where the matter excitation is an exciton. In Chapter 5, however, we will also deal with phonon-polaritons that are created by the strong coupling of a photon with a lattice vibration.

Polaritons can be described using a semiclassical or a quantum theory. We will focus on the quantum description. A discussion of the semiclassical theory, which is based on linear response theory, can be found in Ref. [111, 112].

The exciton-polariton model was originally introduced by Hopfield [113]. He derived it for a bulk semiconductor, and included various coupling terms between excitons and free photons. In particular he considered both the rotating and the counterrotating terms.

---

[4]Note that with semiconductor microcavities it is also possible to achieve the ultrastrong coupling regime [17].

Here, we take a simplified Hopfield model [17] where only rotating terms are kept within the rotating wave approximation(RWA)[5]. Furthermore we describe cavity photons. The resulting Hamiltonian reads

$$\hat{H}_{\text{exc-cav}}(\boldsymbol{k}_{\parallel}) = \hat{H}_{\text{exc}}(\boldsymbol{k}_{\parallel}) + \hat{H}_{\text{cav}}(\boldsymbol{k}_{\parallel}) + \sum_{\boldsymbol{k}_{\parallel},\alpha} \hbar\Omega(\boldsymbol{k}_{\parallel})(\hat{a}^{\dagger}_{\alpha,\boldsymbol{k}_{\parallel}} \hat{c}_{\alpha,\boldsymbol{k}_{\parallel}} + \hat{c}^{\dagger}_{\alpha,\boldsymbol{k}_{\parallel}} \hat{a}_{\alpha,\boldsymbol{k}_{\parallel}}). \qquad (4.19)$$

where $\hat{H}_{\text{cav}}(\boldsymbol{k}_{\parallel})$ is defined in Eq.(4.18). $\hat{H}_{\text{exc}}(\boldsymbol{k}_{\parallel})$ is given in Eq.(4.8), where in the notation the wavevector of the exciton $\boldsymbol{K}$ is replaced by the $\boldsymbol{k}_{\parallel}$, indicating the wavevector of the exciton in the cavity plane. The wavevector component of the exciton along the cavity axis z is fixed by the strong coupling with the cavity photon, so we don't write it explicitly. Note that only transverse excitons, with a polarization α perpendicular to their wavevector, couple to photons. Furthermore, in the interaction term, a single wave number and a single polarization can be used because the in-plane momentum is conserved and different polarizations are not coupled [113]. From now on we will assume that the wavevector dependence of the exciton can be neglected, due to the heavy mass of the exciton ($M \simeq 10^{-1} m_{e,0}$) with respect to the effective mass of the cavity photon [17], so we consider that the exciton's frequency has the constant value ω_x.

The last term of Eq.(4.19) describes the coherent coupling between an exciton and a cavity photon. It arises from the interaction of a dipole with the radiation field, which, in the Coulomb gauge and in cgs units, is characterized by [111, 112][6]

$$H_{\text{dip}} = \frac{-e}{m_{e,0}c} \sum_i \boldsymbol{p}_i \cdot \boldsymbol{A}_i, \qquad (4.20)$$

where the sum runs over all electrons of the crystals and e, $m_{e,0}$ and $\boldsymbol{p}_i$ are the charge, mass and momentum of an electron and $\boldsymbol{A}_i$ the vector potential of the electromagnetic field. One can obtain the final interaction term linking the electron's operator to the polarization field and introducing the second quantized form for the vector potential and the polarization field [112, 113].

The coupling strength describing the exchange of one excitation between the exciton

---

[5]For the RWA to hold we need $\Omega, |\omega_x(\boldsymbol{k}_{\parallel}) - \omega_c(\boldsymbol{k}_{\parallel})| \ll \omega_x(\boldsymbol{k}_{\parallel}) + \omega_c(\boldsymbol{k}_{\parallel})$.

[6]Note that the coupling of a single dipole, with dipole moment $\boldsymbol{d}$ with the electromagnetic field can be expressed equivalently as $H_{\text{dip}} = -\boldsymbol{d} \cdot \boldsymbol{E}$ [74], where $\boldsymbol{E}$ is the electric field.

and the photon mode $\Omega(\boldsymbol{k}_{\parallel})$, referred to as Rabi frequency, is given by

$$\Omega(\boldsymbol{k}_{\parallel}) = \hbar\omega_x \left(\frac{\pi\beta\omega_x}{\omega_c(\boldsymbol{k}_{\parallel})\epsilon_\infty} \right)^{\frac{1}{2}}, \tag{4.21}$$

where $\omega_c(\boldsymbol{k}_{\parallel})$ denotes the dispersion relation of the cavity photon, given in Eq.(4.16)[7]. ϵ_∞ is the frequency independent contribution to the total dielectric function $\epsilon(\omega)$ due to all resonances in the crystal other than the exciton [111]. The polarizability is denoted with β and reads

$$\beta = \frac{e^2}{m_{e,0}\omega_x^2} \frac{f}{V} \tag{4.22}$$

where $m_{e,0}$ is the free electron mass and V the volume of the semiconductor crystal that is confined within the cavity. f denotes here the dimensionless excitonic oscillator strength and is defined as [111]

$$f = \frac{2}{m_{e,0}\hbar\omega_x} |\langle \mathrm{f}| \boldsymbol{e} \cdot \sum_i \boldsymbol{p}_i |\mathrm{i}\rangle|^2, \tag{4.23}$$

for a transition from an initial state $|\mathrm{i}\rangle$, which is the crystal's ground state, to a final state $|\mathrm{f}\rangle$, which is the exciton's state, with one electron in the conduction band. $\boldsymbol{e}$ denotes the polarization vector of the vector potential.

The oscillator strength can also be linked to the dipole matrix element between the crystals ground state and the exciton state according to [111]

$$f = \frac{2m_{e,0}\omega_x}{\hbar} |\langle \mathrm{f}| \boldsymbol{e} \cdot \sum_i \boldsymbol{r}_i |\mathrm{i}\rangle|^2, \tag{4.24}$$

where $\boldsymbol{r}_i$ indicates the position of the ith electron with respect to the hole. Due to the spatial extension of the exciton's wavefunction over many sites of the crystal, the oscillator strength of the exciton assembles the oscillator strength of many atoms [108].

The Hopfield Hamiltonian (4.19) has some resemblance with the Jaynes-Cummings model [76], given in Eq.(1.52), which describes the coupling between a harmonic oscillator and a two-level system. However, Eq.(4.19) characterizes two coupled harmonic oscillators. Both the Hopfiel and the Jaynes-Cummings model, describe a single quantum exchange

---

[7]Note that here we adapted the definition given in Ref. [111, 113] to the case of a bulk semiconductor inside a cavity.

between two coupled systems [114] and lead to the formation of dressed states, called polaritons. In contrast to the Jaynes-Cummings model, where the two-level system saturates with a single excitation, the Hamiltonian (4.19) describes a situation where both modes can store an arbitrary amount of quanta [114]. The frequency at which the excitation is exchanged is called Rabi frequency. In the case of a two-level atom the Rabi frequency is proportional to the dipole moment of the corresponding atomic transition. For N two-level systems interacting with a harmonic oscillator, it scales with $\sqrt{N}$ [108]. The coupling strength Ω as defined in Eq.(4.21) also arises from the dipole interaction and is proportional to a dipole moment but the involved states are the ground state of the crystal and the exciton state. A more detailed discussion of the differences between the Jaynes-Cummings model and the Hopfield model (4.19), can be found in Ref. [115].

In the following we are going to neglect the dependency of the Rabi frequency on the wavevector and consider its constant value at $\boldsymbol{k}_\parallel = 0$, which we will refer to as Ω.

Hopfield showed that the Hamiltonian in Eq.(4.19) can be diagonalized using the unitary transformation

$$\begin{pmatrix} \hat{p}_{\alpha,\boldsymbol{k}_\parallel} \\ \hat{u}_{\alpha,\boldsymbol{k}_\parallel} \end{pmatrix} = \begin{pmatrix} -C_{\boldsymbol{k}_\parallel} & X_{\boldsymbol{k}_\parallel} \\ X_{\boldsymbol{k}_\parallel} & C_{\boldsymbol{k}_\parallel} \end{pmatrix} \begin{pmatrix} \hat{a}_{\alpha,\boldsymbol{k}_\parallel} \\ \hat{c}_{\alpha,\boldsymbol{k}_\parallel} \end{pmatrix}, \qquad (4.25)$$

with $X_{\boldsymbol{k}_\parallel}^2 + C_{\boldsymbol{k}_\parallel}^2 = 1$. Here $\hat{p}_{\alpha,\boldsymbol{k}_\parallel}$ and $\hat{u}_{\alpha,\boldsymbol{k}_\parallel}$ are the annihilation operators of an excitation in the lower and upper exciton-polariton branch respectively. The upper and lower exciton-polariton branch are the eigenstates (normal modes) of the system and they are linear superpositions of one exciton and one photon mode. They correspond to the dressed states. The new quasiparticles, the upper and lower exciton-polariton, are bosons since they are linear combinations of bosonic operators. Their lifetime is determined by the nonradiative lifetime of the exciton and the lifetime of the cavity photon. The coefficients of the transformation read

$$X_{\boldsymbol{k}_\parallel} = \sqrt{\frac{\sqrt{4\Omega^2 + \Delta(\boldsymbol{k}_\parallel)^2} + \Delta(\boldsymbol{k}_\parallel)}{2\sqrt{4\Omega^2 + \Delta(\boldsymbol{k}_\parallel)^2}}}, \qquad C_{\boldsymbol{k}_\parallel} = \sqrt{\frac{\sqrt{4\Omega^2 + \Delta(\boldsymbol{k}_\parallel)^2} - \Delta(\boldsymbol{k}_\parallel)}{2\sqrt{4\Omega^2 + \Delta(\boldsymbol{k}_\parallel)^2}}}, \quad (4.26)$$

where $\Delta(\boldsymbol{k}_\parallel) = \omega_c(\boldsymbol{k}_\parallel) - \omega_x$ denotes the detuning between cavity and exciton. We assume that at $\boldsymbol{k}_\parallel = 0$ the cavity and the exciton are at resonance and thus $\hbar\omega_c^0 = \omega_x$. Note that $X_{\boldsymbol{k}_\parallel}^2$ and $C_{\boldsymbol{k}_\parallel}^2$ are called excitonic and photonic fraction, as they describe the portions of exciton and photon that are contained in the lower exciton-polariton[8].

The eigenvalues, corresponding to the dispersion relation of upper $(+)$ and lower $(-)$

---

[8]For the upper exciton-polariton the situation is inverted and $C_{\boldsymbol{k}_\parallel}^2$ describes the excitonic fraction.

exciton-polariton, read

$$\omega_u(\boldsymbol{k}_\parallel) = \frac{1}{2}\left(\omega_c(\boldsymbol{k}_\parallel) + \omega_x + \sqrt{4\Omega^2 + \Delta(\boldsymbol{k}_\parallel)^2}\right), \tag{4.27}$$

$$\omega_p(\boldsymbol{k}_\parallel) = \frac{1}{2}\left(\omega_c(\boldsymbol{k}_\parallel) + \omega_x - \sqrt{4\Omega^2 + \Delta(\boldsymbol{k}_\parallel)^2}\right). \tag{4.28}$$

Fig.4.5 shows a sketch of the dispersion relations of the cavity photon, the exciton and upper and lower exciton-polariton. At $\boldsymbol{k}_\parallel = 0$ both polaritons contain exciton and photon to equal parts ($X_0^2 = C_0^2 = 0.5$). For increasing $\boldsymbol{k}_\parallel$ the upper polariton becomes more and more photon like, whereas the lower polariton becomes more exciton like due to an increasing $X_{\boldsymbol{k}_\parallel}$.
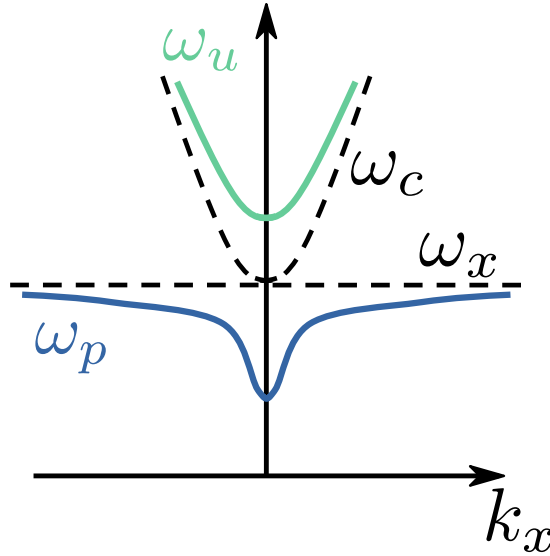
Figure 4.5.: Sketch of the dispersion relations of the cavity photon (ω_c, given by Eq.(4.16)), the exciton (ω_x), upper and lower exciton-polariton modes (ω_u and ω_p, given by the equations (4.27) and (4.28) respectively) along one in-plane direction, here along x. The dispersion are isotropic in the cavity plane and thus look the same along y.

What is the relevance of the polariton concept? From a theoretical point of view going from the exciton-photon picture to the polariton picture consists in a basis change. The advantage of the polaritons is that they are eigenstates diagonalizing the Hamiltonian (4.19) and thus stationary. They are also visible in experiments as we will see in the following section.

4.4. Experiment on exciton-polaritons in a semiconductor microcavity

In this section we discuss the seminal work of Ref. [18]. They demonstrate Bose-Einstein
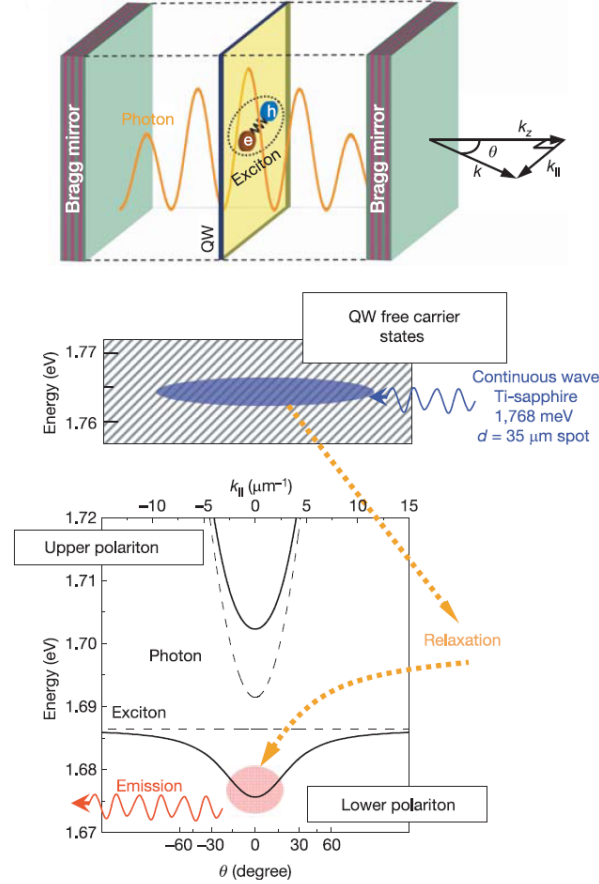
Figure 4.6.: (Top panel) Experimental setup. The semiconductor microcavity consists of two Bragg mirrors and contains excitons in quantum wells (QW). Cavity photon and quantum well exciton strongly couple and form exciton-polaritons. The Rabi frequency is $\Omega = 26\,\mathrm{meV}$. The dispersion relations of photon, exciton and exciton-polaritons are shown in the bottom panel. The cavity is externally pumped by a laser with a uniform excitation spot and an excitation energy far above the polariton energy. Thus free electrons are created in the quantum well and relax via phonon or polariton scattering into the ground state of the lower polariton. Image taken from Ref. [18].

condensation of exciton-polaritons. The experiment is remarkable as it shows Bose-

Einstein condensation[9] in a solid-state system and at temperatures of a few Kelvin that are accessible using standard cryogenic techniques. The critical temperature for condensation is thus much higher than in the case of ultracold atoms, where it is in the nano Kelvin regime [55] (see again Section 1.1). The reason for these different critical temperatures is that exciton-polaritons are 10^9 times lighter than for instance Rubidium atoms. Thus the thermal de-Broglie wavelength, defined in Eq.(1.1), can turn comparable to the interparticle distance at much higher temperatures.

The setup of the experiment is depicted in the top panel of Fig.4.6. In the experiment, they use a CdTe-based semiconductor microcavity consisting of two Bragg mirrors, as we described in Section 4.2. However, in their setup the excitons are additionally confined along the cavity axis in CdTe quantum wells. The microcavity is in the strong coupling regime. The in-plane dispersion of exciton, photon and upper and lower exciton-polariton is shown in the bottom panel of Fig.4.6. A continuous-wave laser excites the microcavity with a uniform excitation spot, as depicted in the middle panel of Fig.4.6. An important point is that the excitation energy of the laser is much higher (around $1.768\,\mathrm{eV}$) than the energy of the ground state of the lower polariton branch (around $1.671\,\mathrm{eV}$). Since the pump energy is much higher than the exciton levels (see again Fig.4.2), it excites free electrons/holes in the quantum well, which can relax, via phonon or polariton scattering, towards the ground state of the lower polariton branch, see bottom panel of Fig.4.6. This pump scheme thus injects lower exciton-polaritons in an incoherent way. The experimental control parameter is the excitation power, which corresponds to the polariton density.

As observable, they can measure the far-field photon emission pattern, providing information about the polariton density distribution along the lower polariton branch in momentum space [17]. As discussed in Section 4.2, the in-plane wavevector $\boldsymbol{k}_\parallel$ is conserved due to the translational invariance of the planar microcavity and thus allows to link the photon emission angle, here denoted with θ, with the intracavity polariton dispersion according to $\boldsymbol{k}_\parallel = \omega/c \sin\theta$. Furthermore they use real-space imaging and thus have access to the spatially resolved emission. Note that in contrast to standard experiments with ultracold atoms, these measurements are done in situ, using all the time the same sample. A drawback is that, as it is a solid-state based setup, there is always disorder due to impurities.

In the case of two-dimensional exciton-polaritons, it is not straightforward to define Bose-Einstein condensation, because instead of having an infinite three dimensional gas of noninteracting, infinitely living bosons without internal structure, the experiment deals

---

[9]Strictly speaking it is not standard BEC as will be discussed below.

with a finite, two dimensional gas of interacting bosons, that possess an internal structure and are short lived. However, the experiment shows the main features of Bose-Einstein condensation and in particular macroscopic occupation of the ground state. In the article, they present more evidence, for example a measurement indicating the build-up of long-range spatial coherence across the cloud. The effects of interactions, dimensionality and internal structure on the transition are discussed in the supplementary material of Ref. [18]. Altogether the experiment revealed questions about the nature of condensation under conditions that deviate from the ideal Bose gas in three dimensions and thus opened up new research directions. Some points could be clarified using existing theories, for example the generalization of a BEC for interacting bosons (in three dimensions and infinitely living) has been done by Penrose and Onsager [116]. The influence of reduced dimensionality and confinement on condensation has also been discussed and is reviewed for example in Ref. [117]. It turns out that, conceptually, the driven-dissipative nature of the system changes the nature of the condensation transition with respect to the equilibrium case [19]. Thus recently a new theoretical treatment has been suggested by Diehl and coworkers [118], using methods of out-of-equilibrium physics as the Kardar-Parisi-Zhang equation [119].
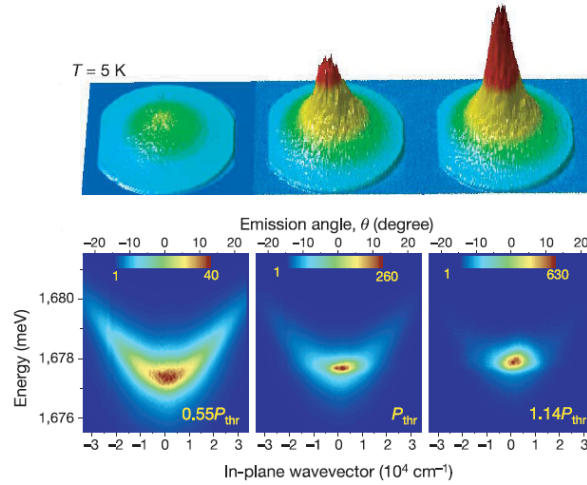
Figure 4.7.: Far-field emission at $5\,\mathrm{K}$ for three excitation intensities, from left to right: $0.55P_{\mathrm{thr}}$, P_{thr}, $1.14P_{\mathrm{thr}}$, where P_{thr} is the threshold power for condensation. (Top panel) Angular distribution of the emission with the emission intensity on the vertical axis. For an increasing pump intensity a peak at the center ($\boldsymbol{k}_{\parallel} = 0$) arises, indicating the macroscopic population of the ground state. (Bottom panel) Energy-and angle resolved emission intensity. The momentum distribution becomes more and more narrow for higher pump intensity. The main contribution to the emission comes from the ground state at $\boldsymbol{k}_{\parallel} = 0$. The image is taken from Ref. [18].

Fig.4.7 shows the far-field emission, measured at a temperature of $T = 5\,\mathrm{K}$ for three different pump intensities: one below the condensation threshold P_{thr} (left panels), one at the threshold (middle panels) and one above the threshold (right panels). The top panel of Fig.4.7 displays the angular distribution of the emission, with the emission intensity on the vertical axis. The bottom panel contains the same data, but energy and angle-resolved. Below the threshold the emission distribution is smooth around the center $\boldsymbol{k}_{\parallel} = 0$. For an increasing pump intensity a sharp peak at the center ($\boldsymbol{k}_{\parallel} = 0$) arises (see Fig.4.7 top panel) which comes along with a shrinking of the momentum distribution (see Fig.4.7 bottom panel). This indicates the macroscopic population of the ground state at $\boldsymbol{k}_{\parallel} = 0$.

4.5. Exciton-polaritons and atoms in an optical cavity: common concepts and differences

In this final introductory section we open a parenthesis to compare the two experimental platforms that are at the basis of our theoretical studies in this thesis, namely ultracold atoms in an optical cavity and exciton-polaritons in a semiconductor cavity.

Both experimental setups are based on the use of an optical Fabry-Pérot cavity. However, the dimensions and characteristics are very different: A semiconductor microcavity, as depicted in Fig.4.8 (a) has a typical thickness of several μm, including the Bragg mirrors, which are planar (radius of curvature ∞) and are several mm long. The finesse is poor with a typical value around $Q = 10^4$ [120]. The lifetime of the cavity photons is in the ps regime corresponding to a decay rate $\kappa \sim 1\,\mathrm{THz}$. The frequency of the cavity mode we are going to use is $\hbar\omega_c = 1680\,\mathrm{meV}$, corresponding to $\omega_c = 2\pi \times 406\,\mathrm{THz}$, which yields a wavelength in the optical regime of $\lambda_c = 740\,\mathrm{nm}$. Thus the mode index (number of nodes) is small.

The optical cavity used in the group of Tilmann Esslinger [41] is depicted in Fig.4.8 (b). It has a high finesse of $Q = 3.4 \times 10^5$. Its thickness is $h = 178\,\mu$m and the mirrors are curved with a radius of curvature of $R = 75\,\mathrm{mm}$. The cavity decay time is $\kappa = 2\pi \times 1.3\,\mathrm{MHz}$. The wavelength of the mode they are typically working with is $\lambda_c = 785\,\mathrm{nm}$.

Furthermore, on both platforms light and matter is in the strong coupling regime, but the reasons are different: In the case of the semiconductor microcavity the strong coupling is due to the large electric-dipole moment [123], yielding a large Rabi frequency. In our calculations we will use $\hbar\Omega = 6\,\mathrm{meV}$, which corresponds to $\Omega = 2\pi \times 1.45\,\mathrm{THz}$.

In the case of ultracold atoms inside the cavity the vacuum Rabi coupling is $g_0 =$
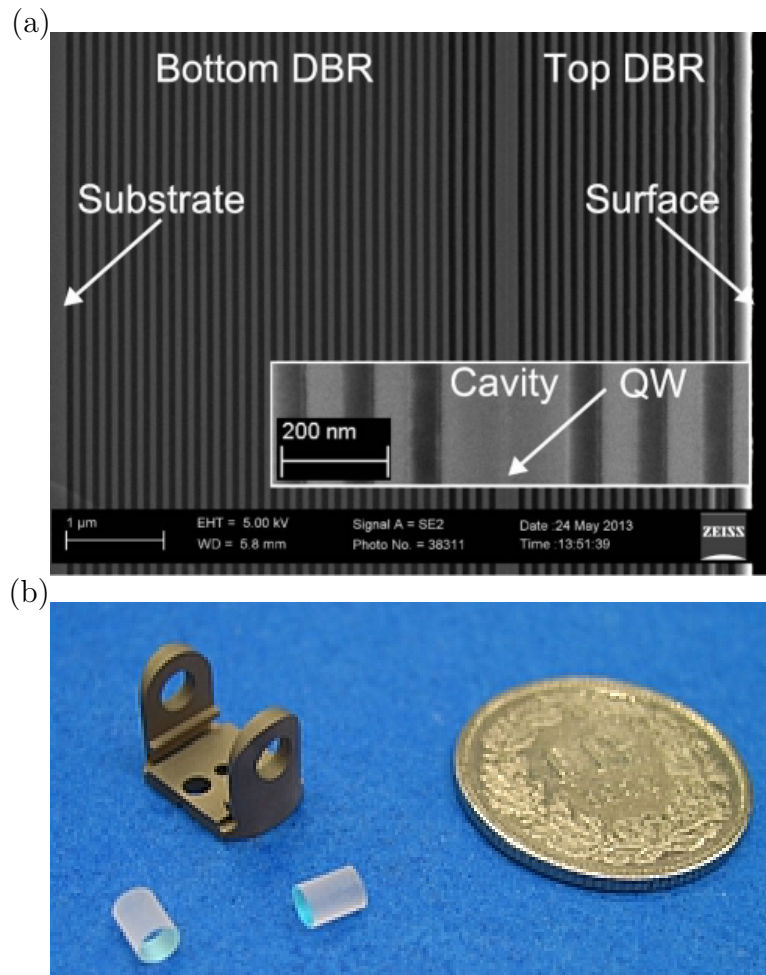
Figure 4.8.: (a) Picture of a semiconductor microcavity used in the Quantum photonics group of Ataç Imamoglu in Zürich. The figure is taken from Ref. [121]. (b) Picture of the optical cavity used in the Quantum optics group of Tilmann Esslinger in Zürich. The figure is taken from Ref. [122].

$2\pi \times 10.6\,\mathrm{MHz}$ [41] and thus very small in contrast to the semiconductor case (even if it is multiplied by the square of the number of atoms). Due to the high finesse of the cavity, the photon decay rate is nevertheless much smaller than the light-matter coupling.

Note that both platforms operate in very different temperature regimes. The experiments with ultracold atoms allow to achieve temperatures in the nano Kelvin regime, whereas the semiconductor microcavity experiments are limited by the minimal temperature of the cryostat. Furthermore there exist also semiconductors, as GaN and ZnO, which have exciton-polaritons at room temperature.

Chapter 5

Derivation of the exciton-TO-phonon interaction

In this chapter we derive the interaction between excitons and transverse optical phonons in a bulk semiconductor, embedded in a semiconductor microcavity. In particular we generalize the derivation of the electron-phonon interaction as shown in Ref. [105, 124], taking into account the electron-hole interaction. We then focus our analysis on the case of the exciton-phonon interaction given in Ref. [125, 126] for the case of TO phonons that interact with bright excitons in a CdTe semiconductor microcavity.

The chapter is organized as follows: first we introduce microscopic details of the semiconductor of our choice, such as crystal structure, symmetry, band structure and lattice vibrations. In Section 5.2 we derive a general form of the electron-phonon interaction Hamiltonian before we extend our description in Section 5.3 to the case of excitons. The band structure and symmetry of CdTe will be taken into account in Section 5.4, in order to estimate the exciton-TO-phonon coupling strength for a $1s$ exciton, as discussed in Section 5.5. In Section 5.6 we identify the excitons that are visible in the experiment due to their strong coupling to cavity photons and transform the Hamiltonian in the corresponding bright exciton basis.

5.1. Microscopic details of CdTe

We consider Cadmium Telluride (CdTe), a semiconductor of type II-VI with zinc-blende structure [104]. Fig.5.1 (a) shows a zinc-blende (non primitive) unit cell. The length of the unit cell is the lattice constant a, which amounts to 6.48Å for CdTe. The zinc-blende structure consists of two face-centered cubic (fcc) lattices that are shifted by one fourth

(a)   (b)
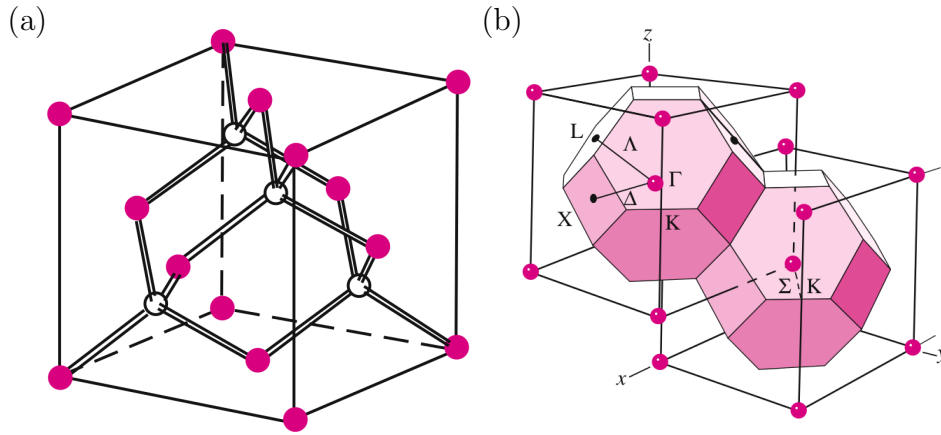
Figure 5.1.: (a) Sketch of one possible unit cell of the crystal structure of CdTe: The zinc-blende structure consists of two face-centered cubic (fcc) lattices that are shifted by one fourth of the diagonal. Every atom is surrounded by four atoms of the other species. They form a tetrahedron which is the primitive cell or Wigner-Seitz cell of the zinc-blende structure. (b) Sketch of the reciprocal lattice of the fcc lattice with the first Brillouin zone and special high-symmetry points and high-symmetry lines. For our purpose, the center of the Brillouin zone, denoted by Γ, will be of special importance. The images are taken from Ref. [104].

of the diagonal. It does not display inversion symmetry [1]. Each unit cell contains four Cd and four Te atoms. Every atom is surrounded by four atoms of the other species. They form a tetrahedron which is the primitive cell or Wigner-Seitz cell of the zinc-blende structure. The first Brillouin zone is the Wigner-Seitz cell of the reciprocal lattice [1] and it is depicted in Fig.5.1 (b). The center of the Brillouin zone $k = 0$ is denoted by Γ. It will be of special importance for us in the following, since the processes we will describe will always happen close to the Γ point. We will now introduce some elements of group theory that will simplify the calculation of matrix elements in the following.

5.1.1. Brief introduction on group theory

This subsection is based on Ref. [104, 106]. A detailed discussion of group theory in solid state physics can also be found in Ref. [124].

Group theory is a mathematical tool for studying the effect of symmetry operations on an object. It is used in solid-state physics to classify wavefunctions in crystals according to their transformation properties under symmetry operations [104] or to derive selection rules. Correspondingly, the first step is to identify the crystal's structure and the possible symmetry operation that leave the crystal unchanged. CdTe has zinc-blende structure and

its space group[1] is T_d^2 (in Schönflies notation), which is identical to the symmetry group of tetrahedron, denoted by T_d [104]. An alternative notation is $F\bar{4}3m$ (international notation). The symmetry group contains 24 symmetry operations: identity (E), eight rotations of 120° (C_3), three rotations of 180° (C_2), six rotations of 90° followed by reflections (S_4), and six reflections (σ). These symmetry operations can be represented using matrices. The matrix representation of a symmetry operation is not unique but depends on the basis choice. The representation of a symmetry group is the group of matrices associated with the elements of the symmetry group [106]. If two representations can be linked via a similarity transformation they are equivalent. A representation is called *reducible* if all matrices that constitute the representation can be brought to the form of a block-diagonal matrix by application of a similarity transformation. Correspondingly for an *irreducible* representation it is not possible to find a similarity transformation that transforms all matrices associated with the elements of the group to block-diagonal form [106]. In order to specify a representation, it is convenient to use its trace, as it is unique, and doesn't change under a similarity transformation. The trace of a representation is called *character* and is denoted with χ. Equivalent representations have the same character. Even if the complete matrices, specifying a representation, contain more information, it is sufficient for many symmetry considerations to determine the number of irreducible representations and their characters. This information is displayed in a character table, that can be calculated using several rules that are specified in Ref. [104, 106].

The symmetry properties of a crystal are helpful for the derivation of the band structure because the irreducible representations of the crystal determine how a wavefunction with wavevector $\boldsymbol{k}$ at a given point in the zone transforms under a symmetry operation. The center of the Brillouin zone is of special interest. Its irreducible representations are labeled with Γ and a subscript[2]. The irreducible representations come along with different possible basis functions, i.e. functions that transform according to the corresponding irreducible representation, e.g. a scalar transforms under the symmetry operations of T_d^2 according to Γ_1 because it stays invariant under all symmetry operations of T_d^2. Table 5.1 shows the character table and possible basis functions of the T_d^2 group [104]. For our purposes the most important irreducible representations are Γ_1 and Γ_4, because in the zinc-blende structured crystal CdTe we consider, scalar functions transform according to Γ_1 and vectors according to Γ_4.

---

[1]The group of translational and rotational operations that leave a zinc-blende structure unchanged.

[2]Note that there are many different notations. We use the notation of Ref. [104]. An overview over different notations can be found for example in Ref. [127].

	$\{E\}$	$\{3C_2\}$	$\{6S_4\}$	$\{6\sigma\}$	$\{8C_3\}$	Basis functions
Γ_1	1	1	1	1	1	constant or xyz
Γ_2	1	1	-1	-1	1	$x^4(y^2 - z^2) + y^4(z^2 - x^2) + z^4(x^2 - y^2)$
Γ_3	2	2	0	0	-1	$\{(x^2 - y^2), z^2 - \frac{1}{2}(x^2 + y^2)\}$
Γ_4	3	-1	-1	1	0	$\{x, y, z\}$
Γ_5	3	-1	1	-1	0	$\{x(y^2 - z^2), y(z^2 - x^2), z(x^2 - y^2)\}$

Table 5.1.: Character table and basis functions of the T_d^2 group, without spin, taken from Ref. [104].

The symmetry properties of a crystal lead to restrictions on matrix elements and thus to selection rules, that are summarized in the *matrix element theorem* [104]: Consider a matrix element $M = \langle \Psi_2 | \, \boldsymbol{p} \, | \Psi_1 \rangle$, between the momentum operator $\boldsymbol{p}$ and two wavefunctions $|\Psi_1\rangle$ and $|\Psi_2\rangle$. The matrix element M is always zero, except if the direct product of the irreducible representations of $\boldsymbol{p}$ and $|\Psi_1\rangle$ contains the irreducible representation according to which $|\Psi_2\rangle$ transforms. Assume for example that $|\Psi_1\rangle$ and $|\Psi_2\rangle$ are wavefunctions in CdTe and both transform like a scalar, according to Γ_1. The vector $\boldsymbol{p}$ transforms like Γ_4. The direct product is

$$\Gamma_4 \otimes \Gamma_1 = \Gamma_4 \tag{5.1}$$

and thus doesn't contain an irreducible representation of $|\Psi_2\rangle$. The matrix element is zero. Instead if $|\Psi_1\rangle$ and $|\Psi_2\rangle$ both transform like a vector, according to Γ_4, the matrix element is not zero, because

$$\Gamma_4 \otimes \Gamma_4 = \Gamma_4 \oplus \Gamma_5 \oplus \Gamma_3 \oplus \Gamma_1. \tag{5.2}$$

Note that the decomposition of the direct products into sums can be obtained with the help of the character table, because the number of times the irreducible representation $\mathcal{D}^\mu$ is contained in the product between the two irreducible representations $\mathcal{D}^\alpha$ and $\mathcal{D}^\nu$ is given by [106]

$$c(\mu, \alpha, \nu) = \frac{1}{h} \sum_R \chi^\mu(R) \chi^\alpha(R) \chi^\nu(R). \tag{5.3}$$

Here h is the number of elements in the symmetry group and the sum goes over all symmetry operations R. Thus e.g. the number of times the irreducible Γ_4 is contained in

$\Gamma_4 \otimes \Gamma_1$ for T_d^2 is given by

$$
c(\Gamma_4, \Gamma_4, \Gamma_1) = \frac{1}{24}(\underbrace{1 \cdot 3 \cdot 3}_{\times 1, \text{from} E} + \underbrace{1 \cdot (-1) \cdot (-1)}_{\times 3, \text{from} C_2} + \underbrace{1 \cdot (-1) \cdot (-1)}_{\times 6, \text{from} S_4} + \underbrace{1 \cdot (1) \cdot (1)}_{\times 6, \text{from} \sigma} + \underbrace{1 \cdot 0 \cdot 0}_{\times 8, \text{from} C_3})
$$
$$
= 1. \tag{5.4}
$$

Up to now we didn't consider the electron's spin. Adding the spin leads to additional symmetry operations. Symmetry groups including the spin are called double groups [104] and we will discuss them briefly in subsection 5.1.2 below.

5.1.2. Band structure of CdTe

This subsection is based on Ref. [104, 127]. We want to understand the band structure of CdTe. There are different techniques to calculate the band structure of semiconductors [106]. A prominent approach is e.g. the pseudopotential method which assumes that the electrons in a semiconductor are nearly free and can be described by plane waves. We will follow the tight-binding or linear combination of atomic orbitals (LCAO) approach to gain an intuition about the formation principle of a semiconductor band structure. The LCAO approach assumes that the electrons in a semiconductor are tightly bound to the corresponding nucleus and that the electronic wavefunctions in a solid are build by combinations of atomic orbitals.

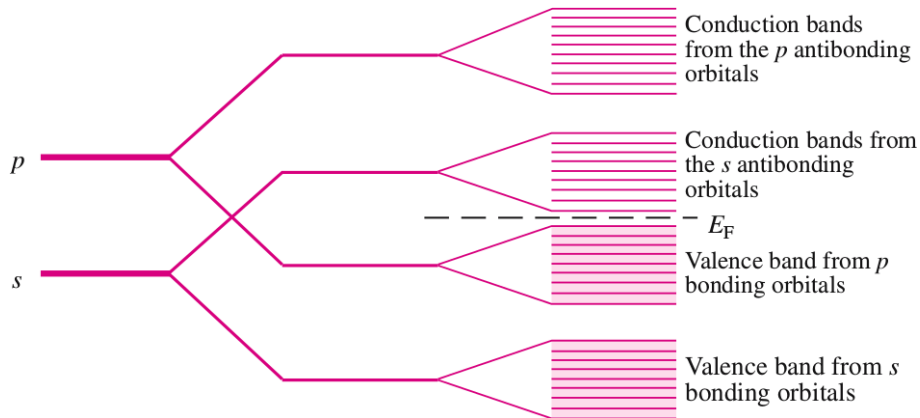**Figure 5.2.:** Atomic s and p orbitals overlap and form bonding and antibonding orbitals. In a solid the bonding and antibonding orbitals broaden and form bands. The empty antibonding orbitals lead to the formation of the conduction bands whereas the filled bonding orbitals yield the valence bands. The highest valence band is p-like and the lowest conduction band s-like. The image is taken from Ref. [104].

Let us consider two atoms of different species that build the basis of a semiconductor of zinc-blende structure[3]. Their valence electrons occupy the atomic s and p orbitals: in the case of CdTe, Cd possesses two valence electrons in the $5s$ shell and Te two valence electrons in the $5s$ shell and four in the $5p$ shell [127]. If the two atoms are brought together such that their distance is of the order of the lattice constant in solids, their atomic wavefunctions of the same symmetry overlap and build respectively two new orbitals that are referred to as bonding orbital and antibonding orbital. As the two atoms are of different species the electron distribution along the bond is not symmetric. One atoms 'pulls' stronger than the other. The bond is heteropolar.

The bonding orbitals contain electrons, the antibonding orbitals are empty. Note that the new orbitals are energetically shifted with respect to the original ones, as depicted in Fig.5.2: The bonding orbitals have lower energy than the antibonding ones, thus the bonding orbital, build up by two overlapping p orbitals, has a lower energy than the antibonding orbital, build up by two overlapping s orbitals. We can generalize the idea of bonding and antibonding orbitals from the case of two atoms to a crystal, if we assume that in a crystal only the nearest neighbor's atom orbitals can overlap. The combination of all these overlapping atomic orbitals in a solid will form bands, as sketched in Fig.5.2. The filled bonding orbitals become the valence bands and the empty antibonding orbitals the conduction bands. The bands of interest are those around the band gap. We see that the conduction band with the lowest energy comes form overlapping s orbitals. It's symmetry is also s-like, which in the language of group theory, means that it transforms according to the irreducible representation Γ_1. In analogy to the atomic orbitals and to provide an intuition to the symmetry predictions of the group theory, this conduction band is associated with a pseudo-orbital momentum $L = 0$. The valence band with the highest energy comes from overlapping p orbitals. Thus the valence band wavefunctions are p-like, which corresponds to the irreducible representation Γ_4. This valence band is associated with a pseudo-orbital momentum $L = 1$. However, the crystal is not spherically symmetric as it is the case for a single atom. So there are corrections to the purely $L = 1$-like behavior of the wavefunctions, as we will see in more details in Section 5.4.

We now want to include the spin of the electron, which is $S = 1/2$[4]. In the language of group theory this means that we need to consider double groups [104, 106]; in particular there are new irreducible representations: the irreducible representation describing a scalar

---

[3]e.g. Cd and Te, but this treatment also applies to other tetrahedrally bonded semiconductors.

[4]In the band structure calculation the effect of the spin is included by taking into account the spin-orbit coupling.
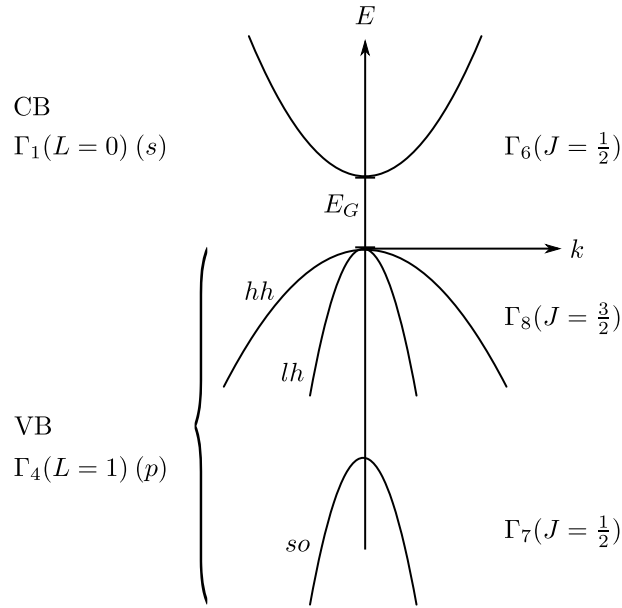
Figure 5.3.: Sketch of the band structure of a general direct band gap semiconductor with zinc-blende structure. Without the spin the symmetry of the valence band (VB) corresponds to the irreducible representation Γ_4. It is p-like, i.e. by analogy to atomic physics, the pseudo-orbital momentum is $L = 0$. The conduction band (CB) has Γ_1 symmetry and is s-like. Including the spin the symmetry groups are given by the double groups [104]: Γ_1 is replaced by Γ_6 and Γ_4 by Γ_7 and Γ_8. The valence band is split in heavy (hh) and light hole (lh) band and the split-off band (so). The image is inspired by Ref. [127].

(or a *s*-like function) Γ_1 is replaced by Γ_6. The irreducible representation of a vector Γ_4 splits into Γ_7 and Γ_8, thus including the spin leads to a splitting of the valence band. In order to better understand the predictions of group theory it is helpful to introduce the total pseudo-angular momentum J, again in analogy to atomic physics. Thus we keep in mind that the total pseudo-angular momentum is just an mnemonic and the 'clean' way is to use group theory [127].

For an electron of spin $S = 1/2$ in the conduction band with pseudo-orbital momentum $L = 0$ the resulting total pseudo-angular momentum is $J = 1/2$. The valence band is split in states with $J = 3/2$, corresponding to the representation Γ_8 and the so-called split-off band with $J = 1/2$, which corresponds to the representation Γ_7. The states with $J = 3/2$ split again in heavy hole (hh) and light hole (lh) band: the heavy hole band is the band with a total angular momentum projection of $\pm 3/2$, the light hole band has the total angular momentum projection of $\pm 1/2$. In Section 5.4 we will introduce and discuss the eigenstates of an electron in the conduction band and of a hole in a valence band.

Fig.5.3 summarizes the symmetry of conduction and valence band states with and without spin for a general direct band gap semiconductor of zinc-blende structure. The band structure of CdTe is illustrated in Fig.5.4.
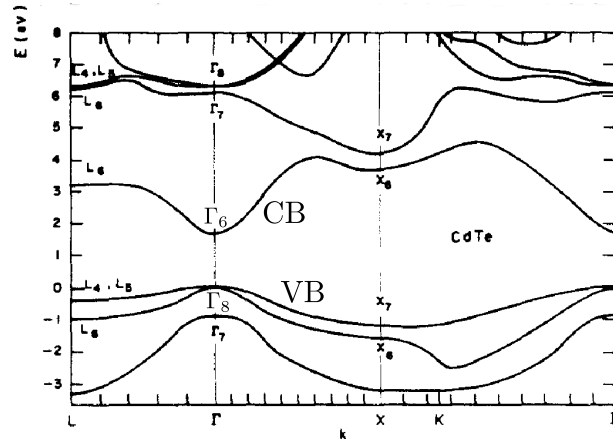
Figure 5.4.: Band structure of CdTe, calculated by the pseudopotential method with spin-orbit effects included. The image is taken from Ref. [128].

5.1.3. Phonons

A lattice vibration is a displacement of the atoms forming a crystal from their equilibrium positions. The dimensionality of the crystal and the number of basis atoms determine the

number of possible normal mode branches of the lattice. The energy of the normal modes is quantized and can be written as the sum over harmonic oscillators [105, 129]

$$\hat{H}_{\mathrm{vib}} = \sum_{\boldsymbol{q},j} \hbar\omega_{\boldsymbol{q},j}(\hat{n}_{\boldsymbol{q},j} + \frac{1}{2}), \tag{5.5}$$

with wavevector $\boldsymbol{q}$ and frequency $\omega_{\boldsymbol{q},j}$, where j denotes the corresponding branch and $\hat{n}_{\boldsymbol{q},j}$ is the excitation number operator of the normal mode. The quantized lattice vibrations are elementary excitations, called phonons [105]. A detailed introduction to phonons can be found in Ref. [105, 129].

As we consider a three dimensional crystal with a basis formed by two atoms (Cd and Te), there are six phonon branches [129]: three optical and three acoustical branches, where respectively two branches are transverse and one is longitudinal. In Appendix C we show the derivation of optical and acoustical branches in one dimension for a crystal with a basis of two atoms. Fig.5.5 shows exemplarily the phonon dispersion relations for ZnTe, another II-VI semiconductor of zinc blende structure. Here LO and TO correspond to the longitudinal and transversal optical phonon branch respectively. LA and TA denote longitudinal and transversal acoustical branch. At the Γ point the transverse branches are degenerate. In Section 4.3 we introduced a polariton as a mixed quasiparticle that is
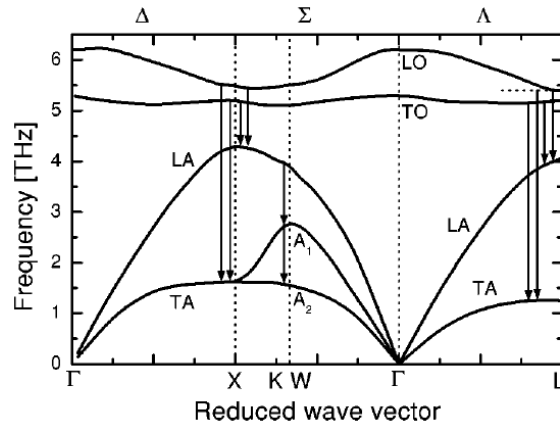
Figure 5.5.: Phonon dispersion relations for ZnTe. The image is taken from Ref. [130].

formed by the strong coupling between a photon and a matter excitation [17]. In the same way as excitons, transverse optical phonons can strongly couple to photons[5] and form

---

[5]Note that only optical phonons can couple to light because in contrast to acoustical phonons they have an oscillating dipole.

phonon-polaritons [1, 131]. In analogy to Hopfield's Hamiltonian [113], the Hamiltonian describing the strong photon-TO phonon coupling in the rotating-wave approximation can be written as

$$\hat{H}_{\text{phon-THz}} = \sum_{\boldsymbol{q}} \hbar\omega_{TO}\hat{b}^\dagger_{\boldsymbol{q},TO}\hat{b}_{\boldsymbol{q},TO} + \hbar\omega_{ir}(\boldsymbol{q})\hat{l}^\dagger_{\boldsymbol{q}}\hat{l}_{\boldsymbol{q}} + \hbar\Omega_{ir}(\hat{b}^\dagger_{\boldsymbol{q},TO}\hat{l}_{\boldsymbol{q}} + \hat{l}^\dagger_{\boldsymbol{q}}\hat{b}_{\boldsymbol{q},TO}),\qquad(5.6)$$

where ω_{TO} is the frequency of the TO phonon and Ω_{ir} the Rabi frequency, neglecting the wavevector dependence. In the case of CdTe we will consider $\hbar\omega_{TO} = 18\,\text{meV}$ [104, 130] and $\hbar\Omega_{ir} = 5.575\,\text{meV}$ [130]. The THz photon dispersion relation is given by

$$\hbar\omega_{ir}(\boldsymbol{q}) = \hbar c_{\text{med,ir}}|\boldsymbol{q}|,\qquad(5.7)$$

where $c_{\text{med,ir}}$ denotes the speed of light in the semiconductor at infrared frequencies. The bosonic operators $\hat{b}^\dagger_{\boldsymbol{q},TO}$ and $\hat{l}^\dagger_{\boldsymbol{q}}$ create a TO phonon and a THz photon with momentum $\boldsymbol{q}$ respectively. The Hamiltonian (5.6) can be diagonalized using Hopfield's transformation to the TO phonons/THz photons subspace

$$\begin{pmatrix}\hat{w}_{\boldsymbol{q}}\\\hat{z}_{\boldsymbol{q}}\end{pmatrix} = \begin{pmatrix}-N_{\boldsymbol{q}} & T_{\boldsymbol{q}}\\T_{\boldsymbol{q}} & N_{\boldsymbol{q}}\end{pmatrix}\begin{pmatrix}\hat{b}_{\boldsymbol{q},TO}\\\hat{l}_{\boldsymbol{q}}\end{pmatrix},\qquad(5.8)$$

where $\hat{w}^\dagger_{\boldsymbol{q}}$ and $\hat{z}^\dagger_{\boldsymbol{q}}$ are the bosonic creation operator of lower and upper phonon-polariton states respectively. $N_{\boldsymbol{q}}$ and $T_{\boldsymbol{q}}$ are the Hopfield coefficients, given by

$$T_{\boldsymbol{q}} = \sqrt{\frac{\sqrt{4\Omega^2_{ir} + \Delta_p(\boldsymbol{q})^2} - \Delta_p(\boldsymbol{q})}{2\sqrt{4\Omega^2_{ir} + \Delta_p(\boldsymbol{q})^2}}}, \qquad N_{\boldsymbol{q}} = \sqrt{\frac{\sqrt{4\Omega^2_{ir} + \Delta_p(\boldsymbol{q})^2} + \Delta_p(\boldsymbol{q})}{2\sqrt{4\Omega^2_{ir} + \Delta_p(\boldsymbol{q})^2}}}, \qquad(5.9)$$

with the detuning between TO phonon and THz photons $\Delta_p(\boldsymbol{q}) = \omega_{TO} - \omega_{ir}(\boldsymbol{q})$ and $T^2_{\boldsymbol{q}} + N^2_{\boldsymbol{q}} = 1$. In analogy to the exciton-polaritons, $N^2_{\boldsymbol{q}}$ and $T^2_{\boldsymbol{q}}$ are the phononic and THz photonic fraction, defined with respect to the lower phonon-polariton branch. The frequencies of upper and lower phonon-polariton branch read

$$\omega_z(\boldsymbol{q}) = \frac{1}{2}\left(\omega_{ir}(\boldsymbol{q}) + \omega_{TO} + \sqrt{4\Omega^2_{ir} + \Delta_p(\boldsymbol{q})^2}\right),\qquad(5.10)$$

$$\omega_w(\boldsymbol{q}) = \frac{1}{2}\left(\omega_{ir}(\boldsymbol{q}) + \omega_{TO} - \sqrt{4\Omega^2_{ir} + \Delta_p(\boldsymbol{q})^2}\right).\qquad(5.11)$$

Fig.5.6 shows a sketch of the dispersion relation of THz photon (ω_{ir}), TO phonon (ω_{TO})

and upper and lower phonon-polariton, given by ω_z and ω_w respectively, as defined in equations (5.10) and (5.11). Notice that ω_{TO} is in the THz regime ($\hbar\omega_{TO} = 18\,\text{meV} \rightarrow \omega_{TO} = 2\pi \times 4.4\,\text{THz}$), hence both the upper branch at small $|\boldsymbol{q}|$ and the lower branch at large $|\boldsymbol{q}|$ belong to the sought THz regime.
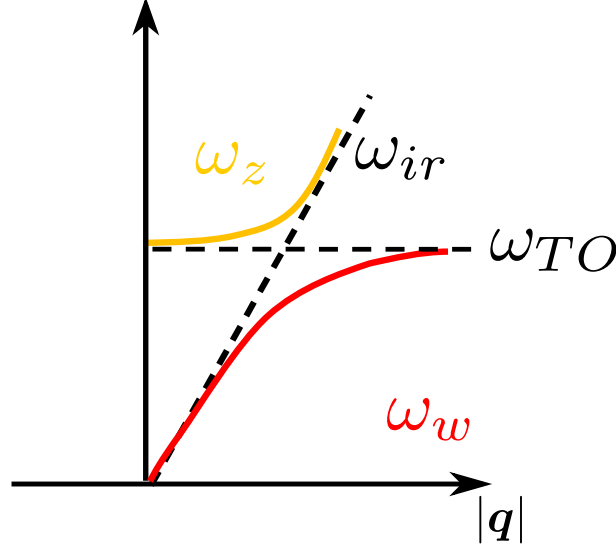
Figure 5.6.: Sketch of the dispersion relation of THz photon (ω_{ir}), TO phonon (ω_{TO}) and upper and lower phonon-polariton, given by ω_z and ω_w respectively, as defined in equations (5.10) and (5.11). For the sake of simplicity the TO-LO splitting is not shown.

Besides the coupling to photons, phonons can also couple to electrons in the crystal via a multitude of different coupling mechanisms. A detailed discussion of the different mechanisms can be found in Ref. [104, 124]. For the purpose of our frequency conversion scheme, we are interested in an interaction between TO phonons and excitons, all other interactions between lattice vibrations and electrons do not serve our purpose. We will indirectly take them into account by introducing a decay rate for excitons and TO phonons.

In the following section we will derive the Hamiltonian describing the interaction between excitons and TO phonons. This interaction occurs via the so-called deformation potential [104], because TO phonons only influence the bond lengths and angles in a primitive cell. Thus they change the potential landscape an electron is experiencing and accordingly deform the electron's energy bands. The deformation potential interaction is the only type of interaction between excitons and TO phonons since, in contrast to acoustical phonons, long-wavelength (small $\boldsymbol{q}$) optical phonons do not lead to a macroscopic distortion of the lattice and thus do not create macroscopic strains [104]. Furthermore,

unlike LO phonons, TO phonons don't alter the charge density distribution within the primitive cell and thus do not couple via a Fröhlich type of mechanism, which is based on Coulomb interactions due to net charge displacement [105].

5.2. Electron-phonon interaction

We consider a crystal consisting of N Wigner-Seitz cells and N valence electrons per valence band. We denote by $V_\alpha(\boldsymbol{x}_p - \boldsymbol{R}_{n,\alpha})$ the interaction potential between an electron at position $\boldsymbol{x}_p$ and an ion of type α at position $\boldsymbol{R}_{n,\alpha} = \boldsymbol{X}_n + \boldsymbol{R}_\alpha + \boldsymbol{u}_{n\alpha}$, with $\boldsymbol{X}_n$ a reference point in the nth Wigner-Seitz cell and $\boldsymbol{R}_\alpha$ indicating the equilibrium position of each ion inside the cell, as depicted in Fig.5.7. The semiconductor of our choice is CdTe, thus we consider a basis with two atoms $\alpha = 1, 2$.
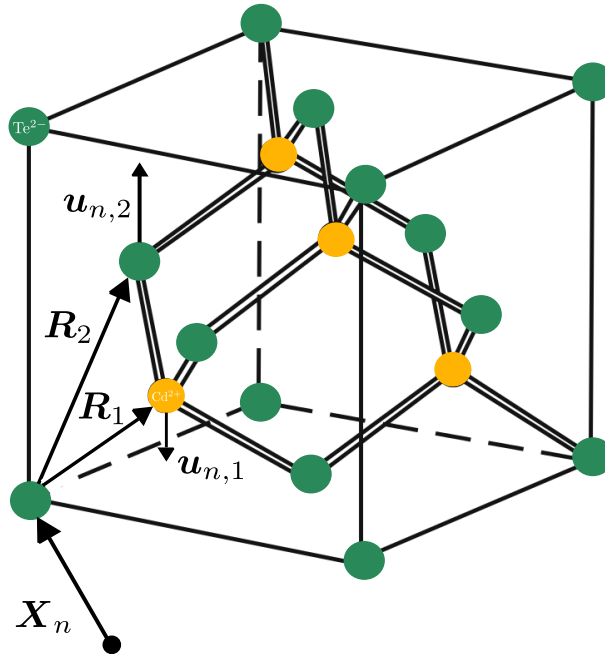
Figure 5.7.: Sketch of one possible unit cell of the crystal structure of CdTe: The zinc-blende structure consists of two face-centered cubic (fcc) lattices that are shifted by one fourth of the diagonal. Every atom is surrounded by four atoms of the other species. They form a tetrahedron which is the primitive cell or Wigner-Seitz cell of the zinc-blende structure. $\boldsymbol{X}_n$ is a reference point in the nth Wigner-Seitz cell. $\boldsymbol{R}_\alpha$ and $\boldsymbol{u}_{n\alpha}$ indicate the equilibrium positions and the displacements of each ion inside the cell. The image is adapted from Ref. [104].

For small ionic displacements $\boldsymbol{u}_{n\alpha}$ from their equilibrium positions, the potential the

electron is feeling can be expanded in powers of the deviation up to first order

$$V_\alpha(\boldsymbol{x}_p - \boldsymbol{R}_{n,\alpha}) = V_\alpha(\boldsymbol{x}_p - \boldsymbol{X}_n - \boldsymbol{R}_\alpha) - \boldsymbol{u}_{n,\alpha} \cdot \boldsymbol{\nabla} V_\alpha(\boldsymbol{x}_p - \boldsymbol{X}_n - \boldsymbol{R}_\alpha). \tag{5.12}$$

The general Hamiltonian of the electron-phonon interaction has the form [105]

$$H_{\text{el−phon}} = -\sum_{n=1}^{N} \sum_{\alpha=1}^{2} \sum_{p=1}^{N} \boldsymbol{u}_{n,\alpha} \cdot \boldsymbol{\nabla} V_\alpha(\boldsymbol{x}_p - \boldsymbol{X}_n - \boldsymbol{R}_\alpha), \tag{5.13}$$

where p denotes the sum over the electron's positions.

We introduce the center-of-mass coordinate $\boldsymbol{C}_n$ and the relative coordinate $\boldsymbol{u}_{\text{rel,n}}$ of one Wigner-Seitz cell [124]

$$\boldsymbol{C}_n = \frac{1}{M_1 + M_2}(M_1 \boldsymbol{u}_{n,1} + M_2 \boldsymbol{u}_{n,2}) \tag{5.14}$$

$$\boldsymbol{u}_{\text{rel},n} = \boldsymbol{u}_{n,1} - \boldsymbol{u}_{n,2}, \tag{5.15}$$

with M_1 and M_2 the masses of the two basis atoms. It follows for the Hamiltonian

$$\begin{aligned} H_{\text{el−phon}} = &-\sum_{n=1}^{N} \sum_{p=1}^{N} \boldsymbol{C}_n \cdot (\boldsymbol{\nabla} V_1(\boldsymbol{x}_p - \boldsymbol{X}_n - \boldsymbol{R}_1) + \boldsymbol{\nabla} V_2(\boldsymbol{x}_p - \boldsymbol{X}_n - \boldsymbol{R}_2)) \\ &-\sum_{n=1}^{N} \sum_{p=1}^{N} \frac{\boldsymbol{u}_{\text{rel},n}}{a} \cdot \boldsymbol{V}_{DP}(\boldsymbol{x}_p - \boldsymbol{X}_n), \end{aligned} \tag{5.16}$$

where we defined the deformation potential [124]

$$\boldsymbol{V}_{DP}(\boldsymbol{x}_p - \boldsymbol{X}_n) = a \left[\frac{M_2}{M_1 + M_2} \boldsymbol{\nabla} V_1(\boldsymbol{x}_p - \boldsymbol{X}_n - \boldsymbol{R}_1) - \frac{M_1}{M_1 + M_2} \boldsymbol{\nabla} V_2(\boldsymbol{x}_p - \boldsymbol{X}_n - \boldsymbol{R}_2) \right] \tag{5.17}$$

and a corresponds to the lattice constant. We want to write the interaction Hamiltonian in second quantization and thus introduce normal modes for the displacement using periodic boundary conditions [105]

$$\boldsymbol{u}_{n\alpha} = \sum_{j=1}^{6} \sum_{\boldsymbol{q}} \left(\frac{\hbar}{2N M_\alpha \omega_{\boldsymbol{q},j}} \right)^{1/2} e^{i\boldsymbol{q} \cdot \boldsymbol{X}_n} \boldsymbol{\epsilon}_{\alpha,j}(\boldsymbol{q}) \left(\hat{b}_{-\boldsymbol{q},j}^\dagger + \hat{b}_{\boldsymbol{q},j} \right), \tag{5.18}$$

with $\hat{b}_{\boldsymbol{q},j}$ and $\hat{b}_{\boldsymbol{q},j}^\dagger$ the bosonic creation and annihilation operators of a phonon in branch j,

with wavevector $\boldsymbol{q}$

$$[\hat{b}_{\boldsymbol{q},i}, \hat{b}^{\dagger}_{-\boldsymbol{q}',j}] = \delta_{i,j}\delta_{\boldsymbol{q},\boldsymbol{q}'}.$$

The phonon frequency is $\omega_{\boldsymbol{q},j}$ and the polarization vector of the phonon is given by $\boldsymbol{\epsilon}_{\alpha,j}(\boldsymbol{q})$, with the normalization

$$\sum_{\alpha=1}^{2}\sum_{m=x,y,z} \epsilon_{\alpha,j}^{*(m)}(\boldsymbol{q})\epsilon_{\alpha,j'}^{(m)}(\boldsymbol{q}) = \delta_{j,j'}. \tag{5.19}$$

For long-wavelength optical phonons the center of mass of the cell is constant and so the corresponding displacement $\boldsymbol{C}_n$ is zero, because

$$\boldsymbol{C}_n \propto \frac{1}{M_1 + M_2}\left(\sqrt{M_1}\boldsymbol{\epsilon}_{1,j} + \sqrt{M_2}\boldsymbol{\epsilon}_{2,j}\right) \tag{5.20}$$

and for optical phonons with small $\boldsymbol{q}$ [129]

$$\sqrt{M_1}\boldsymbol{\epsilon}_{1,\mathrm{O}} = -\sqrt{M_2}\boldsymbol{\epsilon}_{2,\mathrm{O}},$$

as we show in Appendix C. Therefore only the relative displacement of the two sublattices is important [124]. In addition, for optical phonons, we choose the normalization [132]

$$\boldsymbol{\epsilon}_{1,\mathrm{O}} = \boldsymbol{\epsilon}_{\mathrm{O}}\left(\frac{M_2}{M_1 + M_2}\right)^{1/2} \quad \text{and} \quad \boldsymbol{\epsilon}_{2,\mathrm{O}} = -\boldsymbol{\epsilon}_{\mathrm{O}}\left(\frac{M_1}{M_1 + M_2}\right)^{1/2}, \tag{5.21}$$

which leads with Eq.(5.19) to $|\boldsymbol{\epsilon}_{\mathrm{O}}|^2 = 1$. Thus the expression of $\boldsymbol{u}_{\mathrm{rel},n}$ using normal modes can be simplified with the help of $\frac{1}{\sqrt{M_1}}\boldsymbol{\epsilon}_{1,\mathrm{O}} - \frac{1}{\sqrt{M_2}}\boldsymbol{\epsilon}_{2,\mathrm{O}} = \frac{1}{\sqrt{\mu}}\boldsymbol{\epsilon}_{\mathrm{O}}$, with reduced mass $\mu = \frac{M_1 M_2}{M_1 + M_2}$. From now on we will consider only one transverse optical phonon branch and thus the relative displacement reads

$$\boldsymbol{u}_{\mathrm{rel},n} = \sum_{\boldsymbol{q}} \left(\frac{\hbar}{2N\mu\omega_{\boldsymbol{q},TO}}\right)^{1/2} e^{i\boldsymbol{q}\cdot\boldsymbol{X}_n}\boldsymbol{\epsilon}_{TO}(\boldsymbol{q})\left(\hat{b}^{\dagger}_{-\boldsymbol{q},TO} + \hat{b}_{\boldsymbol{q},TO}\right). \tag{5.22}$$

Fig.5.8 shows a sketch of a TO phonon in CdTe. The two ion species oscillate with different phase. The amplitude of the oscillation is perpendicular to the propagation direction.
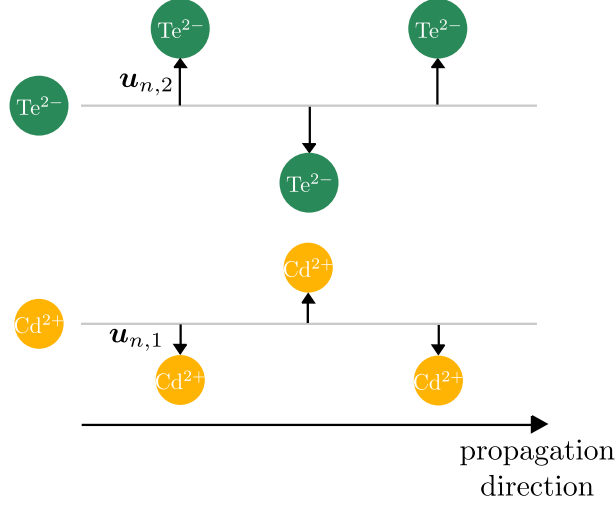
Figure 5.8.: Sketch of a TO phonon in CdTe. The two ion species oscillate with a π phase shift (optical phonon). Furthermore the amplitude of the oscillation is perpendicular to the propagation direction (transverse phonon). The displacement vectors of the two ions in Wigner-Seitz cell n are denoted by $\boldsymbol{u}_{n,1}$ and $\boldsymbol{u}_{n,2}$.

5.3. Exciton-phonon interaction

We now specialize the electron-phonon Hamiltonian to the case of electrons weakly bound to holes to form Wannier excitons. The Hamiltonian of the exciton/TO-phonon interaction is given by [125, 126]

$$
\hat{H}_{\text{exc–TO}} = - \sum_{\substack{\boldsymbol{q},\boldsymbol{K},\boldsymbol{K}' \\ \lambda,\lambda', \\ v,v',c,c'}} G_{\boldsymbol{q},TO}(\lambda \boldsymbol{K} vc, \lambda' \boldsymbol{K}' v'c') \hat{s}^{\dagger}_{\lambda,\boldsymbol{K}}(v,c) \hat{s}_{\lambda',\boldsymbol{K}'}(v',c') \left(\hat{b}^{\dagger}_{-\boldsymbol{q},TO} + \hat{b}_{\boldsymbol{q},TO} \right),
$$

(5.23)

with

$$
G_{\boldsymbol{q},TO}(\lambda \boldsymbol{K} vc, \lambda' \boldsymbol{K}' v'c') = \sum_{n=1}^{N} \left(\frac{\hbar}{2N \mu \omega_{\boldsymbol{q},TO} a^2} \right)^{1/2} e^{i\boldsymbol{q} \cdot \boldsymbol{X}_n} \boldsymbol{\epsilon}_{TO} \cdot \langle \lambda, \boldsymbol{K}, v, c | \, \boldsymbol{V}_{DP} \, | \lambda', \boldsymbol{K}', v', c' \rangle,
$$

(5.24)

where $\hat{s}^{\dagger}_{\boldsymbol{K},\lambda}(c,v)$ [$\hat{s}_{\boldsymbol{K}',\lambda'}(v',c')$] creates [annihilates] an exciton with wavevector $\boldsymbol{K}$ [$\boldsymbol{K}'$] of the center-of-mass motion and inner quantum number λ [λ'], where the electron is in the conduction band c [c'] and the hole in valence band v [v']. In our treatment we

neglect the internal structure of the exciton and assume that an exciton is a boson, thus $[\hat{s}_{\boldsymbol{K}',\lambda'}(v',c'), \hat{s}^\dagger_{\boldsymbol{K},\lambda}(v,c)] = \delta_{\lambda,\lambda'}\delta_{\boldsymbol{K},\boldsymbol{K}'}\delta_{v,v'}\delta_{c,c'}$. In Appendix D we show the derivation of the Hamiltonian (5.23) in detail starting with the second quantization of the deformation potential $\boldsymbol{V}_{DP}$. We recall (see Section 4.1) that in position representation the exciton state $|\lambda', \boldsymbol{K}', v', c'\rangle$ is described by the many-body wavefunction [110]

$$\Psi_{\lambda',\boldsymbol{K}',v',c'}(\boldsymbol{x}_1, \boldsymbol{x}_2, ...\boldsymbol{x}_N) = \frac{1}{\sqrt{N}}\sum_{m',l'} e^{i\boldsymbol{K}'\cdot\boldsymbol{R}^{m',l'}_{\text{com}}} \phi_{\lambda',v',c'}(\boldsymbol{R}_{l'})A_{v',c'}(m', m' + l'), \qquad (5.25)$$

which is a generalization of Eq.(4.9) for several possible valence and conduction bands. $\boldsymbol{R}^{m,l}_{\text{com}}$ is the center of mass of the electron-hole pair and defined in Eq.(4.10). The relative distance between electron and hole is denoted with $\boldsymbol{R}_{l'} = \boldsymbol{R}_{m'+l'} - \boldsymbol{R}_{m'}$. $\phi_{\lambda',v',c'}(\boldsymbol{R}_{l'})$ describes the relative wavefunction of electron and hole, determined solving the hydrogen-like Schrödinger equation for the Coulomb interaction given in Eq.(4.4). $A_{v',c'}(m', m' + l')$ is the Slater determinant introduced in Section 4.1, describing the configuration in which a valence electron at site m' is excited from valence band v' into the conduction band c' at site $m' + l'$. The single-particle wavefunctions in the Slater determinant are given by Wannier functions [62]. For the following, we regroup the terms in the exciton wavefunction that depend on the relative motion and thus we will work with $U_{\lambda',\boldsymbol{K}',v',c'}(\boldsymbol{R}_{l'})$ as defined in Eq.(4.12).

We proceed to evaluate the matrix element $G_{\boldsymbol{q},TO}(\lambda\boldsymbol{K}vc, \lambda'\boldsymbol{K}'v'c')$. The deformation potential is a single-particle operator for the electrons. Using Eq.(5.25), we show in Appendix D that it couples two excitonic states that differ either in their hole or in their electron state, according to

$$\langle\lambda, \boldsymbol{K}, v, c|\boldsymbol{V}_{DP}|\lambda', \boldsymbol{K}', v', c'\rangle$$
$$= \frac{1}{N}\sum_{\substack{m \\ l,l'}} U^*_{v,c,\lambda,\boldsymbol{K}}(\boldsymbol{R}_l)U_{v',c',\lambda',\boldsymbol{K}'}(\boldsymbol{R}_{l'})\times$$
$$\left[-e^{i\boldsymbol{K}'\cdot(\boldsymbol{R}_{m+l}+-\boldsymbol{R}_{l'})}e^{-i\boldsymbol{K}\cdot\boldsymbol{R}_m}\delta_{c,c'}\int_V w^*_{v',\boldsymbol{R}_{m+l-l'}}(\boldsymbol{x})\boldsymbol{V}_{DP}(\boldsymbol{x} - \boldsymbol{X}_n)w_{v,\boldsymbol{R}_m}(\boldsymbol{x})\, d^3x\right.$$
$$\left.+e^{i(\boldsymbol{K}'-\boldsymbol{K})\cdot\boldsymbol{R}_m}\delta_{v,v'}\int_V w^*_{c,\boldsymbol{R}_{m+l}}(\boldsymbol{x})\boldsymbol{V}_{DP}(\boldsymbol{x} - \boldsymbol{X}_n)w_{c',\boldsymbol{R}_{m+l'}}(\boldsymbol{x})\, d^3x\right], \qquad (5.26)$$

with V being the volume of the crystal. We transform the Wannier functions into Bloch

functions [62]

$$w_{c,\boldsymbol{R}_m}(\boldsymbol{x}) = \frac{1}{\sqrt{N}} \sum_{\boldsymbol{k}} \psi_{c,\boldsymbol{k}}(\boldsymbol{x}) e^{-i\boldsymbol{k}\cdot\boldsymbol{R}_m}, \tag{5.27}$$

which corresponds to the three dimensional version of Eq.(1.13). The Bloch's functions are normalized as $\int_V \psi^*_{c',\boldsymbol{k}'}(\boldsymbol{x})\psi_{c,\boldsymbol{k}}(\boldsymbol{x})\, d^3x = \delta_{c,c'}\delta_{\boldsymbol{k},\boldsymbol{k}'}$. We perform the sum over the hole position m which leads to

$$\langle \lambda, \boldsymbol{K}, v, c | \, \boldsymbol{V}_{DP} \, | \lambda', \boldsymbol{K}', v', c' \rangle$$
$$= \frac{1}{N} \sum_{l,l',\boldsymbol{k}} U^*_{v,c,\lambda,\boldsymbol{K}}(\boldsymbol{R}_l) U_{v',c',\lambda',\boldsymbol{K}'}(\boldsymbol{R}_{l'}) \times$$
$$\left[-e^{i(\boldsymbol{k}+\boldsymbol{K})\cdot(\boldsymbol{R}_l-\boldsymbol{R}_{l'})} \delta_{c,c'} \int_V \psi^*_{v',\boldsymbol{k}+\boldsymbol{K}-\boldsymbol{K}'}(\boldsymbol{x}) \boldsymbol{V}_{DP}(\boldsymbol{x}-\boldsymbol{X}_n)\psi_{v,\boldsymbol{k}}(\boldsymbol{x})\, d^3x \right.$$
$$\left. +e^{i\boldsymbol{k}\cdot(\boldsymbol{R}_l-\boldsymbol{R}_{l'})} e^{i(\boldsymbol{K}-\boldsymbol{K}')\cdot\boldsymbol{R}_l} \delta_{v,v'} \int_V \psi^*_{c,\boldsymbol{k}+\boldsymbol{K}-\boldsymbol{K}'}(\boldsymbol{x}) \boldsymbol{V}_{DP}(\boldsymbol{x}-\boldsymbol{X}_n)\psi_{c',\boldsymbol{k}}(\boldsymbol{x})\, d^3x \right].$$

We now substitute $\boldsymbol{x}' = \boldsymbol{x} - \boldsymbol{X}_n$ and use the definition of the Bloch functions

$$\psi_{v,\boldsymbol{k}}(\boldsymbol{x}) = \frac{e^{i\boldsymbol{x}\cdot\boldsymbol{k}}}{\sqrt{V}} u_{v,\boldsymbol{k}}(\boldsymbol{x}), \tag{5.28}$$

where $u_{v,\boldsymbol{k}}(\boldsymbol{x})$ is a periodic, dimensionless function with the periodicity of the lattice $u_{v,\boldsymbol{k}}(\boldsymbol{x}+\boldsymbol{X}_n) = u_{v,\boldsymbol{k}}(\boldsymbol{x})$, whose symmetries depend on the symmetry group of the crystal and of the point in the Brillouin zone $\boldsymbol{k}$. The normalization of the lattice periodic function has the form

$$\int_{\Omega_0} u^*_{c',\boldsymbol{k}}(\boldsymbol{x}) u_{c,\boldsymbol{k}}(\boldsymbol{x})\, d^3x = \Omega_0 \delta_{c,c'}, \tag{5.29}$$

where Ω_0 denotes the volume of the primitive cell and $V = N\Omega_0$.

The sum over the ionic position n in Eq.(5.24) can then be explicitly performed, recalling that $\sum_{n=1}^{N} e^{i\boldsymbol{X}_n\cdot(\boldsymbol{k}+\boldsymbol{q}-\boldsymbol{k}-\boldsymbol{K}+\boldsymbol{K}')} = N \cdot \delta_{\boldsymbol{q}+\boldsymbol{K}_{\text{rec}},\boldsymbol{K}-\boldsymbol{K}'}$ where $\boldsymbol{K}_{\text{rec}}$ is a vector of the reciprocal

lattice. We only consider normal processes [105, 124] with $\boldsymbol{K}_{\text{rec}} = 0$. It follows

$$
\hat{H}_{\text{exc−TO}} = -\sum_{\substack{\boldsymbol{q},\boldsymbol{k}, \\ \boldsymbol{K},\boldsymbol{K}'}} \sum_{\substack{l,l',\lambda,\lambda', \\ v,v',c,c'}} \left(\frac{\hbar}{2N\mu\omega_{\boldsymbol{q},TO}a^2}\right)^{1/2} U^*_{v,c,\lambda,\boldsymbol{K}}(\boldsymbol{R}_l)U_{v',c',\lambda',\boldsymbol{K}'}(\boldsymbol{R}_{l'})\boldsymbol{\epsilon}_{TO} \cdot
$$

$$
\left[-e^{i(\boldsymbol{K}+\boldsymbol{k})\cdot(\boldsymbol{R}_l-\boldsymbol{R}_{l'})}\delta_{c,c'}\boldsymbol{\Theta}_{v',v}(\boldsymbol{k}+\boldsymbol{K}-\boldsymbol{K}',\boldsymbol{k})\right.
$$

$$
\left.+e^{i\boldsymbol{k}\cdot(\boldsymbol{R}_l-\boldsymbol{R}_{l'})}e^{i(\boldsymbol{K}-\boldsymbol{K}')\cdot\boldsymbol{R}_l}\delta_{v,v'}\boldsymbol{\Theta}_{c,c'}(\boldsymbol{k}+\boldsymbol{K}-\boldsymbol{K}',\boldsymbol{k})\right] \times
$$

$$
\hat{s}^\dagger_{\lambda,\boldsymbol{K}}(v,c)\hat{s}_{\lambda',\boldsymbol{K}'}(v',c') \left(\hat{b}^\dagger_{-\boldsymbol{q},TO} + \hat{b}_{\boldsymbol{q},TO}\right) \delta_{\boldsymbol{q},\boldsymbol{K}-\boldsymbol{K}'}, \tag{5.30}
$$

with

$$
\boldsymbol{\Theta}_{n',n}(\boldsymbol{k}+\boldsymbol{K}-\boldsymbol{K}',\boldsymbol{k}) = \int_V \psi^*_{n',\boldsymbol{k}+\boldsymbol{K}-\boldsymbol{K}'}(\boldsymbol{x}')\boldsymbol{V}_{DP}(\boldsymbol{x}')\,\psi_{n,\boldsymbol{k}}(\boldsymbol{x}')\,d^3x'. \tag{5.31}
$$

Since the integrals in Eq.(5.31) only depend on the difference between the wavevectors of the two involved Bloch functions [110], i.e. $\boldsymbol{\Theta}_{n',n}(\boldsymbol{k}+\boldsymbol{K}-\boldsymbol{K}',\boldsymbol{k}) = \boldsymbol{\Theta}_{n',n}(\boldsymbol{K}-\boldsymbol{K}')$, we can sum over $\boldsymbol{k}$ yielding

$$
\hat{H}_{\text{exc−TO}} = -\sum_{\substack{\boldsymbol{q},\boldsymbol{K},\boldsymbol{K}' \\ \lambda,\lambda', \\ v,v',c,c'}} G_{\boldsymbol{q},TO}(\lambda\boldsymbol{K}vc,\lambda'\boldsymbol{K}'v'c')\hat{s}^\dagger_{\lambda,\boldsymbol{K}}(v,c)\hat{s}_{\lambda',\boldsymbol{K}'}(v',c') \left(\hat{b}^\dagger_{-\boldsymbol{q},TO} + \hat{b}_{\boldsymbol{q},TO}\right),
$$

$$
\tag{5.32}
$$

with

$$
G_{\boldsymbol{q},TO}(\lambda\boldsymbol{K}vc,\lambda'\boldsymbol{K}'v'c') = \left(\frac{\hbar N}{2\mu\omega_{\boldsymbol{q},TO}a^2}\right)^{1/2}\boldsymbol{\epsilon}_{TO}\cdot\left[-q_h(\lambda\boldsymbol{K}cv,\lambda'\boldsymbol{K}'v'c)\,\boldsymbol{\Theta}_{v',v}(\boldsymbol{K}-\boldsymbol{K}')\delta_{c,c'}\right.
$$

$$
\left.+q_e(\lambda\boldsymbol{K}cv,\lambda'\boldsymbol{K}'v'c)\,\boldsymbol{\Theta}_{c,c'}(\boldsymbol{K}-\boldsymbol{K}')\delta_{v,v'}\right]\delta_{\boldsymbol{q},\boldsymbol{K}-\boldsymbol{K}'}. \tag{5.33}
$$

Here, using Eq.(4.12), we have set [110]

$$
q_e(\lambda\boldsymbol{K}cv,\lambda'\boldsymbol{K}'v'c) = \sum_l e^{i\frac{m_{\text{h}}}{m_{\text{e}}+m_{\text{h}}}\boldsymbol{R}_l\cdot(\boldsymbol{K}-\boldsymbol{K}')}\phi^*_{\lambda,v,c}(\boldsymbol{R}_l)\phi_{\lambda',v,c'}(\boldsymbol{R}_l),
$$

$$
q_h(\lambda\boldsymbol{K}cv,\lambda'\boldsymbol{K}'v'c) = \sum_l e^{-i\frac{m_{\text{e}}}{m_{\text{e}}+m_{\text{h}}}\boldsymbol{R}_l\cdot(\boldsymbol{K}-\boldsymbol{K}')}\phi^*_{\lambda,v,c}(\boldsymbol{R}_l)\phi_{\lambda',v',c}(\boldsymbol{R}_l). \tag{5.34}
$$

In order to obtain an estimate for the coupling constant $\hbar g_{xb}$, for long-wavelength optical phonons we can evaluate the coupling constant $G_{\boldsymbol{q},TO}(\lambda\boldsymbol{K}vc,\lambda'\boldsymbol{K}'v'c')$ setting

$\boldsymbol{q} = \boldsymbol{K} - \boldsymbol{K}' \simeq 0$. This leads us to evaluate

$$\boldsymbol{\Theta}_{n,n'}(0) = \frac{1}{V} \int_V u_{n,0}^*(\boldsymbol{x}') \boldsymbol{V}_{DP}(\boldsymbol{x}') \, u_{n',0}(\boldsymbol{x}') \, d^3x' \equiv \langle n | \, \boldsymbol{V}_{DP} \, | n' \rangle \,. \qquad (5.35)$$

5.4. Symmetry properties of the deformation potential matrix elements

In order to estimate the matrix elements $\langle v' | \, \boldsymbol{V}_{DP} \, | v \rangle$ and $\langle c | \, \boldsymbol{V}_{DP} \, | c' \rangle$ we perform some symmetry considerations. We introduced the band structure of CdTe in subsection 5.1.2. We only consider the lowest energy conduction band and recall that, without spin, this conduction band is non-degenerate and has Γ_1 symmetry, i.e., in terms of atomic orbitals, it is s-like. The highest energy valence band is doubly degenerate at the Γ point, splitting into light- and heavy-hole bands, and it transforms under symmetry operations of the crystal according to Γ_4 symmetry, i.e. p-like. We will neglect in our analysis the split-off band since it is energetically far ($\approx 0.92 \, \text{eV}$ [104]) from the heavy- and light-hole doublet. The deformation potential $\boldsymbol{V}_{DP}$ transforms like a vector, i.e. it belongs also to the Γ_4 irreducible representation [104, 133]. Note that, in general, the symmetry of the phonon determines the symmetry of the deformation potential operator $\boldsymbol{V}_{DP}$ [134], because the Hamiltonian, which is the product between lattice displacement and deformation potential, must be a scalar function.

From the matrix element theorem, that we introduced in subsection 5.1.1, it follows that

$$\langle c | \, \boldsymbol{V}_{DP} \, | c' \rangle = 0,$$

and thus only the holes are interacting with long wavelength optical phonons via the deformation potential interaction. Intuitively this can be seen as the operator $\boldsymbol{V}_{DP}$ does not couple two states of the same parity.

We show in Appendix E that, at $\boldsymbol{K} - \boldsymbol{K}' = 0$, the expression of the matrix elements $\langle v' | \, \boldsymbol{V}_{DP} \, | v \rangle$ in the Bloch and Luttinger-Kohn basis [124, 135] coincide. In analogy with the literature [124, 132], we choose to work in the Luttinger-Kohn basis [135]. This basis is more convenient because it is the eigenbasis of the total pseudo-angular momentum J that we introduced in subsection 5.1.2. The eigenfunctions describing the different possible

valence band states read

$$\left|J_{\text{hole}}, m_{J,\text{hole}}\right\rangle = \left|\frac{3}{2}, +\frac{3}{2}\right\rangle \equiv \left|\frac{1}{\sqrt{2}}(X + iY)\uparrow\right\rangle \equiv \left|hh^+\right\rangle$$

$$\left|\frac{3}{2}, +\frac{1}{2}\right\rangle \equiv \left|\frac{i}{\sqrt{6}}(X + iY)\downarrow - \sqrt{\frac{2}{3}}iZ\uparrow\right\rangle \equiv \left|lh^+\right\rangle$$

$$\left|\frac{3}{2}, -\frac{1}{2}\right\rangle \equiv \left|\frac{1}{\sqrt{6}}(X - iY)\uparrow + \sqrt{\frac{2}{3}}Z\downarrow\right\rangle \equiv \left|lh^-\right\rangle$$

$$\left|\frac{3}{2}, -\frac{3}{2}\right\rangle \equiv \left|\frac{i}{\sqrt{2}}(X - iY)\downarrow\right\rangle \equiv \left|hh^-\right\rangle. \tag{5.36}$$

Even if only holes interact with TO phonons via the deformation potential, we need to keep in mind the state of the electron. The eigenstates of an electron in the s-like conduction band are given by

$$\left|J_{\text{electron}}, m_{J,\text{electron}}\right\rangle = \left|\frac{1}{2}, \frac{1}{2}\right\rangle \equiv \left|S\uparrow\right\rangle$$

$$\left|\frac{1}{2}, -\frac{1}{2}\right\rangle \equiv \left|S\downarrow\right\rangle. \tag{5.37}$$

Here we introduced $J_{\text{hole/electron}}$ and $m_{J,\text{hole/electron}}$, that denote the eigenvalues of the total pseudo-angular momentum of the hole/electron and its projection to the quantization axis.

The coordinate representations of the states $\left|S\right\rangle, \left|X\right\rangle, \left|Y\right\rangle, \left|Z\right\rangle$ correspond to the Bloch functions, as defined in Eq.(5.28), for $\boldsymbol{k} = 0$ [124, 127]. The coordinate representations of the states $\left|S\right\rangle, \left|X\right\rangle, \left|Y\right\rangle, \left|Z\right\rangle$ are related to cubic harmonics [127] in a similar way as x, y, z are related to spherical harmonics[6]. Cubic harmonics are symmetry-adapted linear combinations of spherical harmonics [106] and take into account the fact that the crystal potential is not spherically symmetric.

We only consider excitons which can couple to light, i.e. excitons where

$$m_{J,\text{hole}} + m_{J,\text{electron}} = \pm 1.$$

This corresponds to the states $\left|hh^+\right\rangle\left|S\downarrow\right\rangle, \left|lh^+\right\rangle\left|S\uparrow\right\rangle, \left|lh^-\right\rangle\left|S\downarrow\right\rangle, \left|hh-\right\rangle\left|S\uparrow\right\rangle$.

We detail exemplarily the calculation of the matrix element of the deformation potential

---

[6]For example $Y_{l=1,m=1} = \frac{x+iy}{\sqrt{2}}$.

between hh^+ and lh^- state

$$\sum_{m=x,y,z} \epsilon_{TO}^{(m)} \langle S \downarrow| \langle hh^+| V_{DP}^{(m)} |lh^- \rangle |S \downarrow\rangle$$

$$= \sum_{m=x,y,z} \epsilon_{TO}^{(m)} \left\langle \frac{1}{\sqrt{2}}(X - iY) \uparrow \middle| V_{DP}^{(m)} \middle| \frac{1}{\sqrt{6}}(X - iY) \uparrow + \sqrt{\frac{2}{3}} Z \downarrow \right\rangle$$

$$= \frac{-i}{\sqrt{12}} \epsilon_{TO}^{(z)} \left(\langle X| V_{DP}^{(z)} |Y\rangle + \langle Y| V_{DP}^{(z)} |X\rangle \right)$$

$$= -i \frac{d_0}{2N} \epsilon_{TO}^{(z)} \equiv j^*, \tag{5.38}$$

where we have set $\langle X| V_{DP}^{(z)} |Y\rangle = \langle Y| V_{DP}^{(z)} |X\rangle = d_0/N\sqrt{3}/2$, with d_0 the deformation potential constant used in Ref. [124]. The factor $1/N$ follows from the fact that the deformation potential constant is defined as the average of the deformation potential over all Wigner-Seitz cells of the crystal.

The matrix element $\langle X| V_{DP}^{(z)} |Y\rangle$ would vanish for pure $p-$wave spherical harmonics. However, in the case of zinc-blende crystals, the cubic harmonics made with $|X\rangle, |Y\rangle, |Z\rangle$ are a superposition of spherical harmonics of p-type and of d- type[7] [136]. In coordinate representation they can be written as

$$\langle \boldsymbol{x} |X\rangle \sim x + \epsilon yz \qquad \langle \boldsymbol{x} |Y\rangle \sim y + \epsilon zx \qquad \langle \boldsymbol{x} |Z\rangle \sim z + \epsilon xy. \tag{5.39}$$

This leads to nonvanishing values for the matrix element $\langle X| V_{DP}^{(z)} |Y\rangle$, because $\langle X| V_{DP}^{(z)} |Y\rangle \sim \int (\epsilon yz + x) z (\epsilon zx + y) \sim \int \epsilon x^2 z^2 + \epsilon y^2 z^2 \neq 0$. Intuitively the ϵ takes into account that in the T_d crystal structure, one ion is pulling stronger on the electronic orbitals and thus deforms them stronger than the other ion. This is also the reason for the noncentrosymmetry.

Note that the matrix elements of type $\langle X| V_{DP}^{(z)} |Y\rangle$ are even nonzero in the case of the centrosymmetric diamond structure (O_h symmetry group), but the reasoning is different [124, 133]: In the case of the diamond lattice, the optical phonon transforms at the point Γ as a pseudovector (symmetry $\Gamma_{25'}$). The valence band has symmetry $\Gamma_{25'}$ as well, thus the matrix element reads $\langle X| V_{DP}^{(z)} |Y\rangle \sim \int yz \times xy \times xz \neq 0$.

Let's come back to CdTe: we want to summarize the results for the calculation of the matrix element of the deformation potential operator between two valence band states, taking into account, that the electron's state has to stay unchanged during the hole-phonon

---

[7]This can be shown be decomposing the irreducible representations of the rotation-inversion group $O(3)$ into the irreducible representations of group T_d, as shown in Ref. [106] for O_h.

interaction, as can be seen in Eq.(5.33). The nonvanishing matrix elements are shown in table 5.2, where $j = i\frac{d_0}{2N}\epsilon_{TO}^{(z)}$ [124, 132]. The table shows that the deformation potential

$\sum_{m=x,y,z} \epsilon_{TO}^{(m)} \langle v'| V_{DP}^{(m)} |v\rangle \delta_{c,c'}$	$|hh^-\rangle |S\uparrow\rangle$	$|lh^-\rangle |S\downarrow\rangle$	$|lh^+\rangle |S\uparrow\rangle$	$|hh^+\rangle |S\downarrow\rangle$
$\langle S\uparrow| \langle hh^-|$	0	0	j	0
$\langle S\downarrow| \langle lh^-|$	0	0	0	j
$\langle S\uparrow| \langle lh^+|$	j^*	0	0	0
$\langle S\downarrow| \langle hh^+|$	0	j^*	0	0

,

Table 5.2.: Matrix elements of the deformation potential between two valence band states, taking into account that the electron's state has to stay the same.

interaction leads to a coupling of light- and heavy-hole states. Hence, it is important to work with a bulk semiconductor instead of quantum wells, usually used in semiconductor microcavities in the strong coupling regime, since in a bulk semiconductor light- and heavy-hole bands are degenerate. Secondly, we notice, that due to its vector symmetry, the deformation potential couples states with different total pseudo-angular momentum. Finally, we see that just one deformation potential constant j is needed to describe all nonvanishing matrix elements, as follows from the Luttinger-Kohn basis functions, defined in Eq.(5.36), together with time-reversal symmetry of the deformation potential operator (see Appendix F for more details).

5.5. Exciton-phonon interaction for zinc-blende crystals

In order to obtain the final expression for the exciton-phonon interaction, we specialize Eq.(5.32) to the case of the $1s$ exciton, i.e. we set $\lambda = \lambda' = 1s$ and omit the conduction band indices, since we have shown that only hole-state matrix elements contribute to the exciton-phonon interaction. Writing explicitly the creation and annihilation operators for excitons with heavy-hole $|hh^{\pm}\rangle$ or light-hole $|lh^{\pm}\rangle$ states, the final exciton-phonon interaction reads

$$
\begin{aligned}
\hat{H}_{\text{exc}-\text{TO}} = -\sum_{\boldsymbol{q},\boldsymbol{K},\boldsymbol{K}'} & \left(\hat{b}^{\dagger}_{-\boldsymbol{q},TO} + \hat{b}_{\boldsymbol{q},TO}\right) \left(G_{\boldsymbol{q},TO}(\boldsymbol{K}hh^-, \boldsymbol{K}'lh^+)\hat{s}^{\dagger}_{\boldsymbol{K}}(hh^-)\hat{s}_{\boldsymbol{K}'}(lh^+)\right. \\
& +G_{\boldsymbol{q},TO}(\boldsymbol{K}lh^+, \boldsymbol{K}'hh^-)\hat{s}^{\dagger}_{\boldsymbol{K}}(lh^+)\hat{s}_{\boldsymbol{K}'}(hh^-) \\
& +G_{\boldsymbol{q},TO}(\boldsymbol{K}lh^-, \boldsymbol{K}'hh^+)\hat{s}^{\dagger}_{\boldsymbol{K}}(lh^-)\hat{s}_{\boldsymbol{K}'}(hh^+) \\
& \left.+G_{\boldsymbol{q},TO}(\boldsymbol{K}hh^+, \boldsymbol{K}'lh^-)\hat{s}^{\dagger}_{\boldsymbol{K}}(hh^+)\hat{s}_{\boldsymbol{K}'}(lh^-)\right),
\end{aligned}
\tag{5.40}
$$

with

$$
\begin{aligned}
G_{\boldsymbol{q},TO}(\boldsymbol{K}hh^-, \boldsymbol{K}'lh^+) &= -q_h(\boldsymbol{K}hh^-, \boldsymbol{K}'lh^+)\sqrt{\frac{N\hbar}{2\mu\omega_{\boldsymbol{q},TO}a^2}}\left\langle lh^+\right|V^{(z)}_{DP}\left|hh^-\right\rangle \\
G_{\boldsymbol{q},TO}(\boldsymbol{K}lh^+, \boldsymbol{K}'hh^-) &= G^*_{\boldsymbol{q},TO}(\boldsymbol{K}hh^-, \boldsymbol{K}'lh^+) \\
G_{\boldsymbol{q},TO}(\boldsymbol{K}lh^-, \boldsymbol{K}'hh^+) &= -q_h(\boldsymbol{K}lh^-, \boldsymbol{K}'hh^+)\sqrt{\frac{N\hbar}{2\mu\omega_{\boldsymbol{q},TO}a^2}}\left\langle hh^+\right|V^{(z)}_{DP}\left|lh^-\right\rangle \\
G_{\boldsymbol{q},TO}(\boldsymbol{K}hh^+, \boldsymbol{K}'lh^-) &= G^*_{\boldsymbol{q},TO}(\boldsymbol{K}lh^-, \boldsymbol{K}'hh^+).
\end{aligned}
\tag{5.41}
$$

Finally, we estimate the value of $q_h(\boldsymbol{K}hh, \boldsymbol{K}'lh)$. For long-wavelength phonon states we assume $\boldsymbol{K} - \boldsymbol{K}' \simeq 0$. Taking the continuum limit of Eq.(5.34) we have

$$
q_h(\boldsymbol{K}hh, \boldsymbol{K}'lh) = \int \phi^*_{1s,hh,c}(\boldsymbol{R})\phi_{1s,lh,c}(\boldsymbol{R})d^3R.
\tag{5.42}
$$

Note that this overlap integral is independent of the angular momentum of the hole since it is only determined by the exciton's relative wavefunction. We use the two $1s$ energy

eigenstates of the hydrogen atom in spherical coordinates

$$\phi_{1s,hh,c}(r) = \frac{1}{\sqrt{\pi(a^*_{B,hh})^3}}e^{-r/a^*_{B,hh}} \qquad \phi_{1s,lh,c}(r) = \frac{1}{\sqrt{\pi(a^*_{B,lh})^3}}e^{-r/a^*_{B,lh}}. \qquad (5.43)$$

The exciton's Bohr radius is given by Eq.(4.6), where in the case of an exciton build by a heavy (light) hole the reduced mass is given by $\mu_{hh} = \frac{m_e m_{hh}}{m_e + m_{hh}}$ ($\mu_{lh} = \frac{m_e m_{lh}}{m_e + m_{lh}}$). Here m_e, m_{hh}, m_{lh} correspond to the effective masses of electron, heavy and light hole respectively. For bulk CdTe we use [137]

$$m_{lh} = 0.051 m_{e,0}$$
$$m_e = 0.047 m_{e,0}$$
$$m_{hh} = 0.879 m_{e,0},$$

with $m_{e,0}$ the mass of the free electron, and we obtain $q_h(\boldsymbol{K}hh, \boldsymbol{K}'lh) \approx 0.9$.

5.6. Bright excitons in strong coupling with cavity photons

For our purpose, we consider only bright exciton states, as only them contribute to the exciton-polariton state. Thus next we want to identify the bright exciton states and transform the Hamiltonian in Eq. (5.40) in the corresponding basis.

Let us first consider upper and lower exciton-polariton states of identical polarization. We show in Appendix G that this assumption leads to a vanishing exciton-phonon interaction in the bright exciton basis. The reason is that the corresponding bright exciton contains the excitons formed by hh^+, lh^+, lh^- and hh^- to equal parts. Thus all the terms in Eq.(5.40) add up with the same weight and, using the results in table 5.2, this yields a vanishing bright-exciton-TO-phonon interaction. To overcome this problem we need a coupling between the excitons and the cavity photons which is sensitive to the total pseudo-angular momentum of the hole. In essence, it should couple differently to hh^- than to hh^+. For this purpose, in order to get a nonvanishing coupling, we consider the polarization degree of freedom of the cavity mode. Note that the Luttinger-Kohn states, as defined in Eq.(5.36), can be mapped onto effective circular polarization states. It is practical to work in a linear

(horizontal/vertical) basis for both cavity photons and excitons, defined as

$$|\mathrm{v}\rangle = -i\frac{|+\rangle - |\text{-}\rangle}{\sqrt{2}},$$
$$|\mathrm{h}\rangle = \frac{|+\rangle + |\text{-}\rangle}{\sqrt{2}}. \tag{5.44}$$

In the basis $\{|cav,\mathrm{v}\rangle, |lh,\mathrm{v}\rangle, |hh,\mathrm{v}\rangle, |cav,\mathrm{h}\rangle, |lh,\mathrm{h}\rangle, |hh,\mathrm{h}\rangle\}$ the effective Hamiltonian which describes the exciton-photon coupled system is given by

$$H_1 = \begin{pmatrix} E_c^{\mathrm{v}} & V_l & V_h & 0 & 0 & 0 \\ V_l & E_{lh}^{\mathrm{v}} & 0 & 0 & 0 & 0 \\ V_h & 0 & E_{hh}^{\mathrm{v}} & 0 & 0 & 0 \\ 0 & 0 & 0 & E_c^{\mathrm{h}} & V_l & V_h \\ 0 & 0 & 0 & V_l & E_{lh}^{\mathrm{h}} & 0 \\ 0 & 0 & 0 & V_h & 0 & E_{hh}^{\mathrm{h}} \end{pmatrix}. \tag{5.45}$$

$E_c^{\mathrm{v,h}}$ is the cavity mode energy and in the following we assume that it is independent of the polarization $E_c^{\mathrm{h}} = E_c^{\mathrm{v}}$, i.e. we neglect the TE-TM splitting. $V_l = V_h = V$ is the photon-exciton coupling, which we assume the same for heavy-hole and light-hole excitons, and $E_{lh}^{\mathrm{h}} = E_{lh}^{\mathrm{v}} = E_{hh}^{\mathrm{h}} = E_{hh}^{\mathrm{v}} = E_x$ are the energies of light-hole and heavy-hole excitons at the Γ point of the band structure. The Hamiltonian H_1 is an extension of the coupled harmonic oscillator model for exciton-polaritons [112, 113]. Here we consider the coupling between three harmonic oscillators (cavity mode, light-hole exciton and heavy-hole exciton) with an additional degree of freedom which is the polarization. Note that a semiclassical model of the coupling between the cavity and different excitonic levels was used e.g. in Ref. [138].

Diagonalization of H_1 yields a two-fold degenerate eigenvalue corresponding to two dark states, $|D,\mathrm{v}\rangle$ and $|D,\mathrm{h}\rangle$, with energy E_x and the degenerate upper and lower, horizontal and vertical exciton-polariton states $|UXP,\alpha\rangle$ and $|LXP,\alpha\rangle$ with eigenenergy $\hbar\omega_{UXP;LXP} = \frac{1}{2}\left(E_c + E_x \pm \sqrt{8V^2 + \hbar^2\delta^2}\right)$, where α stands for "h" or "v" and where we introduced $\delta = E_c - E_x$. In the strong-coupling regime upper and lower exciton-polariton branches are composed by a cavity photon $|cav,\alpha\rangle$ and a bright exciton $|B,\alpha\rangle$. The Hopfield transformation linking the cavity and exciton to the exciton-polariton basis is given by Eq.(4.25). The diagonalization of Hamiltonian Eq.(5.45) together with the transformation defined by Eq.(4.25) allow to establish the transformation matrix between the basis of light- and heavy-hole excitons in linear polarization

basis $\{|cav,\mathrm{v}\rangle, |lh,\mathrm{v}\rangle, |hh,\mathrm{v}\rangle, |cav,\mathrm{h}\rangle, |lh,\mathrm{h}\rangle, |hh,\mathrm{h}\rangle\}$ and the basis of dark and bright excitons $\{|D,\mathrm{v}\rangle, |cav,\mathrm{v}\rangle, |B,\mathrm{v}\rangle, |D,\mathrm{h}\rangle, |cav,\mathrm{h}\rangle, |B,\mathrm{h}\rangle\}$, where the Hamiltonian reads

$$
H_2 = \begin{pmatrix}
E_x & 0 & 0 & 0 & 0 & 0 \\
0 & E_c^{\mathrm{v}} & \hbar\Omega & 0 & 0 & 0 \\
0 & \hbar\Omega & E_x & 0 & 0 & 0 \\
0 & 0 & 0 & E_x & 0 & 0 \\
0 & 0 & 0 & 0 & E_c^{\mathrm{h}} & \hbar\Omega \\
0 & 0 & 0 & 0 & \hbar\Omega & E_x
\end{pmatrix},
\tag{5.46}
$$

and we have set $\hbar\Omega \equiv \sqrt{2}V$. The matrix yielding the basis transformation has the form

$$
\begin{pmatrix}
|cav,\mathrm{v}\rangle \\
|lh,\mathrm{v}\rangle \\
|hh,\mathrm{v}\rangle \\
|cav,\mathrm{h}\rangle \\
|lh,\mathrm{h}\rangle \\
|hh,\mathrm{h}\rangle
\end{pmatrix}
=
\begin{pmatrix}
0 & 1 & 0 & 0 & 0 & 0 \\
-1/\sqrt{2} & 0 & 1/\sqrt{2} & 0 & 0 & 0 \\
1/\sqrt{2} & 0 & 1/\sqrt{2} & 0 & 0 & 0 \\
0 & 0 & 0 & 0 & 1 & 0 \\
0 & 0 & 0 & -1/\sqrt{2} & 0 & 1/\sqrt{2} \\
0 & 0 & 0 & 1/\sqrt{2} & 0 & 1/\sqrt{2}
\end{pmatrix}
\begin{pmatrix}
|D,\mathrm{v}\rangle \\
|cav,\mathrm{v}\rangle \\
|B,\mathrm{v}\rangle \\
|D,\mathrm{h}\rangle \\
|cav,\mathrm{h}\rangle \\
|B,\mathrm{h}\rangle
\end{pmatrix}.
\tag{5.47}
$$

Using Eq.(5.47) and the transformation between linear and circular basis as defined in Eq.(5.44) we readily obtain the bright-exciton projection to the heavy-hole and light-hole states

$$
\left|lh^{\pm}\right\rangle_{bright} = \frac{1}{2}|B,\mathrm{h}\rangle \pm \frac{i}{2}|B,\mathrm{v}\rangle \qquad \left|hh^{\pm}\right\rangle_{bright} = \frac{1}{2}|B,\mathrm{h}\rangle \pm \frac{i}{2}|B,\mathrm{v}\rangle.
\tag{5.48}
$$

Notice that thanks to the use of two polarizations, the $|hh^{\pm}\rangle$ states (and similarly the $|lh^{\pm}\rangle$ states) differ one to the other in their projection to the bright-exciton subspace, thereby yielding the sought mechanism for a nonzero bright-exciton-TO-phonon coupling. Inserting Eq.(5.48) in Eq.(5.40) yields the bright-exciton/TO-phonon coupling Hamiltonian

$$
\hat{H}_{\mathrm{br-exc-TO}} = -\sum_{\boldsymbol{q},\boldsymbol{K},\boldsymbol{K'}} \epsilon_{TO}^{(z)} \hbar g_{xb} \left(\hat{b}_{-\boldsymbol{q},TO}^{\dagger} + \hat{b}_{\boldsymbol{q},TO}\right) \delta_{\boldsymbol{q},\boldsymbol{K}-\boldsymbol{K'}}
$$
$$
\left(\hat{c}_{\boldsymbol{K},\mathrm{v}}^{\dagger}\hat{c}_{\boldsymbol{K'},\mathrm{h}} + \hat{c}_{\boldsymbol{K},\mathrm{h}}^{\dagger}\hat{c}_{\boldsymbol{K'},\mathrm{v}}\right),
\tag{5.49}
$$

where we defined $\hat{c}_{\boldsymbol{K},\alpha}^{\dagger}\hat{c}_{\boldsymbol{K'},\alpha'} = |B,\alpha\rangle\langle B,\alpha'|$, with $\alpha,\alpha' = \mathrm{v,h}$ indicating respectively

vertical or horizontal polarization. The coupling strength is given by

$$\hbar g_{xb} = q_h \sqrt{\frac{\hbar}{2N\mu\omega_{TO}a^2}} \frac{d_0}{2} = q_h \sqrt{\frac{\hbar a}{8V\mu\omega_{TO}}} \frac{d_0}{2},$$
(5.50)

where we used that the number of Wigner-Seitz cells $N = \frac{V}{V_{\text{WS}}}$, with V the total volume of the semiconductor slab and $V_{\text{WS}} = a^3/4$ the volume of the Wigner-Seitz cell. Furthermore we consider a deformation potential constant of $d_0 = 30$ eV for CdTe [139], the lattice constant $a = 6.48$Å and a reduced mass of the two ions of the elementary cell of 10^{-25} kg ($M_{\text{Cd}} = 112$ u, $M_{\text{Te}} = 127$ u). Thus for a CdTe slab of size $V = 18\,\mu\text{m}^3$ we estimate

$$\hbar g_{xb} = 0.2 \ \mu\text{eV}.$$

The wavevectors in Eq.(5.49) are three-dimensional. We will keep in mind that as we deal with excitons in a semiconductor microcavity, their wavevector along the cavity axis is fixed. So, strictly speaking, their wavevector can only vary in the cavity plane. Furthermore we note that the only TO phonons participating to the coupling to excitons are those polarized in the z direction, along the cavity axis, and thus propagating in the cavity plane.

From the structure of the Hamiltonian of Eq.(5.49) we conclude that the bright-exciton/TO-phonon coupling is active, provided that both bright exciton polarization components are excited. This can be achieved using polaritons, through pumping two light polarization modes, and then relying on the strong-coupling mechanism which preserves polarization.

In the next chapter we will use the Hamiltonian of Eq.(5.49) as cornerstone of the frequency conversion scheme. Note that we will omit the index TO of the transverse optical phonon in the following as there won't be any different types of phonons. Furthermore we will use $\boldsymbol{k}$ and $\boldsymbol{k}'$ to denote the wavevector of the center-of-mass motion of the exciton instead of $\boldsymbol{K}$ and $\boldsymbol{K}'$.

Chapter 6
The frequency conversion scheme

This chapter is dedicated to the frequency conversion scheme. We here bring together the ingredients that we introduced in the Chapters 4 and 5. We start in Section 6.1 by introducing the microscopic model of the conversion scheme. We first present the Hamiltonian of the system and discuss our assumptions and the physical picture of the mechanism before we devote Section 6.2 to the calculation of the number of outcoming THz photons by means of Heisenberg-Langevin equations. In Section 6.3 we link our results with the description of the conversion scheme via an effective $\chi^{(2)}$ susceptibility and we briefly conclude in Section 6.4.

6.1. The microscopic model

Our conversion scheme is based on a chain of interactions: optical photons in the semiconductor microcavity strongly couple to excitons. The excitons weakly couple to TO phonons. The TO phonons strongly couple to THz photons. The Hamiltonian describing our system has the form

$$\hat{H} = \hat{H}_{\text{br-exc-cav}} + \hat{H}_{\text{phon-THz}} + \hat{H}_{\text{br-exc-TO}} + \hat{H}_{\text{laser}}, \tag{6.1}$$

where $\hat{H}_{\text{br-exc-cav}}$ is given by Eq.(4.19). It describes the interaction between optical cavity photons (creation operator $\hat{a}^{\dagger}_{\alpha,\boldsymbol{k}_{\parallel}}$ for an in-plane momentum $\boldsymbol{k}_{\parallel}$ and a polarization α) and a bright excitonic state (creation operator $\hat{c}^{\dagger}_{\alpha,\boldsymbol{k}_{\parallel}}$ with an in plane momentum $\boldsymbol{k}_{\parallel}$ and a polarization α) in the strong coupling regime. We consider two linear polarizations, i.e. we set $\alpha = \text{v}, \text{h}$. We choose a Rabi frequency of $\hbar\Omega = 6\,\text{meV}$. The energy of the excitonic transition does not depend on the wavevector and is given by $\hbar\omega_x = 1680$ meV. In the experimental setup we are considering, it is possible to change the thickness of the

cavity using a wedge shaped device [140]. The change of the thickness changes the cavity frequency. Taking this experimental ressource into account, the cavity dispersion relation reads

$$\hbar\omega_c(\boldsymbol{k}_\parallel, \delta) = \hbar\omega_c^0 + \frac{\hbar^2|\boldsymbol{k}_\parallel|^2}{2m_c} + \hbar\delta. \tag{6.2}$$

Note that this is a generalization of Eq.(4.16). Without loss of generality $\hbar\omega_c^0 = \hbar c_{\text{med,opt}}k_z$ is set to be equal to $\hbar\omega_x$, with k_z fixed by the cavity length. The speed of light with frequencies in the optical range in CdTe is typically $c_{\text{med,opt}} \simeq c/2.5$. The effective mass of the cavity photons is given by m_c and defined in Eq.(4.17). It is in the order of 10^{-5} times the free electron mass.

The interaction between TO phonons of frequency ω_{TO} and THz photons is characterized by the Hamiltonian $\hat{H}_{\text{phon-THz}}$, defined in Eq.(5.6). We recall that $\hat{b}_{\boldsymbol{q}}^\dagger$ creates a TO phonon with a $3D$ momentum $\boldsymbol{q}$ and $\hat{l}_{\boldsymbol{q}}^\dagger$ creates a THz photon with momentum $\boldsymbol{q}$. We will use a Rabi frequency of $\hbar\Omega_{ir} = 5.575\,\text{meV}$. The dispersion of the THz photons is given by

$$\hbar\omega_{ir}(\boldsymbol{q}) = \hbar c_{\text{med,ir}}\sqrt{|\boldsymbol{q}_\parallel|^2 + q_z^2}, \tag{6.3}$$

with $\boldsymbol{q}_\parallel = (q_x, q_y)^T$ and the speed of light in CdTe at infrared frequencies is typically $c_{\text{med,ir}} \simeq c/3.57$.

The cornerstone of the conversion mechanism is the weak interaction between bright exciton states and TO phonons via the deformation potential that we derived in Chapter 5. It is described by the Hamiltonian $\hat{H}_{\text{br-exc-TO}}$, given in Eq.(5.49). The only TO phonons that couple to excitons via the mechanism described by the Hamiltonian (5.49) are polarized along the z direction and thus have a $q_z = 0$, so they propagate in the cavity plane (x, y). We have estimated the exciton-phonon coupling $\hbar g_{xb} = 0.2\,\mu\text{eV}$ as shown in Section 5.6.

Being orders of magnitude weaker than Ω and Ω_{ir}, the interaction magnitude g_{xb} will be conveniently treated as a perturbation. Following Hopfield's transformation for both exciton and phonon-polaritons as defined in equations (4.25) and (5.8), we can rewrite $\hat{H}$, as given by Eq.(6.1), in the basis of upper and lower exciton-polariton and of upper and lower phonon-polariton [113]

$$\hat{H} = \hat{H}_{\text{ex-pol}} + \hat{H}_{\text{phon-pol}} + \hat{H}_{\text{br-exc-TO}} + \hat{H}_{\text{laser}}, \tag{6.4}$$

with

$$\hat{H}_{\text{ex-pol}} = \sum_{\alpha=\text{v,h}} \sum_{\boldsymbol{k}_\parallel} \hbar\omega_u(\boldsymbol{k}_\parallel, \delta)\hat{u}^\dagger_{\alpha,\boldsymbol{k}_\parallel}\hat{u}_{\alpha,\boldsymbol{k}_\parallel} + \hbar\omega_p(\boldsymbol{k}_\parallel, \delta)\hat{p}^\dagger_{\alpha,\boldsymbol{k}_\parallel}\hat{p}_{\alpha,\boldsymbol{k}_\parallel}, \tag{6.5}$$

where $\omega_u(\boldsymbol{k}_\parallel, \delta)$ and $\omega_p(\boldsymbol{k}_\parallel, \delta)$ are given by equations (4.27) and (4.28) respectively, where the cavity dispersion is now defined in Eq.(6.2) and we assume that the cavity frequency doesn't depend on the polarization. The phonon-polariton Hamiltonian has the form

$$\hat{H}_{\text{phon-pol}} = \sum_{\boldsymbol{q}} \hbar\omega_w(\boldsymbol{q})\hat{w}^\dagger_{\boldsymbol{q}}\hat{w}_{\boldsymbol{q}} + \hbar\omega_z(\boldsymbol{q})\hat{z}^\dagger_{\boldsymbol{q}}\hat{z}_{\boldsymbol{q}}, \tag{6.6}$$

with $\omega_w(\boldsymbol{q})$ and $\omega_w(\boldsymbol{q})$ defined in equations (5.11) and (5.10). In the phonon and exciton-polariton basis the TO phonon-exciton coupling term reads

$$\hat{H}_{\text{br-exc-TO}} = -\sum_{\boldsymbol{q},\boldsymbol{k},\boldsymbol{k}'} \hbar g_{xb} \left(-N_{-\boldsymbol{q}}\hat{w}^\dagger_{-\boldsymbol{q}} + T_{-\boldsymbol{q}}\hat{z}^\dagger_{-\boldsymbol{q}} - N_{\boldsymbol{q}}\hat{w}_{\boldsymbol{q}} + T_{\boldsymbol{q}}\hat{z}_{\boldsymbol{q}} \right) \delta_{\boldsymbol{k},\boldsymbol{k}'+\boldsymbol{q}}$$
$$\left[X_{\boldsymbol{k}}X_{\boldsymbol{k}'}\hat{p}^\dagger_{\text{v},\boldsymbol{k}}\hat{p}_{\text{h},\boldsymbol{k}'} + X_{\boldsymbol{k}}C_{\boldsymbol{k}'}\hat{p}^\dagger_{\text{v},\boldsymbol{k}}\hat{u}_{\text{h},\boldsymbol{k}'} + C_{\boldsymbol{k}}X_{\boldsymbol{k}'}\hat{u}^\dagger_{\text{v},\boldsymbol{k}}\hat{p}_{\text{h},\boldsymbol{k}'} \right.$$
$$\left. + C_{\boldsymbol{k}}C_{\boldsymbol{k}'}\hat{u}^\dagger_{\text{v},\boldsymbol{k}}\hat{u}_{\text{h},\boldsymbol{k}'} + h.c. \right]. \tag{6.7}$$

In our total Hamiltonian, g_{xb} thus couples the exciton-polaritons and phonon-polaritons subspace; interestingly, since it is very weak as compared to the other coupling magnitudes $g_{xb} \ll \Omega, \Omega_{ir}$ we can assume that the polaritonic states, whether excitons or phonons, remain the proper eigenstates of the system.

The last term in Eq.(6.4) describes the optical excitation that pumps the exciton-polariton states. We consider a two-pump scheme which excites both the lower polariton branch of a given polarization, e.g. $\alpha = \text{v}$, and the upper polariton branch of opposite polarization, i.e. $\alpha = \text{h}$. The pumps have amplitudes $\hbar\eta_\pm$, wavevector $\boldsymbol{k}_\pm$, and frequency $\omega_\pm$. The corresponding Hamiltonian reads

$$\hat{H}_{\text{laser}} = \hbar\eta_- e^{-i\omega_- t}\hat{p}^\dagger_{\text{v},\boldsymbol{k}_-} + \hbar\eta_+ e^{-i\omega_+ t}\hat{u}^\dagger_{\text{h},\boldsymbol{k}_+} + h.c. \tag{6.8}$$

Note that we neglect exciton-exciton interactions. Hence our model is only valid for weak pump excitations.

In the following, we will focus on the two exciton-polariton states which are macroscopically populated by the laser pump, i.e. $\hat{p}_{\text{v},\boldsymbol{k}_-}$ and $\hat{u}_{\text{h},\boldsymbol{k}_+}$. In particular this allows us to neglect the intraband terms ($\hat{p}^\dagger_{\text{v},\boldsymbol{k}}\hat{p}_{\text{h},\boldsymbol{k}'}$ or $\hat{u}^\dagger_{\text{v},\boldsymbol{k}}\hat{u}_{\text{h},\boldsymbol{k}'}$), because while processes that create an

exciton-polariton with $\boldsymbol{k} \neq \boldsymbol{k}_{\pm}$ are possible, they are negligible as the population at $\boldsymbol{k} \neq \boldsymbol{k}_{\pm}$ is negligible. On the other hand, for processes where for example a lower exciton-polariton with horizontal polarization at $\boldsymbol{k}_{-}$ is annihilated in favor of an upper exciton-polariton with vertical polarization $\boldsymbol{k}_{-}$, momentum conservation yields a phonon-polariton with $\boldsymbol{q} = 0$. Furthermore focusing on only two macroscopically populated states, i.e. $\hat{p}_{v,\boldsymbol{k}_{-}}$ and $\hat{u}_{h,\boldsymbol{k}_{+}}$ allows us to neglect all terms that contain $\hat{p}_{h,\boldsymbol{k}_{-}}$ or $\hat{u}_{v,\boldsymbol{k}_{+}}$.

Among the remaining exciton-phonon interaction terms in Eq.(6.7) we keep those which describe the frequency conversion process we are interested in, namely $\hat{p}_{v,\boldsymbol{k}_{-}}^{\dagger} \hat{u}_{h,\boldsymbol{k}_{+}} \hat{w}_{\boldsymbol{q}}^{\dagger}$ and $\hat{p}_{v,\boldsymbol{k}_{-}}^{\dagger} \hat{u}_{h,\boldsymbol{k}_{+}} \hat{z}_{\boldsymbol{q}}^{\dagger}$ (and their Hermitian conjugate) as depicted in Fig.6.1. This conversion process corresponds to difference frequency generation or parametric down conversion [141, 142]. We neglect the terms $\hat{p}_{v,\boldsymbol{k}_{-}} \hat{u}_{h,\boldsymbol{k}_{+}}^{\dagger} \hat{w}_{\boldsymbol{q}}^{\dagger}$ and $\hat{p}_{v,\boldsymbol{k}_{-}} \hat{u}_{h,\boldsymbol{k}_{+}}^{\dagger} \hat{z}_{\boldsymbol{q}}^{\dagger}$ and their Hermitian conjugate as they will not be resonant with the process considered. Under these approximations the
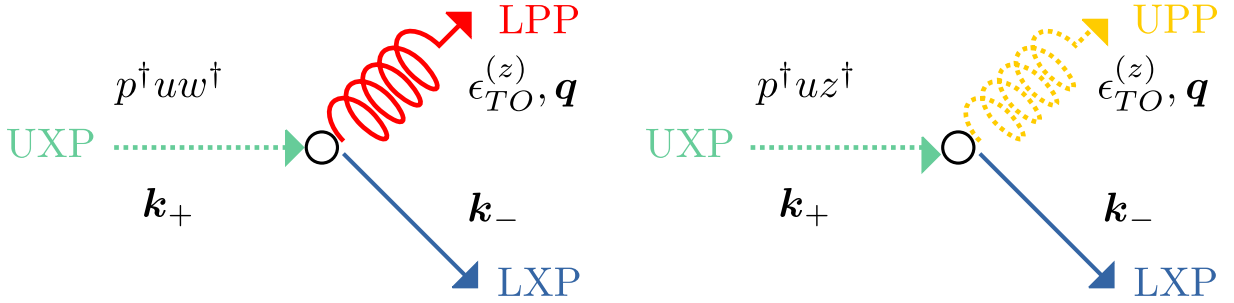

Figure 6.1.: Sketch of interaction mechanisms between exciton-polaritons and phonon-polaritons, that are taken into account: An upper exciton-polariton (UXP) is annihilated and a lower exciton-polariton (LXP) and either a lower or an upper phonon-polariton (LPP and UPP respectively) is created. The wavevector of the outcoming phonon-polariton is fixed due to momentum conservation $\boldsymbol{q} = \boldsymbol{k}_{+} - \boldsymbol{k}_{-}$. Only TO phonons that are polarized along the z axis interact via this mechanism, thus they propagate in the cavity plane.

Hamiltonian describing our conversion mechanism is given by

$$
\begin{aligned}
\hat{H}_{\text{conversion}} = {}& \hbar\omega_u(\boldsymbol{k}_{+}, \delta)\hat{u}_{h,\boldsymbol{k}_{+}}^{\dagger}\hat{u}_{h,\boldsymbol{k}_{+}} + \hbar\omega_p(\boldsymbol{k}_{-}, \delta)\hat{p}_{v,\boldsymbol{k}_{-}}^{\dagger}\hat{p}_{v,\boldsymbol{k}_{-}} \\
&+ \sum_{\boldsymbol{q}} \hbar\omega_w(\boldsymbol{q})\hat{w}_{\boldsymbol{q}}^{\dagger}\hat{w}_{\boldsymbol{q}} + \hbar\omega_z(\boldsymbol{q})\hat{z}_{\boldsymbol{q}}^{\dagger}\hat{z}_{\boldsymbol{q}}\delta_{\boldsymbol{k}_{+},\boldsymbol{k}_{-}+\boldsymbol{q}} \\
&- \sum_{\boldsymbol{q}} \hbar g_{xb}\epsilon_{TO}^{(z)}X_{\boldsymbol{k}_{-}}C_{\boldsymbol{k}_{+}}\left[\hat{p}_{v,\boldsymbol{k}_{-}}^{\dagger}\hat{u}_{h,\boldsymbol{k}_{+}}\left(-N_{-\boldsymbol{q}}\hat{w}_{-\boldsymbol{q}}^{\dagger} + T_{-\boldsymbol{q}}\hat{z}_{-\boldsymbol{q}}^{\dagger}\right)\delta_{\boldsymbol{k}_{-},\boldsymbol{k}_{+}+\boldsymbol{q}} \right. \\
&\left. + \hat{u}_{h,\boldsymbol{k}_{+}}^{\dagger}\hat{p}_{v,\boldsymbol{k}_{-}}\left(-N_{\boldsymbol{q}}\hat{w}_{\boldsymbol{q}} + T_{\boldsymbol{q}}\hat{z}_{\boldsymbol{q}}\right)\delta_{\boldsymbol{k}_{+},\boldsymbol{k}_{-}+\boldsymbol{q}}\right] + \hat{H}_{\text{laser}}.
\end{aligned} \tag{6.9}
$$

At this point we recall that the z component of wavevector of the exciton-polaritons is

fixed by the cavity. The TO phonons that are interacting with excitons via the deformation potential, described by Eq.(5.49), are polarized along the z axis and thus $q_z = 0$. The momentum conservation yields

$$\boldsymbol{q}_\parallel = \boldsymbol{k}_{+,\parallel} - \boldsymbol{k}_{-,\parallel}, \tag{6.10}$$

where $\boldsymbol{k}_{+,\parallel}$ denotes the in-plane component of the pump wavevectors. We will assume that the two pumps are at $\boldsymbol{k}_+ = -\boldsymbol{k}_-$, such that $\boldsymbol{q}_\parallel = 2\boldsymbol{k}_{+,\parallel}$. The phonon-polaritons propagate in the cavity plane and radiatively decay into THz photons at the cavity interface. Fig.6.2 shows a sketch of the experimental setup and the pump scheme.
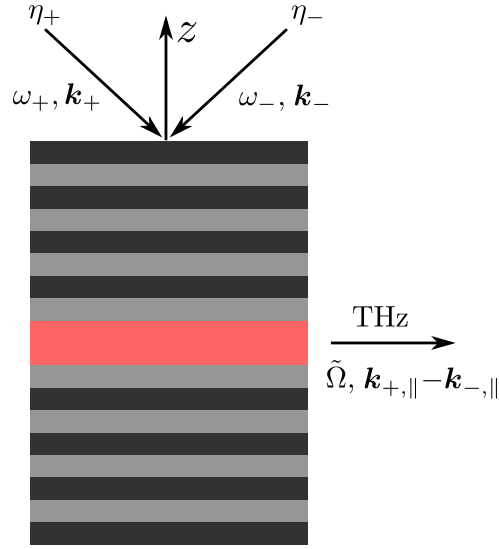

Figure 6.2.: Sketch of the experimental setup and the pump scheme. A semiconductor micro-cavity with cavity axis along z is externally pumped by two pumps with amplitudes $\hbar\eta_\pm$, wavevector $\boldsymbol{k}_\pm$, and frequency $\omega_\pm$. The phonon-polaritons are polarized along the z axis, propagate in the cavity plane with $\boldsymbol{q}_\parallel = \boldsymbol{k}_{+,\parallel} - \boldsymbol{k}_{-,\parallel}$ and decay at the interface into THz photons.

We introduce $\tilde{\Omega}(\boldsymbol{k}_+, \boldsymbol{k}_-, \delta) = \omega_+(\boldsymbol{k}_+, \delta) - \omega_-(\boldsymbol{k}_-, \delta)$. This parameter is easily tunable in actual experiments: its lowest value is fixed by the Rabi splitting 2Ω, while it can be increased several times above at the expense of a decreasing (increasing) excitonic (photonic) fraction of the considered lower (upper) exciton-polariton state. This increase can be achieved either by increasing the laser incidence angle on the microcavity (resulting in increasing $\boldsymbol{k}_\pm$) [143], or by tuning the cavity photon energy $\hbar\omega_c(\boldsymbol{k}_\parallel, \delta)$ using the microcavity intentional wedged shape [140].

The physical picture of our conversion mechanism is the following: by shining laser light onto both the upper and lower polaritons, an excitonic density is created in the microcavity

active region (a slab of bulk semiconductor), which is time modulated at the frequency $\tilde{\Omega}(\boldsymbol{k}_+, \boldsymbol{k}_-, \delta)$. Note that this population beat[1] requires both polaritons modes (upper and lower) to be optically excited simultaneously. It induces a mechanical vibration of the lattice unit cell via the deformation potential interaction. In our scheme, the modulation frequency $\tilde{\Omega}(\boldsymbol{k}_+, \boldsymbol{k}_-, \delta)$ matches that of a TO phonon-polariton state, so that the earlier excites the latter. Finally, the thus created phonon-polaritons propagate in the structure and decay radiatively into THz photons upon reaching an interface. Fig.6.3 shows a sketch of the conversion mechanism.
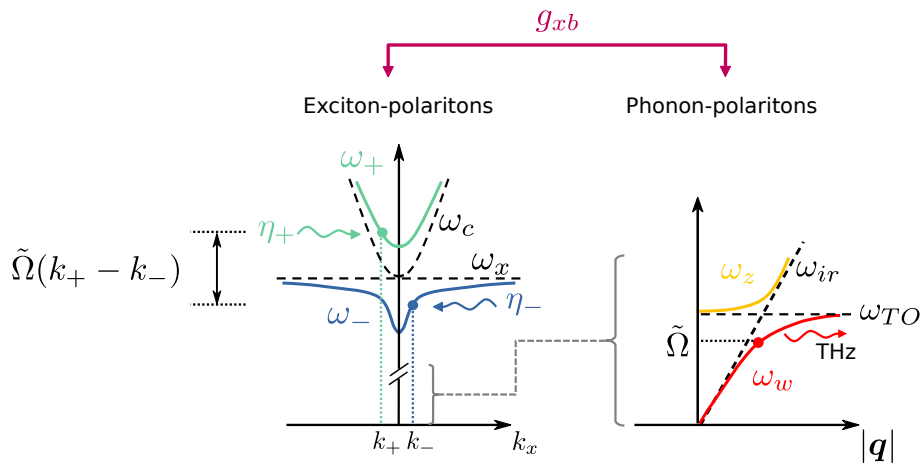

Figure 6.3.: Sketch of the conversion mechanism: We depict the dispersion relations for upper and lower exciton branch along one in-plane axis (here x) and the upper and lower phonon-polariton branch as a function of $|\boldsymbol{q}|$. Upper and lower exciton-polariton are externally pumped with pump strength $\eta_\pm$ and wavevector $\boldsymbol{k}_\pm$. Here we depict the pumps resonant with the exciton-polariton branches $\omega_\pm = \omega_{u,p}$. The simultaneous pumping of both branches leads to a beating between the two dressed states with frequency $\tilde{\Omega}(\boldsymbol{k}_+, \boldsymbol{k}_-, \delta)$ which couples to the phonon-polaritons via the deformation potential interaction. Note that in the figure we omit the dependence of $\tilde{\Omega}$ on δ. Depending on the value of $\tilde{\Omega}(\boldsymbol{k}_+, \boldsymbol{k}_-, \delta)$ either lower or upper phonon-polaritons are created.

Note that it may be experimentally challenging to collect the THz emission in the cavity plane. In order to engineer the emission direction, in the future one could investigate the use of microstructures such as pillars.

---

[1]The population beat corresponds to Rabi oscillations in the exciton, cavity photon basis.

6.2. Dynamics of the conversion mechanism

We now want to quantitatively describe our conversion scheme and predict the output power of THz photons. In order to determine the input-output characteristics of the system in the steady-state (i.e. assuming CW excitation), we use the Heisenberg-Langevin formalism, introduced in Section 1.8. The corresponding Heisenberg-Langevin equations for the polariton annihilation operators read

$$
\begin{aligned}
\dot{\hat{p}}_{v,\boldsymbol{k}_-} &= \frac{1}{i\hbar}[\hat{p}_{v,\boldsymbol{k}_-}, \hat{H}_{\text{conversion}}] - \gamma_p \hat{p}_{v,\boldsymbol{k}_-} + \sqrt{2\gamma_p}\hat{p}_{v,\text{in}}(t) \\
&= -i\omega_p(\boldsymbol{k}_-)\hat{p}_{v,\boldsymbol{k}_-} + ig_{xb}X_{\boldsymbol{k}_-}C_{\boldsymbol{k}_+}\hat{u}_{h,\boldsymbol{k}_+}\left(-N_{-\boldsymbol{q}}\hat{w}^\dagger_{-\boldsymbol{q}} + T_{-\boldsymbol{q}}\hat{z}^\dagger_{-\boldsymbol{q}}\right) - i\eta_- e^{-i\omega_- t} \\
&\quad - \gamma_p \hat{p}_{v,\boldsymbol{k}_-} + \sqrt{2\gamma_p}\hat{p}_{v,\text{in}}(t),
\end{aligned} \tag{6.11}
$$

$$
\begin{aligned}
\dot{\hat{u}}_{h,\boldsymbol{k}_+} &= \frac{1}{i\hbar}[\hat{u}_{h,\boldsymbol{k}_+}, \hat{H}_{\text{conversion}}] - \gamma_u \hat{u}_{h,\boldsymbol{k}_+} + \sqrt{2\gamma_u}\hat{u}_{h,\text{in}}(t) \\
&= -i\omega_u(\boldsymbol{k}_+)\hat{u}_{h,\boldsymbol{k}_+} + ig_{xb}C_{\boldsymbol{k}_+}X_{\boldsymbol{k}_-}\hat{p}_{v,\boldsymbol{k}_-}\left(-N_{\boldsymbol{q}}\hat{w}_{\boldsymbol{q}} + T_{\boldsymbol{q}}\hat{z}_{\boldsymbol{q}}\right) - i\eta_+ e^{-i\omega_+ t} \\
&\quad - \gamma_u \hat{u}_{h,\boldsymbol{k}_+} + \sqrt{2\gamma_u}\hat{u}_{h,\text{in}}(t),
\end{aligned} \tag{6.12}
$$

$$
\begin{aligned}
\dot{\hat{w}}_{\boldsymbol{q}} &= \frac{1}{i\hbar}[\hat{w}_{\boldsymbol{q}}, \hat{H}_{\text{conversion}}] - \gamma_w \hat{w}_{\boldsymbol{q}} + \sqrt{2\gamma_w}\hat{w}_{\text{in}}(t) \\
&= -i\omega_w(\boldsymbol{q})\hat{w}_{\boldsymbol{q}} - ig_{xb}N_{\boldsymbol{q}}X_{\boldsymbol{k}_-}C_{\boldsymbol{k}_+}\hat{p}^\dagger_{v,\boldsymbol{k}_-}\hat{u}_{h,\boldsymbol{k}_+} - \gamma_w \hat{w}_{\boldsymbol{q}} + \sqrt{2\gamma_w}\hat{w}_{\text{in}}(t),
\end{aligned} \tag{6.13}
$$

$$
\begin{aligned}
\dot{\hat{z}}_{\boldsymbol{q}} &= \frac{1}{i\hbar}[\hat{z}_{\boldsymbol{q}}, \hat{H}_{\text{conversion}}] - \gamma_z \hat{z}_{\boldsymbol{q}} + \sqrt{2\gamma_z}\hat{z}_{\text{in}}(t) \\
&= -i\omega_z(\boldsymbol{q})\hat{z}_{\boldsymbol{q}} + ig_{xb}T_{\boldsymbol{q}}X_{\boldsymbol{k}_-}C_{\boldsymbol{k}_+}\hat{p}^\dagger_{v,\boldsymbol{k}_-}\hat{u}_{h,\boldsymbol{k}_+} - \gamma_z \hat{z}_{\boldsymbol{q}} + \sqrt{2\gamma_z}\hat{z}_{\text{in}}(t),
\end{aligned} \tag{6.14}
$$

where the momentum of the phonon-polaritons is fixed to $\boldsymbol{q} = \boldsymbol{k}_+ - \boldsymbol{k}_-$. The decay rates of upper and lower exciton-polariton are defined as [144]

$$
\begin{aligned}
\gamma_u(\boldsymbol{k}_+) &= \gamma_x C^2_{\boldsymbol{k}_+} + \kappa X^2_{\boldsymbol{k}_+}, \\
\gamma_p(\boldsymbol{k}_-) &= \gamma_x X^2_{\boldsymbol{k}_-} + \kappa C^2_{\boldsymbol{k}_-},
\end{aligned} \tag{6.15}
$$

where κ denotes the cavity photon loss rate and γ_x the excitonic (nonradiative) decay rate. Correspondingly we introduce the decay rates of upper and lower phonon-polariton

$$
\begin{aligned}
\gamma_w(\boldsymbol{q}) &= \gamma_b N^2_{\boldsymbol{q}} + \gamma_l T^2_{\boldsymbol{q}}, \\
\gamma_z(\boldsymbol{q}) &= \gamma_b T^2_{\boldsymbol{q}} + \gamma_l N^2_{\boldsymbol{q}},
\end{aligned} \tag{6.16}
$$

with γ_l and γ_b the decay rates of THz photon and TO phonon respectively. Furthermore we consider that the input noises of the polaritons are given by

$$
\begin{aligned}
\sqrt{2\gamma_p}\hat{p}_{\text{v,in}}(t) &= -\sqrt{2\kappa}\hat{a}_{\text{v,in}}(t)C_{\boldsymbol{k}_-} + \sqrt{2\gamma_x}\hat{c}_{\text{v,in}}(t)X_{\boldsymbol{k}_-}, \\
\sqrt{2\gamma_u}\hat{u}_{\text{h,in}}(t) &= \sqrt{2\kappa}\hat{a}_{\text{h,in}}(t)X_{\boldsymbol{k}_+} + \sqrt{2\gamma_x}\hat{c}_{\text{h,in}}(t)C_{\boldsymbol{k}_+}, \\
\sqrt{2\gamma_w}\hat{w}_{\text{in}}(t) &= -\sqrt{2\gamma_b}\hat{b}_{\text{in}}(t)N_{\boldsymbol{q}} + \sqrt{2\gamma_l}\hat{l}_{\text{in}}(t)T_{\boldsymbol{q}}, \\
\sqrt{2\gamma_z}\hat{z}_{\text{in}}(t) &= \sqrt{2\gamma_b}\hat{b}_{\text{in}}(t)T_{\boldsymbol{q}} + \sqrt{2\gamma_l}\hat{l}_{\text{in}}(t)N_{\boldsymbol{q}}.
\end{aligned}
\tag{6.17}
$$

Here $\hat{a}_{i,\text{in}}(t), \hat{c}_{i,\text{in}}(t), \hat{b}_{\text{in}}(t)$ and $\hat{l}_{\text{in}}(t)$ are the input noises for the optical cavity photon with polarization $i = \text{h, v}$, the exciton, the TO phonon and the THz photon respectively. We assume that all noises can be modeled by the coupling of the concerned oscillator with an external thermal bath consisting of harmonic oscillators. Thus their expectation values fulfill the equations (1.45)-(1.47).

Note that for the definitions of the decay rates and the noises for the polaritons, given in equations (6.15)-(6.17), we assumed that the polaritons inherit the decay and noise behavior of their constituents, weighted with the corresponding transformation coefficient (N, T, X, C). Our justification is the strong coupling regime and the fact that we neglect the interdependency of the noises. From measurements found in literature [130] we estimate $\gamma_w = \gamma_z \simeq 0.6\,\text{THz}$ for the phonon-polariton decay rates, taking for simplicity a value which is momentum independent.

We consider room temperature and can thus neglect the occupation of the thermal bath for the optical cavity photons. As we will only be interested in observables that are normally ordered, we can omit the noise on the cavity ($\hat{a}_{\text{v,in}}(t)$ and $\hat{a}_{\text{h,in}}(t)$ respectively). We take for the decay rate of the cavity photon, TO phonon and THz photon $\kappa = 0.1\,\text{THz}$, $\gamma_b = 0.35\,\text{THz}$ [130] and $\gamma_l = 0.6\,\text{THz}$. The typical decay rate of the exciton γ_x is in the order of $0.01\,\text{THz}$ [145] and we will thus neglect it.

The four Heisenberg-Langevin equations (6.11)-(6.14) are nontrivially coupled by the term proportional to g_{xb}. As $g_{xb} \ll \Omega, \Omega_{ir}$, we can decouple them by assuming $g_{xb} \simeq 0$. This allows us to solve equations (6.11) and (6.12) and to calculate the expectation value of $\hat{p}^{\dagger}_{\text{v},\boldsymbol{k}_-}(t)\hat{u}_{\text{h},\boldsymbol{k}_+}(t)$ for times longer than the characteristic time scale of the Rabi oscillations $t \gg T_R$, with $T_R = 1/\tilde{\Omega}$

$$
\begin{aligned}
n_0(t) &= \langle \hat{p}^{\dagger}_{\text{v},\boldsymbol{k}_-}(t)\hat{u}_{\text{h},\boldsymbol{k}_+}(t)\rangle_{t \gg T_R} \\
&= \frac{\eta_-^* \eta_+}{\left(-i\gamma_p - (\omega_p - \omega_-)\right)\left(i\gamma_u - (\omega_u - \omega_+)\right)} e^{-i\tilde{\Omega}t}.
\end{aligned}
\tag{6.18}
$$

We see that there is a beating between upper and lower exciton-polariton mode which is modulated at frequency $\tilde{\Omega}$. Inserting $n_0(t)$ in equations (6.13) and (6.14) shows that pumping both exciton-polariton branches leads to an effective pumping of the phonon-polariton branches. We can now solve the equations (6.13) and (6.14) and obtain the number of phonon-polaritons in lower and upper mode

$$
\begin{aligned}
N_w &= \langle \hat{w}_{\boldsymbol{q}}^\dagger(t)\hat{w}_{\boldsymbol{q}}(t)\rangle_{t\gg T_R} \\
&= \frac{|\tilde{\eta}(\boldsymbol{k}_+,\boldsymbol{k}_-)|^2 N(\boldsymbol{q})^2}{\gamma_w^2 + (\tilde{\Omega}(\boldsymbol{k}_+,\boldsymbol{k}_-,\delta)-\omega_w(\boldsymbol{q}))^2} + \frac{\gamma_b}{\gamma_w}N(\boldsymbol{q})^2\bar{n}_b(\omega_{TO}) \\
&\quad + \frac{\gamma_l}{\gamma_w}T(\boldsymbol{q})^2\bar{n}_l(\omega_{ir}(\boldsymbol{q})),
\end{aligned}
\tag{6.19}
$$

$$
\begin{aligned}
N_z &= \langle \hat{z}_{\boldsymbol{q}}^\dagger(t)\hat{z}_{\boldsymbol{q}}(t)\rangle_{t\gg T_R} \\
&= \frac{|\tilde{\eta}(\boldsymbol{k}_+,\boldsymbol{k}_-)|^2 T(\boldsymbol{q})^2}{\gamma_z^2 + (\tilde{\Omega}(\boldsymbol{k}_+,\boldsymbol{k}_-,\delta)-\omega_z(\boldsymbol{q}))^2} + \frac{\gamma_b}{\gamma_z}T(\boldsymbol{q})^2\bar{n}_b(\omega_{TO}) \\
&\quad + \frac{\gamma_l}{\gamma_z}N(\boldsymbol{q})^2\bar{n}_l(\omega_{ir}(\boldsymbol{q})),
\end{aligned}
\tag{6.20}
$$

with effective pump strength

$$
\tilde{\eta}(\boldsymbol{k}_+,\boldsymbol{k}_-) = \frac{g_{xb}X_{\boldsymbol{k}_-}C_{\boldsymbol{k}_+}\eta_-^*\eta_+}{(-i\gamma_p-(\omega_p-\omega_-))\,(i\gamma_u-(\omega_u-\omega_+))}.
\tag{6.21}
$$

The phonon-polaritons travel in the cavity plane and decay radiatively into THz photons at the interface between the semiconductor slab and the air outside. The number of emitted THz photons can thus be determined by multiplying the number of phonon-polaritons with the corresponding photonic fraction (i.e. T^2 for lower, N^2 for upper phonon-polariton branch). An observable in the experiment is the emission power of THz photons, measuring the energy of the outcoming photons per time. We define it as

$$
P = N_w T^2 \gamma_w \hbar\omega_w + N_z N^2 \gamma_z \hbar\omega_z.
\tag{6.22}
$$

Fig.6.4 shows the emission power of THz photons as function of their frequency $\tilde{\Omega}$ and their in-plane wavevector $q_\parallel = |\boldsymbol{q}_\parallel|$ for a pump strength of $\eta_+ = \eta_- = 1\Omega$ and resonant pumping thus $\omega_- = \omega_p$ and $\omega_+ = \omega_u$. Here we leave $\tilde{\Omega}$ as a free parameter. As we will show below, it can be chosen independently of $q_\parallel$ provided that we suitably choose the detuning δ. The white dashed line corresponds to the dispersion relation for the THz photons inside the medium, as defined in Eq.(6.3). It is the asymptote of upper and
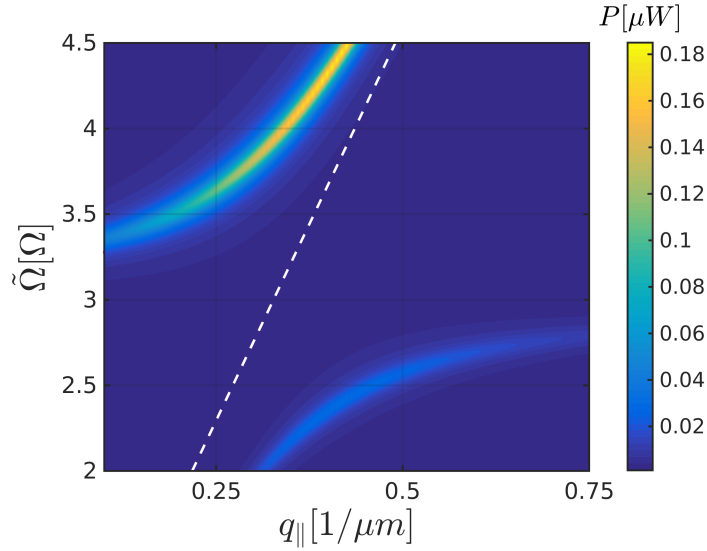
Figure 6.4.: Emission power of THz photons as function of their frequency $\tilde{\Omega}$ in units of Ω and their in-plane wavevector $q_\| = |\boldsymbol{q}_\||$ for $\eta_- = \eta_+ = 1\Omega$. The white dashed line corresponds to the dispersion relation of the THz photons inside the medium as defined in Eq.(6.3).

lower phonon-polariton branch for large and small $q_\|$ respectively. We see that THz photons are emitted if the frequency difference between upper and lower exciton-polariton branch $\tilde{\Omega}$ matches either the lower or the upper phonon-polariton branch. The emission at frequencies above the TO phonon frequency $\omega_{TO} = 3\Omega$ increases for increasing $q_\|$. The opposite behavior is observed for frequencies below ω_{TO}. The reason is that the emission power is proportional to the phonon-polariton energy in Eq.(6.22), which increases for the upper branch while it tends to a constant for the lower branch.

The frequency of the emitted THz photons is given by $\tilde{\Omega}$. It can be tuned both via the wavevectors of the pumps $\boldsymbol{k}_\pm$ and via the detuning between cavity and exciton δ. The wavevectors of the pumps are related to the wavevector of the phonon via momentum conservation, and we assume that we pump at $\boldsymbol{k}_+ = -\boldsymbol{k}_-$, thus it follows $\boldsymbol{q}_\| = 2\boldsymbol{k}_{+,\|}$. For a given value of $\boldsymbol{q}_\|$ we can thus determine the value of the detuning δ in order to generate a desired $\tilde{\Omega}$. For resonant pumping and $\tilde{\Omega}$ matching the frequency of upper (and analogously the lower) phonon-polariton branch it holds

$$\tilde{\Omega}(\boldsymbol{q}_\|, \delta) = \sqrt{4\Omega^2 + (\omega_c(\boldsymbol{k}_{+,\|}, \delta) - \omega_x)^2} \overset{!}{=} \omega_z(\boldsymbol{q}_\|, q_z)$$

$$\Rightarrow \delta = -\frac{\hbar^2|\boldsymbol{q}_\||^2}{4}\frac{1}{2m_c} \pm \sqrt{\omega_z(\boldsymbol{q}_\|, q_z)^2 - 4\Omega^2}. \tag{6.23}$$

Thus the detuning δ depends on the wavevector $q_\parallel$ as illustrated in Fig.6.5, where for simplicity we show only the expressions for δ with the positive sign in Eq.(6.23). We see that its behavior is mainly determined by the dispersion of the phonon branches.
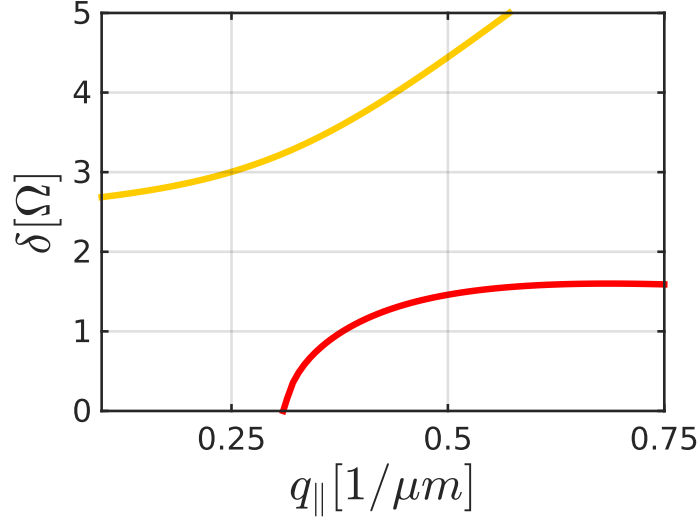

Figure 6.5.: Detuning δ of the cavity, given by Eq.(6.23), in units of Ω as function of the in-plane wavevector of the THz photons $q_\parallel$ for $\tilde{\Omega} = \omega_w$ (red curve) and $\tilde{\Omega} = \omega_z$ (yellow curve).

6.3. Description of the conversion scheme with a nonlinear susceptibility

Up to now we considered the microscopic model of the frequency conversion scheme. In this section which is based on Ref. [141], we want to link it to a macroscopic description using a second order nonlinear susceptibility $\chi^{(2)}$.

In general the susceptibility χ is the proportionality constant between an applied field (e.g. magnetic or electric) and the response of the system (e.g. magnetization or polarization) [146]. The susceptibility can be nonlinear in the sense that the response depends nonlinearly on the strength of the applied field. For instance for nonlinear optical processes the polarization $\mathcal{P}(t)$ can be expressed in powers of the applied electric field

strength $\mathcal{E}(t)$ according to [141][2]

$$\mathcal{P}(t) = \epsilon_0 \left[\chi^{(1)} \mathcal{E}(t) + \chi^{(2)} \mathcal{E}^2(t) + \chi^{(3)} \mathcal{E}^3(t) + ... \right] \tag{6.24}$$
$$\equiv \mathcal{P}^{(1)}(t) + \mathcal{P}^{(2)}(t) + \mathcal{P}^{(3)}(t) + ...,$$

with $\chi^{(1)}$ the linear susceptibility, ϵ_0 the permittivity of free space and $\chi^{(2)}, \chi^{(3)}$ the second- and third-order nonlinear optical susceptibilities. Note that here the polarization and the electric field are considered as scalars for simplicity. Taking into account their vector character, the susceptibilities become tensors.

In the common case the nonlinearity of a crystal is of electronic origin Ref. [141]. The expressions for the nonlinear susceptibilities can be classically derived starting with the anharmonic oscillator model. It is an extension of the Lorentz model of an atom and takes into account a possible nonlinear restoring force on the electron. The corresponding equation of motion for the electron at position x describes a driven damped harmonic oscillator subjected to a nonlinear restoring force and is given by

$$\ddot{x} + 2\gamma\dot{x} + \omega_0^2 x + ax^2 = -\lambda \frac{e\mathcal{E}(t)}{m}, \tag{6.25}$$

where e is the charge of the electron, ω_0 is the oscillator frequency, a denotes the strength of the nonlinearity. It leads to a deviation from the harmonic potential of a standard harmonic oscillator[3]. The electric driving field $\mathcal{E}$ is assumed to read

$$\mathcal{E}(t) = E_1 e^{-i\omega_1 t} + E_2 e^{-i\omega_2 t} + c.c. \tag{6.26}$$

It will be treated as perturbation, λ denotes the perturbation strength. In order to solve Eq.(6.25) we make the ansatz

$$x = \lambda x^{(1)} + \lambda^2 x^{(2)} + ... \tag{6.27}$$

The lowest-order solution corresponds to the solution of the standard Lorentz model

$$x^{(1)}(t) = \sum_{j=1} x^{(1)}(\omega_j) e^{-i\omega_j t} + c.c. \tag{6.28}$$

---

[2]In SI units.

[3]This form of the nonlinearity describes only noncentrosymmetric media as the potential contains both even and odd powers of x and is thus not symmetric under inversion at $x = 0$.

with $x^{(1)}(\omega_j) = \frac{e}{m}\frac{E_j}{D(\omega_j)}$ and $D(\omega_j) = \omega_0^2 - \omega_j^2 - 2i\omega_j\gamma$. The second order term $x^{(2)}(t)$ depends on the square of $x^{(1)}(t)$, containing all different possible combinations of the frequencies ω_1 and ω_2. We are only interested in the difference frequency generation (DFG) which is sketched in Fig.6.6. The term describing DFG corresponds to the response at
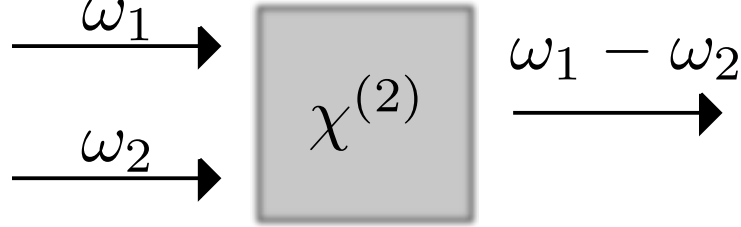

Figure 6.6.: Sketch of difference frequency generation: Two fields with frequencies ω_1 and ω_2 enter a crystal with second-order nonlinear susceptibility $\chi^{(2)}$ and get mixed such that a field with frequency $\omega_1 - \omega_2$ is created.

frequency $\omega_1 - \omega_2$ and is given by

$$x^{(2)}(t) = x^{(2)}(\omega_1 - \omega_2)e^{-i(\omega_1-\omega_2)t}, \tag{6.29}$$

with

$$x^{(2)}(\omega_1 - \omega_2) = -\left(\frac{e}{m}\right)^2 \frac{2a}{D(\omega_1 - \omega_2)D(\omega_1)D(-\omega_2)}E_1(\omega_1)E_2(\omega_2)^*. \tag{6.30}$$

In the case of difference frequency generation the Fourier component of the second-order nonlinear response $x^{(2)}(\omega_1 - \omega_2)$ can be linked to the Fourier component of the nonlinear polarization via

$$\mathcal{P}^{(2)}(\omega_1 - \omega_2) = -\mathcal{N}ex^{(2)}(\omega_1 - \omega_2) = 2\epsilon_0\chi^{(2)}(\omega_1 - \omega_2)E_1(\omega_1)E_2(\omega_2)^*, \tag{6.31}$$

where $\mathcal{N}$ denotes the number of atoms per unit volume. We can now identify the second order susceptibility and express it as function of first order susceptibilities according to

$$\begin{aligned}\chi^{(2)}(\omega_1 - \omega_2) &= \frac{e^3}{\epsilon_0 m^2}\frac{\mathcal{N}a}{D(\omega_1 - \omega_2)D(\omega_1)D(-\omega_2)}\\&= \frac{\epsilon_0^2 ma}{\mathcal{N}^2 e^3}\chi^{(1)}(\omega_1 - \omega_2)\chi^{(1)}(\omega_1)\chi^{(1)}(-\omega_2).\end{aligned} \tag{6.32}$$

The second order susceptibility $\chi^{(2)}$ has units m/V. Its value depends on the material, the frequencies of the applied fields and on the considered nonlinear process. Some

experimental values for the $\chi^{(2)}$ of CdTe for second-harmonic generation at wavelength of several tens of μm are given in Ref. [147]; they are in the order of $10^{-10}\,\mathrm{m/V}$.

In our frequency conversion scheme the origin of the nonlinearity is the exciton-TO phonon coupling. The applied pump fields are directly driving both exciton-polariton modes as described by the pump Hamiltonian in Eq.(6.8). For long times $(t \gg T_R)$ the solutions of equations (6.11) and (6.12) allow to identify a susceptibility $\tilde{\chi}$ as proportionality constant between the external applied field and the response of the exciton-polariton branches

$$\langle \hat{p}_{\mathrm{v},\boldsymbol{k}_-}(t) \rangle_{t \gg T_R} = \tilde{\chi}_p^{(1)}(\omega_-)\eta_- e^{-i\omega_- t},$$
$$\langle \hat{u}_{\mathrm{h},\boldsymbol{k}_+}(t) \rangle_{t \gg T_R} = \tilde{\chi}_u^{(1)}(\omega_+)\eta_+ e^{-i\omega_+ t}, \tag{6.33}$$

with $\tilde{\chi}_p^{(1)}(\omega_-) = \frac{1}{i\gamma_p - (\omega_p - \omega_-)}$ and $\tilde{\chi}_u^{(1)}(\omega_+) = \frac{1}{i\gamma_u - (\omega_u - \omega_+)}$. As we have seen in Section 6.2 the pumping of both exciton-polariton branches leads to an effective pumping of the phonon-polariton branches. The effective pumping is mediated via the exciton-TO phonon coupling that provides a nonlinearity corresponding to difference frequency generation. The response of the phonon-polariton modes to the effective pump is given by the solution of equations (6.14) and (6.13). It can be cast into the form

$$\langle \hat{z}_{\boldsymbol{q}}(t) \rangle_{t \gg T_R} = \tilde{\chi}_z^{(2)}(\tilde{\Omega} = \omega_+ - \omega_-)\eta_-^* \eta_+ e^{i\omega_- t} e^{-i\omega_+ t},$$
$$\langle \hat{w}_{\boldsymbol{q}}(t) \rangle_{t \gg T_R} = \tilde{\chi}_w^{(2)}(\tilde{\Omega} = \omega_+ - \omega_-)\eta_-^* \eta_+ e^{i\omega_- t} e^{-i\omega_+ t}, \tag{6.34}$$

with

$$\tilde{\chi}_z^{(2)}(\tilde{\Omega} = \omega_+ - \omega_-) = -TXCg_{xb}\tilde{\chi}_p^{(1)}(\omega_-)^* \tilde{\chi}_u^{(1)}(\omega_+)\tilde{\chi}_z^{(1)}(\tilde{\Omega}),$$
$$\tilde{\chi}_w^{(2)}(\tilde{\Omega} = \omega_+ - \omega_-) = NXCg_{xb}\tilde{\chi}_p^{(1)}(\omega_-)^* \tilde{\chi}_u^{(1)}(\omega_+)\tilde{\chi}_w^{(1)}(\tilde{\Omega}), \tag{6.35}$$

where $\tilde{\chi}_z^{(1)}(\tilde{\Omega}) = \frac{1}{i\gamma_z - (\omega_z - \tilde{\Omega})}$ and $\tilde{\chi}_w^{(1)}(\tilde{\Omega}) = \frac{1}{i\gamma_w - (\omega_w - \tilde{\Omega})}$. We see that formally we can express the response of the phonon-polariton branches at the frequency $\tilde{\Omega}$ with the help of a second order nonlinear susceptibility $\tilde{\chi}^{(2)}$, which depends on linear susceptibilities in the same way as Eq.(6.32). Notice that the units of our $\tilde{\chi}^{(2)}$ are $1/\mathrm{Hz}^2$ since it is the susceptibility of the number operator. In outlook, it will be interesting to convert our nonlinear susceptibility $\tilde{\chi}^{(2)}$ to the same units as the usual nonlinear susceptibility of the bare CdTe crystal. For this purpose we also need to take into account the tensor character of the fields and of the susceptibility. The nonlinear polarization component l, with $l = x, y, z$ at a frequency

$\omega_n + \omega_m$ is defined as [141]

$$\mathcal{P}_l(\omega_n + \omega_m) = \epsilon_0 \sum_{j,k=x,y,z} \sum_{(m,n)} 2d_{ljk}E_j(\omega_n)E_k(\omega_m), \qquad (6.36)$$

with $d_{ljk} = \frac{1}{2}\chi^{(2)}_{ljk}$. Using a contracted notation the nonlinear polarization leading to difference frequency generation at $\omega_3 = \omega_1 - \omega_2$ reads

$$\begin{bmatrix} \mathcal{P}_x(\omega_3) \\ \mathcal{P}_y(\omega_3) \\ \mathcal{P}_z(\omega_3) \end{bmatrix} = 4\epsilon_0 \begin{bmatrix} d_{11} & d_{12} & d_{13} & d_{14} & d_{15} & d_{16} \\ d_{21} & d_{22} & d_{23} & d_{24} & d_{25} & d_{26} \\ d_{32} & d_{32} & d_{33} & d_{34} & d_{35} & d_{36} \end{bmatrix} \begin{bmatrix} E_x(\omega_1)E_x(-\omega_2) \\ E_y(\omega_1)E_y(-\omega_2) \\ E_z(\omega_1)E_z(-\omega_2) \\ E_y(\omega_1)E_z(-\omega_2) + E_z(\omega_1)E_y(-\omega_2) \\ E_x(\omega_1)E_z(-\omega_2) + E_z(\omega_1)E_x(-\omega_2) \\ E_x(\omega_1)E_y(-\omega_2) + E_y(\omega_1)E_x(-\omega_2) \end{bmatrix}.$$

The only nonvanishing elements for zinc-blende structured crystals are d_{14}, d_{25}, d_{36} which corresponds to elements of the form $\chi^{(2)}_{xzy}$ and all permutations of the indices [141]. We notice the same symmetry of the usual $\chi^{(2)}$ in bulk CdTe as in our calculation of the nonvanishing matrix elements of the deformation potential operator between two hole states (see Section 5.4).

6.4. Conclusion

In this part of the Thesis we have presented a frequency down conversion scheme to convert optical photons in THz photons in a CdTe semiconductor microcavity. The scheme is based on a $\chi^{(2)}$ nonlinearity, coming from the weak interaction between bright excitons and TO phonons, and it doesn't involve any change in the microcavity material nor an externally applied field. For future applications, it will be interesting to extend the present calculation to the case of materials with large band gap. These materials are interesting in two respects: (i) the strong coupling regime is stable also at room temperature, with obvious benefits for the future realization of an actual polaritonic THz devices and (ii) the TO phonons energy ($\hbar\omega_{TO} = (66.5; 69.5)$ meV in GaN and $\hbar\omega_{TO} = (47.7; 51.7)$ meV in ZnO[4]) can be well matched by the Rabi splitting in a state-of-the-art microcavity [148–150]. Due to their wurtzite crystalline structure additional calculations are needed to determine exactly the

---

[4]The first (second) number in the parenthesis correspond to a TO phonon modes polarized parallel (perpendicular) to the wurtzite's C-axis.

value of the bright-exciton-TO phonon coupling strength, but a preliminary analysis based on symmetry considerations suggests that our mechanism should be applicable as well.

Summary and outlook

We presented in this work two projects that deal with different aspects of light-matter interactions in crystals and that are based on two different experimental platforms, namely ultracold atoms and exciton-polaritons in semiconductor microcavities.

In the first project we have studied ultracold atoms in optical lattices, in the context of a cavity quantum electrodynamics setup. In detail we combined an optical lattice and a high-finesse optical cavity mode with incommensurate wavelengths to generate a quasiperiodic potential for a single ultracold atom. This system gives rise to an Aubry-André like Hamiltonian, with a modified site-dependent onsite interaction term and allows to investigate the localization transition of the atom in presence of cavity backaction. We first showed that, in the limit where the cavity backaction is negligible ($|C| \ll 1$), we recover the usual Aubry-André model and obtain a critical point that depends on the incommensurability parameter. Then we demonstrated how our modified Aubry-André model arises from the optomechanical coupling of a single atom which is confined in an optical lattice and dispersively interacts with a single mode of a high finesse cavity. In particular we performed a time-scale separation between the cavity and the atomic motion dynamics allowing us to identify an effective potential for the atom. The competition between this effective potential and the optical lattice leads to a resulting quasiperiodic Hamiltonian. Our main contribution was to analyze the properties of the localization transition and to discuss a possible realization of the modified Aubry-André model with existing experimental setups of CQED with cold atoms. We studied the inverse participation ratio and the Lyapunov exponent as a function of the cooperativity and the strength of the quasiperiodic potential. We also monitored the ground state density distribution for different values of the cooperativity. We observed a sharp extended-to-localized transition for all considered values of the cooperativity $C \neq 0$. While for small cooperativities the Aubry-André model is reproduced, the point where the transition takes place as well as the behavior of the Lyapunov exponent change for an increasing cooperativity. This is due to the increasing importance of the cavity backaction which

means that higher harmonics of the Aubry-André potential become relevant. Close to the parameters where the system exhibits an optomechanical resonance we noticed peculiar features in the functional behavior of the Lyapunov exponent and an enhanced asymmetry in the phase diagram of the inverse participation ratio.

A natural extension of our model is the study of the localization transition of N (non)interacting atoms confined in an optical lattice and coupled to the mode of an optical cavity with incommensurate wavelengths. We conjecture that this leads to an amplification of the intracavity photon number and could thus enhance the experimental accessible signal at the cavity output. However, for $N > 1$, the derivation of the effective potential for the atom due to the cavity requires additional assumptions, as here the infinitely long range interactions mediated by the cavity need to be taken into account [43]. For the case of pumped atoms this derivation and the corresponding phase diagram for fixed disorder are reported in Ref. [45, 77]. An interesting next step is thus to derive the N particle Hamiltonian for the pumped cavity case and to study the phase diagram for variable disorder strengths for both pump scenarios. In the perspective of a tunable quantum simulator of disordered systems, this would allow to analyze the interplay between cavity mediated long range interactions, short range interactions due to atom-atom collisions, and disorder.

The second project we presented is based on exciton-polaritons in semiconductor microcavities. We suggest a frequency conversion scheme in order to create THz radiation emission out of visible light. The conversion scheme is based on a chain of interactions: optical cavity photons strongly interact with bright excitons. The bright excitons weakly couple to transverse optical phonons which again strongly couple to THz photons. The crucial part is the exciton-TO-phonon interaction that we derived by specializing the electron-phonon deformation potential interaction to the case of weakly bound excitons interacting with TO phonons. Taking into account the symmetry properties of CdTe, we showed that in zinc blende structured crystals the deformation potential interaction couples light- and heavy-holes states of different polarization. Furthermore, we saw that the TO phonons required for this interaction are polarized along the z direction and propagate in the cavity plane. In order to obtain a nonvanishing coupling between the bright excitons that strongly couple to the cavity and the TO phonons, we found that it is necessary to consider a polarization dependent light-exciton coupling and thus we considered two differently polarized cavity modes. We then discussed the frequency conversion scheme starting with the microscopic model that describes the chain of interactions. We assumed an external pump of the upper exciton-polariton branch with a different polarization than the pump

of the lower exciton-polariton branch. This lead to an effective exciton-polariton-phonon-polariton interaction Hamiltonian that corresponds to difference frequency generation. We determined the population of the phonon-polariton modes by solving the Heisenberg-Langevin equations of the coupled polariton modes to lowest order in the exciton-phonon interaction strength g_{xb}. Here we found that the beating between the exciton-polariton branches, induced by the two pumps, yields an effective pumping of the phonon-polariton branches. The effective pump strength is proportional to g_{xb}. Phonon-polaritons are thus created if the difference between the two pump frequencies of the exciton-polaritons matches the frequency of either lower or upper phonon-polariton branch. In fact this is one of the main strength points of the proposal since the energy difference between upper and lower exciton-polariton branch in CdTe matches the frequency of the phonon-polaritons, which is in the THz range. The phonon-polaritons propagate in the cavity plane and decay into THz photons upon reaching an interface. We estimated the emission power of THz photons as a function of their frequency and their in-plane wavevector. We also discussed that the frequency difference between upper and lower exciton-polariton branch can be adjusted via the wedge shape of the cavity. We further linked our microscopic model of the exciton-TO-phonon interaction to the description with an effective second order susceptibility.

There are many open questions for the future. For instance, it would be interesting to study if our conversion scheme can be transposed to large band gap semiconductors as GaN or ZnO. They provide exciton-polaritons at room temperature and possess wurtzite-type crystal structure. Preliminary symmetry considerations allow us to conjecture that it is possible, but additional calculations are needed in order to determine the exciton-TO phonon coupling strength g_{xb}. Furthermore, we have shown that g_{xb} is inverse proportional to the semiconductor slab volume. The semiconductor microcavity is a first step towards nanostructuring and a next step could be to investigate the exciton-TO-phonon coupling in different confining structures, such as disks or micropillars, in order to get higher values of g_{xb} and engineer the emission direction of the THz photons. One could also link the susceptibility coming from the exciton-TO phonon interaction with the $\chi^{(2)}$ of the bare CdTe crystal. The description of the conversion mechanism using Heisenberg-Langevin equations also opens the door for the study of quantum effects. In a first step, one could solve the Heisenberg-Langevin equations, taking into account the operator nature of $\hat{p}^{\dagger}\hat{u}$ instead of relying on a mean-field like treatment. Another possibility is to include exciton-exciton interactions to our model. Furthermore, in order to describe strongly pumped excitons, we could incorporate the composite character of the excitons in the

derivation of the exciton-TO-phonon interaction, in the spirit of Ref. [109].

Appendix A
The Stark Shift

In this appendix we derive the Stark Shift following the reasoning of Ref. [59]. The notation is slightly modified. We describe the laser field quantum mechanically and assume that the rotating wave approximation is valid and that the Rabi-frequency ϑ is time-independent

$$\hat{H} = \hat{H}_0 + \hat{V},$$

with $\hat{V} = \hbar\vartheta \left(|e\rangle \langle g| \hat{a} + \hat{a}^\dagger |g\rangle \langle e| \right)$ and $\hat{H}_0 = \hbar\omega_0 |e\rangle \langle e|$. The energy shift of the i-th state, with unperturbed energy $\mathcal{E}_i$, due to the perturbation $\hat{V}$, in second-order time-independent perturbation theory, can be calculated according to

$$\delta\mathcal{E}_i = \sum_{j \neq i} \frac{|\langle j| \hat{V} |i\rangle|^2}{\mathcal{E}_i - \mathcal{E}_j}. \tag{A.1}$$

First we calculate the correction to the ground state of the atom. The unperturbed energy is $\mathcal{E}_{|g,n\rangle} = 0 + \hbar\omega n$, where n is the number of photons in the field. The only state, that can be coupled to $|g,n\rangle$ using $\hat{V}$ is $|e, n-1\rangle$. It's energy is $\mathcal{E}_{|e,n-1\rangle} = \hbar\omega_0 + \hbar\omega(n-1)$. It follows

$$\delta\mathcal{E}_{|g,n\rangle} = \frac{|\langle e, n-1| \hat{V} |g,n\rangle|^2}{\hbar\Delta} = \frac{\hbar\vartheta^2}{\Delta}. \tag{A.2}$$

The energy shift, experienced by the excited state can be calculated analogously

$$\delta\mathcal{E}_{|e,n-1\rangle} \frac{|\langle g, n| \hat{V} |e, n-1\rangle|^2}{-\hbar\Delta} = -\frac{\hbar\vartheta^2}{\Delta}. \tag{A.3}$$

In conclusion, the interaction of a far-detuned laser with a two-level atom leads to a level shift (known as 'light shift' or 'ac Stark shift'). The shift experienced by the ground state and the one experienced by the excited state have opposite sign. The shift of the

ground state corresponds to the dipole potential for the two-level atom. If one can assume that the atom is mainly in the ground state, one can interpret the light shifted ground state as the potential that determines the motion of the atom, as depicted in figure (1.2), also taken from [59].

Appendix B

Elimination of the cavity field

In this appendix we show the derivation of the stationary cavity field as given in Eq.(2.21). We show it exemplarily for the case of the pumped cavity, where $\zeta(\hat{x})$ is given by Eq.(2.12). On the timescale δt we can consider that the atomic operator $\hat{a}$ can be replaced by the stationary cavity field $\hat{a}_{\text{st}}$ (= time averaging of δt as given in Eq.(2.20)). Furthermore we can assume that the atomic position doesn't change on the time scale δt

$$\hat{x}(t + \delta t) \approx \hat{x}(t). \tag{B.1}$$

Now we want to solve the differential Eq.(2.17) on the timescale δt, i.e. the time variable t will only run on the timescale δt. The solution of the homogeneous equation has the form

$$\hat{a}_{\text{hom}} = a_0 e^{(i\delta_c - \kappa)t - iU_0 \int_0^t \cos^2(k_c \hat{x}) d\tau} = a_0 e^{(i\Delta_c(\hat{x}) - \kappa)t}$$

with $a_0 = a(t=0)$ a constant, given by the initial conditions and $\Delta_c(\hat{x}) = \delta_c - U_0 \cos^2(k_c \hat{x})$. Here we used Eq. (B.1). In order to solve the inhomogeneous equation we use variation of constants, so we insert the ansatz $\hat{a}_{\text{inhom}} = \tilde{a}(t) e^{(i\Delta_c(\hat{x}) - \kappa)t}$. It follows

$$\tilde{a}(t) = -i\eta \int_0^t d\tau \ e^{-(i\Delta_c(\hat{x}) - \kappa)\tau} + \int_0^t d\tau \ e^{-(i\Delta_c(\hat{x}) - \kappa)\tau} \sqrt{2\kappa} \hat{a}_{\text{in}}(\tau),$$

and thus for the total solution we find

$$\hat{a}_{\text{tot}}(t) = a_0 e^{(i\Delta_c(\hat{x}) - \kappa)t} - i\eta \int_0^t d\tau \ e^{(i\Delta_c(\hat{x}) - \kappa)(t-\tau)} + \int_0^t d\tau \ e^{(i\Delta_c(\hat{x}) - \kappa)(t-\tau)} \sqrt{2\kappa} \hat{a}_{\text{in}}(\tau). \tag{B.2}$$

Because of the timescale separation we can consider that on the timescale δt the atomic position doesn't depend on time and so the integrals can be calculated. We obtain the

annihilation operator of the stationary resonator field by inserting Eq.(B.2) in Eq.(2.20)

$$\hat{a}_{\text{st}}(t) = \frac{1}{\delta t} \int_t^{t+\delta t} dT \, a_0 e^{(i\Delta_c(\hat{x})-\kappa)T} - \frac{i\eta}{\delta t} \int_t^{t+\delta t} dT \int_0^T d\tau \, e^{(i\Delta_c(\hat{x})-\kappa)(T-\tau)}$$

$$+ \frac{\sqrt{2\kappa}}{\delta t} \int_t^{t+\delta t} dT \int_0^T d\tau \, e^{(i\Delta_c(\hat{x})-\kappa)(T-\tau)} \hat{a}_{\text{in}}(\tau),$$

We integrate and neglect terms of the order $\frac{1}{\delta t(\kappa - i\Delta_c(\hat{x}))}$ and $\frac{1}{\delta t(\kappa - i\Delta_c(\hat{x}))^2}$ because the timescale separation requires $\delta t|\delta_c + i\kappa| \gg 1$. Thus it follows

$$\hat{a}_{\text{st}}(t) = \frac{\eta}{\delta_c + i\kappa - U_0 \cos^2(k_c\hat{x})} + \frac{i\sqrt{2\kappa} \, \bar{\hat{a}}_{\text{in}}(t)}{\delta_c + i\kappa - U_0 \cos^2(k_c\hat{x})}, \tag{B.3}$$

with $\bar{\hat{a}}_{\text{in}}$ the input noise averaged over δt. From now on we will assume that we can neglect the averaged input noise term. In order to legitimate this assumtion, we look at the expectation value of $\hat{a}_{\text{st}}\hat{a}_{\text{st}}^\dagger$

$$\langle \hat{a}_{\text{st}}\hat{a}_{\text{st}}^\dagger \rangle = \left\langle \frac{\eta^2}{(\delta_c - U_0 \cos^2(k_c\hat{x}))^2 + \kappa^2} \right\rangle + \left\langle \frac{2\kappa}{(\delta_c - U_0 \cos^2(k_c\hat{x}))^2 + \kappa^2} \right\rangle \langle \bar{\hat{a}}_{\text{in}}\bar{\hat{a}}_{\text{in}}^\dagger \rangle. \tag{B.4}$$

We know that $\langle \hat{a}_{\text{in}}(\tau) \rangle = 0$ and $\langle \hat{a}_{\text{in}}(\tau)\hat{a}_{\text{in}}^\dagger(\tau') \rangle = \delta(\tau - \tau')$, thus we evaluate

$$\langle \bar{\hat{a}}_{\text{in}}\bar{\hat{a}}_{\text{in}}^\dagger \rangle = \frac{1}{\delta t^2} \int_t^{t+\delta t} d\tau \int_t^{t+\delta t} d\tau' \, \langle \hat{a}_{\text{in}}(\tau)\hat{a}_{\text{in}}^\dagger(\tau') \rangle$$

$$= \frac{1}{\delta t^2} \int_t^{t+\delta t} d\tau \int_t^{t+\delta t} d\tau' \, \delta(\tau - \tau') = \frac{1}{\delta t^2} \int_t^{t+\delta t} d\tau = \frac{1}{\delta t}.$$

Hence we can neglect the input noise term if

$$\eta^2 \gg \frac{2\kappa}{\delta t} \gg 2\kappa \sqrt{\frac{4\omega_r k_B T}{\hbar}}. \tag{B.5}$$

where we used Eq.(2.15) as a lower bound for $1/\delta t$.

Appendix C
Optical phonons

This appendix is devoted to the derivation of the dispersion relation for phonons, in order to show that for longwavelength optical phonons the center of mass displacement is zero (see Section 5.2). For simplicity we consider a 1D lattice with two atoms per Wigner-Seitz (primitive) cell, with equilibrium positions ja and $ja + d$. We are interested in the normal modes of the lattice vibrations and will derive them generalizing the calculus done in [129] for two different masses M_1 and M_2. We assume $d \leq a/2$ and only nearest neighbor interaction, and thus the force for pairs separated by d is stronger than for pairs separated by $a - d$: $K \geq G$. We denote with $u_1(ja)$ the displacement of the ion with mass M_1
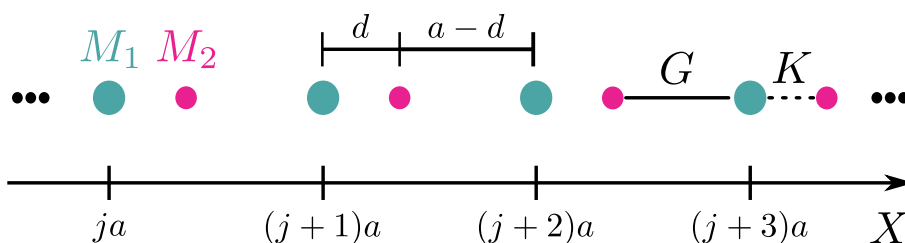

Figure C.1.: Adapted from [129]: The diatomic linear chain with 2 atomic species, connected by springs of alternating strength.

that oscillates around ja and with $u_2(ja)$ the displacement of the ion with mass M_2 that oscillates around $ja + d$. The situation is sketched in figure C.1. The equations of motion are

$$M_1 \ddot{u}_1(ja) = -K \left[u_1(ja) - u_2(ja) \right] - G \left[u_1(ja) - u_2([j-1]a) \right]$$
$$M_2 \ddot{u}_2(ja) = -K \left[u_2(ja) - u_1(ja) \right] - G \left[u_2(ja) - u_1([j+1]a) \right]. \tag{C.1}$$

We make the ansatz

$$u_1(ja) = \epsilon_1 e^{i(kja - \omega t)}$$
$$u_2(ja) = \epsilon_2 e^{i(kja - \omega t)}$$

corresponding to a wave with frequency ω, wave vektor k and polarisation ϵ. Substituting this ansatz into Eq.(C.1) yields the two coupled equations

$$\left[M_1\omega^2 - (K + G)\right]\epsilon_1 + \left[K + Ge^{-ika}\right]\epsilon_2 = 0 \qquad (C.2)$$
$$\left[K + Ge^{ika}\right]\epsilon_1 + \left[M_2\omega^2 - (K + G)\right]\epsilon_2 = 0. \qquad (C.3)$$

They will have a solution if the determinant of the coefficients vanishes,

$$M_1 M_2 \omega^4 - \omega^2(K + G)(M_1 + M_2) + (K + G)^2 - K^2 + G^2 + 2KG\cos(ka) = 0,$$

which is the case for two positive values of ω

$$\Rightarrow \omega^2 = \left(\frac{K + G}{2\mu} \pm \sqrt{\frac{1}{4}\left(\frac{K + G}{M_1 M_2}\right)^2 (M_1 - M_2)^2 + \frac{1}{M_1 M_2}\left(K^2 + G^2 + 2KG\cos(ka)\right)}\right)^{1/2}, \qquad (C.4)$$

where we introduced the reduced mass $\mu = M_1 M_2/(M_1 + M_2)$. The solution containing a $+$ corresponds to the optical branch, whereas the other solution corresponds to the acoustical branch. The eigenvectors fullfill

$$\frac{\epsilon_1}{\epsilon_2} = \frac{-(K + Ge^{-ika})}{M_1\omega^2 - (K + G)}. \qquad (C.5)$$

For optical phonons with small wave vectors (wave vectors close to the center of the Brillouin zone $k \ll \pi/a$) it follows for Eq.(C.4) in lowest order in ka

$$\omega^2 = \frac{K + G}{\mu}. \qquad (C.6)$$

Inserting this into the relation for the eigenvectors for $ka \approx 0$ leads to

$$M_1\epsilon_1 = -M_2\epsilon_2. \qquad (C.7)$$

Note that here we used the notation of [129]. In Chapter 5 we use the notation of [105]. They differ in the definition of the polarization vector by a factor of $\sqrt{M}$

$$\epsilon_1^{\text{Ascroft}}\sqrt{M_1} = \epsilon_1^{\text{Madelung}}. \tag{C.8}$$

Appendix D

Second quantization of the deformation potential

In this appendix we derive the Hamiltonian of the exciton-TO phonon interaction as given by Eq.(5.23). For this purpose we want to write the change in the electron's potential $\boldsymbol{V}_{DP}$ in the second quantization. We consider electrons weakly bound to holes to form Wannier excitons and neglect the internal structure of the electron-hole pair.

An exciton with wave vector $\boldsymbol{K}'$ of the center-of-mass motion and inner quantum number λ', where the electron is in the conduction band c' and the hole in valence band v' is described by the many-body wave function $\Psi_{\lambda',\boldsymbol{K}',v',c'}(\boldsymbol{x}_1, \boldsymbol{x}_2, ...\boldsymbol{x}_N)$ defined in Eq.(5.25). For the second quantization of the deformation potential operator we start with a general exciton wave function which sums over all possible quantum numbers

$$\Psi(\boldsymbol{x}_1, \boldsymbol{x}_2, ...\boldsymbol{x}_N) = \sum_{\lambda',\boldsymbol{K}',v',c'} \Psi_{\lambda',\boldsymbol{K}',v',c'}(\boldsymbol{x}_1, \boldsymbol{x}_2, ...\boldsymbol{x}_N). \tag{D.1}$$

We assume that we only deal with $\lambda' = 1s$ excitons. Furthermore the band structure of CdTe as sketched in figure 5.3 suggests to consider two valence bands (heavy and light hole bands v_{hh} and v_{lh} respectively) and one conduction band c'. In the ground state N electrons are in the valence band v_{hh} and N are in v_{lh}. In the excitonic state one electron can be taken either from the valence band v_{hh} or from the valence band v_{lh} and be excited to the nondegenerate conduction band c'. Using the notation suggested in Eq.(4.12), our general wave function reads

$$\Psi(\boldsymbol{x}_1, \boldsymbol{x}_2, ...\boldsymbol{x}_N) = \frac{1}{\sqrt{N}} \sum_{\boldsymbol{K}',m',l'} \sum_{v'=v_{hh},v_{lh}} e^{i\boldsymbol{K}'\cdot\boldsymbol{R}_{m'}} U_{1s,\boldsymbol{K}',v',c'}(\boldsymbol{R}_{l'}) A_{v',c'}(m', m' + l'). \tag{D.2}$$

$A_{v',c'}(m', m' + l')$ is the Slater determinant describing the configuration in which a valence electron at site m' is excited from valence band v' into the conduction band c' at the $m' + l'$th site. The single-particle wave functions in the Slater determinant are given by Wannier functions [62]. Choosing eg an electron from site m' in the valence band v_{hh} that is promoted to site $m' + l'$ in the conduction band c' the Slater determinant has the form[1]

$$A_{v_{hh},c'}(m', m' + l') =$$

$$\frac{1}{\sqrt{(2N)!}} \begin{vmatrix} w_{v_{hh},\boldsymbol{R}_1}(\boldsymbol{x}_1) & w_{v_{hh},\boldsymbol{R}_1}(\boldsymbol{x}_2) & \dots & w_{v_{hh},\boldsymbol{R}_1}(\boldsymbol{x}_{m'}) & \dots & w_{v_{hh},\boldsymbol{R}_1}(\boldsymbol{x}_{2N}) \\ w_{v_{lh},\boldsymbol{R}_1}(\boldsymbol{x}_1) & w_{v_{lh},\boldsymbol{R}_1}(\boldsymbol{x}_2) & \dots & w_{v_{lh},\boldsymbol{R}_1}(\boldsymbol{x}_{m'}) & \dots & w_{v_{lh},\boldsymbol{R}_1}(\boldsymbol{x}_{2N}) \\ w_{v_{hh},\boldsymbol{R}_2}(\boldsymbol{x}_1) & w_{v_{hh},\boldsymbol{R}_2}(\boldsymbol{x}_2) & \dots & w_{v_{hh},\boldsymbol{R}_2}(\boldsymbol{x}_{m'}) & \dots & w_{v_{hh},\boldsymbol{R}_2}(\boldsymbol{x}_{2N}) \\ w_{v_{lh},\boldsymbol{R}_2}(\boldsymbol{x}_1) & w_{v_{lh},\boldsymbol{R}_2}(\boldsymbol{x}_2) & \dots & w_{v_{lh},\boldsymbol{R}_2}(\boldsymbol{x}_{m'}) & \dots & w_{v_{lh},\boldsymbol{R}_2}(\boldsymbol{x}_{2N}) \\ \vdots & \vdots & \vdots & \vdots & \vdots & \vdots \\ w_{c',\boldsymbol{R}_{m'+l'}}(\boldsymbol{x}_1) & w_{c',\boldsymbol{R}_{m'+l'}}(\boldsymbol{x}_2) & \dots & w_{c',\boldsymbol{R}_{m'+l'}}(\boldsymbol{x}_{m'}) & \dots & w_{c',\boldsymbol{R}_{m'+l'}}(\boldsymbol{x}_{2N}) \\ w_{v_{lh},\boldsymbol{R}_{m'}}(\boldsymbol{x}_1) & w_{v_{lh},\boldsymbol{R}_{m'}}(\boldsymbol{x}_2) & \dots & w_{v_{lh},\boldsymbol{R}_{m'}}(\boldsymbol{x}_{m'}) & \dots & w_{v_{lh},\boldsymbol{R}_{m'}}(\boldsymbol{x}_{2N}) \\ \vdots & \vdots & \vdots & \vdots & \vdots & \vdots \\ w_{v_{hh},\boldsymbol{R}_N}(\boldsymbol{x}_1) & w_{v_{hh},\boldsymbol{R}_N}(\boldsymbol{x}_2) & \dots & w_{v_{hh},\boldsymbol{R}_N}(\boldsymbol{x}_m) & \dots & w_{v_{hh},\boldsymbol{R}_N}(\boldsymbol{x}_{2N}) \\ w_{v_{lh},\boldsymbol{R}_N}(\boldsymbol{x}_1) & w_{v_{lh},\boldsymbol{R}_N}(\boldsymbol{x}_2) & \dots & w_{v_{lh},\boldsymbol{R}_N}(\boldsymbol{x}_m) & \dots & w_{v_{lh},\boldsymbol{R}_N}(\boldsymbol{x}_{2N}) \end{vmatrix} . \quad \text{(D.3)}$$

It consists of $2N$ single-electron Wannier functions, out of which $N-1$ electrons occupy the valence band v_{hh}, N occupy the valence band v_{lh} and 1 electron occupies the conduction band c'. The Wannier function for an electron in the valence band at $\boldsymbol{x}_1$, which is centered at lattice site m' is denoted as $w_{c',\boldsymbol{R}_{m'}}(\boldsymbol{x}_1) = w_{c'}(\boldsymbol{x}_1 - \boldsymbol{R}_{m'})$. The normalization of the Wannier functions reads

$$\int_V w^*_{c',\boldsymbol{R}_{m'}}(\boldsymbol{x}) w_{c,\boldsymbol{R}_m}(\boldsymbol{x}) \, d^3x = \delta_{c,c'}\delta_{\boldsymbol{R}_{m'},\boldsymbol{R}_m}, \quad \text{(D.4)}$$

where V indicates the volume of the entire crystal.

An alternative way of representing the Slater determinant of Eq.(D.3) can be also written in terms of the antisymmetrizing operator $\hat{\mathcal{A}}$

$$A_{v_{hh},c'}(m', m' + l') = \\ \sqrt{(2N)!}\hat{\mathcal{A}} \left(w_{v_{hh},\boldsymbol{R}_1}(\boldsymbol{x}_1) w_{v_{lh},\boldsymbol{R}_1}(\boldsymbol{x}_2)...w_{c',\boldsymbol{R}_{m'+l'}}(\boldsymbol{x}_{2m'}) w_{v_{lh},\boldsymbol{R}_{m'}}(\boldsymbol{x}_{2m'+1})... \right), \quad \text{(D.5)}$$

---

[1]This is a generalization of [151] to two bands.

where

$$\hat{\mathcal{A}} = \frac{1}{(2N)!} \sum_{\sigma \in S_N} (-1)^\sigma \hat{\sigma}, \tag{D.6}$$

with $\hat{\sigma}$ the permutation operator and the sum going over all possible permutations. We note that $\hat{\mathcal{A}}$ is Hermitian and $\hat{\mathcal{A}}^2 = \hat{\mathcal{A}}$.

In order to write the deformation potential in second quantization we follow the approach of [152]: We project an exciton wave function $\chi(\boldsymbol{x}_1, \boldsymbol{x}_2, ...\boldsymbol{x}_N)$ with a fixed set of quantum numbers, choosen examplarily as $1s, \boldsymbol{K}, v_{hh}, c$, onto the deformation potential operator applied to the general excitonic wave function $\Psi(\boldsymbol{x}_1, ...\boldsymbol{x}_N)$ as defined in Eq.(D.2) and integrate over all electron positions

$$\int d^3 x_1 \int d^3 x_2 ... \int d^3 x_N \ \chi^*(\boldsymbol{x}_1, ...\boldsymbol{x}_N) \sum_{p=1}^N \boldsymbol{V}_{DP}(\boldsymbol{x}_p - \boldsymbol{X}_n) \Psi(\boldsymbol{x}_1, ...\boldsymbol{x}_N), \tag{D.7}$$

with

$$\chi(\boldsymbol{x}_1, ...\boldsymbol{x}_N) = e^{i\boldsymbol{K} \cdot \boldsymbol{R}_m} U_{1s, \boldsymbol{K}, v_{hh}, c}(\boldsymbol{R}_l) A_{v,c}(m, m + l). \tag{D.8}$$

In the second quantization procedure one replaces the sum over all electrons by the sum over the quantum numbers and introduces occupation numbers of a given state [152]. The deformation potential operator is a single-particle operator and we will show in the following that it can only link two exciton states that differ either in their hole or in their electron state (Slater Condon rules [153]). Therefore we investigate which terms are non-zero after integration over the positions of the electrons. For this purpose we use that the deformation potential operator $\boldsymbol{V}_{DP}$ is invariant under relabelling of the electrons and thus commutes with the antisymmetrizing operator

$$\hat{\mathcal{A}} \boldsymbol{V}_{DP} \hat{\mathcal{A}} = \hat{\mathcal{A}}^2 \boldsymbol{V}_{DP} = \hat{\mathcal{A}} \boldsymbol{V}_{DP}.$$

It is helpful to point out that for $m \neq m'$

$$A_{v_{hh},c'}(m',m'+l') =$$
$$\sqrt{(2N)!}\hat{\mathcal{A}}\left(...w_{v_{hh},\boldsymbol{R}_m}(\boldsymbol{x}_{2m})w_{v_{lh},\boldsymbol{R}_m}(\boldsymbol{x}_{2m+1})...w_{c',\boldsymbol{R}_{m'+l'}}(\boldsymbol{x}_{2m'})w_{v_{lh},\boldsymbol{R}_{m'}}(\boldsymbol{x}_{2m'+1})...\right),$$
$$A_{v_{lh},c'}(m',m'+l') =$$
$$\sqrt{(2N)!}\hat{\mathcal{A}}\left(...w_{v_{hh},\boldsymbol{R}_m}(\boldsymbol{x}_{2m})w_{v_{lh},\boldsymbol{R}_m}(\boldsymbol{x}_{2m+1})...w_{v_{hh},\boldsymbol{R}_{m'}}(\boldsymbol{x}_{2m'})w_{c',\boldsymbol{R}_{m'+l'}}(\boldsymbol{x}_{2m'+1})...\right),$$
$$A_{v_{hh},c}(m,m+l) =$$
$$\sqrt{(2N)!}\hat{\mathcal{A}}\left(...w_{c,\boldsymbol{R}_{m+l}}(\boldsymbol{x}_{2m})w_{v_{lh},\boldsymbol{R}_m}(\boldsymbol{x}_{2m+1})...w_{v_{hh},\boldsymbol{R}_{m'}}(\boldsymbol{x}_{2m'})w_{v_{lh},\boldsymbol{R}_{m'}}(\boldsymbol{x}_{2m'+1})...\right). \quad \text{(D.9)}$$

Let's us now first consider only zeroth order terms in the permutations. This means that $\hat{\mathcal{A}} = \frac{1}{N!}\mathbb{1}$. The only nonvanishing terms are:

- terms with the same hole state (position $m = m'$ and band index $v' = v_{hh}$) and the same electron state (position $m' + l' = m + l$ and band index $c = c'$)

$$\int d^3x_1\, w^*_{v_{hh},\boldsymbol{R}_1}(\boldsymbol{x}_1)\boldsymbol{V}_{DP}(\boldsymbol{x}_1)w_{v_{hh},\boldsymbol{R}_1}(\boldsymbol{x}_1)...\underbrace{\int d^3x_{2m}\, w^*_{c,\boldsymbol{R}_{m+l}}(\boldsymbol{x}_{2m})w_{c,\boldsymbol{R}_{m+l}}(\boldsymbol{x}_{2m})}_{=1} +$$
$$...\int d^3x_2\, w^*_{v_{hh},\boldsymbol{R}_1}(\boldsymbol{x}_2)\boldsymbol{V}_{DP}(\boldsymbol{x}_2)w_{v_{hh},\boldsymbol{R}_1}(\boldsymbol{x}_2)...$$

- terms with the same hole state (position $m = m'$ and band index $v' = v_{hh}$) and different electron state

$$\underbrace{\int d^3x_1\, w^*_{v_{hh},\boldsymbol{R}_1}(\boldsymbol{x}_1)w_{v_{hh},\boldsymbol{R}_1}(\boldsymbol{x}_1)}_{=1}...\int d^3x_{2m}\, w^*_{c,\boldsymbol{R}_{m+l}}(\boldsymbol{x}_{2m})\boldsymbol{V}_{DP}(\boldsymbol{x}_{2m})w_{c',\boldsymbol{R}_{m'+l'}}(\boldsymbol{x}_{2m})$$

  Only this one term of the sum survives in 3 possible cases:

  - position and band index are different $m + l \neq m' + l' \wedge c \neq c'$

  - same position and different band index $m + l = m' + l' \wedge c \neq c'$

  - different position and same band index $m + l \neq m' + l' \wedge c = c'$

All the other terms vanish, for example

- terms with same electron state (position $m' + l' = m + l$ and band index $c = c'$) and

different hole state

$$\int d^3x_1 \; w^*_{v_{hh},\boldsymbol{R}_1}(\boldsymbol{x}_1)\boldsymbol{V}_{DP}(\boldsymbol{x}_1)w_{v_{hh},\boldsymbol{R}_1}(\boldsymbol{x}_1)...$$

$$\underbrace{\int d^3x_{2m} \; w^*_{c,\boldsymbol{R}_{m+l}}(\boldsymbol{x}_{2m})w_{v_{hh},\boldsymbol{R}_m}(\boldsymbol{x}_{2m})}_{=0} \; ... \; \underbrace{\int d^3x_{2m'+1} \; w^*_{v_{lh},\boldsymbol{R}_m}(\boldsymbol{x}_{2m'+1})w_{c',\boldsymbol{R}_{m'+l'}}(\boldsymbol{x}_{2m'+1})}_{=0}$$

The deformation potential can prevent only one of the two integrals over x_{2m} and x_{2m+1} from being zero. Therefor there is no nonzero contribution for two excitonic states with the same electron state and different hole state, considering only zeroth order in the permutations.

Now we check which terms are nonvanishing in first order in the permutations, which means that we exchange two electrons: $\hat{\mathcal{A}} = -\frac{1}{N!}\sigma(\boldsymbol{x}_{otto}, \boldsymbol{x}_{eva})$. The nonvanishing terms are terms with the same electron state (position $m' + l' = m + l$ and band index $c = c'$) and different hole state:

- If the two holes have the same band index $v' = v_{hh}$ but different positions $m \neq m'$, we get the only nonvanishing term by exchanging the quantum numbers of electron $2m'$ with those of electron $2m$, so that the wave function reads

$$\chi(\boldsymbol{x}_1, ...\sigma(\boldsymbol{x}_{2m})...\sigma(\boldsymbol{x}_{2m'})...\boldsymbol{x}_N) \propto$$
$$\left(...w_{v_{hh},\boldsymbol{R}_{m'}}(\boldsymbol{x}_{2m})w_{v_{lh},\boldsymbol{R}_m}(\boldsymbol{x}_{2m+1})...w_{c,\boldsymbol{R}_{m+l}}(\boldsymbol{x}_{2m'})w_{v_{lh},\boldsymbol{R}_{m'}}(\boldsymbol{x}_{2m'+1})...\right).$$

The only nonvanishing term is

$$-\int d^3x_{2m} \; w^*_{v_{hh},\boldsymbol{R}_{m'}}(\boldsymbol{x}_{2m})\boldsymbol{V}_{DP}(\boldsymbol{x}_{2m})w_{v_{hh},\boldsymbol{R}_m}(\boldsymbol{x}_{2m}).$$

- If the two holes have a different band index $v' \neq v_{hh}$ and a different hole position $m \neq m'$, we get the only nonvanishing term by exchanging the quantum numbers of electron $2m$ with those of electron $2m' + 1$, so that the wave function reads

$$\chi(\boldsymbol{x}_1, ...\sigma(\boldsymbol{x}_{2m})...\sigma(\boldsymbol{x}_{2m'+1})...\boldsymbol{x}_N) \propto$$
$$\left(...w_{v_{lh},\boldsymbol{R}_{m'}}(\boldsymbol{x}_{2m})w_{v_{lh},\boldsymbol{R}_m}(\boldsymbol{x}_{2m+1})...w_{v_{hh},\boldsymbol{R}_{m'}}(\boldsymbol{x}_{2m'})w_{c,\boldsymbol{R}_{m+l}}(\boldsymbol{x}_{2m'+1})...\right).$$

143

The only nonvanishing term is

$$-\int d^3x_{2m}\ w^*_{v_{lh},\boldsymbol{R}_{m'}}(\boldsymbol{x}_{2m})\boldsymbol{V}_{DP}(\boldsymbol{x}_{2m})w_{v_{hh},\boldsymbol{R}_m}(\boldsymbol{x}_{2m}).$$

- If the two holes have a different band index $v' \neq v_{hh}$ and the same hole position $m = m'$, we get the only nonvanishing term by exchanging the quantum numbers of electron $2m$ with those of electron $2m + 1$, so that the wave function reads

$$\chi(\boldsymbol{x}_1, ...\sigma(\boldsymbol{x}_{2m})...\sigma(\boldsymbol{x}_{2m+1})...\boldsymbol{x}_N) \propto$$
$$\big(w_{v_{hh},\boldsymbol{R}_1}(\boldsymbol{x}_1)w_{v_{lh},\boldsymbol{R}_1}(\boldsymbol{x}_2)...w_{c,\boldsymbol{R}_{m+l}}(\boldsymbol{x}_{2m})w_{v_{lh},\boldsymbol{R}_m}(\boldsymbol{x}_{2m+1})...\big) \tag{D.10}$$

The only nonvanishing term is

$$-\int d^3x_{2m}\ w^*_{v_{lh},\boldsymbol{R}_m}(\boldsymbol{x}_{2m})\boldsymbol{V}_{DP}(\boldsymbol{x}_{2m})w_{v_{hh},\boldsymbol{R}_m}(\boldsymbol{x}_{2m}). \tag{D.11}$$

Thus we can write the deformation potential in second quantization

$$\sum_p \boldsymbol{V}_{DP}(\boldsymbol{x}_p) \to \sum_{\substack{\boldsymbol{K},\boldsymbol{K}',\lambda,\lambda' \\ v,v',c,c'}} \langle\lambda,\boldsymbol{K},v,c|\,\boldsymbol{V}_{DP}\,|\lambda',\boldsymbol{K}',v',c'\rangle\, s^\dagger_{\lambda,\boldsymbol{K}}(v,c)s_{\lambda',\boldsymbol{K}'}(v',c') \tag{D.12}$$

taking into account that the exciton states differ either in the hole or in the electron state. Here $s^\dagger_{\boldsymbol{K},\lambda}(c,v)$ $[s_{\boldsymbol{K}',\lambda'}(v',c')]$ creates [annihilates] an exciton with wave vector $\boldsymbol{K}$ $[\boldsymbol{K}']$ of the center-of-mass motion and inner quantum number λ $[\lambda']$, where the electron is in the conduction band c $[c']$ and the hole in valence band v $[v']$. In position representation the exciton state $|\lambda',\boldsymbol{K}',v',c'\rangle$ is given by the many-body wave function

$$\Psi_{c',v',\lambda',\boldsymbol{K}'}(\boldsymbol{x}_1,\boldsymbol{x}_2,...\boldsymbol{x}_N) = \frac{1}{\sqrt{N}}\sum_{m',l'}e^{i\boldsymbol{K}'\cdot\boldsymbol{R}_{m'}}U_{\lambda',\boldsymbol{K}',v',c'}(\boldsymbol{R}_{l'})A_{v',c'}(m',m'+l'). \tag{D.13}$$

The Hamiltonian in second quantization is given by Eq.(5.40), with coupling constant $G_{\boldsymbol{q},TO}(\boldsymbol{K}hh^-,\boldsymbol{K}'lh^+)$ as defined by Eq.(5.41). We want to simplify the expression for the coupling constant and thus evaluate the matrix element: according to the considerations mentioned above (Slater Condon rules) the deformation potential operator can couple two

excitonic states that differ either in their hole or in their electron state. Thus it follows

$$
\langle \lambda, \boldsymbol{K}, v, c | \, \boldsymbol{V}_{DP} \, | \lambda', \boldsymbol{K}', v', c' \rangle
$$

$$
= \frac{1}{N} \sum_{\substack{m,m' \\ l,l'}} U^*_{\lambda,\boldsymbol{K},v,c}(\boldsymbol{R}_l) U_{\lambda',\boldsymbol{K}',v',c'}(\boldsymbol{R}_{l'}) e^{i\boldsymbol{K}' \cdot \boldsymbol{R}_{m'}} e^{-i\boldsymbol{K} \cdot \boldsymbol{R}_m}
$$

$$
\left\{ -\delta_{c,c'}\delta_{m+l,m'+l'} \int_V w^*_{v',\boldsymbol{R}_{m'}}(\boldsymbol{x}) \boldsymbol{V}_{DP}(\boldsymbol{x} - \boldsymbol{X}_n) w_{v,\boldsymbol{R}_m}(\boldsymbol{x}) \, d^3x \right.
$$

$$
\left. + \delta_{m,m'}\delta_{v,v'} \int_V w^*_{c,\boldsymbol{R}_{m+l}}(\boldsymbol{x}) \boldsymbol{V}_{DP}(\boldsymbol{x} - \boldsymbol{X}_n) w_{c',\boldsymbol{R}_{m'+l'}}(\boldsymbol{x}) \, d^3x \right\}
\qquad (D.14)
$$

Appendix E

Transformation in the Luttinger-Kohn basis

In this appendix we show that at $\boldsymbol{K} - \boldsymbol{K}' = 0$ the expression of the matrix elements $\langle v'| \, \boldsymbol{V}_{DP} \, |v\rangle$ in the Bloch and Luttinger-Kohn basis [124, 135] coincide. We used this property in Section 5.4.

We start by introducing the Luttinger-Kohn basis in coordinate representation [135]

$$\chi_{v,\boldsymbol{k}}(\boldsymbol{x}) = e^{i\boldsymbol{k}\cdot\boldsymbol{x}}\psi_{v,\boldsymbol{k}_0}(\boldsymbol{x}) = \frac{e^{i(\boldsymbol{k}+\boldsymbol{k}_0)\cdot\boldsymbol{x}}}{\sqrt{V}}u_{v,\boldsymbol{k}_0}(\boldsymbol{x}), \tag{E.1}$$

where $\boldsymbol{k}_0$ denotes a band extremum. The Luttinger-Kohn functions are normalized $\int_V \chi^*_{v',\boldsymbol{k}'}(\boldsymbol{x})\chi_{v,\boldsymbol{k}}(\boldsymbol{x}) \, d^3x = \delta_{v,v'}\delta_{\boldsymbol{k},\boldsymbol{k}'}$.

We will only consider the situation where the band extremum is in the zone center $\boldsymbol{k}_0 = 0$ (Γ point). A general Bloch function with band index v and wave vector $\boldsymbol{k}$ can be expanded in terms of the Luttinger-Kohn functions according to [135]

$$\psi_{v,\boldsymbol{k}}(\boldsymbol{x}) = \frac{e^{i\boldsymbol{k}\cdot\boldsymbol{x}}}{\sqrt{V}}u_{v,\boldsymbol{k}}(\boldsymbol{x}) = \frac{e^{i\boldsymbol{k}\cdot\boldsymbol{x}}}{\sqrt{V}}\sum_{\mathcal{V}}\beta_{v,\mathcal{V}}(\boldsymbol{k})u_{\mathcal{V},0}(\boldsymbol{x}) = \sum_{\mathcal{V}}\beta_{v,\mathcal{V}}(\boldsymbol{k})\chi_{\mathcal{V},\boldsymbol{k}}(\boldsymbol{x}), \tag{E.2}$$

where the index $\mathcal{V}$ runs over all bands that are taken into account. In order to perform the change from Bloch to Luttinger-Kohn basis, we distinguish two cases:

1) the holes are in the same valence band $v = v'$. The basis change is performed by

summing over all possible conduction bands and thus the new operators read

$$s_{\lambda,\boldsymbol{K}}^{\dagger}(v,c) = \sum_d \langle \boldsymbol{K},d | \boldsymbol{K},c\rangle z_{\lambda,\boldsymbol{K}}^{\dagger}(v,d)$$

$$= \sum_d \int_V \chi_{d,\boldsymbol{K}}^*(\boldsymbol{x})\psi_{c,\boldsymbol{K}}(\boldsymbol{x}) \ d^3x \ \ z_{\lambda,\boldsymbol{K}}^{\dagger}(v,d)$$

$$= \sum_{d,\gamma} \beta_{c,\gamma}(\boldsymbol{K}) \underbrace{\int_V \chi_{d,\boldsymbol{K}}^*(\boldsymbol{x})\chi_{\gamma,\boldsymbol{K}}(\boldsymbol{x}) \ d^3x}_{\delta_{d,\gamma}} \ \ z_{\lambda,\boldsymbol{K}}^{\dagger}(v,d)$$

$$= \sum_d \beta_{c,d}(\boldsymbol{K}) z_{\lambda,\boldsymbol{K}}^{\dagger}(v,d)$$

$$s_{\lambda',\boldsymbol{K}'}(v',c') = \sum_{d'} \langle \boldsymbol{K}',c' | \boldsymbol{K}',d'\rangle z_{\lambda',\boldsymbol{K}'}(v,d') = \sum_{d'} \beta_{c',d'}^*(\boldsymbol{K}') z_{\lambda',\boldsymbol{K}'}(v,d').$$

2) the electrons are in the same conduction band $c = c'$. The basis change is performed by summing over all possible valence bands. The new operators read

$$s_{\lambda,\boldsymbol{K}}^{\dagger}(v,c) = \sum_d \langle \boldsymbol{K},v | \boldsymbol{K},d\rangle z_{\lambda,\boldsymbol{K}}^{\dagger}(d,c) = \sum_d \beta_{v,d}^*(\boldsymbol{K}) z_{\lambda,\boldsymbol{K}}^{\dagger}(d,c)$$

$$s_{\lambda',\boldsymbol{K}'}(v',c') = \sum_{d'} \langle \boldsymbol{K}',d' | \boldsymbol{K}',v'\rangle z_{\lambda',\boldsymbol{K}'}(d',c') = \sum_{d'} \beta_{v',d'}(\boldsymbol{K}') z_{\lambda',\boldsymbol{K}'}(d',c').$$

Note that in the definition of the new operators the expansion coefficients $\beta_{v,d}^*$ and $\beta_{v',d'}$ of the creation and annihilation operator are inverted with respect to case 1) because the creation of an exciton corresponds to the creation of an electron in a conduction band and to the annihilation of a hole in a valence band.

$z_{\boldsymbol{K},\lambda}^{\dagger}(d,c) \ [z_{\boldsymbol{K}',\lambda'}(d',c')]$ creates [annihilates] an exciton with wave vector $\boldsymbol{K} \ [\boldsymbol{K}']$ of the center-of-mass motion and inner quantum number $\lambda \ [\lambda']$, where the electron is in the conduction band $c \ [c']$ and the hole in valence band $d \ [d']$. Using Eq.(E.2) and distinguishing

the two cases mentionned above, the Hamiltonian reads in the Luttinger-Kohn basis

$$H_{\text{exc-TO}} = - \sum_{\substack{\boldsymbol{q},\boldsymbol{K},\boldsymbol{K}' \\ \lambda,\lambda'}} \left(\frac{\hbar N}{2\mu\omega_{\boldsymbol{q},TO}a^2} \right)^{1/2} \boldsymbol{\epsilon}_{TO} \left(b_{-\boldsymbol{q},TO}^\dagger + b_{\boldsymbol{q},TO} \right) \delta_{\boldsymbol{q},\boldsymbol{K}-\boldsymbol{K}'} \times$$

$$\left[\sum_{\substack{c,c',\mathcal{C},\mathcal{C}' \\ d,d'}} q_e(\lambda\boldsymbol{K}vc, \lambda'\boldsymbol{K}'vc') \int_V \beta_{c,d}^*(\boldsymbol{K})\chi_{d,\boldsymbol{K}}^*(\boldsymbol{x}')\boldsymbol{V}_{DP}(\boldsymbol{x}') \, \beta_{c',d'}(\boldsymbol{K}')\chi_{d',\boldsymbol{K}'}(\boldsymbol{x}') \, d^3x' \right.$$

$$\beta_{c,\mathcal{C}}(\boldsymbol{K})\beta_{c',\mathcal{C}'}^*(\boldsymbol{K}')z_{\lambda,\boldsymbol{K}}^\dagger(v,\mathcal{C})z_{\lambda',\boldsymbol{K}'}(v,\mathcal{C}')$$

$$- \sum_{\substack{v,v',\mathcal{V},\mathcal{V}' \\ d,d'}} q_h(\lambda\boldsymbol{K}vc, \lambda'\boldsymbol{K}'v'c) \int_V \beta_{v',d'}^*(\boldsymbol{K}')\chi_{d',\boldsymbol{K}'}^*(\boldsymbol{x}')\boldsymbol{V}_{DP}(\boldsymbol{x}') \, \beta_{v,d}(\boldsymbol{K})\chi_{d,\boldsymbol{K}}(\boldsymbol{x}') \, d^3x'$$

$$\left. \beta_{v,\mathcal{V}}^*(\boldsymbol{K})\beta_{v',\mathcal{V}'}(\boldsymbol{K}')z_{\lambda,\boldsymbol{K}}^\dagger(\mathcal{V},c)z_{\lambda',\boldsymbol{K}'}(\mathcal{V}',c) \right]. \tag{E.3}$$

Now we perform the sum over v, v', c, c', assuming that we can neglect the dependence of q_e and q_h on v, v', c, c'. Using $\sum_v \beta_{v,d}(\boldsymbol{K})\beta_{v,\mathcal{V}}^*(\boldsymbol{K}) = \delta_{d,\mathcal{V}}$ it follows

$$H_{\text{exc-TO}} = - \sum_{\substack{\boldsymbol{q},\boldsymbol{K},\boldsymbol{K}' \\ \lambda,\lambda', \\ \mathcal{V},\mathcal{V}', \\ \mathcal{C},\mathcal{C}'}} G_{\boldsymbol{q},TO}(\mathcal{C}\mathcal{V}\lambda\boldsymbol{K},\mathcal{C}'\mathcal{V}'\lambda'\boldsymbol{K}')z_{\lambda,\boldsymbol{K}}^\dagger(\mathcal{V},\mathcal{C})z_{\lambda',\boldsymbol{K}'}(\mathcal{V}',\mathcal{C}') \left(b_{-\boldsymbol{q},TO}^\dagger + b_{\boldsymbol{q},TO} \right) \delta_{\boldsymbol{q},\boldsymbol{K}-\boldsymbol{K}'}$$

$$\tag{E.4}$$

with

$$G_{\boldsymbol{q},TO}(\mathcal{C}\mathcal{V}\lambda\boldsymbol{K},\mathcal{C}'\mathcal{V}'\lambda'\boldsymbol{K}') = \left(\frac{\hbar N}{2\mu\omega_{\boldsymbol{q},TO}a^2} \right)^{1/2} \boldsymbol{\epsilon}_{TO} \cdot [-q_h(\mathcal{C}\mathcal{V}\lambda\boldsymbol{K},\mathcal{C}\mathcal{V}'\lambda'\boldsymbol{K}')\theta_{\mathcal{V}',\mathcal{V}}(\boldsymbol{K}-\boldsymbol{K}')\delta_{\mathcal{C},\mathcal{C}'}$$

$$+ q_e(\mathcal{C}\mathcal{V}\lambda\boldsymbol{K},\mathcal{C}'\mathcal{V}\lambda'\boldsymbol{K}')\theta_{\mathcal{C},\mathcal{C}'}(\boldsymbol{K}-\boldsymbol{K}')\delta_{\mathcal{V},\mathcal{V}'}], \tag{E.5}$$

and

$$\theta_{n,n'}(\boldsymbol{K}-\boldsymbol{K}') = \frac{1}{V} \int_V e^{-i(\boldsymbol{K}-\boldsymbol{K}')\cdot\boldsymbol{x}'} u_{n,0}^*(\boldsymbol{x}')\boldsymbol{V}_{DP}(\boldsymbol{x}') \, u_{n',0}(\boldsymbol{x}') \, d^3x'. \tag{E.6}$$

For long wavelength TO phonons (small $\boldsymbol{q} = \boldsymbol{K} - \boldsymbol{K}'$) we neglect the wave vector dependence of this integral [125] and recover Eq.(5.35).

Appendix F

Time reversal

We want to understand in more details the form of table 5.2. In this appendix we will show that we can derive all nonvanishing elements starting with just one known element. We consider that we know just one matrix element, namely

$$\boldsymbol{\epsilon}_{TO} \cdot \left\langle hh^- \right| \left\langle S \uparrow \right| \boldsymbol{V}_{DP} \left| S \uparrow \right\rangle \left| lh^+ \right\rangle \equiv j \tag{F.1}$$

As the deformtion potential operator is hermitian it follows directly that

$$\boldsymbol{\epsilon}_{TO} \cdot \left(\left\langle S \uparrow \right| \left\langle lh^+ \right| \boldsymbol{V}_{DP} \left| hh^- \right\rangle \left| S \uparrow \right\rangle \right)^* = j^*. \tag{F.2}$$

We now consider the time reversal operator $\hat{K}$ as introduced in Ref. [124]. Its effect on a given spinor wave function in position representation $\Psi(\boldsymbol{x})$ (considering a spin $s = 1/2$ particle, which in our case will be the hole) consists in taking the complex conjugate and multiplying by the Pauli matrix σ_y

$$\hat{K}\Psi(\boldsymbol{x}) = \hat{K} \begin{pmatrix} \Psi_1(\boldsymbol{x}) \\ \Psi_2(\boldsymbol{x}) \end{pmatrix} = \sigma_y \Psi^*(\boldsymbol{x}) = \begin{pmatrix} 0 & -i \\ i & 0 \end{pmatrix} \begin{pmatrix} \Psi_1^*(\boldsymbol{x}) \\ \Psi_2^*(\boldsymbol{x}) \end{pmatrix} = \begin{pmatrix} -i\Psi_2^*(\boldsymbol{x}) \\ i\Psi_1^*(\boldsymbol{x}) \end{pmatrix}, \tag{F.3}$$

where we used the notation $\Psi_1(\boldsymbol{x}) = \left\langle \uparrow, \boldsymbol{x} | \Psi \right\rangle$ and $\Psi_2 = \left\langle \downarrow, \boldsymbol{x} | \Psi \right\rangle$.

The Luttinger-Kohn functions describing the possible valence band states, Eq.(5.36),

are linked via the time reversal operator

$$\hat{K}\Psi_{hh^+}(\boldsymbol{x}) = \hat{K}\begin{pmatrix} \frac{1}{\sqrt{2}}(X+iY) \\ 0 \end{pmatrix} = \begin{pmatrix} 0 & -i \\ i & 0 \end{pmatrix}\begin{pmatrix} \frac{1}{\sqrt{2}}(X-iY) \\ 0 \end{pmatrix} = \begin{pmatrix} 0 \\ \frac{i}{\sqrt{2}}(X-iY) \end{pmatrix} =$$

$$= \Psi_{hh^-}(\boldsymbol{x})$$

$$\hat{K}\Psi_{hh^-}(\boldsymbol{x}) = -\Psi_{hh^+}(\boldsymbol{x})$$

$$\hat{K}\Psi_{lh^-}(\boldsymbol{x}) = \hat{K}\begin{pmatrix} \frac{1}{\sqrt{6}}(X-iY) \\ \sqrt{\frac{2}{3}}Z \end{pmatrix} = \begin{pmatrix} -i\sqrt{\frac{2}{3}}Z \\ \frac{i}{\sqrt{6}}(X+iY) \end{pmatrix} = \Psi_{lh^+}(\boldsymbol{x})$$

$$\hat{K}\Psi_{lh^+}(\boldsymbol{x}) = -\Psi_{lh^-}(\boldsymbol{x}), \tag{F.4}$$

where we have used $\Psi_{hh^+}(\boldsymbol{x}) = \langle \boldsymbol{x}|hh^+\rangle$. We start again with the matrix element given by Eq.(F.1) and use the relations (F.4) and the notation of Ref. [124]

$$\begin{aligned} j = \boldsymbol{\epsilon}_{TO} \cdot \langle hh^-| \, \boldsymbol{V}_{DP} \, |lh^+\rangle &= \boldsymbol{\epsilon}_{TO} \int \Psi^*_{hh^-}(\boldsymbol{x})\boldsymbol{V}_{DP}\Psi_{lh^+}(\boldsymbol{x})d^3x \\ &= \boldsymbol{\epsilon}_{TO} \int (\hat{K}\Psi_{hh^+}(\boldsymbol{x}))^*\boldsymbol{V}_{DP}\hat{K}\Psi_{lh^-}(\boldsymbol{x})d^3x \\ &= \boldsymbol{\epsilon}_{TO} \int \Psi^*_{lh^-}(\boldsymbol{x})\boldsymbol{V}_{DP}\Psi_{hh^+}(\boldsymbol{x})d^3x \\ &= \boldsymbol{\epsilon}_{TO} \cdot \langle lh^-| \, \boldsymbol{V}_{DP} \, |hh^+\rangle. \end{aligned} \tag{F.5}$$

Here we used in the last step that for an operator $\hat{O}$ which is even upon time reversal (i.e. it doesn't change sign when t is replaced by $-t$) it holds [124]

$$\int (\hat{K}\Psi_n(\boldsymbol{x}))^*\hat{O}\hat{K}\Psi_m(\boldsymbol{x})d^3x = \int \Psi^*_m(\boldsymbol{x})\hat{O}\Psi_n(\boldsymbol{x})d^3x. \tag{F.6}$$

Note that the deformation potential operator as defined in Eq.(5.17) only depends on quantities as coordinates, mass or energy which do not change sign upon time reversal and thus it is even upon time reversal.

Appendix G

Bright exciton transformation for one cavity mode

In this appendix we want to identify the bright excitons in the case where the excitons formed by the states $|hh^+\rangle\,|S\downarrow\rangle\,,|lh^+\rangle\,|S\uparrow\rangle\,,|lh^-\rangle\,|S\downarrow\rangle\,,|hh-\rangle\,|S\uparrow\rangle$, strongly couple to a single cavity mode. We start with the Hamiltonian describing the coupling in the basis $\{|\text{cav}\rangle\,,|\text{lh,+}\rangle\,,|\text{lh,-}\rangle\,,|\text{hh,+}\rangle\,,|\text{hh,-}\rangle\}$

$$H_1 = \begin{pmatrix} E_c & V_l & V_l & V_h & V_h \\ V_l & E_x & 0 & 0 & 0 \\ V_l & 0 & E_x & 0 & 0 \\ V_h & 0 & 0 & E_x & 0 \\ V_h & 0 & 0 & 0 & E_x \end{pmatrix}, \tag{G.1}$$

where we assumed that all the excitons have the same energy. Diagonalization yields

$$H_2 = \begin{pmatrix} E_x & 0 & 0 & 0 & 0 \\ 0 & E_x & 0 & 0 & 0 \\ 0 & 0 & E_x & 0 & 0 \\ 0 & 0 & 0 & \hbar\omega_- & 0 \\ 0 & 0 & 0 & 0 & \hbar\omega_+ \end{pmatrix}, \tag{G.2}$$

where $\hbar\omega_\pm = \frac{1}{2}(E_c + E_x \pm \sqrt{8(V_h^2 + V_l^2) + \delta^2})$, with $\delta = E_c - E_x$. The eigenvectors are given the three dark exciton states (D1..D3) and by the lower and upper exciton polariton

state (LXP and UXP respectively)

$$
|\text{D1}\rangle = \frac{1}{\sqrt{V_l^2 + V_h^2}} \begin{pmatrix} 0 \\ -V_h \\ 0 \\ 0 \\ V_l \end{pmatrix} \qquad |\text{D2}\rangle = \frac{1}{\sqrt{V_l^2 + V_h^2}} \begin{pmatrix} 0 \\ -V_h \\ 0 \\ V_l \\ 0 \end{pmatrix} \qquad |\text{D3}\rangle = \frac{1}{\sqrt{2}} \begin{pmatrix} 0 \\ -1 \\ 1 \\ 0 \\ 0 \end{pmatrix}
$$

$$
|\text{LXP}\rangle = \frac{1}{\tilde{V}} \begin{pmatrix} -C\tilde{V} \\ XV_l \\ XV_l \\ XV_h \\ XV_h \end{pmatrix} \qquad |\text{UXP}\rangle = \frac{1}{\tilde{V}} \begin{pmatrix} X\tilde{V} \\ CV_l \\ CV_l \\ CV_h \\ CV_h \end{pmatrix}, \tag{G.3}
$$

with $\tilde{V} = \sqrt{2(V_l^2 + V_h^2)}$ and

$$
X = \sqrt{\frac{\sqrt{8(V_h^2 + V_l^2) + \delta^2} + \delta}{2\sqrt{8(V_h^2 + V_l^2) + \delta^2}}} \qquad C = \sqrt{\frac{\sqrt{8(V_h^2 + V_l^2) + \delta^2} - \delta}{2\sqrt{8(V_h^2 + V_l^2) + \delta^2}}}. \tag{G.4}
$$

The Hamiltonian in the basis of bright and dark excitons $\{|\text{D1}\rangle, |\text{D2}\rangle, |\text{D3}\rangle, |\text{cav}\rangle, |\text{B}\rangle\}$ can be identified using the transformation

$$
H_3 = \mathcal{D} H_2 \mathcal{D}^{-1} = \begin{pmatrix} E_x & 0 & 0 & 0 & 0 \\ 0 & E_x & 0 & 0 & 0 \\ 0 & 0 & E_x & 0 & 0 \\ 0 & 0 & 0 & E_c & \tilde{V} \\ 0 & 0 & 0 & \tilde{V} & E_x \end{pmatrix}, \tag{G.5}
$$

with transformation matrix

$$
\mathcal{D} = \begin{pmatrix} 1 & 0 & 0 & 0 & 0 \\ 0 & 1 & 0 & 0 & 0 \\ 0 & 0 & 1 & 0 & 0 \\ 0 & 0 & 0 & -C & X \\ 0 & 0 & 0 & X & C \end{pmatrix}. \tag{G.6}
$$

Now the light and heavy hole states can be linked to the bright and dark exciton states via

$$
\begin{pmatrix} |\text{cav}\rangle \\ |\text{lh},+\rangle \\ |\text{lh},-\rangle \\ |\text{hh},+\rangle \\ |\text{hh},-\rangle \end{pmatrix} = R^{-1} D \begin{pmatrix} |\text{D1}\rangle \\ |\text{D2}\rangle \\ |\text{D3}\rangle \\ |\text{cav}\rangle \\ |\text{B}\rangle \end{pmatrix} , \tag{G.7}
$$

where R contains the vectors $|\text{D1}\rangle, |\text{D2}\rangle, |\text{D3}\rangle, |\text{cav}\rangle, |\text{B}\rangle$ as rows. Finally we obtain

$$
\left| lh^{\pm} \right\rangle \propto \frac{V_l}{\tilde{V}} |\text{B}\rangle \qquad \left| hh^{\pm} \right\rangle \propto \frac{V_h}{\tilde{V}} |\text{B}\rangle . \tag{G.8}
$$

We write the Hamiltonian given in Eq.(5.40) in the new basis

$$
\begin{aligned}
s_{\boldsymbol{K}}^{\dagger}(hh^-) s_{\boldsymbol{K'}}(lh^+) &= \left| hh^- \right\rangle \left\langle lh^+ \right| \propto \frac{V_l V_h}{\tilde{V}^2} |\text{B}\rangle \langle \text{B}| \\
s_{\boldsymbol{K}}^{\dagger}(lh^+) s_{\boldsymbol{K'}}(hh^-) &= \left| lh^+ \right\rangle \left\langle hh^- \right| \propto \frac{V_l V_h}{\tilde{V}^2} |\text{B}\rangle \langle \text{B}| \\
s_{\boldsymbol{K}}^{\dagger}(hh^+) s_{\boldsymbol{K'}}(lh^-) &= \left| hh^+ \right\rangle \left\langle lh^- \right| \propto \frac{V_l V_h}{\tilde{V}^2} |\text{B}\rangle \langle \text{B}| \\
s_{\boldsymbol{K}}^{\dagger}(lh^-) s_{\boldsymbol{K'}}(hh^+) &= \left| lh^- \right\rangle \left\langle hh^+ \right| \propto \frac{V_l V_h}{\tilde{V}^2} |\text{B}\rangle \langle \text{B}|
\end{aligned} \tag{G.9}
$$

We see that all terms in Eq.(5.40) contain the same portion of the bright exciton. As two terms are multiplied with j and two terms are multiplied with $-j$, the contributions add up to zero.

Bibliography

[1] C. Kittel, *Einführung in die Festkörperphysik* (R. Oldenbourg Verlag, München, 1991).

[2] I. M. Georgescu, S. Ashhab, and F. Nori, *Quantum simulation*, Rev. Mod. Phys. **86**, 153 (2014).

[3] R. P. Feynman, *Simulating physics with computers*, International Journal of Theoretical Physics **21**, 467 (1982).

[4] I. Bloch, *Ultracold quantum gases in optical lattices*, Nature Physics **1**, 23 (2005).

[5] A. Wobst, *Chaos im Festkörper: Phasenraum-& Zufallsmatrixmethoden*, PhD thesis, 2003.

[6] P. W. Anderson, *Absence of diffusion in certain random lattices*, Phys. Rev. **109**, 1492 (1958).

[7] J. Billy, V. Josse, Z. Zuo, A. Bernard, B. Hambrecht, P. Lugan, D. Clément, L. Sanchez-Palencia, P. Bouyer, and A. Aspect, *Direct observation of Anderson localization of matter waves in a controlled disorder*, Nature **453**, 891 (2008).

[8] C. Aulbach, A. Wobst, G.-L. Ingold, P. Hänggi, and I. Varga, *Phase-space visualization of a metal–insulator transition*, New J. Phys. **6**, 70 (2004).

[9] G. André and S. Aubry, *Analyticity breaking and anderson localization in incommensurate lattices*, Ann. Isr. Phys. Soc. **3**, 133 (1979).

[10] P. G. Harper, *The General Motion of Conduction Electrons in a Uniform Magnetic Field, with Application to the Diamagnetism of Metals*, Proc. Phys. Soc. A **68**, 879 (1955).

[11] G. Roati, C. D'Errico, L. Fallani, M. Fattori, C. Fort, M. Zaccanti, G. Modugno, M. Modugno, and M. Inguscio, *Anderson localization of a non-interacting Bose-Einstein Condensate*, Nature **453**, 895 (2008).

[12] H. Ritsch, P. Domokos, F. Brennecke, and T. Esslinger, *Cold atoms in cavity-generated dynamical optical potentials*, Rev. Mod. Phys. **85**, 553 (2013).

[13] M. Tonouchi, *Cutting-edge terahertz technology*, Nature Photonics **1**, 97 (2007).

[14] J. Faist, F. Capasso, D. L. Sivco, C. Sirtori, A. L. Hutchinson, and A. Y. Cho, *Quantum cascade laser*, Science **264**, 553 (1994).

[15] R. Köhler, A. Tredicucci, F. Beltram, H. E. Beere, E. H. Linfield, A. G. Davies, D. A. Ritchie, R. C. Iotti, and F. Rossi, *Terahertz semiconductor-heterostructure laser*, Nature **417**, 156 (2002).

[16] M. A. Belkin and F. Capasso, *New frontiers in quantum cascade lasers: high performance room temperature terahertz sources*, Physica Scripta **90**, 118002 (2015).

[17] I. Carusotto and C. Ciuti, *Quantum fluids of light*, Rev. Mod. Phys. **85**, 299 (2013).

[18] J. Kasprzak *et al.*, *Bose-Einstein condensation of exciton polaritons*, Nature **443**, 409 (2006).

[19] J. Keeling, L. Sieberer, E. Altman, L. Chen, S. Diehl, and J. Toner, *Superfluidity and phase correlations of driven dissipative condensates*, arXiv preprint arXiv:1601.04495 (2016).

[20] A. V. Kavokin, I. A. Shelykh, T. Taylor, and M. M. Glazov, *Vertical Cavity Surface Emitting Terahertz Laser*, Phys. Rev. Lett. **108**, 197401 (2012).

[21] F. Barachati, S. De Liberato, and S. Kéna-Cohen, *Generation of Rabi-frequency radiation using exciton-polaritons*, Phys. Rev. A **92**, 033828 (2015).

[22] H. Walther, B. T. H. Varcoe, B.-G. Englert, and T. Becker, *Cavity quantum electro-dynamics*, Rep. Prog. Phys. **69**, 1325 (2006).

[23] R. Miller, T. E. Northup, K. M. Birnbaum, A. Boca, A. D. Boozer, and H. J. Kimble, *Trapped atoms in cavity QED: coupling quantized light and matter*, J. Phys. B: At. Mol. Opt. Phys. **38**, S551 (2005).

[24] C. J. Hood, T. W. Lynn, A. C. Doherty, A. S. Parkins, and H. J. Kimble, *The Atom-Cavity Microscope: Single Atoms Bound in Orbit by Single Photons*, Science **287**, 1447 (2000).

[25] P. Pinkse, T. Fischer, P. Maunz, and G. Rempe, *Trapping an atom with single photons*, Nature **404**, 365 (2000).

[26] G. R. Guthöhrlein, M. Keller, K. Hayasaka, W. Lange, and H. Walther, *A single ion as a nanoscopic probe of an optical field*, Nature **414**, 49 (2001).

[27] B. Casabone, A. Stute, K. Friebe, B. Brandstätter, K. Schüppert, R. Blatt, and T. E. Northup, *Heralded Entanglement of Two Ions in an Optical Cavity*, Phys. Rev. Lett. **111**, 100505 (2013).

[28] A. Reiserer, N. Kalb, G. Rempe, and S. Ritter, *A quantum gate between a flying optical photon and a single trapped atom*, Nature **508**, 237 (2014).

[29] A. Reiserer and G. Rempe, *Cavity-based quantum networks with single atoms and optical photons*, Rev. Mod. Phys. **87**, 1379 (2015).

[30] P. Horak, G. Hechenblaikner, K. M. Gheri, H. Stecher, and H. Ritsch, *Cavity-Induced Atom Cooling in the Strong Coupling Regime*, Phys. Rev. Lett. **79**, 4974 (1997).

[31] V. Vuletić and S. Chu, *Laser Cooling of Atoms, Ions, or Molecules by Coherent Scattering*, Phys. Rev. Lett. **84**, 3787 (2000).

[32] P. Maunz, T. Puppe, I. Schuster, N. Syassen, P. W. Pinkse, and G. Rempe, *Cavity cooling of a single atom*, Nature **428**, 50 (2004).

[33] S. Schreppler, N. Spethmann, N. Brahms, T. Botter, M. Barrios, and D. M. Stamper-Kurn, *Optically measuring force near the standard quantum limit*, Science **344**, 1486 (2014).

[34] A. Parkins and H. Kimble, *Quantum state transfer between motion and light*, J. Opt. B **1**, 496 (1999).

[35] G. Morigi, J. Eschner, S. Mancini, and D. Vitali, *Entangled Light Pulses from Single Cold Atoms*, Phys. Rev. Lett. **96**, 023601 (2006).

[36] R. Reimann, W. Alt, T. Kampschulte, T. Macha, L. Ratschbacher, N. Thau, S. Yoon, and D. Meschede, *Cavity-Modified Collective Rayleigh Scattering of Two Atoms*, Phys. Rev. Lett. **114**, 023601 (2015).

[37] A. Neuzner, M. Körber, O. Morin, S. Ritter, and G. Rempe, *Interference and dynamics of light from a distance-controlled atom pair in an optical cavity*, Nature Photonics **10**, 303 (2016).

[38] P. Domokos and H. Ritsch, *Mechanical effects of light in optical resonators*, J. Opt. Soc. Am. B **20**, 1098 (2003).

[39] S. Schütz, H. Habibian, and G. Morigi, *Cooling of atomic ensembles in optical cavities: Semiclassical limit*, Phys. Rev. A **88**, 033427 (2013).

[40] A. T. Black, H. W. Chan, and V. Vuletić, *Observation of Collective Friction Forces due to Spatial Self-Organization of Atoms: From Rayleigh to Bragg Scattering*, Phys. Rev. Lett. **91**, 203001 (2003).

[41] K. Baumann, C. Guerlin, F. Brennecke, and T. Esslinger, *Dicke quantum phase transition with a superfluid gas in an optical cavity*, Nature **464**, 1301 (2010).

[42] K. Baumann, R. Mottl, F. Brennecke, and T. Esslinger, *Exploring Symmetry Breaking at the Dicke Quantum Phase Transition*, Phys. Rev. Lett. **107**, 140402 (2011).

[43] J. Larson, B. Damski, G. Morigi, and M. Lewenstein, *Mott-Insulator States of Ultracold Atoms in Optical Resonators*, Phys. Rev. Lett. **100**, 050401 (2008).

[44] J. Larson, S. Fernández-Vidal, G. Morigi, and M. Lewenstein, *Quantum stability of Mott-insulator states of ultracold atoms in optical resonators*, New J. Phys. **10**, 045002 (2008).

[45] H. Habibian, A. Winter, S. Paganelli, H. Rieger, and G. Morigi, *Bose-Glass Phases of Ultracold Atoms due to Cavity Backaction*, Phys. Rev. Lett. **110**, 075304 (2013).

[46] J. Klinder, H. Keßler, M. R. Bakhtiari, M. Thorwart, and A. Hemmerich, *Observation of a Superradiant Mott Insulator in the Dicke-Hubbard Model*, Phys. Rev. Lett. **115**, 230403 (2015).

[47] R. Landig, L. Hruby, N. Dogra, M. Landini, R. Mottl, T. Donner, and T. Esslinger, *Quantum phases from competing short-and long-range interactions in an optical lattice*, Nature **532**, 476 (2016).

[48] M. Schreiber, S. S. Hodgman, P. Bordia, H. P. Lüschen, M. H. Fischer, R. Vosk, E. Altman, U. Schneider, and I. Bloch, *Observation of many-body localization of interacting fermions in a quasirandom optical lattice*, Science **349**, 842 (2015).

[49] C. D'Errico, M. Moratti, E. Lucioni, L. Tanzi, B. Deissler, M. Inguscio, G. Modugno, M. B. Plenio, and F. Caruso, *Quantum diffusion with disorder, noise and interaction*, New J. Phys. **15**, 045007 (2013).

[50] G. Modugno, *Anderson localization in Bose–Einstein condensates*, Rep. Prog. Phys. **73**, 102401 (2010).

[51] X. Deng, R. Citro, A. Minguzzi, and E. Orignac, *Phase diagram and momentum distribution of an interacting Bose gas in a bichromatic lattice*, Phys. Rev. A **78**, 013625 (2008).

[52] G. Roux, T. Barthel, I. P. McCulloch, C. Kollath, U. Schollwöck, and T. Giamarchi, *Quasiperiodic Bose-Hubbard model and localization in one-dimensional cold atomic gases*, Phys. Rev. A **78**, 023628 (2008).

[53] D. Tanese, E. Gurevich, F. Baboux, T. Jacqmin, A. Lemaître, E. Galopin, I. Sagnes, A. Amo, J. Bloch, and E. Akkermans, *Fractal Energy Spectrum of a Polariton Gas in a Fibonacci Quasiperiodic Potential*, Phys. Rev. Lett. **112**, 146404 (2014).

[54] F. Alpeggiani, L. C. Andreani, and D. Gerace, *Effective bichromatic potential for ultra-high Q-factor photonic crystal slab cavities*, Appl. Phys. Lett. **107**, 261110 (2015).

[55] M. H. Anderson, J. R. Ensher, M. R. Matthews, C. E. Wieman, and E. A. Cornell, *Observation of Bose-Einstein Condensation in a Dilute Atomic Vapor*, Science **269**, 198 (1995).

[56] K. B. Davis, M. O. Mewes, M. R. Andrews, N. J. van Druten, D. S. Durfee, D. M. Kurn, and W. Ketterle, *Bose-Einstein Condensation in a Gas of Sodium Atoms*, Phys. Rev. Lett. **75**, 3969 (1995).

[57] I. Bloch, J. Dalibard, and W. Zwerger, *Many-body physics with ultracold gases*, Rev. Mod. Phys. **80**, 885 (2008).

[58] C. Ryu, M. F. Andersen, P. Cladé, V. Natarajan, K. Helmerson, and W. D. Phillips, *Observation of Persistent Flow of a Bose-Einstein Condensate in a Toroidal Trap*, Phys. Rev. Lett. **99**, 260401 (2007).

[59] R. Grimm, M. Weidemüller, and Y. B. Ovchinnikov, *Optical dipole traps for neutral atoms*, Adv. At. Mol. Opt. Phys. **42**, 95 (2000).

[60] J. Dalibard, *Des cages de lumière pour les atomes : la physique des pièges et des réseaux optiques*, Lecture at Collège de France, 2013.

[61] C. Cohen-Tannoudji and D. Guéry-Odelin, *Advances in atomic physics* (World Scientific, Singapore, 2011).

[62] G. H. Wannier, *The Structure of Electronic Excitation Levels in Insulating Crystals*, Phys. Rev. **52**, 191 (1937).

[63] D. Jaksch, C. Bruder, J. I. Cirac, C. W. Gardiner, and P. Zoller, *Cold Bosonic Atoms in Optical Lattices*, Phys. Rev. Lett. **81**, 3108 (1998).

[64] J. Sakurai, *Modern Quantum Mechanics* (Addison Wesley Longman, Reading, Massachusetts, 1994).

[65] M. P. A. Fisher, P. B. Weichman, G. Grinstein, and D. S. Fisher, *Boson localization and the superfluid-insulator transition*, Phys. Rev. B **40**, 546 (1989).

[66] M. Greiner, O. Mandel, T. Esslinger, T. W. Hänsch, and I. Bloch, *Quantum phase transition from a superfluid to a Mott insulator in a gas of ultracold atoms*, nature **415**, 39 (2002).

[67] M. Modugno, *Exponential localization in one-dimensional quasi-periodic optical lattices*, New J. Phys. **11**, 033023 (2009).

[68] D. J. Thouless, *Electrons in disordered systems and the theory of localization*, Phys. Rep. **13**, 93 (1974).

[69] D. J. Thouless, *Bandwidths for a quasiperiodic tight-binding model*, Phys. Rev. B **28**, 4272 (1983).

[70] X. Deng, R. Citro, E. Orignac, and A. Minguzzi, *Superfluidity and Anderson localisation for a weakly interacting Bose gas in a quasiperiodic potential*, Eur. Phys. J. B **68**, 435 (2009).

[71] A. O. Caldeira and A. J. Leggett, *Influence of Dissipation on Quantum Tunneling in Macroscopic Systems*, Phys. Rev. Lett. **46**, 211 (1981).

[72] C. Gardiner and P. Zoller, *Quantum Noise* (Springer, Heidelberg, 2004).

[73] C. W. Gardiner and M. J. Collett, *Input and output in damped quantum systems: Quantum stochastic differential equations and the master equation*, Phys. Rev. A **31**, 3761 (1985).

[74] W. P. Schleich, *Quantum optics in phase space* (Wiley-VCH, Berlin, 2001).

[75] D. F. Walls and G. J. Milburn, *Quantum optics* (Springer, Berlin, 1994).

[76] E. Jaynes and F. Cummings, *Comparison of quantum and semiclassical radiation theories with application to the beam maser*, Proc. IEEE **51**, 89 (1963).

[77] H. Habibian, A. Winter, S. Paganelli, H. Rieger, and G. Morigi, *Quantum phases of incommensurate optical lattices due to cavity backaction*, Phys. Rev. A **88**, 043618 (2013).

[78] M. Wolke, J. Klinner, H. Keßler, and A. Hemmerich, *Cavity cooling below the recoil limit*, Science **337**, 75 (2012).

[79] J. Dalibard and C. Cohen-Tannoudji, *Atomic motion in laser light: connection between semiclassical and quantum descriptions*, J. Phys. B: At. Mol. Phys. **18**, 1661 (1985).

[80] S. Fernández-Vidal, G. De Chiara, J. Larson, and G. Morigi, *Quantum ground state of self-organized atomic crystals in optical resonators*, Phys. Rev. A **81**, 043407 (2010).

[81] R. Kraus, *Atom Lokalisierung im quasiperiodischen Licht-Potential*, Masterthesis, Universität des Saarlandes, 2016.

[82] M. Gross and S. Haroche, *Superradiance: an essay on the theory of collective spontaneous emission*, Phys. Rep. **93**, 301 (1982).

[83] F. Brennecke, T. Donner, S. Ritter, T. Bourdel, M. Köhl, and T. Esslinger, *Cavity QED with a Bose–Einstein condensate*, Nature **450**, 268 (2007).

[84] V. Guarrera, L. Fallani, J. Lye, C. Fort, and M. Inguscio, *Inhomogeneous broadening of a Mott insulator spectrum*, New J. Phys. **9**, 107 (2007).

[85] W. Kohn, *Analytic Properties of Bloch Waves and Wannier Functions*, Phys. Rev. **115**, 809 (1959).

[86] M. Peyrard and M. Remoissenet, *Solitonlike excitations in a one-dimensional atomic chain with a nonlinear deformable substrate potential*, Phys. Rev. B **26**, 2886 (1982).

[87] J. K. Asbóth, P. Domokos, and H. Ritsch, *Correlated motion of two atoms trapped in a single-mode cavity field*, Phys. Rev. A **70**, 013414 (2004).

[88] C. Cormick and G. Morigi, *Ion chains in high-finesse cavities*, Phys. Rev. A **87**, 013829 (2013).

[89] T. Fogarty, C. Cormick, H. Landa, V. M. Stojanović, E. Demler, and G. Morigi, *Nanofriction in Cavity Quantum Electrodynamics*, Phys. Rev. Lett. **115**, 233602 (2015).

[90] H. J. Kimble, in *Cavity Quantum Electrodynamics*, edited by P. R. Berman (Academic Press, New York, 1994), p. 203.

[91] H. Habibian, *Cavity Quantum Electrodynamics with Ultracold Atoms*, PhD thesis, 2013.

[92] I. B. Mekhov, C. Maschler, and H. Ritsch, *Probing quantum phases of ultracold atoms in optical lattices by transmission spectra in cavity quantum electrodynamics*, Nature Physics **3**, 319 (2007).

[93] T. Schulte, S. Drenkelforth, J. Kruse, W. Ertmer, J. Arlt, K. Sacha, J. Zakrzewski, and M. Lewenstein, *Routes Towards Anderson-Like Localization of Bose-Einstein Condensates in Disordered Optical Lattices*, Phys. Rev. Lett. **95**, 170411 (2005).

[94] J. F. Sherson, C. Weitenberg, M. Endres, M. Cheneau, I. Bloch, and S. Kuhr, *Single-atom-resolved fluorescence imaging of an atomic Mott insulator*, Nature **467**, 68 (2010).

[95] E. Haller, J. Hudson, A. Kelly, D. A. Cotta, B. Peaudecerf, G. D. Bruce, and S. Kuhr, *Single-atom imaging of fermions in a quantum-gas microscope*, Nature Physics **11**, 738 (2015).

[96] S. Gupta, K. L. Moore, K. W. Murch, and D. M. Stamper-Kurn, *Cavity Nonlinear Optics at Low Photon Numbers from Collective Atomic Motion*, Phys. Rev. Lett. **99**, 213601 (2007).

[97] C. Weisbuch, M. Nishioka, A. Ishikawa, and Y. Arakawa, *Observation of the coupled exciton-photon mode splitting in a semiconductor quantum microcavity*, Phys. Rev. Lett. **69**, 3314 (1992).

[98] Y. Hokomoto, Y. Kadoya, and M. Yamanishi, *THz electromagnetic wave radiation from coherent oscillation of exciton population in high-Q semiconductor microcavities*, Appl. Phys. Lett. **74**, 3839 (1999).

[99] M. A. Kaliteevski, K. A. Ivanov, G. Pozina, and A. J. Gallant, *Single and double bosonic stimulation of THz emission in polaritonic systems*, Scientific Reports **4**, 5444 (2014).

[100] S. Huppert, O. Lafont, E. Baudin, J. Tignon, and R. Ferreira, *Terahertz emission from multiple-microcavity exciton-polariton lasers*, Phys. Rev. B **90**, 241302 (2014).

[101] S. De Liberato, C. Ciuti, and C. C. Phillips, *Terahertz lasing from intersubband polariton-polariton scattering in asymmetric quantum wells*, Phys. Rev. B **87**, 241304 (2013).

[102] J. Kasprzak, D. D. Solnyshkov, R. André, L. S. Dang, and G. Malpuech, *Formation of an Exciton Polariton Condensate: Thermodynamic versus Kinetic Regimes*, Phys. Rev. Lett. **101**, 146404 (2008).

[103] R. W. Andrews, R. W. Peterson, T. P. Purdy, K. Cicak, R. W. Simmonds, C. A. Regal, and K. W. Lehnert, *Bidirectional and efficient conversion between microwave and optical light*, Nature Physics **10**, 321 (2014).

[104] M. Cardona and P. Yu, *Fundamentals of Semiconductors Physics and Materials Properties* (Springer, Berlin, 2010).

[105] O. Madelung, *Introduction to Solid-State Theory* (Springer, Berlin, 1978).

[106] F. Bassani and G. Pastori Parravicini, *Electronic states and optical transitions in solids* (Pergamon Press, Oxford, 1975).

[107] J.-P. Karr, *Effets non linéaires et quantiques dans les microcavités semi-conductrices*, PhD thesis, 2002.

[108] Y. Yamamoto, T. Tassone, and H. Cao, *Semiconductor Cavity Quantum Electrodynamics* (Springer, Berlin, 2000).

[109] M. Combescot and S.-Y. Shiau, *Excitons and Cooper pairs* (Oxford University Press, Oxford, 2015).

[110] Y. Toyozawa, *Theory of line-shapes of the exciton absorption bands*, Progress of Theoretical Physics **20**, 53 (1958).

[111] L. C. Andreani, *Confined electrons and photons* (Plenum Press, New York, 1995), pp. 57–112.

[112] V. Savona, C. Piermarocchi, A. Quattropani, P. Schwendimann, and F. Tassone, *Optical properties of microcavity polaritons*, Phase transitions **68**, 169 (1999).

[113] J. J. Hopfield, *Theory of the Contribution of Excitons to the Complex Dielectric Constant of Crystals*, Phys. Rev. **112**, 1555 (1958).

[114] J.-M. Raimond and S. Haroche, *Exploring the quantum* (Oxford University Press, Oxford, 2006).

[115] V. Savona, *The Physics of Semiconductor Microcavities* (Wiley-VCH, Weinheim, 2007).

[116] O. Penrose and L. Onsager, *Bose-Einstein Condensation and Liquid Helium*, Phys. Rev. **104**, 576 (1956).

[117] G. V. Shlyapnikov, *Quantum degeneracy and Bose–Einstein condensation in low-dimensional trapped gases*, Comptes Rendus de l'Académie des Sciences-Series IV-Physics **2**, 407 (2001).

[118] L. M. Sieberer, S. D. Huber, E. Altman, and S. Diehl, *Dynamical Critical Phenomena in Driven-Dissipative Systems*, Phys. Rev. Lett. **110**, 195301 (2013).

[119] M. Kardar, G. Parisi, and Y.-C. Zhang, *Dynamic Scaling of Growing Interfaces*, Phys. Rev. Lett. **56**, 889 (1986).

[120] H. S. Nguyen, D. Gerace, I. Carusotto, D. Sanvitto, E. Galopin, A. Lemaître, I. Sagnes, J. Bloch, and A. Amo, *Acoustic Black Hole in a Stationary Hydrodynamic Flow of Microcavity Polaritons*, Phys. Rev. Lett. **114**, 036402 (2015).

[121] *Quantum photonics group of Ataç Imamoglu in Zürich*, www.ethz.ch/content/specialinterest/phys/quantum-electronics/quantum-photonics.

[122] *Quantumoptics group of Tilmann Esslinger in Zürich*, www.quantumoptics.ethz.ch.

[123] C. Ciuti and I. Carusotto, *Input-output theory of cavities in the ultrastrong coupling regime: The case of time-independent cavity parameters*, Phys. Rev. A **74**, 033811 (2006).

[124] G. Bir and G. Pikus, *Symmetry and strain-induced effects in Semiconductors* (John Wiley and sons, New York, 1974).

[125] A. K. Ganguly and J. L. Birman, *Theory of Lattice Raman Scattering in Insulators*, Phys. Rev. **162**, 806 (1967).

[126] A. Cantarero, C. Trallero-Giner, and M. Cardona, *Excitons in one-phonon resonant Raman scattering: Deformation-potential interaction*, Phys. Rev. B **39**, 8388 (1989).

[127] G. Fishman, *Semi-conducteurs: les bases de la théorie k.p* (Editions de l'école polytechnique, Palaiseau, 2010).

[128] S. Bloom and T. Bergstresser, *Band structure of α-Sn, InSb and CdTe including spin-orbit effects*, Solid State Communications **6**, 465 (1968).

[129] N. Ashcroft and D. Mermin, *Solid State Physics* (Thomson Learning, United States, 1976).

[130] M. Schall, M. Walther, and P. Uhd Jepsen, *Fundamental and second-order phonon processes in CdTe and ZnTe*, Phys. Rev. B **64**, 094301 (2001).

[131] C. H. Henry and J. J. Hopfield, *Raman Scattering by Polaritons*, Phys. Rev. Lett. **15**, 964 (1965).

[132] R. Scholz, *Hole–phonon scattering rates in gallium arsenide*, J. Appl. Phys. **77**, 3219 (1995).

[133] G. Bir and G. Pikus, *Theory of the deformation potential for semiconductors with a complex band structure*, Fizika Tverdogo Tela **2**, 2287 (1960).

[134] K. Reimann, R. A. Kaindl, and M. Woerner, *Optical deformation-potential scattering of holes in multiple quantum well structures*, Phys. Rev. B **65**, 045302 (2001).

[135] J. M. Luttinger and W. Kohn, *Motion of Electrons and Holes in Perturbed Periodic Fields*, Phys. Rev. **97**, 869 (1955).

[136] B. Henderson and R. H. Bartram, *Crystal-field engineering of solid-state laser materials* (Cambridge University Press, Cambridge, 2005), Vol. 25.

[137] A. Rubio-Ponce, D. Olguín, and I. Hernández-Calderón, *Calculation of effective masses of II-VI semiconductor compounds*, Superficies y Vacío **16**, 26 (2003).

[138] R. André, D. Heger, L. S. Dang, and Y. M. d'Aubigné, *Spectroscopy of polaritons in CdTe-based microcavities*, Journal of crystal growth **184**, 758 (1998).

[139] W. Pötz and P. Vogl, *Theory of optical-phonon deformation potentials in tetrahedral semiconductors*, Phys. Rev. B **24**, 2025 (1981).

[140] *The Physics of Semiconductor Microcavities*, edited by B. Deveaud (John Wiley and sons, Weinheim, 2007).

[141] R. Boyd, *Nonlinear Optics* (Academic Press, London, 2008).

[142] S. Blum, G. A. Olivares-Rentería, C. Ottaviani, C. Becher, and G. Morigi, *Single-photon frequency conversion in nonlinear crystals*, Phys. Rev. A **88**, 053807 (2013).

[143] R. Houdré, C. Weisbuch, R. P. Stanley, U. Oesterle, P. Pellandini, and M. Ilegems, *Measurement of Cavity-Polariton Dispersion Curve from Angle-Resolved Photoluminescence Experiments*, Phys. Rev. Lett. **73**, 2043 (1994).

[144] A. Baas, J. P. Karr, H. Eleuch, and E. Giacobino, *Optical bistability in semiconductor microcavities*, Phys. Rev. A **69**, 023809 (2004).

[145] M. Richard, private communication, 2016.

[146] W. Greiner, *Classical Electrodynamics* (Springer, New York, 1998).

[147] D. Akitt, C. J. Johnson, and P. Coleman, *Nonlinear Susceptibility of CdTe*, IEEE Journal of Quantum Electronics **6**, 496 (1970).

[148] F. Li, L. Orosz, O. Kamoun, S. Bouchoule, C. Brimont, P. Disseix, T. Guillet, X. Lafosse, M. Leroux, J. Leymarie, M. Mexis, M. Mihailovic, G. Patriarche, F. Réveret, D. Solnyshkov, J. Zuniga-Perez, and G. Malpuech, *From Excitonic to Photonic Polariton Condensate in a ZnO-Based Microcavity*, Phys. Rev. Lett. **110**, 196406 (2013).

[149] A. Trichet, L. Sun, G. Pavlovic, N. Gippius, G. Malpuech, W. Xie, Z. Chen, M. Richard, and L. S. Dang, *One-dimensional ZnO exciton polaritons with negligible thermal broadening at room temperature*, Phys. Rev. B **83**, 041302 (2011).

[150] G. Christmann, R. Butté, E. Feltin, A. Mouti, P. A. Stadelmann, A. Castiglia, J.-F. m. c. Carlin, and N. Grandjean, *Large vacuum Rabi splitting in a multiple quantum well GaN-based microcavity in the strong-coupling regime*, Phys. Rev. B **77**, 085310 (2008).

[151] J. C. Slater and W. Shockley, *Optical Absorption by the Alkali Halides*, Phys. Rev. **50**, 705 (1936).

[152] A. L. Fetter and J. D. Walecka, *Quantum theory of many-particle systems* (McGraw-Hill Book Company, New York, 1971).

[153] L. Piela, *Ideas of Quantum Chemistry* (Elsevier, Waltham, 2014).

Acknowledgements

I want to thank everybody who was directly or indirectly involved in the genesis of this thesis.

First of all I would like to express my deep gratitude to my supervisors and Doktormütter Dr. Anna Minguzzi and Prof. Dr. Giovanna Morigi, who made this French-German PhD project possible. Thank you very much for navigating me through these three years, for your inspiring enthousiasm for physics, for your continuous support, encouragement and confidence.

I am also very grateful for the opportunity to experience two research environments and to work in strong collaboration with experimentalists. In this context I want to give special thanks to my co-encadrant Dr. Maxime Richard. Thank you for your supervision, advice and patience with me and my endless questions.

I wish to acknowledge financial and ideational support from the Laboratoire d'Alliances Nanoscience-Énergie du Futur (LANEF) and the Deutsch-Französische Hochschule (DFH) as well as counseling by Dr. Joel Cibert.

My grateful thanks are also extended to all people in the LPMMC in Grenoble and the former and actual members of the theoretical quantum physics group in Saarbrücken for creating a pleasant, welcoming, stimulating atmosphere and for their assistance.

Danke Ralf, Simon und Oxana für die nette Büronachbarschaft und eure Hilfe bei fundamentalen Problemen und Alltagskatastrophen. Danke Susanne, Oxana, Marc, Luigi, Stefan, Florian, Andreas, Tim für die netten Diskussionen über Physik und anderes, eure Hilfsbereitschaft und die schöne gemeinsame Zeit. Thank you Mossy and Hessam for our nice and fruitful collaboration. Vielen Dank Rebecca für die spannende, unterhaltsame und produktive Zusammenarbeit, unsere (physikalischen und unphysikalischen) Gespräche, für deine Hilfe im Zusammenschreibendspurt und dafür, dass du mich mit deiner Begeisterung für unser Projekt immer weiter motiviert hast. Herzlichen Dank auch an Frau Michel und Frau Francois für ihre Hilfe beim Kampf mit allen möglichen Formalitäten, beispielsweise zur cotutelle.

Curriculum Vitae

Name	Katharina Rojan
Address	30 rue de New York, 38000 Grenoble
Date of birth	25.04.1989
Place of birth	Sankt Wendel
Nationality	German

- Phd in physics at Universität des Saarlandes and Université Grenoble Alpes

  2014 - present

- Binational Master in physics, Universität des Saarlandes and Université Lorraine

  2011-2014

- Bachelor in physics, Universität des Saarlandes

  2008-2011

- Highschool Gymnasium Wendalinum Sankt Wendel

  1995-2008